Impedance Tuning: A Method for Active Control of the Acoustic Boundary Conditions of Combustion Test Rigs

vorgelegt von
Mirko R. Bothien,
Diplom-Ingenieur (RWTH Aachen),
aus Berlin

Von der Fakultät V – Verkehrs- und Maschinensysteme
der Technischen Universität Berlin
zur Erlangung des akademischen Grades

Doktor der Ingenieurwissenschaften
– Dr.-Ing. –

genehmigte Dissertation

Promotionsausschuss:

Vorsitzender:	Prof. Dr.-Ing. Dieter Peitsch
Gutachter:	Prof. Dr.-Ing. Christian Oliver Paschereit
Gutachter:	Prof. Dr.-Ing. Thomas Sattelmayer (TU München)
Gutachter:	Dr. ès sc. Bruno Schuermans (ALSTOM (Switzerland) Ltd.)

Tag der wissenschaftlichen Aussprache: 10. Dezember 2008

Berlin 2008
D 83

„Werd' ich zum Augenblicke sagen:
Verweile doch! du bist so schön!“
J. W. v. Goethe, Faust I.

Vorwort

Die vorliegende Arbeit entstand während meiner Tätigkeit als Wissenschaftlicher Mitarbeiter am Fachgebiet Experimentelle Strömungsmechanik des Instituts für Strömungsmechanik und Technische Akustik der Technischen Universität Berlin. An dieser Stelle möchte ich mich bei den Menschen bedanken, die zum Gelingen dieser Dissertation beigetragen haben.

Mein ganz besonderer Dank gilt meinem Doktorvater, Herrn Prof. Dr.-Ing. Christian Oliver Paschereit, zunächst einmal dafür, dass ich solch ein interessantes Thema in einem so professionellen Umfeld bearbeiten konnte. Zudem trug seine fachliche Unterstützung wie auch die immer wieder von neuem anspruchsvolle Zielsetzung maßgeblich zur vorliegenden Arbeit bei. Die große Freiheit in der Bearbeitung des Themas ermöglichte es, die eigene Kreativität optimal zu entfalten. Auch die persönliche Seite betreffend, waren und sind Sie, lieber Professor Paschereit, ein wichtiger Mentor für mich. Ich danke Ihnen für die zahl- und sehr hilfreichen Gespräche, die wir der Planung meiner beruflichen Karriere wegen führten.

Sehr herzlich bedanke ich mich auch bei meinen beiden externen Gutachtern, Herrn Prof. Dr.-Ing. Thomas Sattelmayer und Herrn Dr. ès sc. Bruno Schuermans, für die es selbstverständlich war, die Dissertation in sehr kurzer Zeit zu begutachten und deren Arbeiten mich in einigen Punkten inspirierten. In diesem Zusammenhang möchte ich es auch nicht unerwähnt lassen, dass ich mich auf die zukünftige Zusammenarbeit mit Dir, Bruno, sehr freue.

Herrn Prof. Dr.-Ing. Dieter Peitsch, mit dem mich das Studium der Turbomaschinen- und Strahlantriebe an der RWTH Aachen verbindet, danke ich sehr dafür, dass er den Vorsitz des Promotionsausschusses übernommen hat.

Ich hatte das Glück, dass meine Dissertation sich in vielen Punkten mit dem Hauptprojekt, das ich an unserem Fachgebiet bearbeitete, überschnitt. Im Rahmen dieses von der AG Turbo geförderten Projekts (COOREFF-T 2.2.2) kooperierten wir eng mit unserem Industriepartner Siemens Energy. Stellvertretend bei Herrn Dr.-Ing. Werner Krebs möchte ich mich dafür recht herzlich bedanken. Für die finanzielle Unterstützung zeichnete neben Siemens auch das Bundesministerium für Technologie und Wirtschaft verantwortlich.

Am intensivsten zusammengearbeitet habe ich natürlich mit den anderen Wissenschaftlichen Mitarbeitern des Fachgebiets. Ihre große Hilfsbereitschaft und Motivation sowie die freundschaftliche Atmosphäre habe ich sehr geschätzt. Vor allem die enge Zusammenarbeit mit den Jungs aus dem dritten Stock, dem „HFI-Penthouse“, werde ich sehr vermissen; dies sind Daniel Guyot, Arnaud Lacarelle (Danke für die Kameraaufnahmen der Flamme, die in der Arbeit gezeigt werden und deren Auswertung.), Jonas Moeck und Sebastian Schimek.

Hervorheben möchte ich Jonas Moeck, der entscheidend zum Gelingen meiner Arbeit beigetragen hat. Zusammen haben wir die ersten Impedance Tuning Versuche realisiert. Einige der wichtigsten ersten Datenschriebe (auf „mbshared“) datieren von der Nacht zum Sonntag, den 05.02.2007, 1:54 Uhr, einer der zahlreichen Nacht- und Wochenendschichten, die wir gemeinsam im Brennkammerlabor verbrachten, um die jeweiligen Deadlines zu erfüllen. Nach der Deadline ist vor der Deadline. Vielen Dank, Jonas, für die unzähligen fachlichen Diskussionen sowie Deine nützlichen Kommentare und Anregungen zur Dissertation.
All jene Dinge aufzuzählen, bei denen mir Lilli Lindemann in meiner Zeit am Institut geholfen hat, würde den Rahmen des Vorworts sprengen. Hierfür sowie für die vielen kurzweiligen Gespräche und das „sich-um-Alles-kümmern“, vielen Dank.
Aufgrund der stark experimentellen Ausrichtung der Arbeit, war ich sehr auf die Mithilfe unserer Werkstätten angewiesen. Für die kompetente, qualitativ hochwertige, gründliche und oft kreative Arbeit möchte ich deswegen Thorsten Dessin, Willi Postel, Horst Mettchen und Axel Bendiks aus der Metallwerkstatt sowie unserem Elektroniker Heiko Stolpe einen großen Dank aussprechen.
Bei Dr.-Ing. Navid Nayeri möchte ich mich für sein Engagement sowie alle organisatorischen Arbeiten, die die fruchtbare Arbeitsatmosphäre am Institut überhaupt erst ermöglichen, sehr bedanken.
Des Weiteren hat unsere Systemadministratorin Angela Pätzold bei zahlreichen Fragen (und Wünschen) rund um den Rechner immer kompetenten Rat gewusst und mir bei allen Problemen umgehend geholfen. Vielen Dank hierfür.
Ich bedanke mich bei allen Studenten, die mich im Laufe meiner Zeit am Institut unterstützt haben. Dies waren vor allem Robert Bock, Henning Kroll, Sascha Mader und Markus Paul.
Evelyn Kulzer und Rainer Nagel danke ich dafür, dass sie mir immer geholfen haben, wenn ich mich mit einer Frage oder Bitte an sie gewendet habe.
So wichtig das fachliche Umfeld für das Gelingen der Dissertation auf der einen Seite war, so wichtig waren meine Freunde auf der anderen. Meiner Meinung nach sind nachhaltiger beruflicher Erfolg, Kreativität und anhaltender Spaß an der Arbeit nur dann möglich, wenn ein starkes privates Umfeld einen Ausgleich schafft. Ich hatte das große Glück, dass ich in allen Städten, in denen ich bis jetzt gelebt habe, sehr gute Freunde gefunden habe, die mir dies boten.
Die wichtigste Person für mich, die die dreieinhalb Jahre der Dissertation am intensivsten miterlebte, mich dabei emotional unterstützte und mir dadurch sehr half, war und ist meine Freundin, Franziska Ramser.
Allen vorher Genannten hätte ich jedoch nie danken können, wenn mir nicht meine Familie, allen voran meine Eltern, Barbara und Dr.-Ing. Mihajlo R. Bothien und meine Oma, Katharina Thyssen, es überhaupt ermöglicht hätten zu promovieren. Liebe Mama, lieber Papa, liebe Omi, euch kann ich für all das, was ihr in den letzten knapp 30 Jahren für mich getan habt, wie ihr mich gefördert – intellektuell sowie finanziell – und euch um mich gekümmert habt, nie genug danken.

Berlin, im Oktober 2008 *Mirko Ruben Bothien*

Zusammenfassung

Eine der größten Herausforderungen für die Entwicklung zukünftiger schadstoffarmer Gasturbinenkraftwerke ist die Gewährleistung eines stabilen Verbrennungsprozesses. Um die immer strikter werdenden Emissionsrichtlinien, vor allem hinsichtlich NO_x, zu erfüllen, führte die Gasturbinenindustrie die Mager-Vormisch-Verbrennung ein. Zwar kann so den Regierungsvorgaben entsprochen werden, jedoch ist diese Art der Verbrennung anfälliger für das Auftreten selbsterregter Verbrennungsschwingungen. Diese thermoakustisch induzierten Instabilitäten resultieren aus einer Kopplung des akustischen Feldes in der Brennkammer mit Schwankungen in der Wärmefreisetzung. Wenn die Phasenbeziehung zwischen den beiden Mechanismen derart ist, dass sie konstruktiv miteinander interferieren, entstehen Wärmefreisetzungs- und Druckfluktuationen, die hohe Amplituden erreichen und damit den Verbrennungsprozess nachteilig beeinflussen können. Thermoakustische Instabilitäten erhöhen die mechanische Bauteilbelastung sowie die Schadstoff- und Geräuschemissionen und können im schlimmsten Fall sogar zur Zerstörung der Maschine führen.
Innerhalb des Entwicklungsprozesses neuer Gasturbinen kommt der Entwicklung des Brenners eine immens wichtige Rolle zu, da er die Maschinenkomponente ist, die den größten Einfluss auf die Stabilität der Verbrennung hat. Da es bei weitem zu aufwendig und kostenintensiv wäre, die Eigenschaften neuer Brenner in jeder Entwicklungsphase in der Gasturbine zu testen, werden stattdessen Versuche an Brennerprüfständen durchgeführt. Mit Hilfe dieser Versuche, numerischer Berechnungsmethoden – wie CFD und FEM – sowie niederdimensionaler Netzwerkanalysen wird versucht, das Verhalten des Brenners in der Gasturbine vorherzusagen. Dabei liegt das Hauptaugenmerk auf einer Bewertung der thermoakustischen Stabilität und den Schadstoffemissionen. Da das thermoakustische Verhalten sehr stark von den akustischen Randbedingungen der jeweiligen Brennkammer abhängt, ist es nahe liegend, dass die Randbedingungen im Prüfstand jenen in der Gasturbine entsprechen oder ihnen zumindest nahe kommen sollten. Dies ist üblicherweise jedoch nicht der Fall. Deshalb ist es möglich, dass der Verbrennungsprozess im Prüfstand bei bestimmten Betriebsbedingungen stabil ist, in der Gasturbine bei gleichen Bedingungen hingegen Instabilitäten aufweist.
Aus diesem Grund wird in dieser Dissertation die Entwicklung einer neuen Versuchsmethodik vorgestellt, die, basierend auf einem aktiven Regelalgorithmus, in der Lage ist, die akustischen Randbedingungen von Brennerprüfstanden so zu beeinflussen, dass sie mit denen in der Gasturbine übereinstimmen. Um das Eingangssignal für den Regler zu erhalten, wird das ebene akustische Feld im System gemessen und instantan, d.h. im Zeitbereich, in stromab- und stromaufwärts laufende Wellen zerlegt. Ein modellbasierter

Regler generiert daraus das Steuersignal für einen akustischen Aktuator, der das akustische Feld in vorgeschriebener Art und Weise manipuliert. Dadurch ist es möglich, die akustischen Randbedingungen in einem breiten Frequenzintervall stufenlos zwischen reflektionsfrei und vollständig reflektierend einzustellen. Mit Hilfe des Regelkonzepts werden die Randbedingungen eines atmosphärischen Brennerprüfstands, der mit einem drallstabilisierten Brenner ausgerüstet ist, gezielt für die kalte als auch die reagierende Strömung verändert. So wird beispielsweise die Länge des Prüfstands virtuell, d.h. ohne Änderung der Prüfstandsgeometrie, modifiziert, mit dem Resultat, dass die Resonanzfrequenzen des geregelten Systems sich von denen des ungeregelten unterscheiden. Außerdem ist es möglich, die akustische Randbedingung derart einzustellen, dass sie der einer kritisch durchströmten Düse entspricht, ohne dass der vorherrschende Strömungszustand tatsächlich kritisch ist. Somit ist zum ersten Mal überhaupt der experimentelle Nachweis dafür erbracht, dass die Randbedingungen eines Einzelbrennerprüfstands aktiv an die der Gasturbine angepasst werden können.
Zunächst werden Lautsprecher als akustische Aktuatoren verwendet, um das Konzept experimentell zu validieren und seine Leistungsfähigkeit zu bewerten. Hervorragende Ergebnisse, die Möglichkeit eines Einsatzes in breiten Frequenzbereichen und die bequeme Handhabung qualifizieren Lautsprecher für Versuche unter Laborbedingungen sowie zur Validierung und Optimierung des Regelkonzeptes. Eines der Hauptziele dieser Dissertation ist es jedoch, eine profunde Basis dafür zu legen, dass die Versuchsmethodik zu einem Standardwerkzeug in der industriellen Brennerentwicklung werden kann. Da Lautsprecher für den Einsatz in Industrieprüfständen höchstwahrscheinlich nicht robust genug sind und ihre akustische Leistung vor allem unter erhöhtem Systemdruck nicht ausreichend ist, werden zusätzlich andere Aktuatoren untersucht. Mit zwei dieser Aktuatorkonzepte – Proportionalventile und ein elektro-pneumatischer Aktuator – ist es möglich, ähnlich gute Resultate wie mit den Lautsprechern zu erzielen. Beiden liegt dasselbe Prinzip zu Grunde: Durch die Modulation eines Luftmassenstroms wird eine akustische Anregung erzeugt. Um den voneinander abweichenden Übertragungscharakteristiken der Aktuatoren Rechnung zu tragen, kommen unterschiedliche Regelalgorithmen zum Einsatz. Zurzeit werden Industrieprüfstände umgerüstet, um dort die Anwendung des Regelkonzepts mit diesen Aktuatoren zu ermöglichen.
Außer zur Verbesserung des Entwicklungsprozesses neuer Brenner, kann das Regelkonzept auch in anderen Bereichen angewendet werden. Durch die gezielte Regelung der akustischen Randbedingungen von Verbrennungssystemen ist es möglich, den thermoakustischen Kopplungsmechanismus zu unterbrechen und so Verbrennungsinstabilitäten zu unterdrücken. Um dies zu erreichen, können entweder die akustischen Verluste über die Systemgrenzen durch eine Herabsenkung der Reflexion vergrößert werden, oder die Phasenbeziehung zwischen Akustik und Schwankung der Wärmefreisetzung durch eine geeignete Manipulation verändert werden. Die gezielte Transition von instabiler zu stabiler Verbrennung (und umgekehrt) ermöglicht es zudem, die Vorhersagequalität akustischer Netzwerkmodelle anhand experimenteller Daten zu bewerten. Die Vorhersagen der Netzwerksimulationen werden hinsichtlich der linearen Anfachungsrate, des Übergangs von Stabilität zu Instabilität sowie der Frequenz der Mode mit der geringsten Stabilität untersucht.

Abstract

One of the main issues for the development of low-emission gas turbine power plants is the stability of the combustion process. In order to follow stringent NO_x emission restrictions, lean-premixed combustion was introduced by the gas turbine industry. Combustion systems operating in this mode are, however, susceptible to self-excited oscillations arising due to an interaction of the unsteady heat release and the acoustic field in the combustion chamber. If the two mechanisms constructively interfere, high amplitude pressure and heat release fluctuations occur, which have a detrimental effect on the combustion process. These so-called thermoacoustic instabilities cause structural wear, increase noise and pollutant emissions, and can even lead to engine failure.

The most important component influencing the tendency to thermoacoustic instabilities is the burner, making its development a crucial task. Since it is far too expensive, the quality of new burner generations cannot in each step of the design process be assessed in the full-scale engine. This is usually accomplished by means of extensive experimental investigations in combustion test rigs. These experiments in conjunction with computational fluid dynamics, finite element calculations, and low-order network models are then used to predict the burner's performance in the full-scale engine. Especially, information about the thermoacoustic behaviour and the emissions is very important. As the thermoacoustics strongly depend on the acoustic boundary conditions of the system, it is obvious that test rig conditions should match or be close to those of the full-scale engine. This is, however, generally not the case. Hence, if the combustion process in the test rig is stable at certain operating conditions, it may show unfavourable dynamics at the same conditions in the engine.

In this dissertation, therefore, a method is developed which uses an active control scheme to manipulate the acoustic boundary conditions of combustion test rigs. To achieve this, multiple pressure measurements are used to decompose the plane wave acoustic field in the system online, i.e., in the time domain, into its up- and downstream propagating parts to generate the control input. A model-based controller calculates the driving signal for an acoustic actuator, which manipulates the acoustic field. Using this method, the boundary conditions can be continuously modified, ranging from anechoic to fully reflecting in a broad frequency range. The concept is applied to an atmospheric combustion test rig with a swirl-stabilized burner both in isothermal and reactive flow conditions. For the first time, it is shown that the test rig properties can be tuned to correspond to those of the full-scale engine. For example, the test rig length can be virtually extended, thereby introducing different resonance frequencies, without having to implement any hardware changes. Furthermore, the acoustic boundary condition can be changed to that of a choked flow without

the need that the flow is actually choked.
The concept is first experimentally validated and thoroughly assessed by using woofers as actuating devices. Excellent results, operability over a broad frequency range, and easy handling make woofers the number one choice for lab-scale experiments and optimization as well as validation of the control scheme. One major objective of this thesis is, however, to provide a profound basis for the control concept to become a standard tool in the industrial burner development process. Since woofers most probably will not withstand the harsh environmental conditions encountered in industrial test rigs and do not exhibit sufficient control authority, especially at elevated pressures and high thermal powers, other actuators are tested to avoid these shortcomings. Two of these, a proportional high-bandwidth valve and an electro-pneumatic transducer, both relying on the same principle of modulating high air mass flows, prove to be able to produce almost as good results as it is the case for the woofers. Different formulations of the controller, tailored to satisfy the specific needs posed by the different actuators, are set up. Currently, industrial test rigs are prepared to allow for the application of the control concept with these actuators.
Besides its main objective of improving the burner development process, the control scheme has also alternative fields of applications. Controlling the acoustic boundary conditions of combustion systems is an effective means to disrupt the thermoacoustic feedback cycle to mitigate combustion instabilities. This can either be done by increasing the losses across the system boundaries or by manipulating the phase relationship between unsteady heat release and acoustic field. Being, thus, able to invoke a controlled transition from instability to stability and vice versa, allows to experimentally assess the predictive capabilities of low-order network models. This is done regarding frequency of the least stable mode, linear growth rate, and transition from stable to unstable operation.

Contents

List of Figures

List of Tables

Nomenclature

Latin characters

$\begin{smallmatrix}\mathbf{A} & \mathbf{B}\\ \mathbf{C} & \mathbf{D}\end{smallmatrix}$	state-space matrices	-
A, C	constants	-
a, b	constants	-
$\mathcal{A}$	attenuation of first higher order mode	-
C	complex calibration coefficient	-
c	speed of sound	m/s
c_{NO}	concentration of NO	$\mathrm{mol/m^3}$
c_p	heat capacity at constant pressure	$\mathrm{J\,kg^{-1}\,K^{-1}}$
c_v	heat capacity at constant volume	$\mathrm{J\,kg^{-1}\,K^{-1}}$
D	wave decomposer	-
d	diameter	m
E_{a}	activation energy	J/mol
e	control signal	V
e	specific internal energy	J/kg
$\mathcal{E}$	acoustic energy density	$\mathrm{J/m^3}$
f	downstream travelling wave	m/s
f	frequency	Hz
f	placeholder for external forces	$\mathrm{kg/m^3}$, $\mathrm{kg\,m^{-2}\,s^{-1}}$, $\mathrm{J/m^3}$
$\boldsymbol{\mathcal{F}}$	acoustic energy flux	$\mathrm{J/m^2}$
$\mathcal{F}$	flame transfer function	$\mathrm{W\ (m/s)^{-1}}$
G	actuator transfer function	-
g	upstream travelling wave	m/s
$\mathbf{H}$	matrix accounting for wave propagation between microphones	-
$\mathbf{I}$	identity matrix	-
J_m	m-th order Bessel function of the first kind	-
j, m, n	counters	-
K	(transfer function of) control law	-
k	wave number ($k = \omega/c$)	1/m
L	length	m
l	length	m
$\dot{m}$	mass flow	kg/s
$\mathbf{n}$	normal vector	-
N	number	-
p	pressure	Pa

$\Delta\bar{p}$	pressure loss across burner	Pa
$\dot{Q}$	heat release per unit volume	$\mathrm{W/m^3}$
$\mathbf{q}$	conductive heat flux	$\mathrm{W/m^2}$
q	placeholder for production terms	$\mathrm{kg/m^3}$, $\mathrm{kg\ m^{-2}\,s^{-1}}$, $\mathrm{J/m^3}$
R	reflection coefficient	-
R	specific gas constant	$\mathrm{J\,kg^{-1}\,K^{-1}}$
R_m	molar gas constant ($8.314472\,\mathrm{J\,mol^{-1}\,K^{-1}}$)	$\mathrm{J\,mol^{-1}\,K^{-1}}$
r	radial coordinate	m
$\mathbf{S}$	scattering matrix	-
S	surface, cross section	$\mathrm{m^2}$
s	specific entropy	$\mathrm{J\,kg^{-1}\,K^{-1}}$
$\mathcal{S}$	placeholder for source terms	$\mathrm{J/m^3}$
T	period of harmonic oscillation ($T = 1/f$)	s
T	temperature	K
t	time	s
$\mathbf{u}$	vector of velocities in Cartesian coordinates	m/s
u	axial (acoustic particle or mean) velocity	m/s
V	volume	$\mathrm{m^3}$
X_{xy}	cross power spectral density of signal x and y	-
x	axial coordinate	m
$\mathbf{x}$	state vector	-
$\mathbf{x}$	vector of spatial Cartesian coordinates	m
Z	acoustic impedance	-

Greek symbols

α	constant	-
γ	ratio of specific heats	-
δ	acoustic boundary layer thickness	m
δ	residual for error estimation of Multi-Microphone Method	-
ζ	pressure loss coefficient	-
η, ξ	placeholders	s
θ	azimuthal coordinate	rad
κ	thermal conductivity	$\mathrm{W\ m^{-1}\,K^{-1}}$
λ	wavelength	m
μ	dynamic viscosity	$\mathrm{kg\ m^{-1}\,s^{-1}}$
ν	kinematic viscosity	$\mathrm{m^2/s}$
ρ	fluid density	$\mathrm{kg/m^3}$
$\boldsymbol{\tau}$	viscous stress tensor	$\mathrm{N/m^2}$
τ	time-delay	s
ϕ	equivalence ratio	-
φ	generic flow variable	Pa, $\mathrm{kg/m^3}$, $\mathrm{J\,kg^{-1}\,K^{-1}}$, K, m/s
φ	phase angle	rad
Ψ	arbitrary extensive variable	kg, kg m/s, J
ψ	density of arbitrary extensive variable	$\mathrm{kg/m^3}$, $\mathrm{kg\ m^{-2}\,s^{-1}}$, $\mathrm{J/m^3}$
ω	angular frequency ($\omega = 2\pi f$)	1/s

Dimensionless numbers

He	Helmholtz number ($He = \frac{kd}{2}$)	-
M	Mach number ($M = \frac{\bar{u}}{\bar{c}}$)	-
Pr	Prandtl number ($Pr = \frac{\mu c_p}{\kappa}$)	-
St	Strouhal number ($St = \frac{fd}{\bar{u}}$)	-

Subscripts

0	denoting a constant quantity or initial state
A, B	excitation states
calc	calculated
cl	closed-loop
corr	corrected
ds	downstream
eig	eigenvalue
exc	excitation
exp	experimentally determined
G	related to actuator transfer function
g	gain
GR	growth rate
i	imaginary
K	related to control law transfer function
LD	Ling Driver
LS	derived by Levine & Schwinger
max	maximum
mech	mechanical
ol	open-loop
osc	oscillation frequency
R	related to reflection coefficient
r	real
ref	reference
res	resonance
s	specific
set	prescribed quantity
sys	system
t	total
th	thermal
us	upstream
V	volume, volumetric
v	viscous

Superscripts

$(\cdot)'$	perturbation from mean state
$(\cdot)^*$	complex conjugate

$(\cdot)^+$	in mean flow direction
$(\cdot)^-$	against mean flow direction
$(\cdot)^\dagger$	pseudo inverse of a matrix
$(\cdot)^\mathrm{T}$	(conjugate) transpose of a vector or a matrix
$(\cdot)^{-1}$	inverse of a matrix
$\overline{(\cdot)}$	mean state
$\dot{(\cdot)}$	derivative with respect to time
$\hat{(\cdot)}$	Fourier transform
$\hat{(\cdot)}$	oscillation amplitude
$\tilde{(\cdot)}$	characteristic or modified quantity

Functions and operators

$\Re\{\cdot\}$	real part
$\Im\{\cdot\}$	imaginary part
i	imaginary unit (i=$\sqrt{-1}$)
$\mathcal{O}(\cdot)$	order of magnitude
$\nabla(\cdot)$	gradient: $\nabla(\cdot) = \left(\frac{\partial}{\partial x}, \frac{\partial}{\partial y}, \frac{\partial}{\partial z}\right)^\mathrm{T} (\cdot)$
$\nabla \cdot (\cdot)$	divergence: $\nabla \cdot (\cdot) = \left(\frac{\partial}{\partial x} + \frac{\partial}{\partial y} + \frac{\partial}{\partial z}\right) \cdot (\cdot)$
∇^2	Laplace operator (= divergence of gradient): $\nabla^2 = \nabla \cdot \nabla = \frac{\partial^2}{\partial x^2} + \frac{\partial^2}{\partial y^2} + \frac{\partial^2}{\partial z^2}$
$\frac{\mathrm{D}}{\mathrm{D}t}$	Lagrangian derivative: $\frac{\mathrm{D}}{\mathrm{D}t} = \frac{\partial}{\partial t} + \mathbf{u} \cdot \nabla$

Acronyms

BC	boundary condition
CFD	computational fluid dynamics
DC	direct current
DDV	direct drive valve
FEM	finite element method
GR	growth rate
ICCD	intensified charge-coupled device
LES	large eddy simulation
LU	look-up table
MMM	Multi-Microphone Method
PDF	probability density function
RMS	root mean square
SISO	single input single output
TMM	Two-Microphone Method

"I asked Yoona how she found the secret room.
'Curiosity,' she said.
I didn't know the word. 'Is curiosity a torch, or a key?'
Yoona said it was both."

D. Mitchell, Cloud Atlas.

Chapter 1

Introduction and Motivation

In this introductory chapter, first the importance of gas turbines in the world's energy mix is discussed. Section 1.2 addresses the relevance of coping with thermoacoustic instabilities in many fields of industry, the emphasis lying on combustion in gas turbines. It is elucidated why these instabilities became and still are the major issue in gas turbine combustion. Furthermore, the thermoacoustic feedback cycle is explained in more detail, covering the driving mechanisms, which are responsible for thermoacoustic instabilities to occur. A short historical overview starting from the first observations of the phenomenon of a coupling between unsteady heat release and acoustic field is given. Ways of controlling instabilities by both active and passive means are briefly presented, the focus lying on the concepts that were actually implemented in full-scale engines. The major goal of this work is to provide the basis for the industrial implementation of the developed control concept. Thus, the potential it has to improve future development processes of new gas turbine burners forms the motivation of this thesis, which is presented in Sec. 1.3. In Sec. 1.4, the underlying ideas of the impedance tuning concept are explained and an overview of existing approaches in the literature is given. The focus of this study lies on both the profound understanding and the general proof of feasibility of the control concept on the one hand and the satisfaction of industrial needs on the other. The chapter closes with an overview of the thesis' structure (Sec. 1.5).

1.1 General Background

World's ever increasing energy demand poses great challenges to power generation in the future. In reference scenarios of the International Energy Agency (IEA) and the U.S. Department of Energy (DOE), the electricity generation is projected to double in the next 25 years [53, 81]. Although the portion of renewables has to increase dramatically, the lion's

share will, at least in a mid-term perspective, i.e., until 2050, be covered by fossil fuels [63]. In the IEA and DOE reference scenarios, gas turbines, especially in combined cycle power plants, are one of the key technologies with a projected share of 25% of the total power generation in 2030, as shown in Fig. 1.1. Coal-fired power plants are expected to deliver

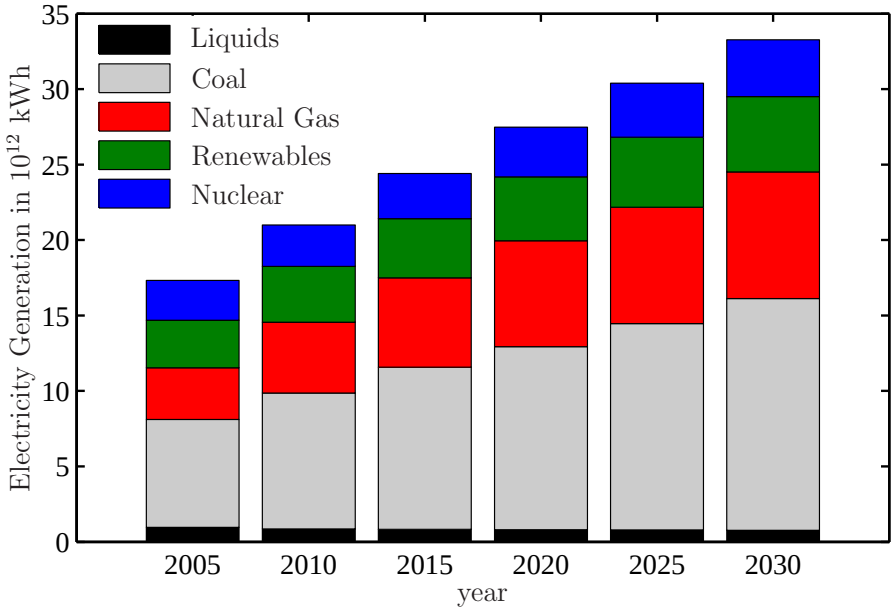

Figure 1.1: Energy mix of world electricity generation by fuels (reproduced from data in reference [53]).

45%. Other studies see gas turbine power plants even at 30-40% in 2030 [60, 99].
Both the IEA and the DOE scenarios are based on the assumption of a continuation of present policies. It is, however, to be expected that emission restrictions will get even more stringent in the future. Gas turbines feature emission characteristics that are by far better than those of coal-fired power plants. This includes CO_2, NO_x, and SO_2. Compared to coal-fired plants, gas turbines in combined cycle operation achieve a CO_2 reduction of approximately 50%. This is due to the lower carbon content in natural gas and a higher efficiency, which for combined cycle plants reaches a value of nearly 60% compared to 45% for coal-fired power plants. Therefore, either the percentage of gas turbines in the energy mix might increase, or parts of the coal-share might be replaced by renewables and the gas turbine portion will be at 25%, as it was projected in an "*alternative policy scenario*" in reference [81].
Lechner & Seume [99] and the German Federal Ministry of Economics and Technology [60] stated that today gas turbines in single and combined cycle power plants account for more than 50% of the power of new installed plants worldwide.
Besides better emission characteristics and a higher efficiency, gas turbine power plants exhibit several other advantages. These are lower specific investment costs compared to other technologies, flexibility in terms of peak-, part-, and base-load operation, as well as fast installation and amortization times and a smaller footprint [99].
Also, the increase of installed power generated by wind power plants, a fast growing industry, is up to now accompanied by an increase of the installed power of fossil power plants, i.e., mainly gas turbines [59]. This is necessary in order to be able to compensate the power

outage in case of an unsteadiness of the wind.
The remarks made in this section underline the importance of gas turbines in the energy mix and thus the importance of getting the problem of thermoacoustic instabilities, which are one of the main issues for gas turbine manufacturers, under control.

1.2 Thermoacoustic Instabilities: Background

The term thermoacoustic instability refers to a state of self-excited high amplitude pressure and heat release fluctuations that result from a positive coupling of unsteady heat release and the acoustic field in the system. This constructive interference leads to an energy transfer from the steady combustion process or the mean flow to unsteady coherent oscillations. Thermoacoustic instabilities are observed in a multitude of technical systems covering a wide range of applications including land-based gas turbines, industrial furnaces, domestic as well as industrial boilers and heating systems, rockets, ramjets, and afterburners. If thermoacoustic instabilities occur, they can have a severe detrimental impact on the combustion system. In land-based gas turbines, the system pressure ranges up to 3.5 MPa and pressure fluctuations of the order of 1% of the mean pressure were observed, which could reach up to 0.1 MPa. In solid propellant and liquid-fuelled rocket engines, where the mean pressure level is considerably higher, i.e., up to 40 MPa, pressure fluctuations can easily reach up to 10% of the mean pressure. Even pressure amplitudes of 100% of the mean pressure occured, as was, for example, reported by Blomshield [25] (approximately 6 MPa in the MANPADS Sustainer Motor) and Zinn & Lieuwen [234] (more than 14 MPa in the F-1 engine of the Saturn rockets).
The effects, thermoacoustic instabilities might have, are manifold and are here divided in three categories:

1. Impact on the quality of the combustion process by increasing NO_x and CO emissions, causing flashback, or leading to extinction.

2. Reduction of component lifetime and, in the worst case, total system failure. This can be due to structural vibrations causing wear and tear that result in low- or high-cycle fatigue as well as increased heat transfer to the combustor walls causing increased thermal stresses. For land-based gas turbines, for example, Rea et al. [176] and Sewell et al. [201] reported on broken transition pieces that led to engine breakdown.

3. Increased noise emissions and impact on health.

Generally, all three of them involve a deterioration of system performance, as they cause thrust oscillations and limited operating regimes that may prohibit the operation at the design point.
Thermoacoustic instabilities became a major issue for gas turbine manufacturers after they first gained technical relevance in rocket engines. Because of ever increasing restrictions for emission levels, the gas turbine industry stood abreast of changes by the introduction of lean premixed combustion and changes in combustor design. Primarily, this was done to decrease the NO_x emissions (main contribution NO but also NO_2), which today have to be

below 25 ppm in Europe and even below 9 ppm in California (both normalized to 15% O_2 in the hot products).

Basically, there are four different mechanisms for the production of NO: Thermal NO, prompt NO, NO generation from fuel-bound nitrogen, and oxidation of N_2O. A detailed description of each of them is beyond the scope of this work and might be found elsewhere [42, 101, 229]. Only the production of thermal NO, which develops at temperatures above 1850 K, is further investigated here, as it is addressed by lean premixed combustion. In Fig. 1.2 (left), thermal and prompt NO emissions are plotted versus the air/fuel ratio. The

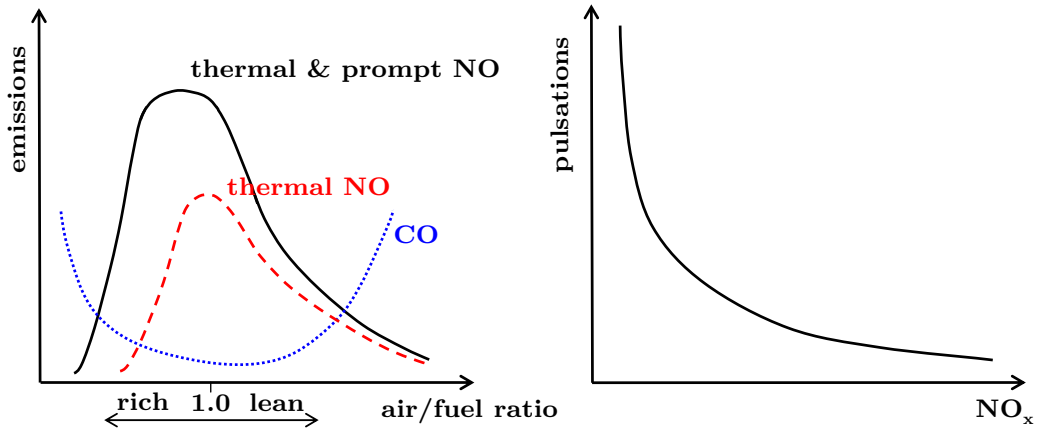

Figure 1.2: Left: NO and CO emissions versus air/fuel ratio (reproduced from references [17, 229]). Right: Relation between pressure pulsations and NO_x emissions.

leaner the mixture of fuel and air, the larger is the contribution of thermal NO compared to that of prompt NO.

The explicit temperature dependence for the formation rate of NO can be expressed in the Arrhenius-like form

$$\frac{\mathrm{d}c_{\mathrm{NO}}}{\mathrm{d}t} \propto e^{-E_\mathrm{a}/(R_\mathrm{m}\,T)}, \tag{1.1}$$

where the ratio of activation energy E_a and molar gas constant R_m is approximately 38000 K [42, 229]. From this exponential relation it follows that by decreasing the temperature, the formation rate $\mathrm{d}c_{\mathrm{NO}}/\mathrm{d}t$ might be strongly decreased. At typical conditions in a gas turbine combustion chamber with $T = 2200$ K, the production rate of NO is doubled or halved if the temperature is changed by 90 K. Burning in the lean regime decreases the temperature of the combustion process.

By pre-mixing fuel and air, a more homogeneous temperature distribution is achieved, avoiding locally high temperature regions that increase the overall NO_x emissions. The drawback, however, is that the leaner a combustion system operates, the more it is prone to thermoacoustic instabilities. This relation is indicated in the right graph of Fig. 1.2. Additionally, because nearly all the air is used to be premixed with the fuel, the combustion chambers are no longer cooled by injecting cooling air into the combustor walls, but only by convective means. Thus, acoustic damping originally introduced by the liners is dramatically decreased. Note that because of an increase of CO at low temperatures (see Fig. 1.2 left) and a decrease of efficiency, limits for decreasing the temperature are posed and an optimal trade-off has to be found.

To reduce the surface to be cooled and to decrease the residence times of combustion products in the engine, the combustor design was changed. The longer the residence time, the closer to NO equilibrium the system becomes [229]. Within only ten years, the combustion chambers were changed from the typical silo combustion chamber with energy power densities of $20\,\mathrm{MW/m^3}$ to the more compact can or annular designs exhibiting power densities of $200\,\mathrm{MW/m^3}$ [46, 91]. This also enhanced the susceptibility to thermoacoustically induced combustion instabilities, as the acoustic source terms were increased, whereas the damping related to the volume was decreased. Moreover, an improved mixing of fuel and air causes the removal of fuel concentration gradients, which would provide better flame stability and is, thus, a further destabilizing mechanism, as was stated by Sattelmayer & Polifke [184].
Since in civil aviation the most important factor is operational reliability and safety, application of lean premixed, prevaporized combustion up to now bears too high risks. Therefore, an immense potential of pollutant reduction remains unused at the moment. However, to reach the aims formulated by the Advisory Council for Aeronautic Research in Europe [2], i.e., a reduction of 80% NO_x in 2020 compared to 2000, the combustion process has to be changed to lean premixed prevaporized technology; its realization posing a huge development task for researchers in the near future.
The effect of converting energy as a result of an in-phase coupling of heat release and acoustic field is not always unwanted. In so-called thermoacoustic engines, it is used to convert heat or chemical energy into acoustic power. Through the thermoacoustic process, it is possible to reach almost the same efficiency of energy conversion as internal combustion engines with the benefit of having no moving parts. Application of thermoacoustic coupling to refrigerators [77], Stirling engines [6], and mixture separation [216] is possible. Comprehensive overviews about this topic and suggestions for further reading might also be found in references [214, 215].
Pulse combustion also makes use of coupling the unsteady heat release with the acoustic field. Putnam et al. [173] gave an extensive review on the principle. They state that besides the intent there are no differences between combustion-driven oscillations and pulse combustion. The simplified operating cycle is as follows: A combustible mixture is ignited, burns, expands, and moves outward the combustion chamber, which at its upstream end is closed by a valve. As a result, the pressure in the combustion chamber decreases and eventually falls below atmospheric pressure. The valve opens and fresh mixture enters the chamber. The pressure is increased and the cycle is repeated. Because of the low pressure that is generated by the process, no additional pumping, i.e., no external energy, is necessary to insert the fresh mixture, making pulse combustion attractive for thrust generation and heating applications. A comprehensive list of application fields can be found in reference [173].
Concluding the introduction on thermoacoustic instabilities, a note on the terminology should be made. The term thermoacoustic *instability* is somehow misleading, because it is – also in this work – used to describe the state of a combustion system that, due to a constructive feedback-interference of heat release and acoustics, exhibits high amplitude oscillations of both, whose amplitudes actually are determined by a *stable* limit-cycle.
In case of destructive interference or losses across the system boundaries that exceed the net gain of acoustic energy, the system is in a stable fixed point. Perturbations will be observed nonetheless, however, they are governed by combustion noise only. Small fluctuations around this stable stationary state can be described by a linear system. Consider now

the case for which a system parameter, for example, power or equivalence ratio, is changed as such that a positive thermoacoustic feedback is established and the net gain is larger than the losses. Through this, the fixed point is not stable anymore and infinitely small perturbations cause the system to become linearly unstable. Therefore, it is shifted from its initially stable equilibrium state with low-amplitude oscillations to one with a *stable* limit-cycle exhibiting high amplitude coherent oscillations. Literally, the combustion system is only linearly *unstable* during the onset of the instability, which causes an exponential growth of the pressure and heat release oscillations. From a mathematical point of view, an unstable linear system would grow infinitely in time. However, in all practical cases, the amplitude will somehow be saturated by non-linear effects, which, at a certain amplitude, balance the production terms.
An illustration is given in Fig. 1.3, where the gain/loss-amplitude relationship is plotted.

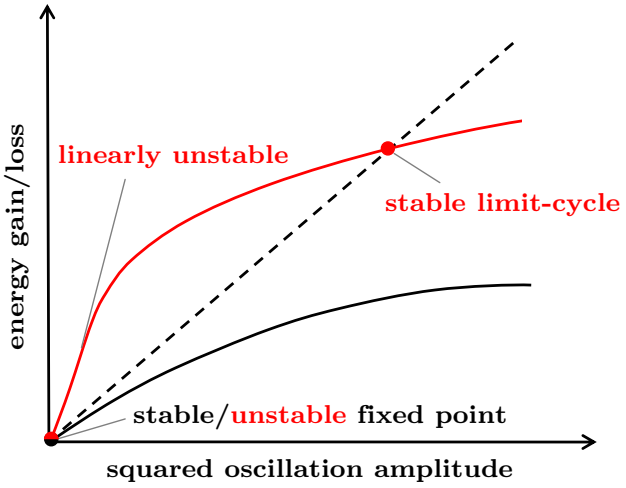

Figure 1.3: Acoustic energy gain (solid) and loss (dashed) versus squared oscillation amplitude of pressure.

Since the damping usually takes place in regions without heat release, it can be considered completely acoustic and is, therefore, assumed to be linear. In its initial state, the slope of the loss curve (dashed) is larger than that of the gain (black). The system remains in its stable fixed point. In practice, this state will also show perturbations caused by combustion noise, however, no coherent oscillations will be observed. Changing a system parameter as described above, results in a change of the gain curve (red), whose slope exceeds that of the losses at small oscillation amplitudes. Due to this, infinitely small disturbances move the system away from the fixed point, which now is unstable. The next attracting equilibrium solution in state-space is the point where both curves intersect again. This is a stable limit-cycle exhibiting high amplitude oscillations.

1.2.1 Thermoacoustic Feedback Cycle

Turbulence, inherent in the inlet air and fuel mass flows, causes a fluctuating heat release and thus a fluctuation of density and pressure, i.e., a generation of sound. These pressure disturbances propagate as acoustic waves through the combustion chamber, are reflected at the boundaries, and travel back to the burner. Here, they modulate the inlet mass flows

and the thermoacoustic feedback cycle is closed. If the phase relationship is as such that it promotes constructive interference, disturbances, which were initially infinitely small, might grow until the process is saturated by non-linear effects. At a first glance, this thermoacoustic feedback cycle is rather easy to understand. However, the physical mechanisms involved, are manifold and very complex.

Although known for more than 230 years and having an industrial relevance for nearly 80 years, thermoacoustic instabilities still pose what is probably the largest problem in ultra low-NO_x gas turbines. A great many of researchers from industry and academia were and are devoted to this problem and a vast amount on excellent publications on the individual driving mechanisms exists. Although probably all major mechanisms leading to thermoacoustic instabilities are identified, up to know, not all of these mechanisms, above all their non-linear saturation effects as well as the importance of each of them, are fully understood. Furthermore, the complex interactions between these mechanisms often do not allow to decouple them and usually more than one is responsible for an instability to occur.

Figure 1.4 illustrates several of the interaction mechanisms which are responsible for thermoacoustic instabilities in gas turbines. It is a merged and slightly extended version of the schematics proposed by Paschereit et al. [155, 156] and Sattelmayer [182]. From Fig. 1.4,

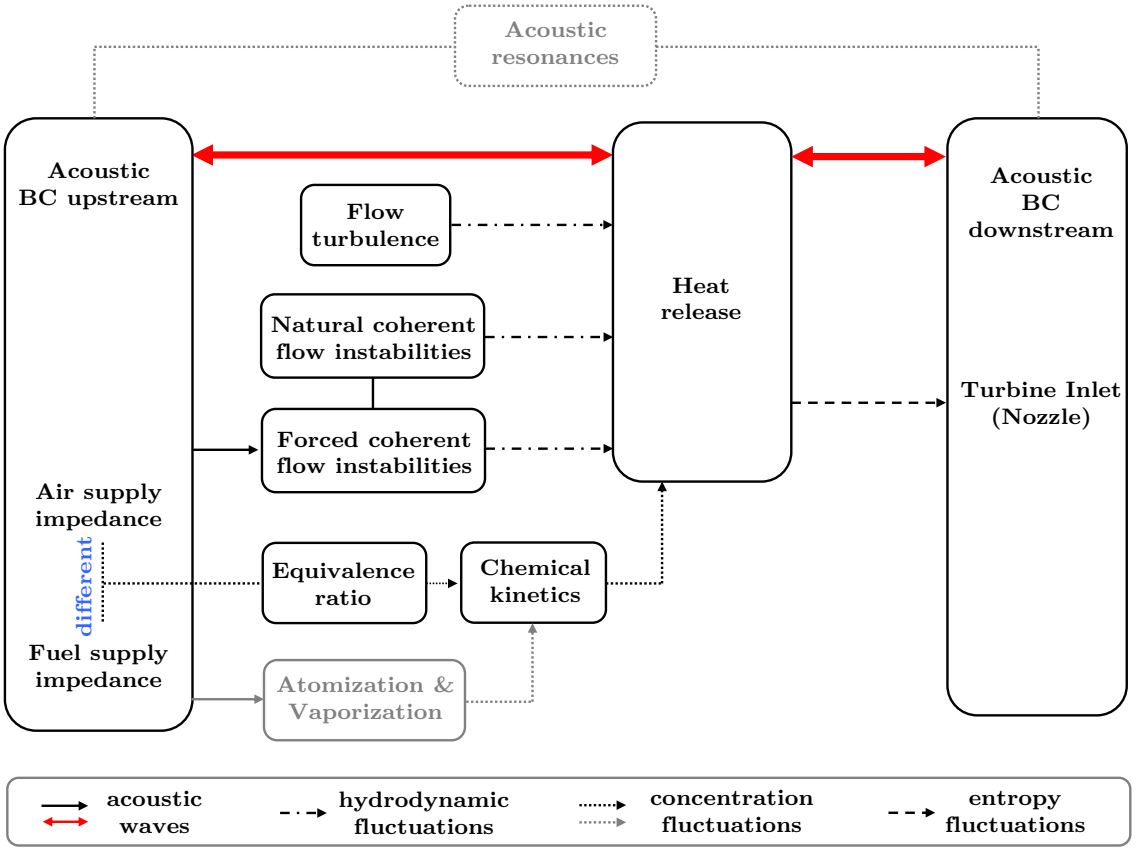

Figure 1.4: Schematic of the mechanisms driving combustion instabilities in gas turbines.

the importance of acoustic boundary conditions can readily be understood. The acoustics have a governing influence for the instability to occur, as acoustic waves travelling in both the up- and the downstream direction are responsible for closing the feedback loop. Therefore, usually the instability frequency is close to the acoustic resonance frequency of the

system [50, 166, 167, 234].
There are numerous publications covering the aspects which might lead to a driving of combustion instabilities. The reader is referred to summaries of Sattelmayer & Polifke [182, 184], Zinn & Lieuwen [234], Candel [35], Ducruix et al. [51], and Wangher et al. [228] as well as references therein. Most of those being important in gas turbines are listed in the following.

- Turbulence in the flow and the flame causes an unsteady variation of the flame shape and the local reaction rates, thus, causing a broadband noise level, commonly referred to as combustion noise.
- Large-scale coherent vortical structures, for example, resulting from flow separation, are present that can force oscillations, as was shown by Paschereit et al. [152]. In swirl-stabilized burners, swirling vortices, i.e., precessing vortex cores, caused by the vortex breakdown phenomenon are observed. These coherent structures control the mixing between fuel, air, and hot combustion products [186].
- Natural flow instabilities might couple with velocity fluctuations in the system resulting in amplified forced coherent flow structures. Paschereit & Gutmark et al. [145, 148, 150, 152] extensively investigated these natural flow instabilities, their structure, and the influence they have on thermoacoustic instabilities for a swirl-stabilized burner.
- Although the combustion is termed premixed, in practice, not all fuel and air will form a prefect homogeneous mixture before being burnt. Therefore, usually a difference is made between technically premixed and pre-premixed combustion; the latter describing the case in which the mixing took place way upstream of the combustion chamber. If the impedances of fuel and air supply lines differ from each other, as it is the case in gas turbines, the impact of acoustic perturbations on fuel and air mass flows will be different too and will, thus, generate equivalence ratio fluctuations which have an influence on the reaction rates.
- For liquid fuel combustion, pressure pulsations affect the atomization and vaporization process.
- Fluctuations of the acoustic particle velocity might also directly act on the flame, causing periodic changes in flame area and shape (for example, wrinkling).
- Entropy fluctuations, i.e., temperature non-uniformities, are convected downstream to the turbine inlet, where they are accelerated. Due to the choked flow conditions in the turbine inlet, these hot spots generate fluctuations of mass flow and momentum flux and thus are a source of sound. Up to know, it is not definitely resolved, whether this phenomenon has a noticeable influence on the feedback cycle in full-scale engines. The reason for this is that its separation from direct combustion noise is difficult. Most probably it is of minor importance in stationary gas turbines, because temperature non-uniformities are smoothed before they reach the turbine inlet, due to the combustor length. In aero engines that are short in length they could become

increasingly important for the emitted sound level, because noise caused by other sources of sound could be reduced [8].

- Acoustic fluctuations generate oscillations of the autoignition time, for example, in reheat systems [17].

It should be noted that at different operating conditions of a gas turbine (start-up, base load, part load, turn-down), different mechanism might be responsible for a combustion instability to occur.
Besides the direct coupling between acoustic velocity fluctuations and the flame, all these mechanisms involve time lags. If the ratio between their characteristic timescales and the acoustic mode is close to an integer, energy might be added to the acoustic field. The time lags result from the fact that the perturbations are generated at some location in the system and cause a fluctuation in the heat release rate after a certain time. This was illustrated in a very descriptive way by Zinn & Lieuwen [234] and is, therefore, reproduced in Fig. 1.5. It

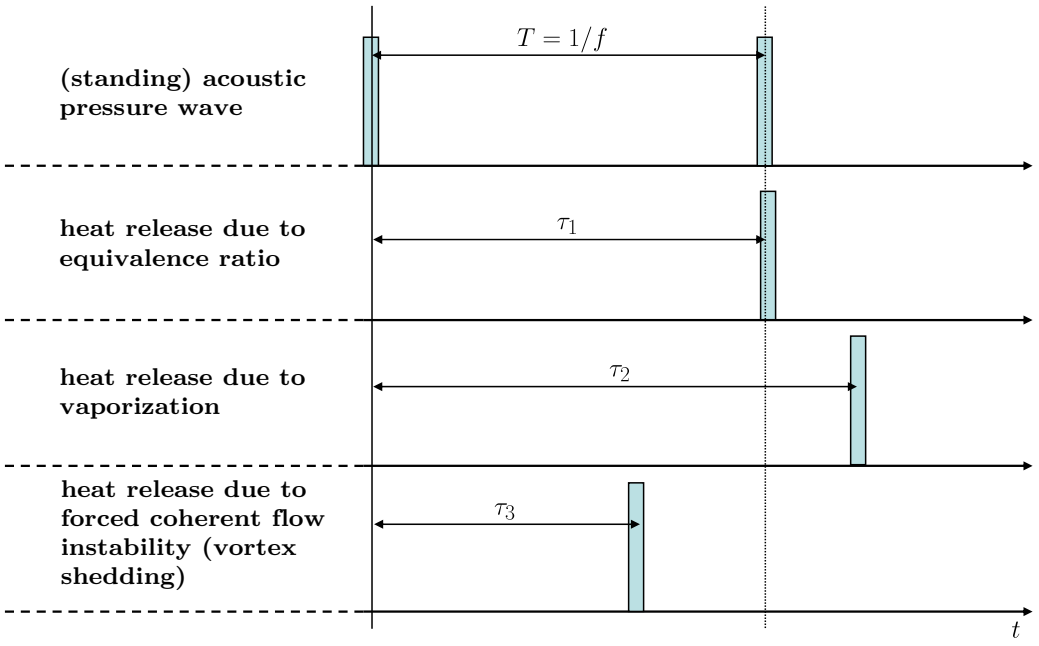

Figure 1.5: Time lags of different mechanisms in response to a periodic pressure fluctuation (reproduced from Zinn & Lieuwen [234] with slight adaptations).

shows the response in heat release of different driving mechanisms after a hypothetical time lag τ_i caused by a pressure fluctuation with a period of T. In this (theoretical) example, the time lag τ_1 of the equivalence ratio fluctuation matches the period of the pressure fluctuations and is in phase with it, whereas the two other mechanisms, vaporization and forced vortex shedding, have different time lags. Therefore, the equivalence ratio fluctuation is responsible for a constructive interference between acoustic field and unsteady heat release. If the net energy gain exceeds the losses, the system will become unstable. Clearly, the mechanisms depicted in Fig. 1.5 are a coarse simplification of the processes occurring in real systems. However, they provide good insight into the time lag mechanism.
As the oscillations in the combustion system are of sinusoidal shape and do not exhibit the pulse-like characteristic that was merely chosen because of its clearness, the ratio of

characteristic timescales does not have to exactly match an integer. For constructive interference to occur, it is sufficient if the phases between the harmonic oscillations lie between $-\pi/2$ and $\pi/2$. A graph similar to Fig. 1.5 accounting for this harmonic fluctuations can be found in reference [110]. As was pointed out by Sattelmayer [182], burner and combustor designs that feature a wide range of convective time scales result in more favourable stability characteristics of the combustor.
Note that there might be several mechanisms driving a combustion instability, but the underlying effect always is that energy is transferred from the steady combustion process or the mean flow to unsteady coherent oscillations. In gas turbines, the turbulent fluctuations of the flame are the source of broadband noise. An estimation of the order of magnitude of the ratio between this combustion noise and the chemical energy density might be made. However, the calculation is quite complex, as can be seen in the discussions of Lefebvre [101][1] and Strahle [207, 208], who derived expressions for the sound energy production terms resulting from combustion noise and will, therefore, not be investigated in detail here. Different references are discussed by Lefebvre [101] and the resulting values have a considerable range between $\mathcal{O}(10^{-8})$ and $\mathcal{O}(10^{-5})$.
In case of a thermoacoustic instability, the ratio between power densities associated with the pressure fluctuations and the energy density of the combustion process can reach values of $\mathcal{O}(10^{-6})$ for rocket engines, as was stated by Candel [35]. For this estimation a mean power density of $50\,\mathrm{GW/m^3}$ and a pressure fluctuation of 1 MPa, i.e., 10% of the mean pressure, were taken. If an analogous estimation is made for gas turbines, the ratio is $\mathcal{O}(10^{-5})$. This results from a mean power density in modern gas turbines of the order of $200\,\mathrm{MW/m^3}$ [46, 91] and a root mean square (RMS) pressure fluctuation of 3% of the mean pressure, i.e., 0.1 MPa. The derivation of an expression for the acoustic energy density, which has been used for this calculation, is given in Sec. 2.6 and will, therefore, not be presented here. Krebs et al. [90] stated that for land-based gas turbines, the ratio is of the order of 10^{-4}. In conclusion, it can be said that although the energy density of the pressure fluctuations is only a minimal fraction of the mean energy density, it is large enough to have substantial detrimental consequences, as was described in the introduction of this chapter.

1.2.2 A Short History of Thermoacoustic Instabilities

Long before thermoacoustic instabilities gained relevance in technical applications, be it positive or negative, interactions between sound and flames were observed. In 1777, shortly after the discovery of hydrogen, Higgins was the first to document the "singing flame" [33]. He placed a hydrogen diffusion flame in an open end tube and realized that sound was only produced for certain lengths of tube and fuel supply line.
Sixty years later, in 1837, Pinaud [161] documented the observations he made while manufacturing a differential thermometer. Using a glass pipe he blew a small bulb and noted that as long as this sphere was discharging heat, a tone was audible. He explained the phenomenon as a consequence of the expansion of the water vapor from his breath, which was due to the heat release and its compression due to the cold walls. This process followed a cyclic change and thus emitted sound. As it was a rather easy experiment he was wondering why no glass blower did observe this before.

[1] see pp. 258 therein

In 1842, Marx [120] stated that he discovered this phenomenon by chance 13 years earlier than Pinaud and that he intended to build a "*peculiar type of instrument*"[2] using the interaction between heat release and acoustics, which he actually did. He resolutely disagreed with both Pinaud's explanation for the phenomenon and that no one did document it before. He quotes a Dr. Castberg from Vienna, who reported about the singing tube in *Gilbert's Annalen der Physik* in 1804.
Generalizing and extending these experiments, Sondhauss [203] made extensive parametric studies of this phenomenon and disproved both Pinaud's explanation that the existence of water vapor is essential for the phenomenon to occur and Marx's explanation that the hot air impinges on the cold air and thus generates sound.
The sensitivity of flames to music was in 1858 noted by Le Conte [100], who "*observed that the flame [...] exhibited pulsations in height, which were exactly synchronous with the audible beats*".
In 1859, Rijke [175] discovered that sound might be produced by placing a heated gauze in the lower half of an open-ended, vertical tube. He found that the sound production was maximal when the gauze was placed a quarter of the tube length from the bottom. When he located the gauze in the upper half of the tube no sound was produced. Because of its simplicity and its relation to thermoacoustically induced combustion instabilities, the Rijke tube was widely used for research purposes in the past and is also investigated today. Rijke's explanation of the phenomena involved were also incorrect, as he assumed that the sound generation was due to the periodic heating and expansion of the naturally convected air and its cooling and compression at the colder walls.
The effect was not fully understood until 1878 when Lord Rayleigh formulated his famous Rayleigh criterion in the course of the Friday Evening Lecture of the Royal Institution of Great Britain [210]. His original statement read: "*If heat be periodically communicated to, and abstracted from, a mass of air vibrating (for example) in a cylinder bounded by a piston, the effect produced will depend upon the phase of the vibration at which the transfer of heat takes place. If heat be given to the air at the moment of greatest condensation, or taken from it at the moment of greatest rarefaction, the vibration is encouraged. On the other hand, if heat be given at the moment of greatest rarefaction, or abstracted at the moment of greatest condensation, the vibration is discouraged.*" Or in other words, if heat release and pressure fluctuation are in phase, acoustic energy will be produced. Regarding the optimal gauze position at a quarter of the tube's length he noted that "*the variable transfer of heat depends upon the motion of vibration, while the effect of the transfer depends upon the variation of pressure. The gauze must therefore be placed where both effects are sensible, i.e. neither near a node nor near a loop*", i.e., if the heat release device is placed at a velocity node, nothing will happen. The mathematical formulation of the Rayleigh criterion reads

$$\oint p' \dot{Q}' \mathrm{d}t > 0, \tag{1.2}$$

[2] In his own phrasing: "*[...] ward ich vor etwa 13 Jahren zuerst auf dieses Phänomen aufmerksam und glaubte sofort, es zur Construction eines eigenthühmlichen musikalischen Instrumentes benutzen zu können. Ich kam auch mit einem solchen zu Stande und bewahre noch jetzt ein solches, wo 13 Röhren, welche die Töne c – ā angeben, so angeordnet sind, dass sie durch einen mit Weingeist gespeisten Lampenapparat gleichzeitig zum Glühen gebracht werden können.*"

where p' and $\dot{Q}'$ denote acoustic pressure and unsteady heat release, respectively and the integral is taken over one cycle. If the phase φ between p' and $\dot{Q}'$ meets the condition $-\pi/2 < \varphi < \pi/2$, energy will be fed into the acoustic field. This mathematical description was not given by Lord Rayleigh himself but for the first time derived by Putnam & Dennis [174] in 1953, who gave a thermodynamic proof for the phase relationships needed. A more rigorous treatment of the Rayleigh criterion is given in Sec. 2.6.
It was not before the late 1930s that combustion instabilities were of technical relevance. In the following, it will be briefly shown which fields have been affected.
The effect was used for the first pulse combustion devices [173]. At this time they were also firstly encountered in liquid and solid propellant rockets. Between 1940 and 1950 they became a problem in afterburners. Since 1950, combustion instabilities also occurred in ramjets. They were of great concern in the 1970s, 1980s, and 1990s because of the introduction of compact dump combustors, which were used to increase the power densities. Well known missions, as, for instance, the Minuteman, Ariane, Soyuz, and Space Shuttle, were seriously affected. For more information, the interested reader may refer to Culick [43] and Blomshield [25], who gave comprehensive chronological overviews of combustion instabilities in rocket engines.
In the 1960s, the thermoacoustic effect was constructively used in thermoacoustic refrigerators [214].
Putnam's monograph from 1971 [172] was motivated by the fact that combustion instabilities had become a severe issue in industrial furnaces. Because of the furnaces' dimensions, typical frequencies of self-excited oscillations are below 10 Hz. Additional to the detrimental influence on system performance, this so-called infrasound has a serious impact on health. The amplitudes in blast-furnace stoves were reported to reach up to "*several inches of water*", i.e., $\mathcal{O}(1\,\mathrm{kPa})$.
With the introduction of lean-premixed combustion they then also became a severe problem in stationary gas turbines in the 1990s, which is still not solved.

1.2.3 Analogy to Thermodynamic Cycles

The mechanism of thermoacoustic instabilites might become more descriptive by comparison with a thermodynamic cycle. The cycle of an acoustic wave is an isentropic process. Thus, if a small gas volume is considered, the compression and expansion due to the acoustic perturbation is represented by an isentropic change of state in a p, V-diagram, as depicted in Fig. 1.6 (red curve).
In the classical cycle of a heat engine, heat is added to the medium at the maximal system pressure and the cycle moves clockwise generating mechanical energy. In an ideal gas turbine process, which is represented by the Brayton- or Joule cycle, the working fluid is first isentropically compressed. Then heat is added to the fluid in the combustion chamber causing an isobaric expansion. Finally, the fluid is isentropically expanded in the turbine. In the ideal thermodynamic cycle, the medium is then brought back to its initial state by heat rejection to the atmosphere.
A thermoacoustic cycle can be described equivalently with the only difference that the system is not brought back to its initial state as the small gas volume will not reject the heat

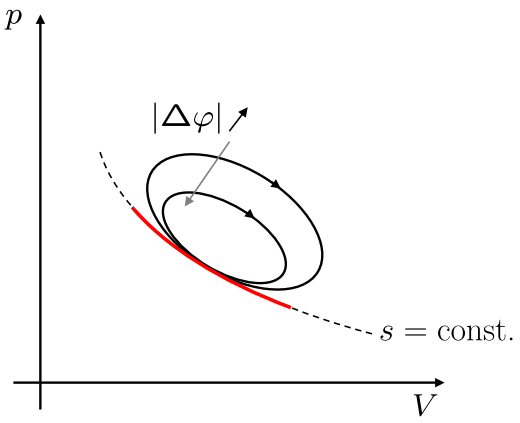

Figure 1.6: Schematic p, V-diagram for isentropic pressure fluctuation (red) and constructive interference between unsteady heat release $\dot{Q}'$ and acoustic pressure p' (black). $\Delta\varphi$ denotes the phase difference between $\dot{Q}'$ and p'.

after being expanded. If heat is added periodically to the isentropic expansion and compression of the acoustic wave, the volume of the gas will be increased. If the heat is added in phase with the pressure fluctuation (confer to Rayleigh's observations [210]), the state of the gas volume will follow a clockwise moving cyclic change. A self-sustained instability might occur if the energy addition exceeds the losses across the system boundaries and due to viscous dissipation.
The energy which is fed into the acoustic field by the fluctuating flame is represented by the area enclosed by the cyclic process in the p, V-diagram. It reaches its maximum when pressure fluctuation and periodic heat release are perfectly in phase ($|\Delta\varphi = 0|$). The larger $|\Delta\varphi|$, the smaller is the encircled area and the smaller is the transferred energy. If $|\Delta\varphi|$ exceeds $\pi/2$, energy will be extracted from the acoustic field and the cycle will move in counter-clockwise direction. The work done by this thermoacoustic engine is equivalent to the work needed for the change of volume in a heat engine. It is proportional to the Rayleigh integral (see Eq. (1.2)) as was pointed out by Polifke [167]. In this reference, more information on the analogy between thermoacoustic instabilities and thermodynamic cycles can be found. As was mentioned above, pulse combustion also relies on a (wanted) coupling between unsteady heat release and acoustic field. Putnam et al. [173] compared the cycle of pulse combustion to that of a Diesel engine, comprising the four phases: Ignition and combustion – expansion – purge and recharge – recharge and compression.

1.2.4 Active and Passive Control Methods

Basically, three mechanisms are important for the damping of thermoacoustic instabilities [85, 234]:

1. Radiation and convection of acoustic energy out of the system.
2. Dissipation of acoustic energy through viscous and heat-transfer mechanisms (in acoustic boundary and shear layers).

3. Shift of acoustic energy from the unstable mode to another mode.

Active and passive control strategies, which are either acting on these mechanisms or try to decouple unsteady heat release and acoustic field, can be applied to mitigate thermoacoustic instabilities. Numerous research groups have been working on these topics. However, only a few publications exist reporting the implementation of these concepts in the real engine. It is not the intention of this section to give a review of the manifold approaches but rather to focus on "real-world" applications that were actually implemented in the engine. If thermoacoustic instabilities are observed at the end of the design phase because they could not be predicted until the first full-scale engine tests, methodologies are sought for, which can be used in the field and fulfill both the control objective and the demands on life time. In case of gas turbines, the maintenance intervals, which define the minimum life time requirements, often exceed 24000 h. Comprehensive reviews on the underlying principles, the different approaches, and many references for lab-scale experiments of active control solutions were conducted by Candel [36] as well as McManus et al. [124] for the work before 1992. A more recent study was accomplished by Dowling & Morgans [49]. Richards et al. [177] reviewed passive control strategies.
For gas turbines, engine applications of active control strategies are really scarce and were, to the knowledge of the author, only shown by Seume et al. [200], Hermann & Orthmann [74], and Hoffmann et al. [76] for the Vx4.3A gas turbine family of SIEMENS and by Richards et al. [178] for a test engine of Solar Turbines.
During prototype tests of the SIEMENS V84.3A gas turbine, exactly the aforementioned problem of unexpected combustion instabilities in the last design stage were encountered. This gas turbine model features an annular combustion chamber and has an electrical power output of 170 MW. Seume et al. [200] equipped each of the 24 burners with a direct drive valve (similar to the one used in this thesis, see Sec. 6.4.2) to modulate the pilot fuel. Six circumferentially mounted pressure transducers provided for the input signals of 6 independent feedback control loops, each featuring four valves. They were able to suppress the dominant frequencies at 217 Hz and 433 Hz by up to 86%. Hermann & Orthmann [74] and Hoffmann et al. [76] later extended and adapted this control concept and applied it to the V94.3A model (270 MW). This active control approach remains the first and only one which was actually applied in the field. Over 50 engines were equipped with this active instability control device [75].
Richards et al. [178] chose an open-loop active control approach to suppress thermoacoustic instabilities in an annular type test engine featuring 12 burners. Each of the burners was equipped with off-the-shelf solenoid valves that were used to modulate the equivalence ratio. They were able to reduce the oscillation amplitude by one-third. The valves were expected to have a lifetime of several years.
Passive means are more common and were presented by a couple of authors. Paschereit et al. [145] used an extended pilot fuel lance of an ALSTOM EV-burner to stabilize the location of the vortex breakdown. By doing so, they could suppress pulsation levels, which initially occurred in the start-up phase, by 90%. Bellucci et al. [18] equipped an ALSTOM GT11N2 with Helmholtz dampers. They achieved a 53%-reduction of the dominant pressure peak. Berenbrink & Hoffmann [20] modified the flame response of the SIEMENS hybrid burner by adding a cylindrical extension tube to its fuel nozzle similar to the approach suggested in the patent of Paschereit & Gutmark [151] for the EV-burner. Through this, the time

lags were changed. Addionally, they used an asymmetric burner setup by incling the axes of neigbouring burners to diminish the fluid dynamic feedback. Both approaches were applied to a SIEMENS V94.3A gas turbine and resulted in an increase of the power output by enlarging the stable operating regime. More information and references for engine applications were summarized in comprehensive reviews on passive control strategies in gas turbines conducted by Richards et al. [177] and Paschereit & Gutmark [147]. Different industrial approaches can also be found in the exhaustive book on combustion instabilities in gas turbines edited by Lieuwen & Yang [114].
Clearly, although successful implementations are reported, gas turbine manufacturers would prefer a system without pressure pulsations rather than a controlled one. Besides the fact that the application of active and passive means might not always be successful, also negative effects, for example, on maintenance intervals or pollutants, might arise when applying a control scheme, the latter having been reported by Richards et al. [178].

1.3 Motivation for this Thesis

Being able to assess the system's tendency to thermoacoustic instabilities already in the early design stage becomes an increasingly important task for industry. If the thermoacoustic stability characteristics are known, adequate measures for the mitigation of instabilities can be taken and the operational range of gas turbines can be assessed and possibly extended. Thus, time to market requirements are met [22, 84]. The most important component influencing the tendency to thermoacoustic instabilities is the burner, making its development a crucial task. However, the quality of new burner generations cannot be tested in each step of the early design phase in the full-scale engine, as this would be far too expensive. Assessment of burner properties is usually accomplished by extensive experimental investigations in single or multi burner combustion test rigs. Industrial strategies for the development process of new burners were reported by many authors. Table 1.1 lists references for several gas turbine manufacturers.
The development schedule is quite similar for all cited industrial approaches. A representative test campaign for a new burner comprises the following steps:

(i) Cold flow tests in water channels to determine mixing of air and fuel and to investigate the flow field, e.g., for the flame stabilization position and convective time-delays for an estimate of the flame transfer function, i.e., the relationship between heat release and velocity fluctuations.

(ii) Single burner tests under atmospheric conditions to down-select the number of prototype variants. This is possible, as flame shape and position are independent of pressure as long as preheat air temperature, burner velocity, etc. are kept the same as under engine conditions as was pointed by Zajadatz et al. [231].

(iii) Atmospheric multi burner tests to evaluate possible influences between neighbouring burners [104]. Gruschka et al. [64], for instance, used atmospheric multi burner tests to study different approaches of scaling main swirlers and pilot swirler and to make a pre-selection for high pressure tests.

Table 1.1: References for burner development strategies in gas turbine industry.

Company	Reference	Comment
SIEMENS Energy	Gruschka et al. [64]	Description of the SIEMENS development efforts for the ultra low-NO_x system. Used atmospheric multi burner, high pressure single can, and full-scale engine tests.
	Streb et al. [209]	Report upon the design, testing and field evaluation steps.
	Lepers et al. [104]	Present tests at the SIEMENS atmospheric multi burner combustion test rig at Ansaldo Energia.
ALSTOM Power	Zajadatz et al. [231]	Comprehensive description of ALSTOM's burner development process with detailed specifications of the single steps.
	Paschereit et al. [145]	Development process for extended fuel lance from first cold tests to engine implementation.
	Döbbeling et al. [46]	Laboratory and engine tests for EV burner. List which experiments were conducted in high pressure test rigs.
	Aigner & Müller [3]	Development phases for the first generation EV burner.
General Electric Aircraft Engines	Mongia et al. [129]	Emphasize the need for a reliable assessment of thermoacoustics at an early design stage and the shortcomings of component tests. Explain the GE concept of a tunable laboratory scale combustor. Give several references for the burner development process of GE LM series gas turbines.
	Leonard & Stegmaier [103]	Describe GE development phases that are conducted prior to engine tests and the desired outcomes.
General Electric Energy	Lacy et al. [95]	List the single development steps.
Rolls-Royce Deutschland	Lazik et al. [98]	Detailed documentation of RRD burner development. Give an overview of technology readiness level corresponding to used test facility.
Ansaldo Energia	Bonzani & Piana [29]	Ansaldo approaches for development of low NO_x burners for SIEMENS Energy.

(iv) High pressure tests (single or multi) to get a more reliable estimate of pollutants, temperature profiles, thermal loading, fuel flexibility, and robustness.

(v) Full-scale engine tests in gas turbine test beds to study the real system behaviour during base load, part load, as well as transients and to determine the engine envelope.

In chronological direction of this workflow, the number of conducted experiments decreases as time and cost expenses drastically increase. Also, the technology readiness level increases.
With the experiments of steps (i)-(iv), computational fluid dynamics (CFD), finite element calculations, and low-order network tools, the burner's performance is sought to be predicted for the full-scale engine. A reliable assessment of the quality of this prediction, however, can only be made at the very end of the design process after the burner is tested in the full-scale engine. At this point, changes in component design are very expensive and will cause severe delays in the schedule [119, 129]. Evidently, the later problems regarding the thermoacoustic characteristics are recognized in the development process, the worse is the impact on the schedule and the costlier are appropriate counter measures. This underlines the need for a procedure allowing a reliable prediction of burner behaviour in the engine as early as possible. Alternatives to component design modifications then are only active and passive control strategies (see Sec. 1.2.4). Their application is an empirical process, which sometimes might be unsuccessful. Furthermore, pollutants might increase when applying active control in engine applications, as was observed by Richards et al. [178].
Generally, the acoustic characteristics of the test rig are significantly different from those of the full-scale engine making the prediction difficult. This is due to higher static pressures and temperatures and, in particular, due to a different geometry [83]. Thermoacoustic instabilities usually appear close to the acoustic resonance frequencies of the combustion chamber, whenever the flame response at these frequencies is sufficiently large and the phase relationships involved promote constructive interference [50, 166, 167, 234]. For this reason, a burner that shows a desirable behaviour with respect to pressure pulsations and emissions in the test rig might exhibit essentially different characteristics in the engine. This is because the thermoacoustic behaviour of the engine is properly represented by the test rig only if both, the dynamic flame response (significantly influenced by the burner) and the acoustic boundary conditions, match. As a matter of fact, solely assessing the stability characteristics of new burners without considering the acoustic environment of the engine, is a risky approach.
The problem of different acoustic boundary conditions in engines and test rigs and the adversities which arise due to this is beyond question in the gas turbine and combustion community. Major manufactures of gas turbines both for stationary (SIEMENS Energy and ALSTOM Power) and for aeroderivative devices (Pratt & Whitney) evinced a keen interest in the active impedance tuning approach developed in this thesis. Krebs and coworkers [22, 84, 90] (SIEMENS), Zajadatz et al. [231] (ALSTOM), Mongia et al. [129] (GE), Brogan [32] (Pratt & Whitney), and Cazalens et al. [38] (SNECMA) emphasized the importance and industrial needs to reproduce engine conditions at test rigs. Most noticeably, Mongia et al. [129], Krebs et al. [90], and Zajadatz et al. [231] explicitly stressed the need for acoustically tunable test rigs. One reason for selecting can type combustion systems for the latest brand of SIEMENS gas turbines, was the reduction of the implementation risk

of new combustion technologies because of the better reproducibility of engine behaviour in single burner test rigs, as was pointed out by Kaufmann et al. [84]. The combustion group of CERFACS stressed this problem as well [38, 119]. Yet, their approach is different as they suggest to solve it by using extensive large eddy simulations (LES) to support the burner development process. However, as they mention themselves, LES is very expensive in terms of computation time even on today's computers and LES does not suggest why instabilities arise and how to find adequate counter measures.
Accounting for the different acoustic boundary conditions by modification of industrial-scale test rigs is expensive and time-consuming. Nonetheless, a length adjustment of an industrial test rig was used to change its resonance frequency as is mentioned in reference [231]. Mongia et al. [129] presented a laboratory scale combustor, whose resonance frequencies could conveniently be changed. The test rig basically consisted of an upstream tube, the burner, and a downstream tube. The tubes' lengths and thus the test rig's resonances could be continuously varied using perforated pistons. The combustion group at Georgia Tech uses a similar setup to tune the upstream end of their combustion test facility [221, 235]. Although in both latter cases a change of test rig resonances is quite straightforward, the degree of reflectivity remains constant and problems are to be expected when applying the system to industrial test rigs with higher power, i.e., higher mass flow and elevated pressure. As geometries of industrial test rigs usually do not only consist of simple ducts, incorporating a movable piston is challenging. If the cross section of the test rig is not constant, the piston dimensions have to be smaller than the smallest diameter of the test rig. Therefore, the blockage would be different for different piston positions. This could introduce unwanted effects. Also sealing issues might arise at high operating pressures.
Another way to adjust the boundary conditions to those of the engine has motivated this thesis. Instead of implementing hardware changes, they are actively tuned, i.e., artificially changed. This can be done by using an active control scheme, which detects the acoustic field at the combustion chamber outlet and feeds back a suitable signal to drive an acoustic actuator. The actuator modifies the acoustic field in the system to match the desired one. By this, an estimate of pressure amplitudes possibly occurring in the engine configuration is possible and thus an assessment of modifications to be made. An additional advantage of this method is that the same test rig can be used to simulate the acoustic conditions of different full-scale engines. For instance, the test rig length can be virtually extended, thereby, introducing different resonance frequencies, without having to implement any hardware changes. Furthermore, the acoustic boundary condition can be changed to that of a choked flow without the need that the flow is choked. Also, by incorporating the real acoustic boundary conditions to the test rig, it is possible to have a realistic estimate about the whole combustion process subject to the engine acoustics, including their influence on NO_x emissions.

1.4 The Principle of Impedance Tuning

In this work, the term impedance tuning refers to the fact that the acoustic impedance of a system is actively changed. In this sense, equivalent terminological expressions are active

impedance control, active impedance matching, active control of the acoustic boundary condition, active control / tuning of the reflection coefficient.

1.4.1 The Underlying Idea

Active impedance control relies on the idea that the impact of a geometry change on the plane wave acoustic field *physically* can be represented by a change of the impedance at a certain position. In the following, the setup depicted in Fig. 1.7 is considered. The acoustic or thermoacoustic system is connected to a duct. Only plane wave propagation is considered. The duct is terminated by an acoustic boundary condition Z_1. Here, Z denotes the acoustic impedance, a complex valued function of frequency. It is defined as

$$Z = \frac{\hat{p}}{\hat{u}}, \tag{1.3}$$

where $\hat{p}$ and $\hat{u}$ denote Fourier transforms of acoustic pressure and particle velocity normal to the boundary, respectively. The system considered in Fig. 1.7 has certain characteristics

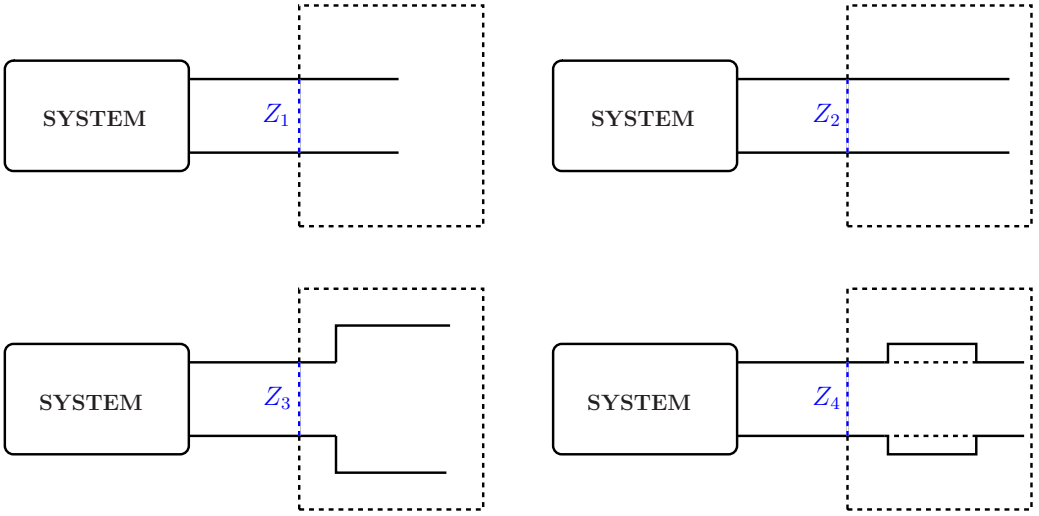

Figure 1.7: System with different acoustic boundary conditions induced by a change in geometry or by implementation of a liner.

depending on the acoustic field associated with Z_1. For other acoustic boundary conditions, e.g., induced by a change in length (Z_2), an area change (Z_3), or by some damping device mounted in the duct (Z_4), the system may exhibit essentially different characteristics. This might, e.g., be related to higher or lower resonance frequencies as well as to increased damping by implementation of a liner.
The aim of the control scheme to be presented is to mimic certain prescribed impedances. In this way, the impact of different acoustic boundary conditions on the system characteristics can be studied, without actually implementing the devices that alter the boundary impedance. To do so, the system part encircled by the dashed rectangle is regarded as a black box. By actively manipulating the acoustic field in this box, the acoustics of the total system are adjusted to prescribed conditions. Figure 1.8 shows the corresponding setup. Except for an actuator, which is mounted at the downstream end of the black box element,

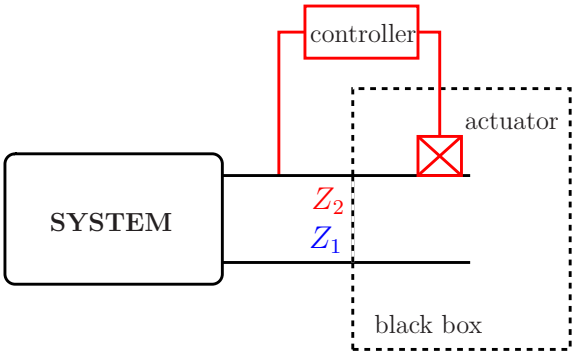

Figure 1.8: Acoustics of system with fixed geometry are actively tuned. This is done by feeding back the instantaneous acoustic field to an acoustic actuator.

no further hardware changes are made compared to the initial system in the upper left frame of Fig. 1.7. In the uncontrolled case, the acoustic boundary condition would be described by Z_1. By adequately feeding back the instantaneous acoustic field to the acoustic actuator, the acoustic boundary condition is, for example, tuned to that of the longer duct shown in Fig. 1.7 (top right), which is defined by Z_2. If the system incorporates a burner, this burner would then be exposed to the same acoustics as if it would be mounted in the uncontrolled system with the geometry characterized by Z_2.

1.4.2 Active Impedance Tuning in the Literature

Basically, all active sound absorption approaches, which do not directly influence the primary source of noise, rely on the fact that the acoustic impedance at a certain location in a system is changed. In this respect, Olson & May [142] were amongst the first to actively tune the acoustic impedance in experiments using a control scheme for sound absorption. They suggested a simple setup consisting of a microphone, an amplifier, and a loudspeaker to reduce the sound pressure at the microphone position. In terms of impedance, their approach was to adjust an impedance at the microphone location as close to zero as possible. Probably, the first active feedback scheme to mitigate combustion instabilities was proposed by Tsien [224] a year earlier in 1952. Noticeably, he suggested a setup to change the capacitance (which can be regarded as a contribution to the impedance) of the fuel supply line and thus the upstream boundary condition of a rocket combustor. In this merely theoretical study, a sensor was used to detect the pressure fluctuations in the combustion chamber. This sensor signal was manipulated by an adequate control circuit to drive a piston that modulated the fuel line impedance.
However, it should be noted that if active control of combustion-acoustic interaction is regarded, also the source of instability, the driving mechanism, is changed, as well. Thus, the approach described here essentially differs from the anti-sound approach followed by Olson & May [142]. Some interesting remarks on this can also be found in the recently published monograph of Culick [43][3].
A more general formulation and extension of the active sound absorption was proposed

[3] see Chapter 9 therein

30 years later. In 1984, Guicking & Karcher [65] introduced the concept of changing the impedance through active control of the acoustic boundary condition. They were able to realize reflection coefficients ranging from nearly fully absorbing to fully reflecting. Even reflection coefficients larger than unity were experimentally realized, representing the case of an acoustically active boundary condition. Two microphones were used to detect the sound field in a straight duct. The microphone signals were processed by a simple phase-shift controller that drove a loudspeaker to tune the reflection coefficient. Only fixed frequency harmonic signals were considered and the control parameters were tuned empirically.
The idea to actively change the acoustic boundary condition originally emanated from the attempt to improve passive damping devices. Room and duct acoustics were the original fields of application. Guicking & Lorenz [66] increased the damping coefficient, i.e., decreased the reflection coefficient, and the frequency bandwidth of porous plates by active means. This was down by backing the damping device by a loudspeaker. In the gap between loudspeaker and porous plate, a microphone was installed. The control objective was then to obtain a pressure node at the microphone to realize a quasi active $\lambda/4$ resonator. Thenail et al. [217] also imposed a pressure node, i.e., a zero impedance boundary condition, in a similar setup and theoretically derived optimal absorption criteria, which were verified in experiments.
Aiming at the same purpose, Beyene & Burdisso [23], Furstoss et al. [58], and Smith et al. [202] modified and extended the zero impedance approach. They cancelled the waves reflected at the damping device by imposing a reflection coefficient of zero, i.e., an impedance that is not zero but equal to the characteristic impedance of the medium. Their approaches, however, only focused on producing anechoic terminations. The sensor/controller setups were confined to specific applications and not suited for combustion experiments.
Orduña-Bustamente & Nelson [143] also investigated the active absorption of sound, however, they gave a more generalized formulation of a control approach to be able to adjust arbitrary reflection coefficients, as initially suggested by Guicking & Karcher [65]. By using an adaptive control algorithm, the so-called filtered-X least mean squares algorithm, the control parameters did not have to be tuned manually. In their setup, a source loudspeaker generated an acoustic field. Two microphones were used to determine an error signal, indicating the difference between desired and actual impedance. This error signal was fed to the adaptive controller, which drove a secondary loudspeaker acting on the acoustic field in the desired way. Using an adaptive controller, changes in the acoustic system could also be compensated.
A couple of years ago, Li et al. [106, 107] were the first to apply the control concept to non-reactive thermoacoustic systems. They used a similar method to reduce the resonator length of a thermoacoustic cooler. A duct was instrumented with loudspeakers at both ends. Accelerometers determined the movement of the loudspeakers' membranes and served as the control input. Two different adaptive control approaches were used to adjust the desired ratio of acoustic particle velocities and thus to match the impedance of a longer duct. They were able to tune the system in a frequency band of approximately 100 Hz.
All experiments in the cited publications were conducted in rather clean environments and at favourable signal-to-noise ratios. Up to now, the impedance tuning concept was never applied to combustion systems and not even in the presence of mean flow but only to very simple configurations. Furthermore, the approaches described above featured either controllers that had to be tuned manually or used rather complex adaptive control schemes.

In contrast, the approach followed in this thesis is to use model-based controllers. Doing so, the physical insight into the underlying mechanisms is much broader and allows a better understanding of the control scheme's impact on the complex interaction mechanisms between acoustics and combustion. As one main objective is to provide a control approach that can be used for industrial burner development, a straightforward controller setup is preferred. Additionally, the methods that are used to build up the control law are also used for linear stability analysis of thermoacoustic systems and therefore not unknown for engineers in this field.

1.5 Outline of the Thesis

The remaining parts of the thesis are structured as follows. Chapter 2 deals with the mathematical description of acoustic wave propagation, boundary conditions, and conditions for thermoacoustic instabilities to occur. Starting from the general conservation equations, an acoustic energy balance incorporating the acoustic boundary conditions is derived. It shows the importance of acoustic boundary conditions on the stability of the system.
An overview of the test facilities, the actuators used for excitation, as well as the measurement and control equipment is given in Chapter 3. Additionally, the calibration procedure for the pressure transducers as well as the steps that are needed to determine the plane wave pressure field using multiple microphones, namely the Multi-Microphone Method, are described.
For the control approach and alternative applications of the impedance tuning scheme, a basic understanding of low-order network models is advantageous. A brief summary is presented in Chapter 4. In the course of the work, the common approach was modified allowing for a fast computation of linear growth rates and instability frequencies in the time-domain.
The control approach is elucidated in Chapter 5. After an introduction of the principle, the control law is derived. To provide physical insight, the controller is model-based. Therefore, frequency domain system identification techniques have to be used to obtain its transfer function. Both controllers for discrete- and multi-frequency tuning are presented. The chapter closes with a modified version of the Multi-Microphone Method, which in contrast to the traditional formulation has a stable representation in the time-domain. This allows for an online decomposition of the plane-wave pressure field into the Riemann invariants from multiple measured pressures. A mathematical proof of stability is given in Appendix A.
Chapter 6 comprises all impedance tuning results. This includes network simulations of the control concept and preliminary tests at cold flow conditions. Section 6.4 is the main part of this chapter as it reports results in reactive flow for three different actuators, two of which are very robust and exhibit high control authorities, thus, are applicable to be used in industrial high-power rigs at elevated pressure. One of these actuators exhibited a strong non-linear response characteristic. Therefore, in Sec. 6.4.3, a modified controller is derived accounting for this non-linear characteristics. A comparison of the different actuator concepts with pros and cons is given in Sec. 6.4.4. If the actuators lack sufficient

control authority, the calculated control signal has to be limited to prevent from actuator overloading. In Sec. 6.5, the system behaviour for these cases is studied, proving that the control objective could be achieved nonetheless. Since the control concept often was applied to a system passively stabilized by a modification of the downstream termination and then used to reproduce the self-excited instability of the unstable system, the impact of this hardware change on the flame shape and position was investigated. The results are presented in Sec. 6.6.

The concept was also used for active control of combustion instabilities and to validate linear stability analyses with experimental data, as will be shown in Chapter 7. By tuning the downstream reflectivity of the combustion test rig, thermoacoustic instabilities could be mitigated. Additionally, the predictive capabilities of a network model regarding frequency of instability, linear growth rate, and transition from stability to instability could be assessed.

In Chapter 8, the main achievements of this thesis are summarized and a conclusion is drawn. Suggestions for further investigations as well as improvements of the impedance tuning scheme are given in the outlook (Sec. 8.2).

Figure 1.9 visually summarizes the explanations given above and shows major connections between the individual chapters.

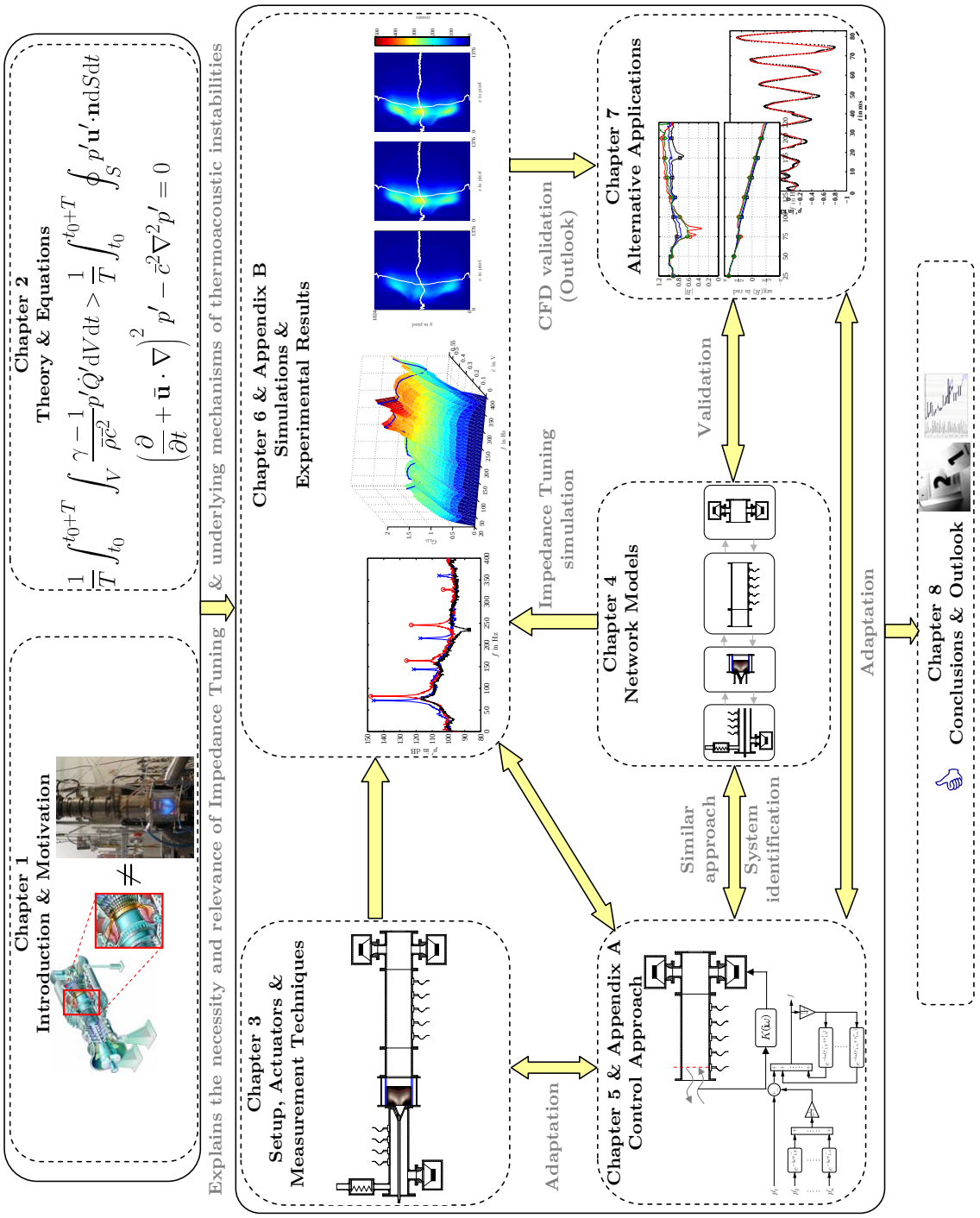

Figure 1.9: Thesis overview visually summarized.

"Wie alles sich zum Ganzen webt,
Eins in dem andern wirkt und lebt!"
J. W. v. Goethe, Faust I.

Chapter 2

Fundamental Thermoacoustic Theory and Equations

There is a vast amount of excellent books on classical acoustics and works on thermoacoustic theory. Most of these references, however, are very extensive and cover many aspects, which are not necessarily needed here or which focus on a different topic. On the other hand, not all aspects that are considered important for this study, can be found in a compact and well-suited way in one single reference. As it is by no means intended to cover the whole subject matter of thermoacoustics, this chapter, therefore, only provides the fundamental acoustic and thermoacoustic theory which is important to understand the underlying mechanisms and ideas of this dissertation.
Since this work emphasizes the relevance of acoustic boundary conditions for the stability of a thermoacoustic system, one of the main objectives of this chapter is to show how this important issue can be expressed mathematically. The underlying thread is as follows: Starting from the basic conservation equations, the wave equation is derived for different cases (Secs. 2.1 and 2.2). In Sec. 2.3, a solution for the one-dimensional convective wave equation is given. This includes the description of the system's acoustic properties by means of primitive acoustic variables and Riemann invariants as well as the definition of its acoustic boundary conditions. If thermoacoustic systems are considered, the classical wave equation has to be extended to include the effect of heat release. This is shown in Sec. 2.4. Classical acoustics cover the evolution of small amplitude disturbances superimposing the mean quantities. Thus, a brief study on the limits of linearity is given in Sec. 2.5. Finally, in Sec. 2.6, an expression for the acoustic energy inherent in a thermoacoustic system is derived. Using this expression, the influence of the acoustic boundary conditions on the system's stability will be investigated.
In preparing this chapter, especially references [7, 14, 17, 43, 133, 160, 179, 189, 229] were consulted.

2.1 Description of the Acoustic Field: The Wave Equation

When thermoacoustic instabilities occur, the frequency of oscillation is usually close to the acoustic resonance frequencies of the system considered. Since the acoustics of the system play such a crucial role, it is necessary to understand the underlying acoustic phenomena involved. Therefore, the equations describing the acoustic field and the propagation characteristics of acoustic waves in fluids are derived in this section. This is done starting from the conservation equations of mass, momentum, and energy. Here, only the most important steps will be explained. A more detailed derivation with additional information on the single terms in the equations and their meaning can, for instance, be found in references [14, 160, 179, 187, 229].
In the following, the element depicted in Fig. 2.1 is considered. It has a volume of V and

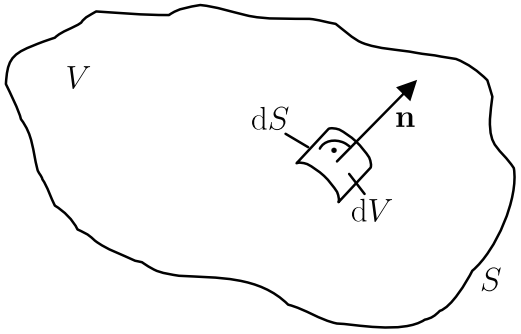

Figure 2.1: Generic system of volume V enclosed by a reasonably shaped surface S.

its surrounding surface is denoted by S. The integral notation of a conservation equation for an arbitrary extensive variable Ψ inside this surface takes the form

$$\int_V \frac{\partial \psi(\mathbf{x},t)}{\partial t} \mathrm{d}V + \oint_S \left[\psi(\mathbf{x},t)\cdot\mathbf{u}\right]\mathbf{n}\mathrm{d}S = \int_V q\mathrm{d}V + \int_V f\mathrm{d}V, \tag{2.1}$$

expressing the fact that the temporal change of the density ψ of the quantity Ψ ($\psi = \frac{\mathrm{d}\Psi}{\mathrm{d}V}$) in the volume V plus the net flux $\psi\mathbf{u}$ of this quantity across the system boundary are equal to the integration of a production term q and external forces f per unit volume over the volume. The other quantities in Eq. (2.1) are the velocity vector $\mathbf{u}$, the vector of spatial coordinates $\mathbf{x}$, the time t, and the normal vector $\mathbf{n}$ that is normal to and points out of the system boundary.
Considering an infinitesimal element $\mathrm{d}V$ and making use of Gauss' theorem[1], the differential form of the conservation equation is obtained if the medium is assumed to be continuous in $\mathrm{d}V$:

$$\frac{\partial \psi}{\partial t} + \nabla\cdot(\psi\mathbf{u}) = q + f. \tag{2.2}$$

[1] Gauss' theorem relates the flux of a vector field $\mathbf{F}$ through a surface to the divergence of the vector field in the volume enclosed by the surface: $\oint_S \mathbf{F}\cdot\mathbf{n}\mathrm{d}S = \int_V \nabla\cdot\mathbf{F}\mathrm{d}V$. Here, the differential operator $\nabla\cdot$ denotes the divergence of a vector, i.e., $\nabla\cdot = \frac{\partial}{\partial x} + \frac{\partial}{\partial y} + \frac{\partial}{\partial z}$; the divergence of a vector is a scalar. The '$\cdot$' denotes a scalar product.

From this general conservation equation, the conservation of mass, momentum, and energy can be derived.
Continuity of mass ($\psi = \rho$):

$$\frac{\partial \rho}{\partial t} + \nabla \cdot (\rho \mathbf{u}) = 0, \tag{2.3}$$

with ρ being the fluid density. If the mass of a single species in a combustion process is considered, there would be a production term on the right hand side due to chemical reactions.
Conservation of momentum ($\psi = \rho\mathbf{u}$):

$$\frac{\partial (\rho \mathbf{u})}{\partial t} + \nabla \cdot (\rho \mathbf{u}\mathbf{u}) = -\nabla p + \nabla \cdot \boldsymbol{\tau} + f, \tag{2.4}$$

where the gradient of pressure[2] ∇p and the divergence of the viscous stress tensor[3] $\nabla \cdot \boldsymbol{\tau}$ describe the momentum change due to pressure and viscous forces, respectively, and the notation $\mathbf{uu}$ denotes the dyadic product of two vectors.
Conservation of energy ($\psi = \rho e = \rho(e_\mathrm{t} - \frac{1}{2}\mathbf{u} \cdot \mathbf{u})$):

$$\frac{\partial (\rho e)}{\partial t} + \nabla \cdot (\rho e \mathbf{u}) = \boldsymbol{\tau} : \nabla \mathbf{u} - p \nabla \cdot \mathbf{u} - \nabla \cdot \mathbf{q} + \dot{Q}, \tag{2.5}$$

where e is the specific internal energy, $\boldsymbol{\tau}:\nabla\mathbf{u}$ represents the dissipation due to viscous forces[4], $\mathbf{q}$ stands for the conductive heat flux, and $\dot{Q}$ is the heat release per unit volume. Note that the equation for the energy conservation is not written for the specific total energy e_t but the specific internal energy e. It results from the conservation equation for e_t by subtracting Eq. (2.4) multiplied by $\mathbf{u}$ [179, 187]. Equation (2.4) can also be written in the non-conservative form as

$$\rho \frac{\mathrm{D}\mathbf{u}}{\mathrm{D}t} = -\nabla p + \nabla \cdot \boldsymbol{\tau} + f, \tag{2.6}$$

with the total or Lagrangian derivative $\frac{\mathrm{D}}{\mathrm{D}t}$ defined as $\frac{\mathrm{D}}{\mathrm{D}t} = \frac{\partial}{\partial t} + \mathbf{u} \cdot \nabla$. Additionally, instead of internal energy, Eq. (2.5) can also be written in terms of temperature, enthalpy, or entropy. The latter takes the form

$$\rho T \frac{\mathrm{D}s}{\mathrm{D}t} = \boldsymbol{\tau} : \nabla \mathbf{u} - \nabla \cdot \mathbf{q} + \dot{Q}, \tag{2.7}$$

where s is the specific entropy and T the temperature. This transformation can easily be obtained by using the fundamental law of thermodynamics for the entropy, given further below in Eq. (2.53), Eq. (2.62), and the continuity equation, Eq. (2.3).
Formed by Eqs. (2.3), (2.6), and (2.7), the system consists of 5 equations and has 7 unknowns. Thus, for closure, two more equations are needed.

[2] If the differential operator is applied to a scalar, as, e.g., the pressure, it will be written without '$\cdot$'. $\nabla = (\frac{\partial}{\partial x}, \frac{\partial}{\partial y}, \frac{\partial}{\partial z})^\mathrm{T}$, i.e., the gradient of a scalar is a vector and the gradient of a vector is a tensor.

[3] The viscous stress tensor is defined by $\boldsymbol{\tau} = \mu \left[(\nabla \mathbf{u} + (\nabla \mathbf{u})^\mathrm{T}) - \frac{2}{3}(\nabla \cdot \mathbf{u})\mathbf{I} \right]$, where μ is the mean dynamic viscosity and $\mathbf{I}$ is the identity matrix [179, 229]

[4] In the expression for the dissipation due to viscous forces, the operator ':' is the double contraction of two tensors yielding a scalar, i.e., $\boldsymbol{\tau}:\nabla\mathbf{u} = \nabla \cdot (\boldsymbol{\tau} \cdot \mathbf{u}) - \mathbf{u} \cdot (\nabla \cdot \boldsymbol{\tau})$.

These are the ideal gas law

$$p = \rho R T, \tag{2.8}$$

where R is the specific gas constant and the equation of state

$$p = p(\rho, s). \tag{2.9}$$

In the following, the equation of state will be needed in its differential form. Being a state variable, the pressure has a total differential of the form

$$\frac{\mathrm{D}p}{\mathrm{D}t} = \left(\frac{\partial p}{\partial \rho}\right)_s \frac{\mathrm{D}\rho}{\mathrm{D}t} + \left(\frac{\partial p}{\partial s}\right)_\rho \frac{\mathrm{D}s}{\mathrm{D}t}. \tag{2.10}$$

A further simplification of the system of conservation equations is obtained if viscous dissipation as well as heat conduction are negligible and neither heat release terms nor external forces are present:

$$\frac{\mathrm{D}\rho}{\mathrm{D}t} + \rho \nabla \cdot \mathbf{u} = 0, \tag{2.11}$$

$$\rho \frac{\mathrm{D}\mathbf{u}}{\mathrm{D}t} + \nabla p = 0, \tag{2.12}$$

$$\rho T \frac{\mathrm{D}s}{\mathrm{D}t} = 0. \tag{2.13}$$

Acoustic perturbations can be regarded as small-amplitude fluctuations superimposing the mean quantities. This is expressed by

$$\varphi(\mathbf{x}, t) = \bar{\varphi}(\mathbf{x}) + \varphi'(\mathbf{x}, t), \tag{2.14}$$

where φ is a generic flow variable, i.e., p, ρ, s, T, or $\mathbf{u}$. Superscripts $\bar{(\cdot)}$ and $(\cdot)'$ denote steady mean and fluctuating part, respectively. If the amplitudes are sufficiently small, $\varphi' \ll \bar{\varphi}$ (see also Sec. 2.5), the acoustic equations may be derived by a first-order approximation of the conservation equations neglecting non-linear second- or higher-order effects. In classical acoustics, a homogeneous, quiescent fluid is considered, i.e., a fluid with zero mean flow velocity ($\bar{\mathbf{u}} = 0$) and constant mean quantities ($\bar{\varphi}(\mathbf{x}) = \text{const.}$). Substituting Eq. (2.14) in Eqs. (2.11)-(2.13) and linearizing yields the linear acoustic equations of mass continuity

$$\frac{\partial \rho'}{\partial t} + \bar{\rho} \nabla \cdot \mathbf{u}' = 0, \tag{2.15}$$

conservation of momentum

$$\bar{\rho} \frac{\partial \mathbf{u}'}{\partial t} + \nabla p' = 0, \tag{2.16}$$

and conservation of energy

$$\rho T \frac{\partial s'}{\partial t} = 0. \tag{2.17}$$

Note that for any fluctuating quantity $\frac{\mathrm{D}}{\mathrm{D}t} \approx \frac{\partial}{\partial t}$ holds because in case of zero mean flow the convective term is always of second order. Linearizing the relation between pressure and density, Eq. (2.10) yields

$$\frac{\partial p'}{\partial t} = \left(\frac{\partial p}{\partial \rho}\right)_s \frac{\partial \rho'}{\partial t} + \left(\frac{\partial p}{\partial s}\right)_\rho \frac{\partial s'}{\partial t}. \tag{2.18}$$

With Eq. (2.17) this becomes

$$p' = \left(\frac{\partial p}{\partial \rho}\right)_s \rho', \tag{2.19}$$

with the constant factor being referred to as the square of the speed of sound c

$$\bar{c}^2 := \left(\frac{\partial p}{\partial \rho}\right)_s. \tag{2.20}$$

For an ideal gas the speed of sound can be calculated from

$$\bar{c} = \sqrt{\gamma R T}, \tag{2.21}$$

where γ is the ratio of specific heats. Taking the time derivative of Eq. (2.15) as well as the divergence of Eq. (2.16) yields

$$\frac{1}{\bar{c}^2}\frac{\partial^2 p'}{\partial t^2} + \bar{\rho}\frac{\partial}{\partial t}\nabla \cdot \mathbf{u}' = 0, \tag{2.22}$$

where the density has been replaced by Eq. (2.19) and

$$\bar{\rho}\nabla \cdot \frac{\partial \mathbf{u}'}{\partial t} + \nabla^2 p' = 0.^{5} \tag{2.23}$$

Combining Eqs. (2.22) and (2.23) results in the *wave equation* of classical acoustics

$$\frac{\partial^2 p'}{\partial t^2} - \bar{c}^2 \nabla^2 p' = 0, \tag{2.24}$$

which describes the propagation of sound waves in a homogeneous and quiescent fluid. Since visco-thermal effects are neglected, the equations are not valid in the viscous and thermal acoustic boundary layers, whose thicknesses are given by

$$\delta_\mathrm{v} = \sqrt{\frac{2\nu}{\omega}} \tag{2.25a}$$

[5] The Laplace operator ∇^2 is the divergence of the gradient, $\nabla \cdot \nabla = \frac{\partial^2}{\partial x^2} + \frac{\partial^2}{\partial y^2} + \frac{\partial^2}{\partial z^2}$, i.e., a scalar.

and

$$\delta_{\mathrm{th}} = \frac{\delta_{\mathrm{v}}}{\sqrt{Pr}}, \tag{2.25b}$$

respectively. Here ν is the kinematic viscosity, ω the angular frequency, and Pr the Prandtl number[6] of the medium. For the applications considered here, the dimensions of the geometries in which the acoustic waves propagate are much larger than the acoustic boundary layer thicknesses δ_{v} and δ_{th}. These are at 100 Hz in air at atmospheric conditions and 1300 K ($\nu = 186 \times 10^{-6}\,\mathrm{m^2/s}$) of the order 10^{-3} m. Damping effects on the wave propagation might either be neglected or incorporated in the boundary conditions. However, in case of ducts where the boundary layer thicknesses are not small compared to the diameter as well as for porous walls, this might not be valid, and a propagation equation accounting for dissipative losses would have to be derived, as was done by Tijdeman [220] and Morse & Ingard [132][7]. Also, these assumptions certainly do not hold for the zone in which combustion takes place.

2.2 The Convective Wave Equation

In this section, the influence of a constant, uniform mean flow $\bar{\mathbf{u}}$ on the propagation of acoustic waves will be derived. This can be done in an equivalent manner as for the classical wave equation by considering a non-zero mean flow in the initial linearized conservation equations. However, this involves some rather tedious calculation steps and vector analysis operations (see, e.g., Rienstra & Hirschberg [179]), which can be avoided by using the classical wave equation obtained in the preceding section. This approach was, for instance, followed by Munjal [133].

A stationary observer would see the propagation of an acoustic wave with the speed of sound $\bar{c}$ superposed by the mean flow $\bar{\mathbf{u}}$. This corresponds to an Eularian observer for whom the local time derivative $\frac{\partial}{\partial t}$ in presence of a mean flow has to be replaced by the substantial or convective derivative $\frac{\partial}{\partial t} + \bar{\mathbf{u}} \cdot \nabla$ to yield

$$\left(\frac{\partial}{\partial t} + \bar{\mathbf{u}} \cdot \nabla\right)^2 p' - \bar{c}^2 \nabla^2 p' = 0. \tag{2.26}$$

This is the *convective wave equation*, which is also valid for the case $\mathcal{O}(\bar{\mathbf{u}}) = \mathcal{O}(\mathbf{u}')$. Accordingly, a convective acoustic momentum equation may be derived from Eq. (2.16)

$$\bar{\rho}\left(\frac{\partial}{\partial t} + \bar{\mathbf{u}} \cdot \nabla\right)\mathbf{u}' + \nabla p' = 0, \tag{2.27}$$

relating acoustic particle velocity to acoustic pressure. Note that in deriving this equation, use has been made of the fact that in the linear, first-order theory, the flow field might be decoupled into an acoustic, vorticity, and entropy part, the so-called modes, as was proposed by Chu & Kovásznay [40]. This is necessary since in presence of mean flow,

[6] The Prandtl number is defined as $Pr = \frac{\mu c_p}{\kappa}$, where c_p is the heat capacity at constant pressure and κ is the thermal conductivity.

[7] see pp. 519 therein

perturbations in velocity might also be transported, i.e., convected, with the mean flow. Thus, the velocity perturbation $\mathbf{u}'$ has two parts $\mathbf{u}'_{\text{total}} = \mathbf{u}'_{\text{acoustic}} + \mathbf{u}'_{\text{vorticity}}$. Decoupling these yields an equation for the acoustic convective momentum and one for the vorticity, i.e., $\left(\frac{\partial}{\partial t} + \bar{\mathbf{u}} \cdot \nabla\right) \mathbf{u}'_{\text{vorticity}} = 0$. Interaction or coupling of the modes is then a second-order phenomenon and has, therefore, not to be considered in the linear regime.

2.3 Solution of the One-Dimensional Convective Wave Equation

In this work, only one-dimensional wave propagation is considered. Evidently, complex geometries as they appear in gas turbines evoke a three-dimensional acoustic field. However, for the case of rather simple test rig combustors, where the control concept is to be applied and by restricting the analysis to plane waves (see below), this simplification is valid. Solutions for the convective wave equation for the three-dimensional case might be found in references [43, 133, 160]. The restriction to one-dimensional phenomena allows to formulate the solution of the wave equation in a very descriptive way. In the following, the x-coordinate is considered, i.e., $\mathbf{u} = u$, $\mathbf{x} = x$, and $\nabla = \frac{\partial}{\partial x}$.
The one-dimensional convective wave equation (Eq. (2.26)) is a partial differential equation involving two independent variables, the spatial coordinate x and the time coordinate t. Assuming the time dependence to be harmonic, i.e., $e^{\mathrm{i}\omega t} = \cos(\omega t) + \mathrm{i}\sin(\omega t)$, the acoustic pressure can be expressed by

$$p'(x,t) = \Re\left\{\hat{p}(x,\omega)e^{\mathrm{i}\omega t}\right\}, \tag{2.28}$$

where $\Re$ denotes the real part and $\hat{p}(x,\omega)$ is the complex acoustic pressure depending on the spatial coordinate and the frequency. If, furthermore, the time derivative $\frac{\partial}{\partial t}$ is replaced by its frequency domain equivalent $\mathrm{i}\omega$, the convective wave equation can conveniently be transformed into a convective form of the Helmholtz equation

$$(1 - M^2)\frac{\partial^2 \hat{p}(x,\omega)}{\partial x^2} - 2\,M\,\mathrm{i}\,k\,\frac{\partial \hat{p}(x,\omega)}{\partial x} + k^2 \hat{p}(x,\omega) = 0. \tag{2.29}$$

Here, the wave number k

$$k = \frac{\omega}{\bar{c}} \tag{2.30}$$

and the Mach number M

$$M = \frac{\bar{u}}{\bar{c}} \tag{2.31}$$

were introduced and $\bar{u}$ is the mean flow velocity in positive x-direction. As can be seen, in the Helmholtz equation, the number of independent variables is reduced to one. For this second-order differential equation with constant coefficients, an ansatz of the form

$\hat{p}(x,\omega) = e^{\sigma x}$ can be made. Inserting this in Eq. (2.29) and solving for σ yields

$$\sigma^{\pm} = \mp \frac{\mathrm{i}k}{1 \pm M}. \tag{2.32}$$

Thus, the solution for the complex acoustic pressure takes the form

$$\hat{p}(x,\omega) = \hat{p}^{+}(x,\omega)\, e^{-\mathrm{i}k^{+}x} + \hat{p}^{-}(x,\omega)\, e^{+\mathrm{i}k^{-}x}, \tag{2.33}$$

with

$$k^{\pm} = \frac{k}{1 \pm M}. \tag{2.34}$$

By considering the harmonic time dependence, this becomes

$$p'(x,t) = \hat{p}^{+}\, e^{-\mathrm{i}k^{+}x+\mathrm{i}\omega t} + \hat{p}^{-}\, e^{+\mathrm{i}k^{-}x+\mathrm{i}\omega t}, \tag{2.35}$$

where, for ease of notation, the arguments on the right hand side have been dropped. Note, the measured acoustic pressure again is the real part of $p'(x,t)$.
The acoustic particle velocity can be calculated by assuming that it is of the same form as the acoustic pressure

$$u'(x,t) = C_1\, e^{-\mathrm{i}k^{+}x+\mathrm{i}\omega t} + C_2\, e^{+\mathrm{i}k^{-}x+\mathrm{i}\omega t}. \tag{2.36}$$

Substituting this in the acoustic convective momentum equation (Eq. (2.27)) and comparing the coefficients of the exponential terms then gives $C_1 = \hat{p}^{+}/\bar{\rho}\bar{c}$ and $C_2 = -\hat{p}^{-}/\bar{\rho}\bar{c}$ and thus

$$u'(x,t) = \frac{1}{\bar{\rho}\bar{c}} \left(\hat{p}^{+}\, e^{-\mathrm{i}k^{+}x+\mathrm{i}\omega t} - \hat{p}^{-}\, e^{+\mathrm{i}k^{-}x+\mathrm{i}\omega t} \right). \tag{2.37}$$

The integration constants $\hat{p}^{\pm}$ are determined by the boundary conditions closing the differential equation. They represent the complex amplitudes of down- and upstream travelling waves. These waves often are referred to as the Riemann invariants. The superscripts emphasize in which x-direction they travel. $\hat{p}^{+}$ travels downstream with the propagation velocity $c^{+} = \bar{c} + \bar{u}$, whereas $\hat{p}^{-}$ travels upstream with $c^{-} = \bar{c} - \bar{u}$. Henceforth, the summands will be replaced by the downstream travelling wave f and the upstream travelling component g, as it often can be found in literature, i.e.,

$$f(x,t) = f\left(t - \frac{x}{\bar{c} + \bar{u}}\right) := \frac{1}{\bar{\rho}\bar{c}}\, \hat{p}^{+}\, e^{-\mathrm{i}k^{+}x+\mathrm{i}\omega t} \tag{2.38a}$$

and

$$g(x,t) = g\left(t + \frac{x}{\bar{c} - \bar{u}}\right) := \frac{1}{\bar{\rho}\bar{c}}\, \hat{p}^{-}\, e^{+\mathrm{i}k^{-}x+\mathrm{i}\omega t}. \tag{2.38b}$$

The product of density and speed of sound $\bar{\rho}\bar{c}$ is termed characteristic impedance of the medium. It can be seen that the Riemann invariants for the case of the uniform, one-dimensional flow are functions of shifted arguments. Introducing Eqs. (2.38) into Eqs. (2.35) and (2.37), the relationship between the primitive acoustic variables and the Riemann

invariants takes the form

$$p' = \bar{\rho}\bar{c}\,(f+g)\,, \tag{2.39a}$$
$$u' = f - g. \tag{2.39b}$$

Due to linearity, Eqs. (2.39) hold in time as well as in frequency domain.

2.3.1 Acoustic Boundary Conditions

The complete solution of the Helmholtz equation for a specific problem is given by specifying the acoustic boundary conditions of the system under consideration. Two equivalent ways of describing these boundary conditions exists. The first one is to describe the relation between acoustic pressure and particle velocity at the system boundary in terms of an acoustic impedance. The acoustic impedance Z is defined as the ratio of the primitive acoustic variables in frequency domain

$$Z(x,\omega) = \frac{\hat{p}(x,\omega)}{\hat{u}(x,\omega)\cdot\mathbf{n}(x)}, \tag{2.40}$$

where $\mathbf{n}$ is inward normal to the system boundary, i.e., pointing into the system boundary and out of the fluid. It is a measure on how the impact of the acoustic pressure on the system boundary is *impeded*. Commonly, the impedance is assumed to be locally reacting. If a surface is considered, this means that the reaction of one point of the surface to the acoustic pressure is linear and independent of the motion of any other part of this surface. Thus, the local impedance is not dependent on the spatial distribution of the acoustic field but only a property of the surface. For more information reference [132][8] can be consulted. In the following, a dimensionless form of the impedance will be used. To do so, the impedance is scaled by the characteristic impedance of the medium:

$$Z_\mathrm{s}(x,\omega) = \frac{Z(x,\omega)}{\bar{\rho}\bar{c}}. \tag{2.41}$$

The acoustic impedance is a complex valued quantity

$$Z_\mathrm{s}(x,\omega) = \Re\left\{Z_\mathrm{s}(x,\omega)\right\} + \mathrm{i}\Im\left\{Z_\mathrm{s}(x,\omega)\right\}, \tag{2.42}$$

the real and imaginary part being referred to as specific acoustic resistance and reactance, respectively. The resistance describes the dissipation of acoustic energy. A specific impedance of 1, i.e., the impedance being the same as the characteristic impedance of the medium, corresponds to the fact that the acoustic waves are not reflected. Thus, for propagating waves, a change in temperature or medium at a certain location will cause reflection, as the characteristic impedance is changed. The reactance represents the ability of the surface to store acoustic energy and return or reflect it with a certain phase shift. From this it follows that an anechoic termination can only be achieved for purely real valued specific impedances being equal to 1.
Equivalently, the boundary conditions might be specified by defining reflection coefficients

[8] See pp. 260 therein.

of the system terminations. The reflection coefficient is defined as the ratio of reflected to incident wave. In case of the system's downstream end, i.e., f is the incident and g the reflected wave, it reads

$$R(x,\omega) = \frac{\hat{g}(x,\omega)}{\hat{f}(x,\omega)}. \tag{2.43}$$

Since the reflection coefficient as well as the impedance are defined in the frequency domain and therefore always depend on the frequency and the spatial coordinate, the arguments will be dropped in the following. The reflection coefficient is also a complex valued function, viz.,

$$R = |R| e^{\mathrm{i}\varphi_R}, \tag{2.44}$$

$|R|$ describing the ratio of the wave amplitudes and the φ_R the phase shift between the waves. Using the relation between Riemann invariants and primitive acoustic variables given in Eqs. (2.39), a bilinear transform between reflection coefficient and specific impedance is obtained

$$R = \frac{Z_\mathrm{s} - 1}{Z_\mathrm{s} + 1}. \tag{2.45}$$

From this distinct relationship, it can be seen that reflection coefficient and impedance are equivalent descriptions of the acoustic boundary conditions. Figure 2.2 shows this relationship for a real-valued impedance. Evidently, a reflection coefficient that describes a part of the system without acoustic sources has a magnitude less than or equal to unity[9]. In Fig. 2.2, it can be seen that in this limited range the impedance might accordingly take values ranging from zero to infinity. For this reason, in addition to be more descriptive, taking R as an acoustic boundary condition is often more convenient, as will be shown later on. Three distinct points can be identified in Fig. 2.2:

(i) $R = -1,\ Z_\mathrm{s} = 0 \rightarrow \hat{p} = 0$
There is a pressure node at the system boundary. This is the case for an open end, also referred to as an acoustically or sound soft end. The incident wave is fully reflected with a phase shift of π.

(ii) $R = 0,\ Z_\mathrm{s} = 1 \rightarrow \hat{p} = \bar{\rho}\bar{c}\,\hat{u}$
The impedance is equal to the characteristic impedance of the medium. This case corresponds to a perfectly absorbing or fully transmissive system boundary. The whole acoustic energy is transferred out of the system and the reflected wave amplitude is zero.

[9] Strictly, this is only valid for $M = 0$. In case of mean flow, the reflection coefficient of an open-ended duct may exceed unity. To understand this, consider the case for which the total acoustic energy is reflected at the duct's open end. For low Strouhal numbers ($St = \frac{fd}{\bar{u}}$) and without imposing the Kutta condition at the edges of the duct's end, the reflection coefficient's magnitude scales with $\frac{1+M}{1-M}$, which is larger than unity and may, thus, cause a reflection coefficient larger than unity. If the Kutta condition holds, the dependence of the magnitude on the Mach-number is more complex. Interesting discussions on this can be found in references [37, 52, 134, 158] and references therein.

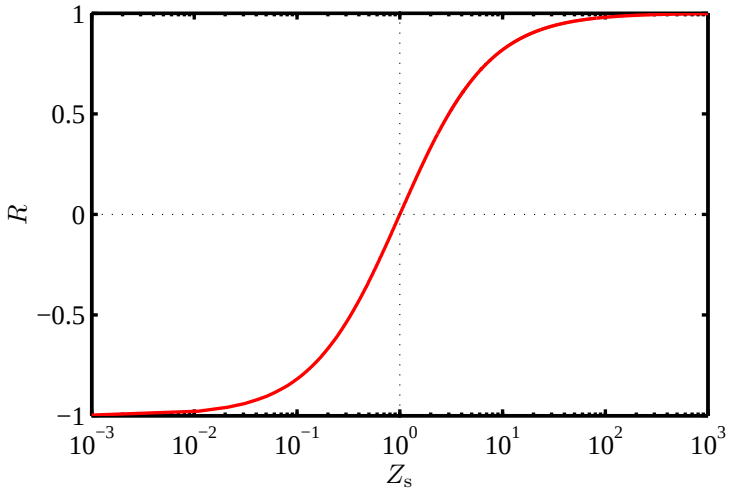

Figure 2.2: Range of reflection coefficient R as a function of the specific impedance Z_s ($\Im\{Z_\mathrm{s}\} = 0$).

(iii) $R = 1,\ Z_\mathrm{s} = \infty \rightarrow \hat{u} = 0$
There is a velocity node at the system boundary. This is the case for a closed end, i.e., a rigid surface, also referred to as an acoustically or sound hard end. The incident wave is fully reflected without a phase shift.

2.3.2 Cut-On Frequency

As stated before, the analysis in this study is restricted to one-dimensional acoustic fields. Therefore, the investigations are limited to a certain maximum frequency below which this simplification is valid. In this paragraph, it is briefly shown how this frequency is determined.
According to Munjal [133][10], the solution of the three-dimensional wave equation for wave propagation in circular ducts can be written in polar coordinates as

$$p'(r,\theta,x,t) = \sum_{m=-\infty}^{\infty}\sum_{n=0}^{\infty} J_m(k_{r,m,n}r)\, e^{\mathrm{i}m\theta} e^{\mathrm{i}\omega t} \cdots \\ \times \left(\hat{p}^{+}_{m,n}\, e^{-\mathrm{i}k^{+}_{x,m,n}x} + \hat{p}^{-}_{m,n}\, e^{+\mathrm{i}k^{-}_{x,m,n}x}\right), \tag{2.46}$$

where J_m is the m-th order Bessel function of the first kind, $k_{r,m,n}$ the n-th zero of J'_m, and m and n are the azimuthal and radial mode numbers, respectively. The axial transition wave number $k^{\pm}_{x,m,n}$ can be calculated by

$$k^{\pm}_{x,m,n} = \frac{\mp Mk + \sqrt{k^2 - (1-M^2)\, k^2_{r,m,n}}}{1-M^2}. \tag{2.47}$$

Higher-order modes ($m, n \geq 1$) can only propagate unattenuated if the transition wave number is purely real. Therefore, if the radicand in Eq. (2.47) is negative, only plane waves

[10] see pp. 19 therein

propagate. Note, if attenuation of plane waves due to viscous and thermal-conduction effects have to be accounted for, this would also be expressed by an imaginary wave number (see, for example, references [132] and [133][11]). With the definition of the wave number and the first zero of the Bessel function, this yields a limitation for the maximum frequency above which the first higher-order mode starts to propagate:

$$f < \frac{1.84\,\bar{c}}{\pi d}\sqrt{1-M^2}. \tag{2.48}$$

Here, d is the diameter of the duct. This means that depending on the diameter of the duct, the mean flow velocity, and the speed of sound, i.e., the temperature and the medium, the cut-on frequency of the first non-planar mode takes different values. An analogous form may be derived in Cartesian coordinates for rectangular ducts and can also be found in reference [133].
Note that higher-order modes might be present, although only frequencies below the cut-on frequency are accounted for. Consider, for instance, a turbulent flame or a woofer that is mounted circumferentially to the main duct in which the acoustic field is determined. In the vicinity of these sources, higher-order modes will distort the plane wave field. A certain distance from this source location is needed so that the attenuation of them is large enough. Therefore, attention has to be paid to the fact that measurement devices are located sufficiently far away to prevent the data of being contaminated by higher-order modes. When designing a measurement tube, FEM tools as, for example, COMSOL Multiphysics might be used to determine this distance. To get a rough a priori estimate for the attenuation of the first higher-mode, the azimuthal mode,

$$\mathcal{A} = e^{-\mathrm{i}x\sqrt{k^2-k^2_{\text{cut-on}}}} = e^{-\mathrm{i}x\sqrt{k^2-(\frac{1.84}{d/2})^2}} \tag{2.49}$$

might be used, where M is assumed to be low. The larger the axial distance x, the more is the azimuthal mode attenuated, i.e., the smaller is the value of $\mathcal{A}$. Note that only a statement on how the mode is attenuated can be made and not on the actual ratio between plane wave field and higher-order mode.

2.4 Influence of Fluctuating Heat Release on Wave Equation

Since thermoacoustic instabilities arise due to an interaction between unsteady heat release and acoustic field, a wave equation accounting for this has to be derived. Considering heat release, the flow is not isentropic anymore and the equations have to be changed to this respect. The simplified energy balance, Eq. (2.13), now reads

$$\rho T\frac{\mathrm{D}s}{\mathrm{D}t} = \dot{Q}. \tag{2.50}$$

[11] pp. 468 in [132] and pp. 13 in [133]

Therefore, in the equation of state, Eq. (2.10), the second term is not zero

$$\frac{\mathrm{D}p}{\mathrm{D}t} = \bar{c}^2 \frac{\mathrm{D}\rho}{\mathrm{D}t} + \left(\frac{\partial p}{\partial s}\right)_\rho \frac{\dot{Q}}{\rho T}. \tag{2.51}$$

The second term can be recast as follows:

$$\left(\frac{\partial p}{\partial s}\right)_\rho = \frac{\left(\frac{\partial p}{\partial T}\right)_\rho}{\left(\frac{\partial s}{\partial T}\right)_\rho}. \tag{2.52}$$

Using the ideal gas law and the fundamental law of thermodynamics for the entropy [7]

$$T\mathrm{d}s = \mathrm{d}e + p\mathrm{d}\rho^{-1}, \tag{2.53}$$

this can be further transformed to

$$\left(\frac{\partial p}{\partial s}\right)_\rho = \frac{\left(\frac{\partial p}{\partial T}\right)_\rho}{\left(\frac{\partial s}{\partial T}\right)_\rho} = \frac{\rho R}{c_v/T}. \tag{2.54}$$

Here, use has been made of the fact that for an ideal gas $\mathrm{d}e = c_v(T)\mathrm{d}T$ and that the specific heat at constant volume c_v can be regarded constant for small changes in T. With this and $c_v = R/(\gamma - 1)$, the equation of state is recast to

$$\frac{\mathrm{D}p}{\mathrm{D}t} = \bar{c}^2 \frac{\mathrm{D}\rho}{\mathrm{D}t} + (\gamma - 1)\dot{Q}. \tag{2.55}$$

For $\bar{u} = 0$, linearization yields

$$\frac{\partial p'}{\partial t} = \bar{c}^2 \frac{\partial \rho'}{\partial t} + u'\nabla\bar{\rho} + (\gamma - 1)\dot{Q}', \tag{2.56}$$

with the reasonable assumption that a spatial change in mean pressure is mainly caused by the mean flow and thus is small (even in presence of mean flow). From this, a wave equation in p' can only be obtained if the medium is assumed to be homogeneous, i.e., $\nabla\bar{\rho} = 0$. Neglecting this term in Eq. (2.56) in case of combustion might, though, be a precarious assumption. However, assuming the heat release zone to be infinitesimally small and using the equation only up- *or* downstream of the flame, where the medium is regarded homogeneous, analogously to the homogeneous convective wave equation, one may derive

$$\left(\frac{\partial}{\partial t} + \bar{u}\nabla\right)^2 p' - \bar{c}^2\nabla^2 p' = (\gamma - 1)\frac{\partial \dot{Q}'}{\partial t}. \tag{2.57}$$

This inhomogeneous convective wave equation shows the acoustic source character of a fluctuating heat release term.

2.5 Limits of Linearity

Since the acoustic wave propagation is regarded as a linear, first-order perturbation superimposing the mean flow quantities, it has to be examined up to which amplitudes this linearity assumption is valid. Here, the explanation of Pierce [160][12] is adopted.
The validity criterion results from the fact that each non-linear term must be much smaller than each of the dominant retained linear terms, to be neglected in an equation. An estimate of the individual terms in an equation can be made by assigning a characteristic time $\tilde{T}$ and length $\tilde{L}$ such that

$$\begin{aligned} \mathcal{O}\left(\frac{\partial \varphi'}{\partial t}\right) &= \frac{1}{\tilde{T}}\mathcal{O}(\varphi'), \\ \mathcal{O}(\nabla \varphi') &= \frac{1}{\tilde{L}}\mathcal{O}(\varphi') \end{aligned} \tag{2.58}$$

are valid for any acoustic quantity φ'. For plane wave propagation, the characteristic time $\tilde{T}$ is the period divided by 2π, whereas the characteristic length $\tilde{L}$ is the wavelength λ divided by 2π. Thus, the ratio between both is the speed of sound ($\tilde{L}/\tilde{T} = \lambda f = c$). Following Pierce [160], this results in the following criteria:

$$\frac{|p'|}{\bar{\rho}\bar{c}^2} = \frac{|p'|}{\gamma \bar{p}} \ll 1, \qquad \frac{|u'|}{\bar{c}} \ll 1, \qquad \frac{|\rho'|}{\bar{\rho}} \ll 1. \tag{2.59}$$

In a combustion chamber operated at atmospheric pressure, an acoustic pressure amplitude of 1 kPa would result in $|p'|/\gamma\bar{p} = 0.007$ (with $\gamma = 1.4$). If use is made of $u' = \mathcal{O}(p'/\rho c)$ and $p' = \bar{c}^2\rho'$, the two other conditions are equally matched. Note that for an ideal gas these conditions are invariant of temperature. For this case, the ratios given in Eq. (2.59) are smaller 1%, i.e., two orders of magnitude smaller than 1 and thus satify the validity criteria. In conclusion, 1 kPa can for the case of atmospheric combustion test rigs, which usually satisfy $\mathcal{O}(L) \leq \mathcal{O}(\lambda)$, be regarded as a threshold of the linearity assumption. In stationary gas turbines, pressure fluctuations can reach values of the order of 1% of the mean pressure, as was stated by Paschereit et al. [154, 156]. Note that at typical system pressures of 3 MPa, these pressure fluctuations, thus, can reach a considerable portion of the atmospheric pressure.
If the acoustic particle velocity is not small compared to the speed of sound, higher harmonics are generated. This gets very descriptive by considering a plane travelling wave of constant frequency generated at time t_0. It can be shown that each amplitude portion of this wave travels with a propagation speed that is composed of the sum of the speed of sound and the acoustic particle velocity, dependent on the amplitude [132, 160][13]. The larger the amplitude, the larger is the propagation velocity. Thus, a pressure maximum travels faster than a minimum. Due to this, at a time $t_0 + \Delta t$, the initially pure sine wave is distorted; the wave form is steepened, thus, generating harmonics.
In case of thermoacoustic instabilities, strong non-linearities are observed in the acoustic pressure signal. However, the predominant cause for this non-linearity is usually considered to be introduced by the flame [47, 109, 194].

[12] p. 16 therein
[13] pp. 874 in [132], pp. 566 in [160]

2.6 Thermoacoustic Instabilities: Acoustic Energy Balance

Generally, a thermoacoustic system gets unstable, i.e., disturbances of the flow variables will grow until they reach a limit-cycling state, if the net acoustic energy gain exceeds the losses. Starting from the linearized equations of mass and momentum, an acoustic energy equation will be derived, which is of the differential form of the general conservation equation given by Eq. (2.1). This equation reads

$$\frac{\partial \mathcal{E}}{\partial t} + \nabla \cdot \boldsymbol{\mathcal{F}} = \mathcal{S}, \tag{2.60}$$

where $\mathcal{E}$ is the acoustic energy density, $\boldsymbol{\mathcal{F}}$ the corresponding acoustic energy flux, and $\mathcal{S}$ a placeholder for source terms.

The derivation of an expression $\mathcal{E}$ which fits into the form of Eq. (2.60) is somewhat arbitrary. It depends on what actually is defined as a contribution to acoustic energy. Several approaches might be found in the literature; confer, for example, to Morfey [131] for a comprehensive discussion. The one which is followed here is similar to the ones that can be found in the work of Chu [39] and a recent investigation of this issue conducted by Nicoud & Poinsot [139], the latter reference considering an even more general form than the first. Chu [39] stated that "*the [total] energy of a disturbance should be a positive definite quantity which, in absence of heat transfer at the boundaries and of work done by them, must be a monotone non-increasing function of time; the rate of change of the quantity should depend on the coefficients of viscosity, μ_0, and heat conduction, K_0, and is zero when $\mu_0 = K_0 = 0$*", which is the case considered here.

As was stated by Myers [136], expressions for energy are of second degree in the disturbance variable, however, "*if that disturbance is treated according to a first-order approximate theory*", as it is the case for linear acoustics, "*then a useful measure of energy must contain only first-order approximations as well*". It will be shown how the acoustic energy density is constructed and how it might be related to a fluctuating heat release source term $\dot{Q}'$. For the derivation shown here, a fluid at rest, $\bar{\mathbf{u}} = 0$, with $\nabla \bar{s} = 0$ is considered, i.e., viscous effects and heat conduction are neglected. Particularly the latter is certainly a coarse simplification of the combustion process in a gas turbine as it clearly induces a non-uniform entropy field in space. However, to understand the underlying mechanisms of thermoacoustic instabilities, this approach promotes a good trade-off between clarity and simplifications and is, therefore, very useful. Moreover, there will always be a non-zero mean flow. However, restricting the investigation to the low Mach number limit only is reasonable for gas turbine combustors as long as the turbine inlet is not considered and will, therefore, not introduce severe errors. Mach number effects might be modeled by means of a "*compact nozzle*" boundary condition for nozzle dimensions that are small compared to the acoustic wavelengths, as was shown by Marble & Candel [118]. Derivations with $\bar{\mathbf{u}} \neq 0$ can, e.g., be found in references [39, 135, 136, 160, 179]. Nicoud & Poinsot [139] derived an energy expression, considering viscous effects, heat conduction, and non-uniform entropy. However, they assumed the mean flow to be zero. Giauque et al. [61] recently extended the derivations given by Myers [136], which they qualified as the most general forms, by including heat release effects. However, these general expressions are rather complex and if physical insight into the underlying mechanisms is sought for, the simplified equations

presented here are suited better.
Including a fluctuating heat release term, the linearized energy equation, Eq. (2.17), reads

$$\bar{\rho}\bar{T}\frac{\partial s'}{\partial t} = \dot{Q}'. \tag{2.61}$$

For the subsequent calculation steps, it is convenient to replace the entropy in this equation with the temperature. Considering an ideal gas and using

$$\mathrm{d}\rho^{-1} = \frac{\mathrm{d}\rho^{-1}}{\mathrm{d}\rho}\mathrm{d}\rho = -\frac{1}{\rho^2}\mathrm{d}\rho, \tag{2.62}$$

the fundamental thermodynamic equation for the entropy, Eq. (2.53), is recast to yield

$$\mathrm{d}s = c_v(T)\frac{\mathrm{d}T}{T} - \frac{R}{\rho}\mathrm{d}\rho. \tag{2.63}$$

For small fluctuations φ' around the mean value $\bar{\varphi}$ this becomes

$$s' = c_v\frac{T'}{\bar{T}} - R\frac{\rho'}{\bar{\rho}}, \tag{2.64}$$

where the specific heat at constant volume c_v can be regarded constant for small T'. Introducing this into Eq. (2.61) and using the linearized continuity equation, Eq. (2.15), to replace the density fluctuations yields

$$\bar{\rho}c_v\frac{\partial T'}{\partial t} + p\nabla\cdot\mathbf{u}' = \dot{Q}'. \tag{2.65}$$

Multiplying the linearized conservation equations of mass (Eq. (2.15)) with $\frac{\bar{c}^2\rho'}{\gamma\bar{\rho}}$, momentum (Eq. (2.16)) with $\mathbf{u}$, and Eq. (2.65) with $T'/\bar{T}$ and taking the sum of all three yields

$$\begin{aligned}\frac{1}{2}\bar{\rho}\frac{\partial(\mathbf{u}')^2}{\partial t} + \frac{1}{2}\frac{\bar{c}^2}{\gamma\bar{\rho}}\frac{\partial(\rho')^2}{\partial t} + \frac{1}{2}\frac{\bar{\rho}c_v}{\bar{T}}\frac{\partial(T')^2}{\partial t}\cdots \\ + \left(\frac{\bar{c}^2}{\gamma}\rho' + \frac{\bar{p}}{\bar{T}}T'\right)\nabla\cdot\mathbf{u}' + \mathbf{u}'\cdot\nabla p' = \frac{T'}{\bar{T}}\dot{Q}'.\end{aligned} \tag{2.66}$$

With the linearized ideal gas law

$$\frac{p'}{\bar{p}} = \frac{\rho'}{\bar{\rho}} + \frac{T'}{\bar{T}}, \tag{2.67}$$

[14]

one obtains

$$\frac{1}{2}\bar{\rho}\frac{\partial(\mathbf{u}')^2}{\partial t} + \frac{1}{2}\frac{\bar{c}^2}{\gamma\bar{\rho}}\frac{\partial(\rho')^2}{\partial t} + \frac{1}{2}\frac{\bar{\rho}c_v}{\bar{T}}\frac{\partial(T')^2}{\partial t} + \nabla\cdot(p'\mathbf{u}') = \frac{T'}{\bar{T}}\dot{Q}'. \tag{2.68}$$

[14] The ideal gas law reads $p = \rho RT$. Linearizing around the mean value gives $p - \bar{p} = p' = \left(\frac{\partial p}{\partial\rho}\right)_{\bar{T},\bar{\rho}}\rho' + \left(\frac{\partial p}{\partial T}\right)_{\bar{T},\bar{\rho}}T'$ and thus $p' = R\bar{T}\rho' + \bar{\rho}RT'$, which divided by $\bar{p}$ yields Eq. (2.67).

Comparison with Eq. (2.60) results in the expression for the acoustic energy density

$$\mathcal{E} = \frac{1}{2}\bar{\rho}\mathbf{u}'^2 + \frac{1}{2}\frac{\bar{c}^2}{\gamma\bar{\rho}}\rho'^2 + \frac{1}{2}\frac{\bar{\rho}c_v}{\bar{T}}T'^2 \tag{2.69}$$

and the acoustic energy flux

$$\boldsymbol{\mathcal{F}} = p'\mathbf{u}'. \tag{2.70}$$

Following Chu [39], the expression for the acoustic energy density can be recast yielding

$$\mathcal{E} = \frac{1}{2}\bar{\rho}\mathbf{u}'^2 + \frac{1}{2}\frac{1}{\bar{\rho}\bar{c}^2}p'^2 + \frac{1}{2}\frac{\bar{\rho}\bar{T}}{c_p}s'^2, \tag{2.71}$$

stating that the total acoustic energy density in the disturbance is composed of the sum of the kinetic energy and the potential energy associated with compression and heat exchange, respectively. Here, use has been made of the linearized ideal gas law and Eq. (2.64).
In the theory of small amplitude disturbances, pressure and entropy fluctuations are two independent, uncoupled modes of fluctuations [40]. Since only these linear regimes are considered, using the result of Eq. (2.71) in Eq. (2.68), the latter might be decomposed into the two following parts [39]

$$\frac{\partial\mathcal{E}_{\text{mech}}}{\partial t} = \frac{1}{2}\bar{\rho}\frac{\partial(\mathbf{u}')^2}{\partial t} + \frac{1}{2}\frac{1}{\bar{\rho}\bar{c}^2}\frac{\partial(p')^2}{\partial t} = \frac{\gamma-1}{\bar{\rho}\bar{c}^2}p'\dot{Q}' - \nabla\cdot(p'\mathbf{u}') \tag{2.72a}$$

and

$$\frac{1}{2}\bar{\rho}\bar{T}\frac{\partial(s')^2}{\partial t} = s'\dot{Q}'. \tag{2.72b}$$

Equation (2.72a) represents the change of mechanical energy, composed of the kinetic energy and the potential energy associated with compression, whereas Eq. (2.72b) describes the change in level of entropy fluctuation. Note that the objective of this derivation is only to explain the mechanism that is responsible for the onset of thermoacoustic instabilities. In case of high amplitude limit-cycle oscillations, these simplifications certainly will note hold.
In order to investigate the energy balance of the system, the spatial and temporal integrals of Eqs. (2.72) are taken into account. If harmonic fluctuations are considered, integration has to be carried out over one period of oscillation T. This yields

$$\begin{aligned}\Delta\mathcal{E}_{V,\text{mech}} &= \frac{1}{T}\int_{t_0}^{t_0+T}\int_V \frac{\partial\mathcal{E}_{\text{mech}}}{\partial t}\mathrm{d}V\mathrm{d}t \\ &= \frac{1}{T}\int_{t_0}^{t_0+T}\int_V \frac{\gamma-1}{\bar{\rho}\bar{c}^2}p'\dot{Q}'\mathrm{d}V\mathrm{d}t - \frac{1}{T}\int_{t_0}^{t_0+T}\oint_S p'\mathbf{u}'\cdot\mathbf{n}\mathrm{d}S\mathrm{d}t\end{aligned} \tag{2.73a}$$

and

$$\frac{1}{T}\int_{t_0}^{t_0+T}\int_V \frac{1}{2}\bar{\rho}\bar{T}\frac{\partial(s')^2}{\partial t}\mathrm{d}V\mathrm{d}t = \frac{1}{T}\int_{t_0}^{t_0+T}\int_V s'\dot{Q}'\mathrm{d}V\mathrm{d}t, \tag{2.73b}$$

where $\mathbf{n}$ is the normal vector pointing out of the volume and use has been made of Gauss' theorem (see Sec. 2.1). The index V denotes that $\mathcal{E}$ is the acoustic energy density integrated

over the volume. Equation (2.73a) is the generalized form of the famous Rayleigh criterion. In its classical form given in Eq. (1.2), the energy fluxes at the system boundary are set to zero and therefore the acoustic energy in the system is increased if in the source term on the right hand side, the pressure fluctuations are in phase with the heat release fluctuations. The extended version of the Rayleigh criterion accounts for the more realistic case of boundary conditions that are not perfectly acoustically soft or hard resulting in a non-zero energy flux. It reads

$$\frac{1}{T}\int_{t_0}^{t_0+T}\int_V \frac{\gamma-1}{\bar{\rho}\bar{c}^2}p'\dot{Q}'\mathrm{d}V\mathrm{d}t > \frac{1}{T}\int_{t_0}^{t_0+T}\oint_S p'\mathbf{u}'\cdot\mathbf{n}\mathrm{d}S\mathrm{d}t, \tag{2.74}$$

stating that a system might get unstable if pressure and heat release fluctuations are in phase in the source term *and* exceed the energy flux across the system boundaries.
From the preceding discussion, it can be seen that the classical Rayleigh criterion is neither a necessary nor a sufficient condition for thermoacoustic instability to occur. It merely states under which conditions unsteady heat release promotes an onset of oscillations. Yet, the former is often stated in literature. This can be understood considering Eq. (2.73b), which further extends the prediction of instability to the case of entropy fluctuations. It amends the sole consideration of acoustic energy to the more general case of fluctuation energy [139]. If pressure and heat release fluctuations were out of phase, the merely acoustical treatment of Eq. (1.2) – and also Eq. (2.74) – would predict a stable system. However, due to entropy fluctuations that are in phase with heat release fluctuations, the system might get unstable nonetheless. If Eq. (2.68) is not decomposed but directly integrated, the condition for instability could equivalently be expressed in terms of in-phase fluctuations of temperature and heat release when entropy fluctuations are considered in the equation for the acoustic energy. And it is also not a sufficient criterion as the source term might be smaller than dissipation effects that are not accounted for. However, as entropy fluctuations might often be neglected, it might be (and is still) used as a rule of thumb in today's practice.
Viscous effects will increase the damping. Mathematically, this effect is captured by the fact that a viscosity term then appears on the right hand side of Eq. (2.74), see, for example, references [39, 48, 139].
From these explanations, it is clear that a thermoacoustic system gets unstable if the phase relationship between pressure and heat release promotes constructive interference and the net energy gain exceeds the losses. The influence of the acoustic boundary conditions on the system stability can readily be understood from this fact as they determine the pressure field in the system. This becomes even more obvious if the boundary conditions are introduced into Eq. (2.73a). A similar derivation of system stability as well as two additional approaches were previously presented by Schuermans [189].
Consider the system shown in Fig. 2.3. The heat release zone is located in an infinitesimally small sheet. The system is terminated with an up- and downstream impedance, defined at the locations that are denoted with 1 and 2, respectively. Neglecting entropy fluctuations, the energy balance for this system reads

$$\begin{aligned}\Delta\mathcal{E}_V = \frac{1}{T}\int_{t_0}^{t_0+T}\int_V \frac{\gamma-1}{\bar{\rho}\bar{c}^2}p'\dot{Q}'\mathrm{d}V\mathrm{d}t\ldots \\ + \frac{1}{T}\int_{t_0}^{t_0+T}\oint_{S_1} p_1'\mathbf{u_1'}\cdot\mathrm{d}\mathbf{S}_1\mathrm{d}t - \frac{1}{T}\int_{t_0}^{t_0+T}\oint_{S_2} p_2'\mathbf{u_2'}\cdot\mathrm{d}\mathbf{S}_2\mathrm{d}t,\end{aligned} \tag{2.75}$$

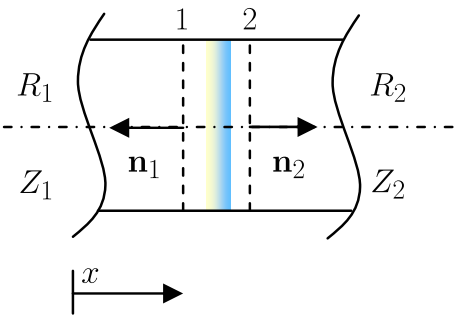

Figure 2.3: Schematic of a thermoacoustic system consisting of a duct with heat release zone and up- and downstream boundary conditions.

where $\mathrm{d}\mathbf{S}_j$ replaces $\mathbf{n_j}\mathrm{d}S_j$. Under the assumption that only plane waves propagate in the system, i.e., acoustic pressure and particle velocity are constant across the cross section S, this can be simplified to yield

$$\Delta\mathcal{E}_V = \frac{1}{T}\int_{t_0}^{t_0+T}\frac{\gamma-1}{\bar{\rho}\bar{c}^2}p'\int_V \dot{Q}'\mathrm{d}V\mathrm{d}t + \frac{S}{T}\int_{t_0}^{t_0+T} p_1'u_1'\mathrm{d}t - \frac{S}{T}\int_{t_0}^{t_0+T} p_2'u_2'\mathrm{d}t. \tag{2.76}$$

If harmonic perturbations are considered, the acoustic pressure $p'(t)$ in time domain is related to its frequency domain expression $\hat{p}(\omega)$ by Eq. (2.28). After a few transformations[15], this equation can be rewritten as

$$p'(t) = \Re\left\{\hat{p}(\omega)e^{\mathrm{i}\omega t}\right\} = \frac{1}{2}\left[\hat{p}(\omega)e^{\mathrm{i}\omega t} + \hat{p}^*(\omega)e^{-\mathrm{i}\omega t}\right], \tag{2.77}$$

where $\hat{p}^*$ denotes the complex conjugate of $\hat{p}$. It will now be shown how the integrals over one cycle can be calculated. For ease of notation, the argument will be neglected in the following:

$$\begin{aligned}\frac{1}{T}\int_{t_0}^{t_0+T} p'u'\mathrm{d}t &= \frac{1}{4T}\int_{t_0}^{t_0+T}\left(\hat{p}e^{\mathrm{i}\omega t} + \hat{p}^*e^{-\mathrm{i}\omega t}\right)\left(\hat{u}e^{\mathrm{i}\omega t} + \hat{u}^*e^{-\mathrm{i}\omega t}\right)\mathrm{d}t \\ &= \frac{1}{4T}\int_{t_0}^{t_0+T}\hat{p}\hat{u}e^{\mathrm{i}\omega 2t} + \hat{p}\hat{u}^* + \hat{p}^*\hat{u} + \hat{p}^*\hat{u}^*e^{-\mathrm{i}\omega 2t}\,\mathrm{d}t \\ &= \frac{1}{4T}\int_{t_0}^{t_0+T}\hat{p}\hat{u}^* + \hat{p}^*\hat{u}\,\mathrm{d}t.\end{aligned} \tag{2.78}$$

Replacing $\hat{u}$ by the impedance Z, this becomes

$$\begin{aligned}\frac{1}{4T}\int_{t_0}^{t_0+T}\hat{p}\hat{p}^*\frac{1}{Z^*} + \hat{p}^*\hat{p}\frac{1}{Z}\mathrm{d}t &= \frac{1}{4T}\int_{t_0}^{t_0+T}|\hat{p}|^2\frac{2\Re\{Z\}}{|Z|^2}\mathrm{d}t \text{[16]} \\ &= \frac{1}{2}|\hat{p}|^2\frac{\Re\{Z\}}{|Z|^2} \\ &= \frac{1}{2}|\hat{u}|^2\Re\{Z\}.\end{aligned} \tag{2.79}$$

[15] Consider a complex quantity $z = a + \mathrm{i}b$. The real part of z can be transformed as follows:
$\Re\{z\} = \frac{1}{2}\Re\{z\} + \frac{1}{2}\Re\{z\} = \frac{1}{2}\left[\Re\{z\} + \Re\{z^*\}\right] = \frac{1}{2}(z + z^*)$
Equation (2.77) then follows from the fact that the complex conjugate of $z = \hat{p}(\omega)e^{\mathrm{i}\omega t}$ is $z^* = \hat{p}^*(\omega)e^{-\mathrm{i}\omega t}$.

Analogously, an expression for the temporal integral of the source term in Eq. (2.76) can be derived. This is done by introducing a flame transfer function $\mathcal{F}$, which relates heat release to velocity perturbations, i.e., $\mathcal{F} = \hat{\dot{Q}}_V/\hat{u}_1$. Here, the spatial integral of $\dot{Q}'$ was replaced by $\dot{Q}'_V$, i.e., $\dot{Q}'_V = \int_V \dot{Q}' \mathrm{d}V$ in Eq. (2.76). This yields

$$\frac{1}{T}\int_{t_0}^{t_0+T} p'_1 Q'_V \mathrm{d}t = \frac{1}{4T}\int_{t_0}^{t_0+T} \hat{p}_1 \hat{\dot{Q}}_V^* + \hat{p}_1^* \hat{\dot{Q}}_V \,\mathrm{d}t \quad = -\frac{1}{2}|\hat{p}_1|^2 \frac{\Re\{\mathcal{F}Z_1\}}{|Z_1|^2}. \tag{2.80}$$

The negative sign results from the fact that the impedance at the upstream end is defined by $Z_1 = -\hat{p}_1/\hat{u}_1$ since the normal vector $\mathbf{n}_1$ in Fig. 2.3 points into the system boundary, i.e., in negative direction. Thus, the energy balance reads

$$\Delta\mathcal{E}_V = \frac{1}{2}|\hat{p}|^2 \left(-\frac{\gamma-1}{\bar{\rho}\bar{c}^2}\frac{\Re\{\mathcal{F}Z_1\}}{|Z_1|^2} - S\frac{\Re\{Z_1\}}{|Z_1|^2} - S\frac{\Re\{Z_2\}}{|Z_2|^2} \right), \tag{2.81}$$

taking advantage of the fact that in the low Mach number limit, which is considered here, the acoustic pressure remains constant across the flame. This follows, if the flame is regarded as a discontinuity and the Rankine-Hugoniot equations are applied to relate acoustic quantities up- and downstream of the flame [108, 195].
Since it is more instructive to consider the reflection coefficient instead of the impedance, Eq. (2.81) is rewritten in terms of reflection coefficients using the bilinear transform between Z and R given in Eq. (2.45) and the relationship between Riemann invariants and acoustic pressure $\hat{p} = \bar{\rho}\bar{c}(\hat{f} + \hat{g})$.

$$\begin{aligned}\Delta\mathcal{E}_V = &-\frac{1}{2}\frac{\gamma-1}{\bar{\rho}\bar{c}^2}|\hat{p}|^2\frac{\Re\{\mathcal{F}Z_1\}}{|Z_1|^2}\ldots \\ &-\frac{1}{2}S|\hat{g}_1|^2|1-R_1|^2\,\Re\left\{\frac{1+R_1}{1-R_1}\right\}\ldots \\ &-\frac{1}{2}S|\hat{f}_2|^2|1-R_2|^2\,\Re\left\{\frac{1+R_2}{1-R_2}\right\}.\end{aligned} \tag{2.82}$$

This can further be recast to[17]

$$\begin{aligned}\Delta\mathcal{E}_V = &-\frac{1}{2}\frac{\gamma-1}{\bar{\rho}\bar{c}^2}|\hat{p}|^2\frac{\Re\{\mathcal{F}Z_1\}}{|Z_1|^2}\ldots \\ &-\frac{1}{2}S|\hat{g}_1|^2(1-|R_1|^2) - \frac{1}{2}S|\hat{f}_2|^2(1-|R_2|^2).\end{aligned} \tag{2.83}$$

Physically, the first term in Eq. (2.83) is the production term, whereas the two other terms define the losses across the system boundaries. This means that the overall acoustic energy of the system $\Delta\mathcal{E}_V$ is increased when the production term exceeds the losses across the system boundaries. In Fig. 2.4, the acoustic loss term of the downstream side is plotted

[16] $\frac{1}{Z^*} + \frac{1}{Z} = \frac{Z+Z^*}{ZZ^*} = \frac{2\Re\{Z\}}{|Z|^2}$

[17] For any complex number $R = a + \mathrm{i}b$, the expression $|1-R|^2\,\Re\left\{\frac{1+R}{1-R}\right\}$ can be rearranged as follows: First, note that $|1-R|^2 = |1-a-\mathrm{i}b|^2 = (1-a)^2+b^2$ and $\Re\left\{\frac{1+R}{1-R}\right\} = \frac{(1+a+\mathrm{i}b)(1-a+\mathrm{i}b)}{(1-a)^2+b^2}$. With this, one obtains $|1-R|^2\,\Re\left\{\frac{1+R}{1-R}\right\} = \Re\{(1+a+\mathrm{i}b)(1-a+\mathrm{i}b)\} = 1-(a^2+b^2) = 1-|a+\mathrm{i}b|^2 = 1-|R|^2$.

versus the reflection coefficient. If $R_2 = 0$, no acoustic waves are reflected and the acoustic

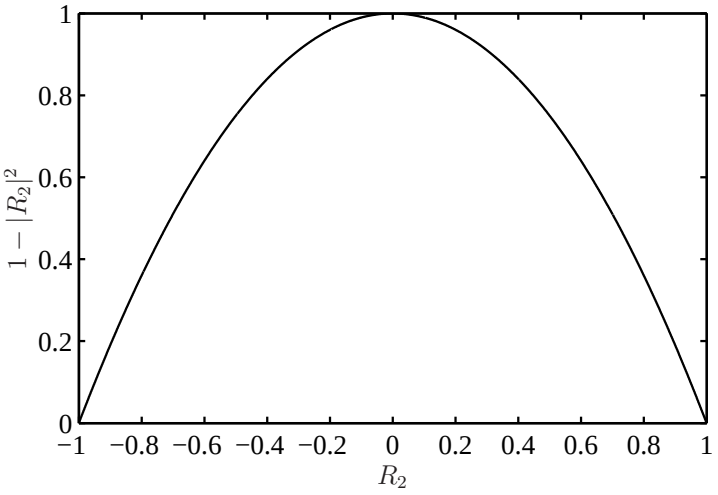

Figure 2.4: Acoustic loss term of downstream reflection coefficient $1 - |R_2|^2$ versus R_2.

loss term is maximal; the total incident acoustic energy ($\propto |\hat{f}_2|^2$) is transmitted via the system boundaries. If the downstream boundary condition is fully reflecting, i.e., $R_2 = \pm 1$, no acoustic energy is transferred since the acoustic loss term is zero.

From the discussion, it became obvious that increasing the transfer of acoustic energy across the system boundaries, for example, by decreasing the reflection of acoustic waves, can reach a level at which the net gain does not exceed the losses, although the coupling might be positive. In this case, $\Delta\mathcal{E}_V$ would not increase.

Not only the loss of acoustic energy across the system boundaries, but also the phase relationship between acoustic pressure and unsteady heat release are determined by the acoustic boundary conditions of the system. A change in the phase of a reflection coefficient causes a different distribution of the acoustic pressure in the system and thus a different coupling. The latter point is illustrated by considering a thermoacoustic model of the combustion test rig used for the experiments in this thesis. How a so-called network model can be derived and how it can be used to predict the thermoacoustic response of the test rig is elucidated in detail in Chapter 4. The test rig is presented in Chapter 3. For now, it is only important that it is possible to describe the one-dimensional, linear thermoacoustic properties with this model.

The description is done in such a way that the test rig is "divided" into an upstream part comprising the fuel supply lines, the burner, and the flame response, which is thermoacoustically described by an upstream reflection coefficient R_{us} and another part that represents the acoustics of the downstream side, i.e., R_{ds}. Figure 2.5 shows these two parts. Between the up- and the downstream end a virtual duct is implemented in the model. All parts are interconnected by means of Riemann invariants. For example, the g-wave that leaves the downstream part R_{ds} is the same that enters the virtual duct on its downstream side.

A change of the phase relationship between unsteady heat release and acoustics can be represented by a change of system length. With the model, it is possible to predict the resonance frequency of the system subject to a modification of the virtual duct. The length of the central duct is changed between 0 m and 2.54 m. In Fig. 2.6 (top), the variation of the resonance frequency f_{res} as a function of the system extension Δl can be seen. The

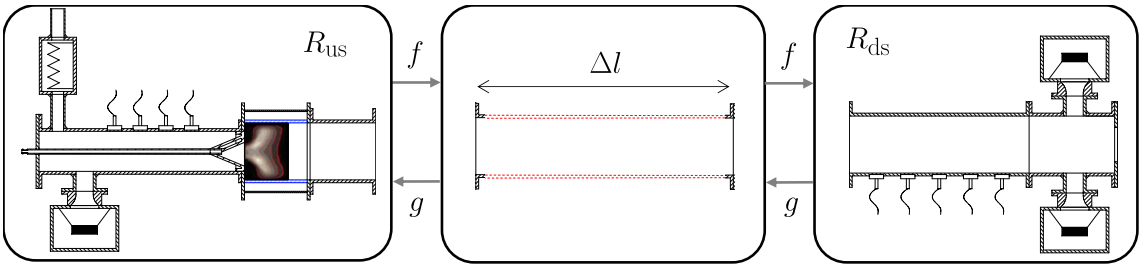

Figure 2.5: Schematic of a model describing the thermoacoustic properties of a combustion test rig.

physical system ($\Delta l = 0$) has a resonance frequency of 87 Hz. With increasing length, this resonance frequency is changed to lower values. Not only the resonance frequency, but also the linear growth rate of the combustion system is altered. This can be seen in the bottom frame of Fig. 2.6. Depending on the adjusted length, i.e., the phase between unsteady heat

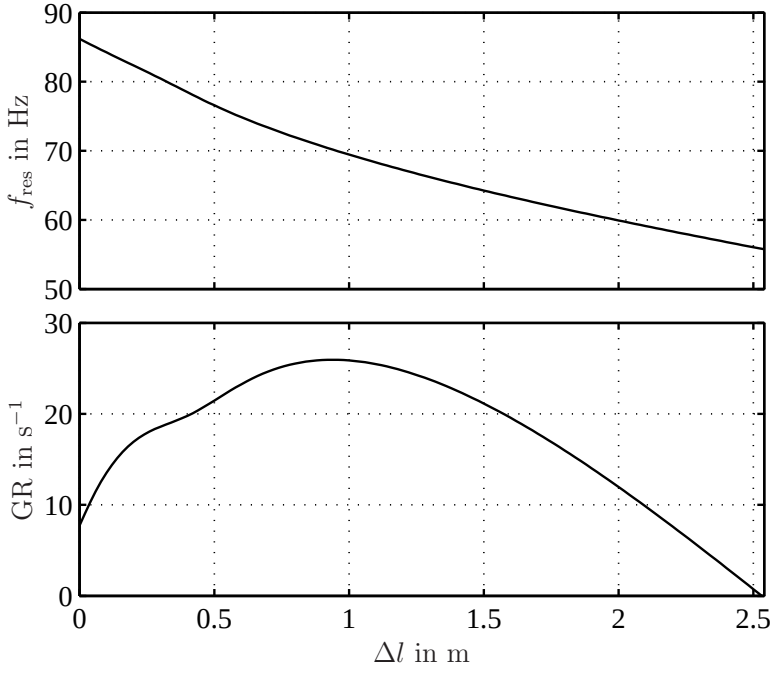

Figure 2.6: Resonance frequency (top) and linear growth rate (bottom) predicted by the model versus the length of the combustion system.

release and acoustic pressure, the system exhibits different growth rates mainly because of the flame response changing with frequency. For an additional length larger than 2.52 m, the growth rate is smaller zero, i.e., the system is stable. As this model is linear, the resulting limit-cycle amplitudes cannot be predicted. It can be stated, however, that the considerable change in growth rate will also have an influence on the limit-cycle amplitude. In summary, the derivation of the acoustic energy balance and the linear stability analysis of the combustion system mathematically proved that for thermoacoustic instabilities to occur both the flame dynamics and the acoustic boundary conditions are crucial factors. Different acoustic boundary conditions clearly result in a different system behaviour.

"Es ist nicht genug, zu wissen, man muß auch anwenden; es ist nicht genug, zu wollen, man muß auch tun."
J. W. v. Goethe, Wilhelm Meisters Wanderjahre.

Chapter 3

Experimental Setup and Measurement Techniques

The cold acoustic and combustion test rigs where the experimental investigations were conducted are described in Sec. 3.1. Section 3.2 gives an overview of the actuators that have been used to manipulate the acoustic field. The last section deals with the measurement equipment, the data acquisition and evaluation, as well as the controller soft- and hardware. Also, the microphone calibration procedure and the Multi-Microphone Method are explained.

3.1 Test Facilities

The impedance tuning scheme was applied to two test configurations, one being a cold acoustic test rig, the other one an atmospheric swirl-stabilized combustion chamber.

3.1.1 Cold Acoustic Test Rig

The cold acoustic test rig is shown in Fig. 3.1. It basically consists of aluminum duct segments 0.14 m in diameter with a wall thickness of 10 mm. At ambient conditions without flow, this corresponds to a cut-on frequency for the first non-planar mode of 1435 Hz (see Eq. (2.48)). In the setup shown, the up- and downstream end are equipped with anechoic terminations. If needed, these can be removed. Directly in front of the anechoic terminations, loudspeakers are mounted circumferentially providing for acoustic excitation.

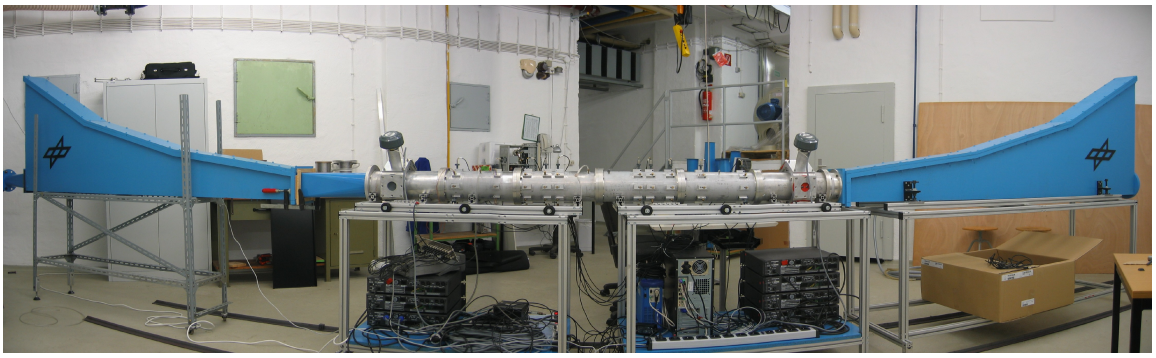

Figure 3.1: Photograph of the cold acoustic combustion test rig equipped with anechoic terminations (by courtesy of DLR Berlin).

3.1.2 Atmospheric Combustion Test Rig

Both cold flow and reactive experiments were conducted in an atmospheric combustion test rig, which is shown in Fig. 3.2. A schematic, rotated by −90°, is depicted in Fig. 3.3. The

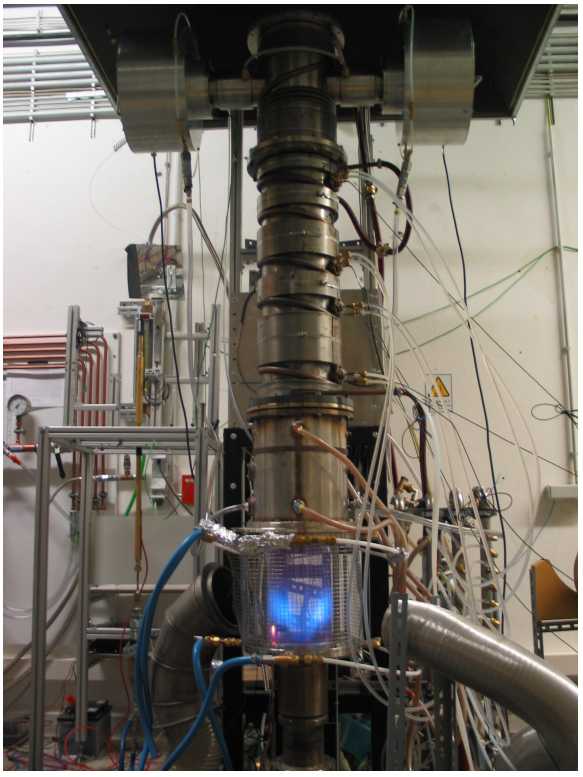

Figure 3.2: Photograph of the atmospheric combustion test rig.

diameter of the part downstream of the burner is 0.2 m. Its length can be adjusted between 0.6 m and 2 m. A quartz glass combustion chamber allows for optical observation of the flame. Downstream of this quartz glass tube is a 0.3 m long radiation-cooled stainless steel tube. This tube is followed by a water-cooled measurement section that can be instrumented with microphones and an emission probe. At the downstream end, a T-junction element allows mounting of the actuators. The connecting side tubes have a diameter of 0.105 m and a length of 0.2 m. Both latter elements are water-cooled as well. All ducts

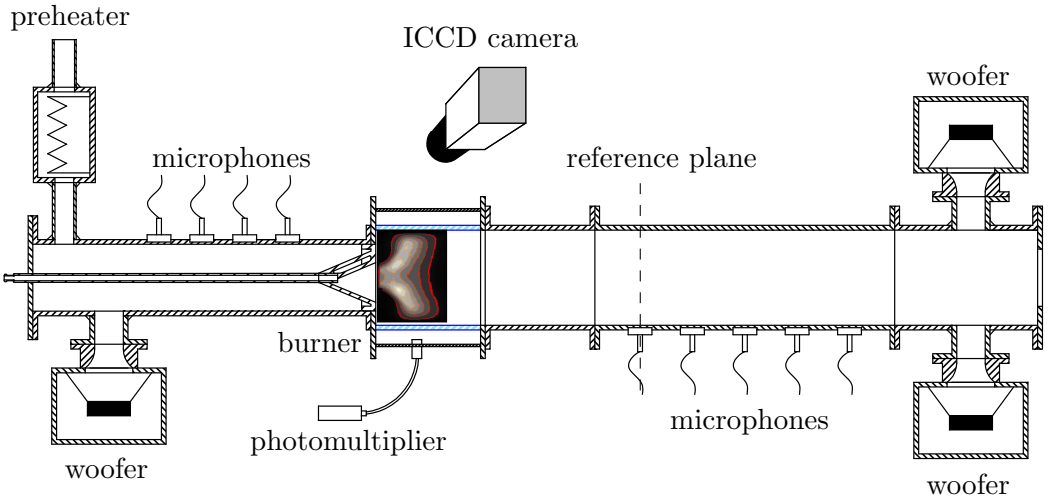

Figure 3.3: Schematic setup of the atmospheric combustion test rig.

have a wall thickness of 8 mm and are made of stainless steel.
To simulate conditions which are closer to those in full-scale engines, an electrical preheater can be used to provide higher air temperatures at the burner inlet. The preheater has an electrical power of 29 kW and can provide a maximum air temperature of 600 K.
The combustor is operated in lean-premixed mode and features a so-called environmental burner (EV-10). Figure 3.4 shows this swirl-stabilized burner developed by ABB. It is

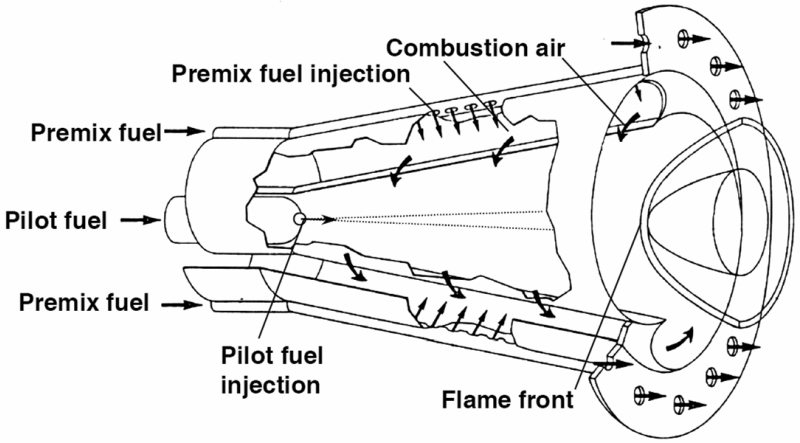

Figure 3.4: Sketch of the environmental burner (EV-10).

composed of two half cones shifted in such a way that the air is forced to enter the cone circumferentially through two slots. The resulting swirling airflow generates a recirculation zone along the centerline at the burner outlet, commonly referred to as vortex breakdown. This phenomenon results from a flow instability generated by an internal stagnation point on the vortex axis followed by a reversed flow [102, 116]. It serves as an aerodynamic stabilization for the flame front. The burner has an area expansion ratio of approximately 4. The main fuel is injected through holes, which are distributed equidistantly along the two air slots. Mixing of swirling air and main fuel results in nearly premixed combustion, also termed technically premixed. Pilot fuel can be injected at the EV-10 cone apex using

a pilot lance. More information on the burner can be found in references [46, 183].
The utilized fuel is natural gas with the averaged chemical composition given in Tab. 3.1. The resulting net calorific value is 49.1 MJ/kg and the stoichiometric air-fuel ratio is 17.1.

Table 3.1: Chemical composition of natural gas in %-vol. (average value of 2006 in Berlin).

Component	%-vol.
Methane	97.86
Ethane	0.91
Propane	0.26
Butane	0.09
Pentane	0.01
Nitrogen	0.87

Gas mass flows are monitored with Coriolis flow meters (Endress & Hauser Promass 80), whereas the air mass flow is measured by a laminar flow element (Hasting Instruments Teledyne). They are adjusted by pneumatic valves which are controlled by a LabVIEW program. This program also monitors all temperatures that are measured at the test rig, the exhaust section, and the cooling circuits. Maximum gas and air mass flows are 5 g/s and 200 g/s, respectively, the limiting factor of the gas mass flow being the operating temperature of the exhaust fan. Typical operating parameters for this study are an air mass flow between 30 and 70 g/s, a gas mass flow of 1.8 to 2.5 g/s, and equivalence ratios between 0.6 and 0.85.
In the setup shown, woofers are mounted at both ends of the rig allowing for acoustic excitation. These woofers can be replaced by other actuators. The combustor outlet can be equipped with different terminations, such as, e.g., an orifice to reduce the reflection of low-frequency acoustic waves [15, 150]. Following Bechert [15], the reflection coefficient of an open end can be significantly decreased if an orifice plate is mounted for which the area contraction ratio is equal to the Mach number of the flow in the orifice. In this case, acoustic energy is transferred into vortices shedding from the orifice's edges. Paschereit et al. [150] used this procedure to vary the outlet boundary condition of their combustion test facility.
The reference plane drawn in Fig. 3.3 marks the location where the downstream travelling wave, serving as the control input, is identified. Also, it is the location where all pressure spectra as well as the up- and downstream reflection coefficients and the actuator transfer functions shown in the following sections are determined. Note here that this plane is located upstream of the speaker casings. Therefore, the influence of the casings will be included in all reflection coefficients of the downstream end shown.

3.2 Actuators

A number of different actuators were used to generate the acoustic excitation needed to adjust the acoustic boundary condition. The first one was an oil combustor, whose fuel supply could be modulated by a proportional valve. Doing so, the heat release was forced to oscillate at the frequency of modulation, thus, generating sound. As the handling of this actuator was quite intricate, the concept of a modulated secondary combustion was not further followed. The flame sometimes blew off at high excitation amplitudes and frequencies, the achievable frequency range was too small, and the resulting pressure fluctuations were not sufficiently high especially for frequencies above 100 Hz.
Furthermore, the applicability of electrodynamic zero-mass-flux actuators in the impedance tuning concept was assessed. Originally, these shakers were used by Nagib et al. [137] for active flow control at a tiltrotor aircraft. By adequately modulating the flow around the vehicle, a reduction of the download during hover was successfully achieved. However, it turned out that the actuators were not suited for the harsh environmental conditions in the combustion test rig, as the allowed operating temperature was too low. Also, they lacked of sufficient control authority.
In the following, the actuators that were finally used in the control scheme are presented in detail.

3.2.1 Woofers

For the first validation experiments, the combustion test facility was equipped with the Kappa 12 model of Eminence Speaker LLC. This woofer has a power rating of 450 W (RMS) and can be used for frequencies between 20 Hz and 4000 Hz. The speakers are mounted in casings that are purged with air to prevent hot gases from entering. The distance between the centerline of the actuators and the reference plane in Fig. 3.3 is 0.936 m. Fidek type FPA-10A amplifiers are used to drive the woofers.
In terms of usability and frequency response characteristics, woofers exhibit excellent characteristics. In laboratory-scale experiments under atmospheric conditions, woofers are the actuator of choice. However, if the acoustic boundary conditions should be tuned for industrial high power test rigs, woofers might probably not be used. Besides lacking sufficient control authority, they might not withstand the harsh environmental conditions occurring in industrial combustion test rigs, particularly at elevated pressures. Thus, alternative actuators have been investigated.

3.2.2 Proportional Valves

To avoid the shortcomings of the woofers, proportional valves manufactured by Moog Inc. were used in the control scheme. These are electromagnetically driven high bandwidth valves. A power and control unit, equipped with an external voltage supply (DC $\pm$ 48 V), controls a linear motor inside the valve. This motor drives a spool that opens and closes the valve. The spool position is monitored and controlled by a linear variable displacement transducer, which feeds back the actual spool position to the control unit. In absence of

a control signal, the spool position is adjusted to be 50% open. Around this neutral position, a modulation is then imposed. The driving signal can have an arbitrary frequency dependent form. At ±10 V, the valve fully opens and closes. More information on the valve principle can be found in reference [130]. The so-called direct drive valves (DDVs) were used to modulate an air mass flow to excite the test rig. Seume et al. [200] and Hermann & Orthmann [74] used similar valves for active instability control in heavy duty gas turbines by modulating the pilot fuel. In this field application, they proved to be very robust.
A schematic of the setup used for the experiments in this thesis is shown in Fig. 3.5. As the woofers, the valves are mounted at the downstream end of the test rig. The DDV is

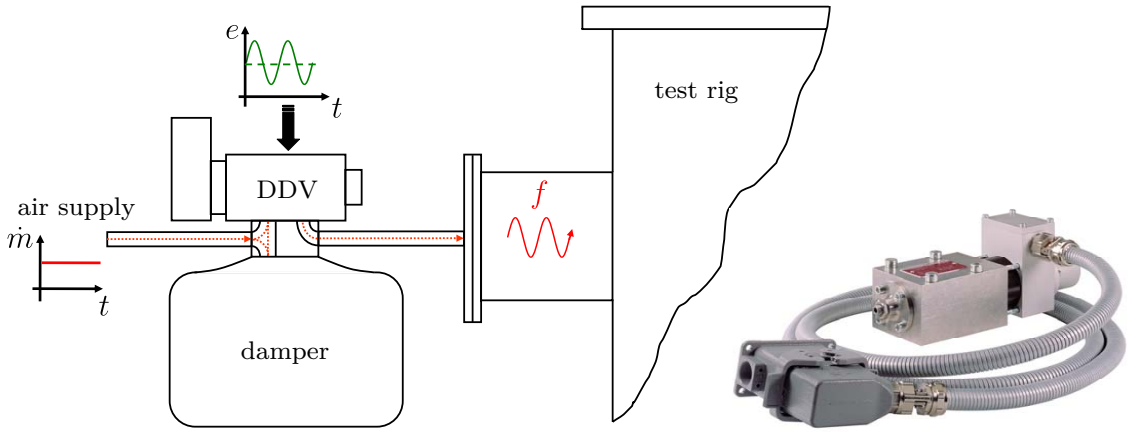

Figure 3.5: Photograph of DDV and setup of valve mounted at downstream end of the test rig.

connected to the pressurized air supply. Upstream of the valve a damper, i.e., a volume, is mounted to prevent the imposed modulation from travelling upstream. The valves presented here are a special version of the ones used in references [74, 200], manufactured to modulate higher mass flows. With this special design, it is possible to modulate 0.25 kg/s of air up to 300 Hz. Due to a special spool coating, no extra lubrication is needed. Moreover, they fulfill another major actuator requirement, the linearity between actuator input and generated perturbation. This linearity implies both, the increase of acoustic excitation with increasing control command and increasing air mass flow.

3.2.3 Electro-Pneumatic Actuator: Ling Driver

An actuator which already has proven to deliver sufficiently high amplitudes for medium pressure applications in industrial test rigs is the so-called Ling Driver. The Ling Electronics model EPT-94B electro-pneumatic transducer is an electrically controlled air modulator, capable of modulating a maximal air flow of 0.26 kg/s at a pressure drop of 0.4 MPa across the piston. Figure 3.6 depicts a schematic of the actuator. Flow enters from the right side, follows the flow path indicated by the dashed arrow, and is modulated shortly upstream of the outlet on the left side by a piston that opens and closes the flow path in radial direction. The electrodynamically operated pneumatic valve in the transducer is capable of reproducing sine, random, or any complex wave form within a frequency range of 20 to

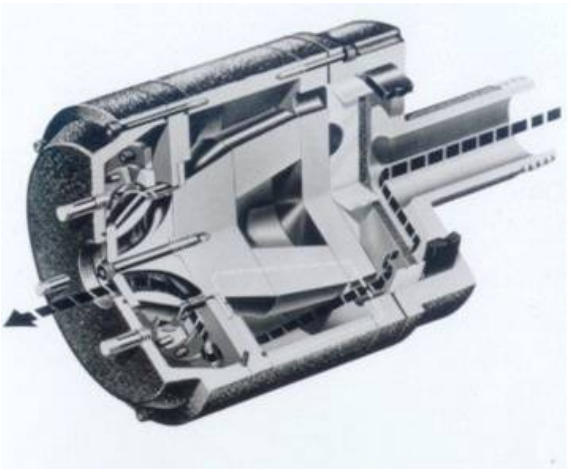

Figure 3.6: Schematic of electro-pneumatic transducer (Ling Driver).

500 Hz. Since the piston stroke is slightly frequency dependent and increases with decreasing frequency, the supply unit's gain should be set to deliver the maximum allowable control current, i.e., 6 A (RMS), at 20 Hz.
The Ling Driver itself is not extra lubricated and therefore needs a minimal mass flow of 0.05 kg/s at full drive, i.e., valve fully opens and closes, to prevent from overheating. The minimal mass flow linearly decreases with piston stroke, i.e., with applied control voltage. For control signals below 1 A (RMS) no mass flow is necessary.

3.3 Measurement Equipment and Techniques

3.3.1 Pressure Transducers

To allow for full identification of the plane wave pressure field, the combustion test rig is instrumented with several pressure transducers up- and downstream of the flame. For all measurements, 1/4" condenser microphones (G.R.A.S. 40BP with pre-amplifiers 26AC) are used. In total, four microphones can be mounted upstream of the burner and five at the downstream measurement tube. For the downstream tube, the one nearest to the burner exit is at the reference location, $x = 0$, which is marked in Fig. 3.3 and the others are at axial distances of $x = 0.195$ m, 0.315 m, 0.465 m, and 0.575 m.
All microphones are mounted in water-cooled holders. For reactive tests the water temperature is set to yield a temperature of 333 K at the microphone pre-amplifier that has a maximal operation temperature of 343 K. The reason for this is twofold: First the microphones are protected from the hot temperature environment. In fact, for this purpose a lower temperature could be chosen. However, the second reason is to prevent water from the exhaust gases to condensate on the microphone membranes. The lower the temperature the higher would be the risk of water condensation. A borehole, 1 mm in diameter, connects the microphone membrane with the combustion chamber. The microphones are placed on plastic plates to electrically decouple them from the surroundings. Otherwise, strong 50 Hz oscillations from the supply net might distort the measurements.

The ducts of the cold acoustic test rig can be instrumented with wall-flushed microphones at 10 axial and 8 circumferential positions. For the tests presented, the frequencies remained well below the plane wave limit and 7 axially distributed microphones were used. The condenser microphones were supplied by a 16-channel power unit built in-house. This device also serves as the amplifier for the recorded microphone signals and has a built-in analog low-pass filter with adjustable cut-off frequency.

Microphone calibration

Generally, all microphones exhibit small deviations regarding phase and amplitude response to each other. Moreover, the setup with the probe holders might introduce further inaccuracies. Thus, the microphones have to be calibrated relative to each other. A test rig, basically consisting of a straight duct with holes for the microphones, was constructed for microphone calibration. Eight microphones mounted in the probe holders can be installed at one axial position. A loudspeaker at one end of the calibration test rig provides for acoustic excitation. On the opposite end, the test rig is equipped with a low-reflecting termination to prevent pressure nodes at the microphone location. Below the cut-on frequency, only plane waves propagate and thus the acoustic pressure depends only on the axial coordinate. Assuming the microphones to be identical, all would monitor the same pressure fluctuation. Evidently, this is not the case. With the calibration setup, the differences between the microphone measurements can be determined, and a complex calibration coefficient is calculated accounting for phase and amplitude deviations. At the same axial position, a wall flush-mounted microphone is taken as a reference. This microphone is then absolutely calibrated with a pistonphone (Brüel & Kjær Type 4228) at 124 dB and 250 Hz allowing to determine the absolute pressure level in the test rig.
Typical calibration curves for three microphones are shown in Fig. 3.7. For this measurement, the loudspeaker was driven by a frequency sweep ranging from 30 to 800 Hz. The values for the wall flush-mounted reference microphone, i.e., a magnitude of unity and a phase of zero, are shown in black. Solid curves represent results for a cooling temperature of 333 K, whereas dashed curves are for the case of $T = 293$ K. Regarding the magnitude, all curves show the same trend, suggesting that the microphones themselves only differ by a constant value. The difference in slope compared to the reference microphone can be attributed to the transfer function of the probe holders. This transfer behaviour seems to be similar for all holders. For the chosen microphones, the differences in phase are negligible. Note that this is not always the case. Due to the needs of the impedance tuning concept, for the results depicted in Fig. 3.7 microphones have been chosen as such that the phase difference is minimal.
Additionally, the influence of a temperature change is visible. For the lower temperature, a drift of the calibration coefficients to higher values is observable. As can be seen, the changes are different for each microphone and can in total exceed 5%. These results suggest that the microphones should be calibrated at their operating temperature.

3.3.2 Multi-Microphone Method

As will be seen in the following, the decomposition of the plane wave acoustic field into its up- and downstream propagating parts $\hat{g}$ and $\hat{f}$ is a crucial task. It is the basis for

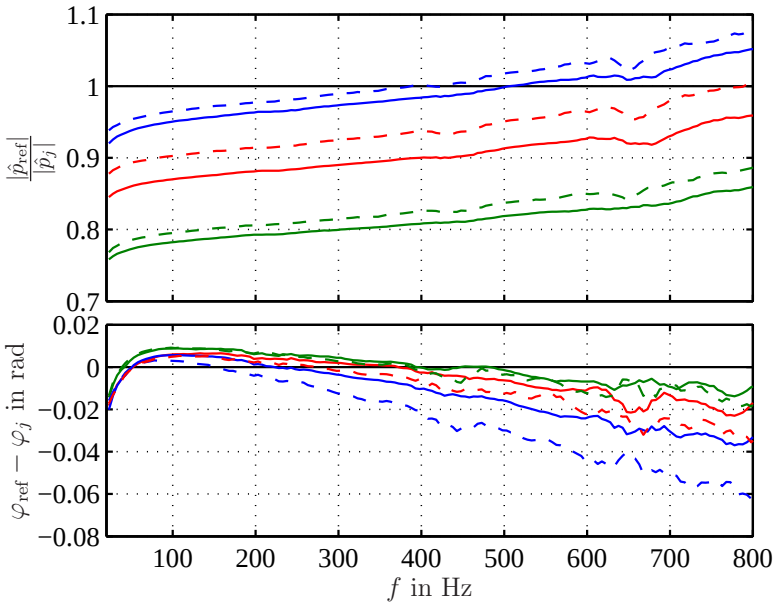

Figure 3.7: Calibration coefficients of 3 microphones (red, blue, green) in probe holders; top: magnitude, bottom: phase. Reference microphone (black) is wall flush-mounted. Solid: $T = 333\,\mathrm{K}$, dashed: $T = 293\,\mathrm{K}$.

determining the frequency responses of the system. Simply using the frequency domain representations of Eqs. (2.39) is not possible because the acoustic velocity cannot be measured directly with sufficient accuracy. However, as the analytic form of the plane acoustic field is known, multiple axially distributed pressure measurements can be used to find a good approximation to the Riemann invariants in frequency domain. This is done by means of the well-known Multi-Microphone Method (MMM) [156, 163, 190]. The MMM finds a least squares solution to an overdetermined linear system of equations for $\hat{f}$ and $\hat{g}$. It is applied in a post-processing step, for which pressure records for a certain time interval are available. Another advantage of the MMM, thus, is that, by averaging over several microphones, flow noise is suppressed.

The relationship between Riemann invariants and primitive acoustic variables was derived in Sec. 2.3. If the expressions for the Riemann invariants, Eqs. (2.38), are divided into a part depending on frequency only and another one depending only on the spatial coordinate and this expression is then inserted into Eqs. (2.39), one obtains

$$\hat{p}(x,\omega) = \hat{f}(\omega)e^{-\mathrm{i}k^+x} + \hat{g}(\omega)e^{\mathrm{i}k^-x}, \tag{3.1a}$$

$$\hat{v}(x,\omega) = \hat{f}(\omega)e^{-\mathrm{i}k^+x} - \hat{g}(\omega)e^{\mathrm{i}k^-x}. \tag{3.1b}$$

For ease of notation, here, as in the following if not explicitely mentioned, the acoustic pressure has been scaled by the characteristic impedance, $\bar{\rho}\bar{c}$. Given the experimentally determined pressure phasors $\hat{p}_j$ at multiple axial locations, Eqs. (3.1) can be formally

inverted in a least squares sense to yield

$$\begin{bmatrix} \hat{f}(\omega) \\ \hat{g}(\omega) \end{bmatrix} = \mathbf{H}^{\dagger} \begin{bmatrix} \hat{p}(x_1, \omega) \\ \hat{p}(x_2, \omega) \\ \vdots \\ \hat{p}(x_n, \omega) \end{bmatrix}, \tag{3.2}$$

where x_j denotes the axial distance of the pressure transducer j to the reference location, i.e., the location at which $\hat{f}$ and $\hat{g}$ are determined. $\mathbf{H}$ is given by

$$\mathbf{H} = \begin{bmatrix} e^{-\mathrm{i}k^+ x_1} & e^{\mathrm{i}k^- x_1} \\ e^{-\mathrm{i}k^+ x_2} & e^{\mathrm{i}k^- x_2} \\ \vdots & \vdots \\ e^{-\mathrm{i}k^+ x_n} & e^{\mathrm{i}k^- x_n} \end{bmatrix}, \tag{3.3}$$

and the operator $(\cdot)^{\dagger}$ denotes the pseudoinverse or Moore-Penrose inverse of a matrix. The pseudoinverse of a $(n \times m)$-matrix $\mathbf{H}$ (with $m < n$) for which the inverse of $\mathbf{H}^{\mathrm{T}}\mathbf{H}$ exists, i.e., for which the rank of $\mathbf{H}$ is full [62], is defined by [97]

$$\mathbf{H}^{\dagger} = (\mathbf{H}^{\mathrm{T}}\mathbf{H})^{-1}\mathbf{H}^{\mathrm{T}}, \tag{3.4}$$

where the superscripts -1 and T denote the inverse and the conjugate transpose of a matrix, respectively.
An estimate of the error of the approximate solution for the Riemann invariants can be calculated from

$$\delta = \frac{\left\| (\mathbf{I}^n - \mathbf{H}\mathbf{H}^{\dagger})\hat{\mathbf{p}} \right\|_2}{\|\hat{\mathbf{p}}\|_2}, \tag{3.5}$$

where n is the number of microphones used, $\mathbf{I}^n$ is the identity matrix of size $n \times n$, the vector $\hat{\mathbf{p}}$ contains the complex amplitudes of the measured pressures, and $\|\cdot\|_2$ denotes the l^2-norm.
The smaller the residual δ, the better is the correspondence of measured pressures and calculated Riemann invariants. Typically, for a good measurement, this frequency dependent residual takes values around 1% to 5%. Besides noise contributions, a possible source of error might be a change in one or more of the calibration coefficients of the microphones during tests. Thus, microphones should be calibrated prior *and* after experiments. Another one is the speed of sound, i.e., the temperature, which is taken to calculate the wave number k. The relationships between Riemann invariants and primitive acoustic variables were derived for a constant axial temperature profile. Therefore, errors might be introduced if this simplification is not valid. Besides the obvious reason of taking a wrong speed of sound and therefore a wrong propagation time between the microphones, another reason is that a temperature difference will always cause a reflection of acoustic waves, because of the gradual change of characteristic impedance. If this nonuniformity in the axial mean temperature distribution is not negligible, $\hat{f}$ and $\hat{g}$ will be spuriously calculated from the acoustic pressures. In the experiments reported in Chapters 6 and 7, however, the assumption of a constant axial temperature leads to reasonable results. If this would not be the

case, an analytical solution for a temperature dependent wave equation would have to be found. This was, for instance, done by Sujith et al. [213] and Manoj Kumar & Sujith [117] for linear, exponential, and polynomial mean temperature profiles.
In fact, to identify the Riemann invariants, it would also be sufficient to measure the pressure at only 2 axial positions. However, when doing so, singularities arise at certain frequencies and in case of measurement uncertainty the results deteriorate. These issues as well as a comparison between both methods are dealt with in Sec. 5.5.

3.3.3 Optical Measurement Devices

The flame is the driving mechanism for thermoacoustic instabilities. Therefore, monitoring the heat release rate is crucial to observe the unsteady processes in the system. In this study, only the qualitative behaviour of the heat release rate is of interest. Taking the radiation of certain excited species produced by chemical reactions is regarded a suitable means to describe the qualitative rate of heat release. This is recognized by many authors [70, 71, 72]. If a quantitative estimate is sought for, the application to technically premixed flames, however, leads to erroneous results as was pointed out by Schuermans et al. [192] and authors cited therein. The reason for this is that heat release and chemiluminescence intensity have a different functional dependency on equivalence ratio and mass flow, both being subject to fluctuations in technically premixed flames.
Each radical emits light at a different wavelength. To separate the different molecules, bandpass filters have to be used. In the results shown in Sec. 6, the fluctuation of the OH^*-chemiluminescence (the * denoting the excited state) is taken as the qualitative measure for heat release fluctuations. It is monitored with a photomultiplier (Hamamatsu H5784-04) connected to the combustion chamber via a fibre optic cable (see Fig. 3.3). The photomultiplier is equipped with an optical band-pass filter centered at 308.2 nm, the wavelength of OH^*, and a full-width half-height of 11.2 nm. The fibre optic cable is mounted so as to cover the entire heat release region. Thereby, the contribution of a flame movement caused by unsteady combustion to the detected fluctuations is eliminated. This is particularly important for the EV-burner, as depending on the equivalence ratio two stable flame positions exist, as was observed in references [24, 69, 127]. If thermoacoustic instabilities occur, the flame might move between these stable anchoring positions [69]. The photomultiplier signals are amplified and low-pass filtered by DISA 55D26 signal conditioners.
To record the spatial distribution and temporal evolution of the OH^*-chemiluminescence, an intensified charge-coupled device (ICCD) camera (IRO & Imager from LaVision) equipped with an UV lens and a band-pass filter centered at 312 ± 2 nm is used. For all experiments, the shutter time is set to 0.1 ms, corresponding to a resolution of 3.6° at a typical instability frequency of 100 Hz. The maximum camera frame rate at full resolution (1376 × 1024 pixels) is around 6 Hz. Evidently, this sampling frequency is far too low to resolve the structure evolution in the frequency range of interest. By using an appropriate post-processing method (see, e.g., Lacarelle et al. [94]), the structures can be extracted allowing to reconstruct their phase-averaged evolutions.

3.3.4 Data Acquisition and Evaluation

Time traces of all measured quantities are simultaneously acquired with 16 bit data acquisition cards from National Instruments (NI PXI-6143 S-Series mounted in NI PXI-1031). They are recorded by a routine written in LabVIEW. For all measurements, the sampling frequency is set to 2^{13} Hz. All signals are analogously low-pass filtered at 2^{12} Hz or 2^{11} Hz to prevent aliasing.
To determine the respective transfer functions, Welch's method is used. Pressure and OH*-chemiluminescence signals are cross-correlated with the excitation signal before the Fourier transforms are calculated. This is done in order to suppress flow noise and to minimize measurement uncertainties. If no external excitation is present, Fourier transforms are obtained by either correlating with the signal of one reference microphone or for cases where no phase information is needed, for example, for pressure spectra, with auto-correlation. For the results shown in the following, the Fourier transforms are obtained by averaging over a certain period. For this purpose, the time signals are segmented into intervals of equal length. Then, windowing techniques with rectangular or Hamming-windows are used.
In the following, it is briefly outlined how the frequency responses, for instance, for the reflection coefficients or the actuator transfer functions, are obtained from the measured microphone signals. An instructive and comprehensive description on obtaining transfer functions in a similar way was given by Campos-Delgado et al. [34]. The acoustic pressure at microphone j is calculated by

$$\hat{p}_j = \frac{\hat{X}^j_{pe}}{\sqrt{\hat{X}_{ee}}} \frac{1}{\hat{C}_j}, \tag{3.6}$$

where $\hat{X}^j_{pe}$ is the cross power spectral density of the discrete time series of measured pressure p' and excitation signal e and $\sqrt{\hat{X}_{ee}}$ is the auto spectral density of e. The frequency dependent factor $\hat{C}_j$ is the complex calibration coefficient. From this, the Riemann invariants are calculated using the MMM (see Sec. 3.3.2) and the downstream reflection coefficient takes the form

$$R_{\mathrm{ds}} = \frac{\hat{X}_{ge}}{\hat{X}_{fe}}, \tag{3.7}$$

$\hat{X}_{ge}$ and $\hat{X}_{fe}$ denoting the Riemann invariants calculated from the pressure signals cross-correlated with the excitation signal. Analogously, the actuator transfer function is derived. Note, if absolute pressure spectra are calculated, correction factors might have to be accounted for depending on the averaging procedure, i.e., window length and type. If the frequency responses are calculated, this is not necessary, as they always describe a ratio of two averaged quantities. Thus, the correction factor is cancelled.

3.3.5 Controller Hardware and Software

The controller runs on a DS1103 PPC control board (dSPACE), which generates the command signal for the actuators, at a sampling frequency of 2^{13} Hz. This model features an application memory of 32 MB. An interface device provides for 8 input and 20 output ports

as well as conversion from analog to digital and vice versa.
The controller is implemented in MATLAB/Simulink – including Control System, Signal Processing, and Realtime Workshop Toolboxes – and then compiled and loaded onto the DSP processor. During experiments the DS1103 software ControlDesk allows for visualization of signals in the control circuit as well as the adjustment of values, such as, for example, control gain, additional time-delays, or saturation limits.

"That which sustains the universe beyond thought and language, and that which is at the core of us and struggles for expression, is the same thing.
The finite within the infinite, the infinite within the finite."
Y. Martel, Life of Pi.

Chapter 4

Low-Order Network Models

It is common practice to represent the linear behaviour of thermoacoustic systems by so-called low-order network models. This modelling method allows a fast prediction of linear stability and is widely spread in industry as well as academia.
There are a couple of reasons why the concept of network modelling is introduced here. First, the principle of describing acoustic systems in terms of a lumped element representation is used for the derivation of the control law and the model for the controller (Chapter 5). Furthermore, the one-dimensional network tool allows to simulate the impedance tuning approach prior to applying it to experiments (Sec. 6.1) and to optimize the tubing geometry of extension ducts connecting the actuators to the combustion test rig. Also, the behaviour of a limitation of the control gain on the system response is studied (Sec. 6.5). Finally, the impedance tuning concept might effectively be used to validate linear stability analysis. For this purpose, the atmospheric combustion test rig is represented by a low-order network model. A comparison between experiments and the predictions of this network model in terms of linear growth rate, transition from stability to instability, and frequency of instability for different boundary conditions is shown in Sec. 7.2.
An enormous amount of publications deal with those network tools and different approaches to obtain them; thus, they will not be described in every detail here, and the interested reader is referred to the references cited in Tab. 4.1. However, based on existing network tools described in the literature, a modified approach was developed in the course of this dissertation. The method used here is strongly related to the one proposed by Schuermans et al. [191]. It provides a straightforward calculation of unstable modes and linear growth rates in the time domain and has certain advantages compared to the traditional approach in the frequency domain. Therefore, this approach as well as the advantages network models exhibit over detailed numerical studies will briefly be discussed in this chapter.

Table 4.1: References for the use of low-order network models in industry and academia.

Company / Institution	Reference	Name
ALSTOM Power	Paschereit et al. [146, 154], Schuermans et al. [191, 196], Belluci et al. [19]	Thermoacoustic 3-dimensional network (TA3)
SIEMENS Energy	Krüger et al [92, 93], Lepers et al [104], Krebs et al [90]	Transfer Matrix Approach (TMA)
General Electric	McManus et al. [123]	
Rolls Royce	Stow & Dowling [206]	Low-order thermoacoustic network model (LOTAN)
TU Berlin	Paschereit et al. [153], Bothien et al. [30], Moeck et al. [127]	
TU München	Evesque & Polifke [56], Sattelmayer & Polifke [184, 185], Kopitz et al. [87], Alemela et al. [4]	
Georgia Tech	Lieuwen et al. [111, 112]	
Cambridge	Dowling & Stow [47, 50, 205, 206], Hubbard & Dowling [79]	Low-order thermoacoustic network model (LOTAN)
RWTH Aachen	Bohn & Deuker [28, 44]	

4.1 Introduction

Due to the high complexity of geometry and interaction mechanisms in combustion systems, a comprehensive description of their acoustic field, accounting for reaction, flow and acoustics, is cumbersome. Although detailed numerical simulations were shown to be able to accurately calculate these thermoacoustic interaction mechanisms in single burner configurations (see, e.g., Roux et al. [180], Schmitt et al. [188], and Sengissen et al. [198]) or even for complete annular combustion chambers of helicopters as was done by Boudier et al. [31] and Staffelbach et al. [204], time expense and computing power requirements are very high. Especially for industrial applications they are still far too time-consuming as was, among others, stated by Kaufmann et al. [84], Selle et al. [197], or Sensiau et al. [199]. Also, it is anything but trivial to implement the complex acoustic boundary conditions, described by complex-valued impedances or reflection coefficients, in time domain in CFD codes. The latter is underlined by the current research effort run by several groups as, for example, Widenhorn et al. [230] and Huber et al. [80].
Recently, Schuermans et al. [193] and Moeck et al. [128] showed that it is possible to decrease the computational effort by coupling low-order acoustic models, representing complex impedance boundary conditions, to a CFD solver. Especially if stability has to be assessed

for a high number of parameter combinations, the use of a CFD code is not practicable. Moreover, as a CFD simulation is only able to observe the dominant mode of the instability, it is usually not possible to assess more linearly unstable modes [88, 138, 167]. Additionally, marginally stable modes cannot be detected, which is in contrast to the network approach described in the following. Sattelmayer & Polifke [184, 185] stated that it is extremely difficult to derive suitable measures to improve the system stability using results of LES calculations, although these are able to give detailed information on the periodic reacting flow. Therefore, methods based on analytical modelling will remain the most practicable stability assessment tool in early design stages in the relatively near future.

One further step to reduce computational effort is to use low-order models to describe the whole combustion system. The common approach is to divide the total system into several subsystems, which are described by transfer functions accounting for plane wave propagation. Connection of these subsystems results in a low-order representation of the total system's acoustic properties. The network approach has the main advantages that information about the system's acoustics and insight into the physical processes can be obtained very quickly, which is of major importance in early design phases. Furthermore, changes in geometry or setup, to test, for example, the performance of different burners, can easily be implemented in the model by simply exchanging a subsystem. Due to this modular setup, it is possible to incorporate an experimentally determined flame transfer function into the model.

A drawback of this approach is the limitation to plane wave acoustics. To overcome this problem, multidimensional models have to be considered. It was shown that quasi 3-d geometries can be described by adequate network models. Evesque and Polifke [56] set up a 2-d low-order network, which was validated against a 3-d FEM solver showing good agreement. The model was able to account for mode coupling of axial and azimuthal modes. Krüger et al. [93] set up a model to predict the azimuthal modes in an annular combustion chamber.

Traditionally, stability analysis of thermoacoustic systems is accomplished by setting up a low-order network model, which is then investigated in the frequency domain. This is either done by solving the system's dispersion relation [79, 141, 196, 205], or by graphical methods (Nyquist plots) as described by Sattelmayer & Polifke [184, 185], Polifke et al [169], and Kopitz & Polifke [88]. In contrast to the traditional *frequency domain* approach, another procedure is followed here, by modelling the acoustic properties of the system in the *time domain*. Therefore, all subsystems are characterized in state-space form. For the resulting state-space network system, only a matrix eigenvalue problem has to be solved to perform a stability analysis, which is numerically straightforward. This approach is based on the work of Schuermans et al. [191] and Bellucci et al. [19], who also described the system in state-space form. They used modal expansion techniques to characterize the individual subsystems. In contrast to this, here the subsystems are initially derived in the frequency domain. A time domain representation is then obtained by applying adequate frequency domain system identification tools.

4.2 Principle

As in the frequency domain transfer matrix approach, it is assumed that only plane waves propagate between two subsystems. This assumption is valid for elements that are coupled via ducts, for which the frequencies considered are below the cut-on frequency of the first non-planar mode. Since the impedance tuning concept only accounts for plane wave acoustic fields, this does not pose an additional limitation. Neglecting entropy waves results in two degrees of freedom for all coupling planes. The variables accounting for that can be either acoustic pressure and velocity or the Riemann invariants. At least for the cases studied here, entropy waves do not play a significant role. However, if choked flows are considered, they might become important, as was, for example, shown in references [9, 118, 168]. Network models accounting for entropy waves were, for instance, developed by Stow & Dowling [205].
Individual elements are described by 2×2 linear time-invariant input-output relations (so-called acoustic two-ports). An interior element is sufficiently described by a 2×2 mapping of acoustic variables. There are various forms of this mapping. Fischer [57] gave a nice overview of the different representations and how they can be transformed to each other. Subsequently, they are characterized using the scattering form, i.e., the f-wave upstream and the g-wave downstream are treated as inputs and, accordingly, the f-wave downstream and the g-wave upstream are obtained as outputs. The generic acoustic element in state-space form can then be written as

$$\begin{aligned} \dot{\mathbf{x}} &= \mathbf{A}\mathbf{x} + \mathbf{B} \begin{bmatrix} f_{\mathrm{us}} \\ g_{\mathrm{ds}} \end{bmatrix} \\ \begin{bmatrix} f_{\mathrm{ds}} \\ g_{\mathrm{us}} \end{bmatrix} &= \mathbf{C}\mathbf{x} + \mathbf{D} \begin{bmatrix} f_{\mathrm{us}} \\ g_{\mathrm{ds}} \end{bmatrix}, \end{aligned} \tag{4.1}$$

where subscripts us and ds denote quantities up- and downstream of the element. $\mathbf{A}$, $\mathbf{B}$, $\mathbf{C}$, and $\mathbf{D}$ are $N \times N$, $N \times 2$, $2 \times N$ and 2×2 matrices, respectively, and $\mathbf{x}$ is the N-dimensional state vector. The state dimension depends on the acoustic subsystem to be characterized and has to be chosen sufficiently large so that the system's frequency response is represented with acceptable accuracy in the frequency range considered. An inlet or exit boundary condition can be written similar to Eq. (4.1) as a single input single output (SISO) system.
The modular setup allows for different ways of describing the subsystems, i.e., by analytical considerations [154], experimental data [21, 156], or numerical methods, for example, using FEM [157] or CFD [89, 170, 225]. Usually, acoustic subsystem characterization based on numerical computations or experiments results in frequency domain data. In the frequency domain, the relation of the Riemann invariants is represented by the scattering matrix $\mathbf{S}$

$$\begin{bmatrix} f_{\mathrm{ds}} \\ g_{\mathrm{us}} \end{bmatrix} = \begin{bmatrix} S_{11} & S_{12} \\ S_{21} & S_{22} \end{bmatrix} \begin{bmatrix} f_{\mathrm{us}} \\ g_{\mathrm{ds}} \end{bmatrix}, \tag{4.2}$$

where the elements S_{ij} are complex valued functions of frequency. Once a subsystem's acoustic transfer function is given in this frequency dependent form, it can easily be transformed into the corresponding state-space form of Eq. (4.1) by using frequency domain

system identification tools. The algorithm used here is described in Sec. 5.3 in detail.
The description of elements with simple geometries (e.g., ducts) is done analytically. Neglecting sound absorption at the walls and in the fluid, a duct only represents a time-delay $\Delta\tau$ in the system. That is, an acoustic wave is transmitted with a delay, depending on the element's length and the speed of sound. For a duct of constant cross-section and length L, the scattering matrix simply reads

$$\mathbf{S}_{\text{duct}} = \begin{bmatrix} e^{-\frac{\mathrm{i}kL}{1+M}} & 0 \\ 0 & e^{-\frac{\mathrm{i}kL}{1-M}} \end{bmatrix}. \tag{4.3}$$

It is not possible to exactly describe a system with time-delay with a rational transfer function. Therefore, the exponential function is described by a Padé approximation. The Padé approximation of a time-delay is a finite dimensional approximation of $e^{-\mathrm{i}\omega\Delta\tau}$ by a rational transfer function. The order of the Padé approximation, which is necessary for a sufficient accuracy, depends on the desired frequency range and the time-delay. For instance, a duct with a length of 0.5 m at ambient conditions requires an order of 8 in a frequency band ranging from 100 Hz to 1000 Hz to have a phase error of $\mathcal{O}(10^{-3})$ rad.
For more complex subsystems, the transfer functions are determined by means of experiments. For this purpose, the element is regarded as a black box, for which the four unknown elements of the scattering matrix have to be identified. The system given by Eq. (4.2) consists of two equations. Thus, two linearly independent states are necessary to solve for the four unknowns S_{ij}. The test states are created by successive acoustic excitation on both sides of the element. This procedure has been applied previously and the interested reader might consult the literature [96, 156, 195].
Figure 4.1 depicts a network model of the combustion rig consisting of the upstream end, burner and flame, the measurement section, and the downstream termination. Both end

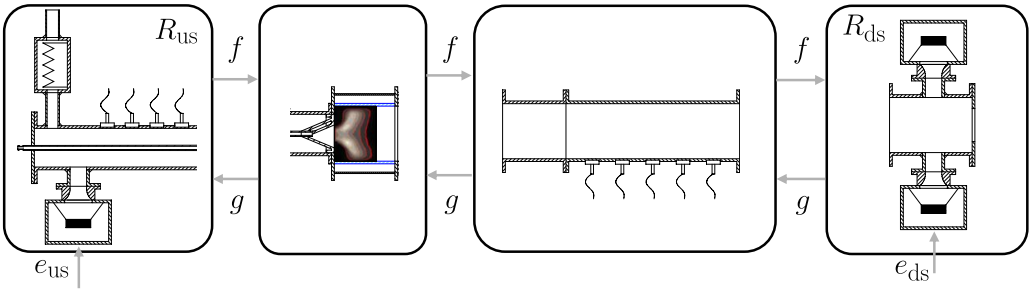

Figure 4.1: Network representation of combustion test rig. Elements are connected in terms of Riemann invariants.

elements account for the description of the actuators' response characteristics. The upstream end also comprises the acoustic properties of the fuel and air supply lines.
It is exemplarily shown how the subsystem for the downstream end in Fig. 4.1 can be derived. The actuated end element has two inputs and one output. If it is assumed that the outgoing $\hat{g}$-wave can be obtained as a linear superposition of the geometrical reflection of the incident wave $\hat{f}$ and the wave generation due to the actuator, the response characteristic of the end element is described by

$$\hat{g} = R_{\text{ds}}\hat{f} + G\hat{e}_{\text{ds}}. \tag{4.4}$$

Here, R_{ds} is the downstream reflection coefficient, G the actuator transfer function, and $\hat{e}_{\mathrm{ds}}$ the signal driving the actuator. Validity of this assumption was previously shown by Bothien et al. [30]. The transfer functions R_{ds} and G can both be obtained experimentally from frequency response measurements in conjunction with the Multi-Microphone Method described in Sec. 3.3.2.
Excitation with the upstream woofer (index A) yields

$$\hat{g}_{\mathrm{A}} = R_{\mathrm{ds}} \hat{f}_{\mathrm{A}}, \tag{4.5}$$

as $\hat{e}_{\mathrm{ds}}$ is zero in Eq. (4.4). This allows for direct calculation of the reflection coefficient R_{ds}. Subsequent excitation with the downstream speaker (index B) allows to compute the actuator transfer function from Eq. (4.4)

$$G = \frac{\hat{f}_{\mathrm{B}} - R_{\mathrm{ds}}\, \hat{g}_{\mathrm{B}}}{\hat{e}_{\mathrm{ds}}}, \tag{4.6}$$

taking into account the reflection coefficient calculated in the previous step.
For both transfer functions, SISO state-space models according to Eq. (4.1) can be identified. These then have to be concatenated to a double input single output state-space system, which completely describes the downstream end:

$$\begin{aligned} \dot{\mathbf{x}} &= \begin{bmatrix} \mathbf{A}_R & 0 \\ 0 & \mathbf{A}_G \end{bmatrix} \mathbf{x} + \begin{bmatrix} \mathbf{B}_R & 0 \\ 0 & \mathbf{B}_G \end{bmatrix} f \\ g &= \begin{bmatrix} \mathbf{C}_R & \mathbf{C}_G \end{bmatrix} \mathbf{x} + \begin{bmatrix} \mathbf{D}_R & \mathbf{D}_G \end{bmatrix} f. \end{aligned} \tag{4.7}$$

Indices R and G denote the matrices of the reflection coefficient's and the actuator's state-space systems, respectively.
When models for all subsystems exist, the outputs of each subsystem have to be connected with the inputs of its adjacent subsystems. Linking together the subsystems' state-space representations results in one single state-space model for the complete system. This combination is a matrix operation referred to as the Redheffer Star Product [191, 233]. Applied to all subsystems, this method yields one single state-space expression of the total system. Interconnection of the individual state-space systems can conveniently be done with built-in MATLAB routines.
Interconnecting all subsystems may result in a system with a high order of states. To reduce the order of the complete system, model reduction techniques such as, for example, balanced truncation [5], can be used, allowing the elimination of all states with negligible influence on the input-output behaviour.

4.3 Linear Stability Analysis

In the frequency domain approach, all subsystem descriptions are combined into a system accounting for proper matching conditions. This system is of the form

$$\mathbf{A}_{\mathrm{sys}}\, \mathbf{x}_{p,u} = \mathbf{s}, \tag{4.8}$$

where $\mathbf{A}_{\text{sys}}$ is the system matrix comprising the transfer matrices of each subsystem, $\mathbf{x}_{p,u}$ is the vector of acoustic variables in the coupling planes, and $\mathbf{s}$ accounts for source terms. To assess the linear stability of the thermoacoustic system, the dispersion relation of the complete system has to be solved [79, 141, 196, 205]. The dispersion relation is the frequency dependent determinant of the system matrix $\det(\mathbf{A}_{\text{sys}}) = 0$. Its solution usually is not straightforward as it is in general a complex-valued transcendental equation, rapidly increasing in length with network size. Since the acoustic wave propagation is governed by a partial differential equation, the transfer matrices of the subsystems are normally of a non-rational form. Also, solving the dispersion relation for complex frequencies will only be possible if all transfer matrices are available in analytical form. Except for academic examples this will not be the case. At least some elements will have to be determined from CFD or FEM computations or experimentally. However, even if closed-form expressions would be available for all transfer matrices involved, solving for the system's eigenvalues can be quite cumbersome.

A similar procedure to the traditional frequency domain approach can be followed for the network model based on state-space descriptions of the network components. Since for stability the evolution of free oscillations has to be considered, no inputs will be present so that a homogeneous linear system

$$\dot{\mathbf{x}} = \mathbf{A}_{\text{total}}\mathbf{x} \tag{4.9}$$

is obtained, where $\mathbf{A}_{\text{total}}$ is the dynamics matrix of the total system that results from the concatenation of all subsystems. Similar to the roots of the transcendental dispersion relation in the traditional approach, the eigenvalues of the $\mathbf{A}_{\text{total}}$ matrix, $\omega_{\text{eig}} = \omega_{\text{osc}} + \mathrm{i}\omega_{\text{GR}}$ (say), govern the stability of the system. Since a harmonic time dependence of the form $e^{\mathrm{i}\omega t}$ was assumed (see Sec. 2.3), $\Im(\omega_{\text{eig}}) < 0$ indicates an unstable mode with frequency $|\Re(\omega_{\text{eig}})|/2\pi$.[1]

From a numerical point of view, determining system stability from the state-space approach is straightforward, since calculating the eigenvalues from a given matrix can be performed with standard linear algebra routines. In contrast to that, solving the transcendental dispersion relation is usually not a trivial task even for networks of medium complexity. The dispersion relation generally has an infinite number of solutions with only those in the low-frequency regime being of physical relevance.

Evidently, the state-space approach can only provide a finite number of eigenvalues equal to the dimension of $\mathbf{A}_{\text{total}}$. This is due to the fact that the infinite-dimensional system has been reduced to a finite-dimensional state-space. In practice, however, the analysis will be limited to the low frequency regime, since thermoacoustic instabilities most commonly appear in the form of low frequency oscillations.

The major drawback of linear stability analysis is that limit-cycle amplitudes cannot be calculated and phenomenons like hysteresis cannot be predicted. Although an amplitude dependence in the acoustic boundary conditions may be observed at high oscillation amplitudes, too (see, e.g., Heckl [73]), the predominant nonlinearity is usually attributed to saturation effects in the flame in response to velocity fluctuations [47, 109, 194]. Experimental investigations have shown that the response of lean premixed flames to velocity

[1] The time dependence for a certain mode reads $e^{\mathrm{i}\omega_{\text{eig}}t} = e^{-\omega_{\text{GR}}t}(\cos(\omega_{\text{osc}}t) + \mathrm{i}\sin(\omega_{\text{osc}}t))$, where the prefactor determines whether the harmonic wave is attenuated or amplified.

fluctuations generally tends to saturate at high amplitudes ($u'/\bar{u} = \mathcal{O}(1)$) [10, 16], but more complex behaviour with a non-monotonic decrease in response was also observed [218, 219]. Therefore, Moeck et al. [128] and Noiray et al. [141] extended linear network models to account for non-linear effects, too. The latter authors developed models for a non-linear flame response that make use of the Flame Describing Function approach [140, 141].

"Wohltätig ist des Feuers Macht,
Wenn sie der Mensch bezähmt, bewacht"
F. v. Schiller, Das Lied von der Glocke.

Chapter 5

Control Approach

This chapter deals with the general control principle and the steps that are needed to determine the controller transfer function. After the general introduction of the underlying principle in Sec. 5.1, two basically different ways of setting up the controller are presented; one for tuning the system within a broad frequency range (Sec. 5.2), the other for adjusting the boundary condition at discrete frequencies only (Sec. 5.4). In case of the multi-frequency tuning approach, frequency domain system identification tools are necessary to identify a model for the controller. The methodology and the algorithm, which are used in this study, are presented in Sec. 5.3.
For the control concept to work, it is necessary that the acoustic field is decomposed into its up- and downstream travelling part in the time-domain. Therefore, a wave decomposition scheme analogous to the Multi-Microphone Method in frequency domain is derived to allow an instantaneous determination of the downstream travelling wave. In Sec. 5.5, the setup of this scheme is explained.
In this chapter, only control approaches for linearly responding actuators are derived. Expectedly, especially actuators that provide high actuation amplitudes by means of mass flow modulation, might exhibit non-linear response characteristic. Such an actuator, the Ling Driver, is also used in the experiments conducted in this study. Since it is more instructive to derive a control loop accounting for non-linear transfer characteristics after the actuator's non-linear response has been studied, an appropriate controller is introduced in Sec. 6.4.3 after the Ling Driver's excitation characteristics have been examined.

5.1 Control Principle

To develop the control scheme, the setup in Fig. 5.1 is considered. The (thermo-)acoustic system that should be exposed to prescribed acoustic boundary conditions is connected to a duct, in which only plane waves propagate. The duct's end-impedance that is to be

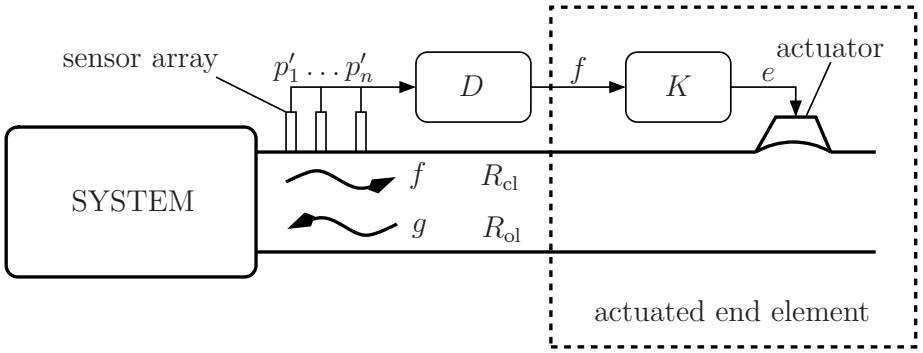

Figure 5.1: Schematic of active control concept. The downstream boundary condition of the (thermo-)acoustic system is actively adjusted in the way prescribed by the control law K.

manipulated, is equipped with a sensor array, consisting of several microphones at different axial positions and an actuator. As stated previously, the downstream termination, referred to as actuated end element, is regarded as a black box. The actuator manipulates the uncontrolled acoustic field in a certain prescribed way to achieve the control objective. For this, the sensor signals p'_j are fed to a control scheme, which generates the command signal and acts on the acoustic field via the actuator.
Instead of the measured acoustic pressures, it is more convenient to consider the downstream propagating wave f as the actual control input, as will be shown in the course of this chapter. For this reason, the control scheme depicted in Fig. 5.1 has been split into two parts:

(i) a wave decomposer, labelled D, that extracts the downstream propagating wave from the pressure signals p'_j and

(ii) the actual control law K.

Accordingly, finding a wave decomposition scheme D that works accurately over a range of frequencies is necessary. A method for time domain wave decomposition is presented in Sec. 5.5. For the remainder of this part, the f-wave is considered to be known so that it can serve as the input to the controller.
The problem now is to find a suitable control law K that, given the downstream propagating wave f, is able to drive the actuator in such a way that the closed-loop reflection coefficient R_{cl} is close to the desired one. K can be built if the uncontrolled (or open-loop) reflection coefficient R_{ol} and the actuator transfer function are known, as will be shown below. Since it is more instructive to consider the reflection coefficient than the impedance, the control law is derived for tuning the reflection coefficient. In contrast to Guicking & Karcher's approach [65], there is no need for manual parameter tuning and the controller acts over a range of frequencies. Also, the scheme presented here will not only work for time-harmonic but also for transient signals. This is particularly important when considering combustion noise, where no distinct frequencies prevail.
A more detailed schematic of the controller as it is implemented on the dSPACE board is shown in Fig. 5.2. The inputs are the measured and amplified microphone signals p'_j. These are fed through an analog digital converter (ADC). As was mentioned in Sec. 3.3.1, a complex calibration coefficient has to be considered for each microphone. Clearly, these

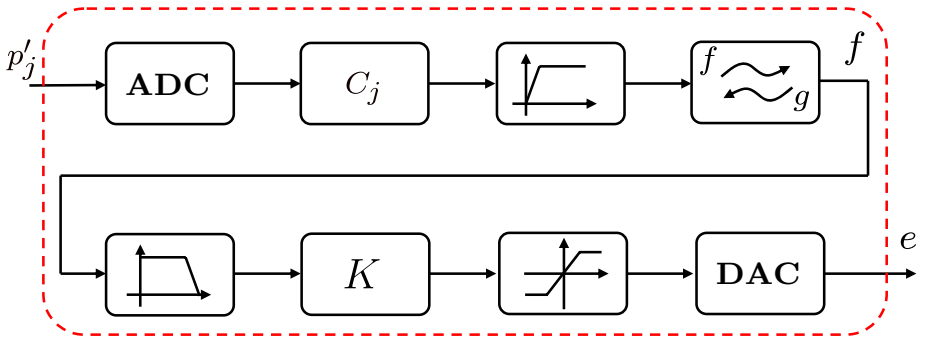

Figure 5.2: Schematic of control loop implemented on dSPACE board.

also have to be implemented on the controller board. To save processor capacity, which is needed for the online wave decomposition scheme and the controller model, only constant factors C_j are introduced. Besides this, identification of a transfer function for each sensor is a laborious, time-consuming task. The calibration curves that are shown in Fig. 3.7 justify this approximation. Usually, the magnitudes of the calibration coefficients only differ by a constant factor. Regarding the phases, it has to be made sure that combinations of microphones are chosen that exhibit only slight differences. Also, mounting of the microphones in the probe holders as well as mounting of the probe holders themselves has to be done with great care to minimize errors originating from the sensor setup. The experimental results prove that this procedure by all means performed very well.
In practice, the recorded time traces will have a small constant offset introduced somewhere in the signal routing from microphone membrane to dSPACE board. For a correct processing, the DC components have to be filtered out. This is achieved by using adequate high pass filters with a cut-off frequency between 10 and 20 Hz. The wave decomposer extracts the f-wave, which is low-pass filtered and processed by the control law K. To prevent the actuators and their control units from being damaged by an overload, a saturation block is implemented situated directly in front of the controller output. After being converted from digital to analog (DAC), the control signal e is given to the actuator.
Each filter that is implemented in the control loop causes an additional delay, as its phase is different from zero. Evidently, for the scheme to work properly, these delays have to be accounted for when designing the control law. Otherwise, the phase of the generated wave would not be correct obviating to achieve the control objective.

5.2 Calculation of the Control Law

As was mentioned earlier, in this study, only plane wave acoustic fields are considered, where the acoustic pressure and the particle velocity only depend on the axial coordinate. Practically, this means that only frequencies below the cut-on frequency for the first non-planar mode, confer to Eq. (2.48), can be accounted for.
To derive a suitable control law, a model for the actuated end element shown in Fig. 5.3 is written in the frequency domain, similar to as it was done for the network model in Sec. 4.2:

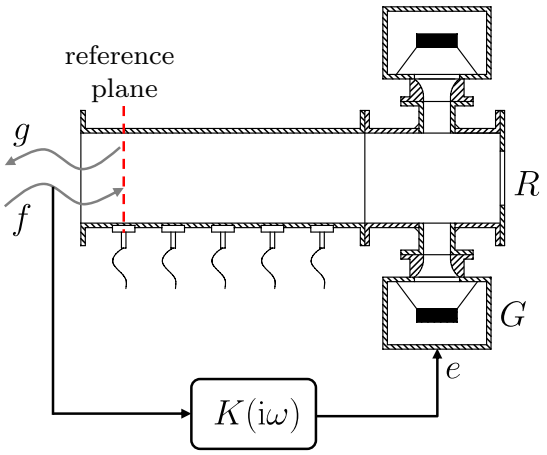

Figure 5.3: Sketch of actuated end element for derivation of the control law K.

$$\hat{g} = R_{\mathrm{ol}}\hat{f} + G\hat{e}, \tag{5.1}$$

where G is the actuator transfer function and $\hat{e}$ is the control command. Given that $\hat{f}$ can be extracted from the microphone signals and is fed to the controller ($\hat{e} = K\hat{f}$), the end element's $\hat{g}$ response reads

$$\hat{g} = (R_{\mathrm{ol}} + GK)\hat{f}. \tag{5.2}$$

Hence, the closed-loop reflection coefficient is given by

$$R_{\mathrm{cl}} = \frac{\hat{g}}{\hat{f}} = R_{\mathrm{ol}} + GK. \tag{5.3}$$

If the uncontrolled reflection coefficient R_{ol} and the actuator transfer function G are known, then, given a desired reflection coefficient R_{cl}, the control law K can be calculated from

$$K = \frac{R_{\mathrm{cl}} - R_{\mathrm{ol}}}{G}. \tag{5.4}$$

To determine K, in essence, means to identify the model for the $\hat{g}$ response of the actuated end element given by Eq. (5.1). Exciting at the up- and downstream end of the test rig according to the procedure explained in Sec. 4.2 yields R_{ol} and G.

Direct feedback of acoustic pressure

Generally, it could also be thought of generating the control signal by a direct feedback of the measured pressure p'. Thereby, no scheme for online wave decomposition would be necessary. In this case, the control law would read

$$\hat{e} = \tilde{K}\hat{p}. \tag{5.5}$$

Again, considering the end-element in Fig. 5.3, Eq. (5.1) has to be written in terms of acoustic velocity and pressure to give

$$\hat{u} = \frac{1}{Z_{\mathrm{ol}}}\hat{p} + \tilde{G}\hat{e}, \tag{5.6}$$

where $\tilde{G}$ is the transfer function from control signal to acoustic velocity at the reference position and Z_{ol} is the uncontrolled impedance of the downstream end. If the modified control law $\tilde{K}$ is derived analogously to the one which processes the f-wave, see Eq. (5.4), one obtains

$$\tilde{K} = \frac{1/Z_{\mathrm{cl}} - 1/Z_{\mathrm{ol}}}{\tilde{G}}. \tag{5.7}$$

Beside the fact that consideration of the reflection coefficients for the controlled and uncontrolled case is more instructive than the corresponding impedances, there are constraints that prohibit using the impedance formulation. First and most important, the longer the (virtual) length of the test rig, the more frequencies will occur at which pressure nodes exist at the reference location. Consequently, for these frequencies, the reciprocal value of the impedance in Eq. (5.7) tends to infinity. To achieve the control objective nonetheless, the control law exhibits resonances at this frequencies. These resonances are not ideal peaks and therefore will amplify neighbouring frequencies as well as noise. As a matter of fact, this would render the system unstable and control would not be possible. Another problem is that a sound soft termination implies an impedance of zero. In this case, the control law would also tend to infinity and thus would not be proper.

5.3 Identification of State-Space Model for the Controller

The procedure explained above provides the controller transfer function K as discrete frequency response data. However, to apply it in a control scheme, a model accurately capturing its response is necessary. In this study, the models were obtained by using appropriate frequency domain system identification algorithms. The best results were obtained when using the public domain MATLAB routine *Vector Fitting*, which was developed by Gustavsen & Semlyen [67, 68].

Vector Fitting is a robust numerical tool that allows to identify state-space models for single or multi input-output systems. It is straightforward to handle and can easily be adjusted to the user's needs. The most important advantage it has over comparable system identification tools that were also tested is, however, that the identified model will always have stable poles – a major requirement for the resulting controller transfer function. In the following, it is briefly described how the algorithm works. Some information on the routine presented here is taken from [67, 68], where a comprehensive description may be found.

Measured discrete frequency responses serve as input for the identification process. The algorithm fits a rational approximation to the measured data in the frequency domain. The order of this partial fractional expansion, i.e., the number of its poles, accords to the number of states of the identified model. For a SISO system, as it is the case for the control

law K,

$$\hat{e} = K\hat{f} \tag{5.8}$$

the routine identifies the corresponding linear time-invariant state-space model in the time domain

$$\begin{aligned} \dot{\mathbf{x}} &= \mathbf{A}\mathbf{x} + \mathbf{B}f, \\ e &= \mathbf{C}\mathbf{x} + Df, \end{aligned} \tag{5.9}$$

where $\mathbf{A}$, $\mathbf{B}$, and $\mathbf{C}$ are $N \times N$, $N \times 1$, and $1 \times N$ matrices, respectively and D is a scalar. The system variables are the elements of the N-dimensional state-vector $\mathbf{x}$. $\mathbf{A}$ is the system matrix and contains the information about the dynamical behaviour of the system. Depending on how the system's state-space variables are defined, the elements of the matrix and the vectors of this state-space realization are determined. The same input-output behaviour can be obtained from different definitions of the systems state variables. If these variables are derived from the poles of a partial fraction expansion of the the frequency domain data, which is the case for *Vector Fitting*, the system matrix $\mathbf{A}$ assumes the so-called Jordan canonical form. In this case, the diagonal elements comprise the poles of the partial fraction expansion. The routine finds a least squares solution for K by estimating all coefficients in the rational function approximation

$$K(\mathrm{i}\omega) \approx \sum_{n=1}^{N} \frac{c_n}{\mathrm{i}\omega - a_n} + d. \tag{5.10}$$

To obtain the state-space system of Eq. (5.9) this approximation is then expressed as

$$K(\mathrm{i}\omega) \approx \mathbf{C}(\mathrm{i}\omega\mathbf{I} - \mathbf{A})^{-1}\mathbf{B} + D, \tag{5.11}$$

where $\mathbf{I}$ is the identity matrix and the elements of $\mathbf{C}$ and $\mathbf{A}$ are formed by the residues c_n and poles a_n of Eq. (5.10). Reference [233] provides additional detailed information on how this and other state-space formulations can be derived.
Depending on the complexity of the frequency response, the number of poles of the resulting model can be adjusted. Furthermore, the routine can be modified to impose arbitrary weighting factors to certain frequency bands. Using this feature, the user can control in which frequency regions the approximation should be more accurate than in others. This enables to reduce the number of poles for complex frequency responses for which the response characteristic has only to be accurate for certain frequencies and may have a larger variance at others.

Example for controller transfer function

For cold flow conditions, Fig. 5.4 shows the uncontrolled reflection coefficient (black) and the woofer transfer function (green) for the case for which an orifice plate was mounted at the downstream end of the combustion test rig. The woofer transfer function sharply decreases at frequencies below 50 Hz and, though somewhat more moderately, above 350 Hz. According to Eq. (5.4), this results in a rapid increase of the controller transfer function in

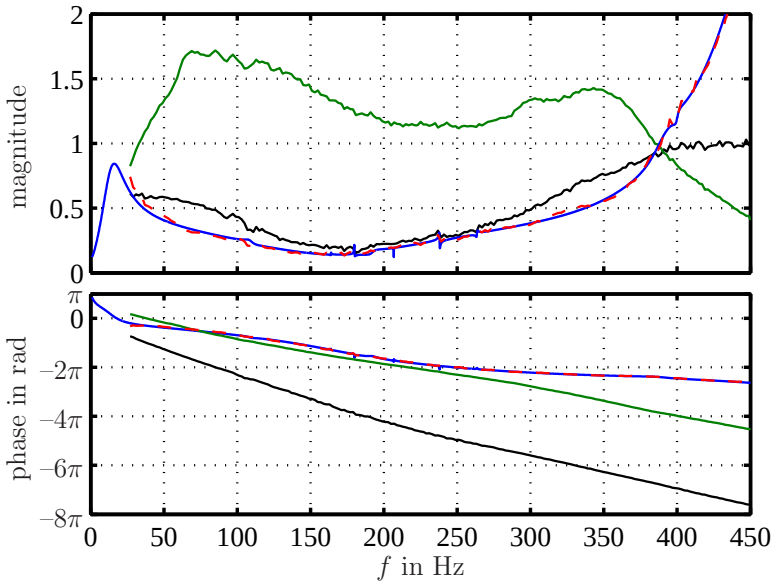

Figure 5.4: Frequency responses for downstream reflection coefficient (black), woofer (green), and control law to adjust an anechoic end (red dashed and blue). Top: magnitude, bottom: phase.

these frequency bands. This is generally not desirable, because an increase of the controller transfer function leads to a strong amplification of the microphone signals and could, therefore, limit the actuator performance.
Additionally, the controller transfer function K to adjust a non-reflecting end, i.e., $R_{\mathrm{cl}} = 0$, is plotted (Fig. 5.4, red dashed). In this case, K is simply obtained as the ratio of the uncontrolled reflection coefficient and the speaker transfer function (see Eq. (5.4)). Unlike the measured K data, the identified controller model is valid for all frequencies between zero and infinity. Therefore, it is necessary to ensure that the model for the controller transfer function decreases for very low and high frequencies. This is achieved by adequately fitting the discrete frequency data as shown in Fig. 5.4. The identified model (blue curve) follows the measured speaker transfer function K down to approximately 30 Hz but for lower frequencies, where no measured values are available, it is forced to decrease. In the case shown, the identified model is of order 25.

5.4 Controller for Tuning at Discrete Frequencies

Identifying a stable controller transfer function K for a broad frequency range can sometimes be cumbersome if not impossible. This is due to the reason that the expression for K might be too complex or even unphysical. Consider, for example, an actuator transfer function G with a time-delay larger than that of the numerator in Eq. (5.4). This would result in a phase increase of K, which physically would correspond to the fact that the controller would have to generate a signal prior to getting its input, i.e., the controller would not be causal. Thus, the applicability of the model identification routine strongly depends on the specific test setup as well as the uncontrolled and desired reflection coefficients. It can generally be stated that the larger the time-delay between actuator input signal and

generated acoustic excitation at the reference location in the test rig, the more difficult is the model identification. For instance, a long tubing between actuator and test rig may impede the identification process. Another problem is that K is determined from measured frequency response data and therefore is only prescribed in a certain frequency range. A model, however, is valid for all frequencies between zero and infinity. In addition to an accurate model identification, the K-model must not overshoot at frequencies approaching zero or infinity. Otherwise, the control output would have to be saturated and control is not possible.
These problems can be avoided if the impedance is only tuned at discrete frequencies. The idea is to build the controller using the transfer function K, calculated at a single frequency f_0 ($f_0 = \omega_0/2\pi$), say, from Eq. (5.4) and a band-pass filter centered at ω_0. This modified controller setup is shown in Fig. 5.5. The calculated control law now only consists of a gain

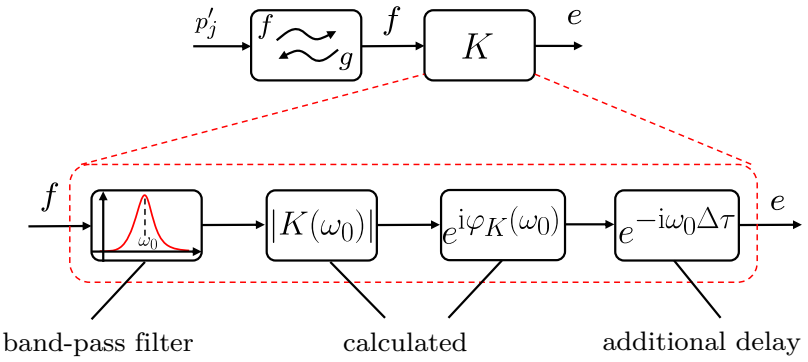

Figure 5.5: Control schematic for impedance tuning at discrete frequencies.

$|K(\omega_0)|$ and a single time-delay $\exp(i\varphi_K(\omega_0))$ at the frequency of interest. Applying the band-pass filter ensures that the control signal is only acted upon for frequencies around ω_0. Otherwise, the extracted f-wave would be amplified for all frequencies and makes control most probably impossible, as the control law $K(\omega_0)$ is only valid for the single frequency ω_0 and would at other frequencies force the system to unwanted states.
MATLAB/Simulink was used to implement the controller. As there is no built-in function for a band-pass filter, it is generated by multiplication of a high- and a low-pass filter.

Method to generate an instability at ω_0

In the following, it is outlined how the concept can be used to tune the system in such a way that unsteady heat release and acoustic pressure are perfectly in phase, i.e., to promote perfect constructive interference. In this case, the production of acoustic energy reaches its maximum, as stated by the Rayleigh integral in Eq. (2.74). Thus, the pressure amplitude of the resulting thermoacoustic instability would be largest, producing the "worst case scenario". As remarked in the preceding chapter, it is common practice to represent the linear behaviour of thermoacoustic systems by 1-d network models. The most simple form of such a network model is obtained if the system properties are described by an up- and downstream reflection coefficient, which are interconnected. This is shown in Fig. 5.6, where the reference location is chosen as such that the upstream reflection coefficient comprises the flame response and the downstream reflection coefficient is the one to be tuned. This system may get unstable if g_{in} and g_{out} are in phase and the reflection coefficients' magnitudes are

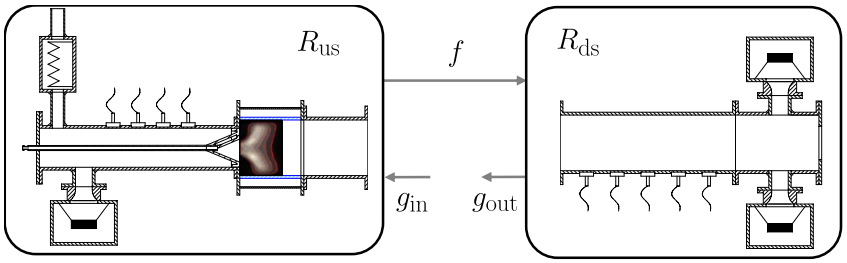

Figure 5.6: Representation of the test rig as a network model consisting of an up- and downstream reflection coefficient.

high enough, i.e,

$$\varphi_{\mathrm{cl}}(\omega_0) + \varphi_{\mathrm{us}}(\omega_0) = 2n\pi, \qquad n = 0, 1, 2, ... \tag{5.12a}$$

$$|R_{\mathrm{cl}}(\omega_0)||R_{\mathrm{us}}(\omega_0)| \geq 1. \tag{5.12b}$$

This procedure is not fully correct, as the frequency of a growing oscillation is complex,

$$\omega = \omega_{\mathrm{osc}} + \mathrm{i}\omega_{\mathrm{GR}}, \tag{5.13}$$

$\omega_{\mathrm{osc}}/2\pi$ being the frequency of oscillation and $-\omega_{\mathrm{GR}}$ representing the growth rate (see also explanations on this in Sec. 4.3). In contrast to this, K is calculated for ω_0, a real frequency. The higher the growth rate, i.e., the larger the negative imaginary part, the more the experimentally observed frequency will differ from ω_0. Moreover, if the system exhibits limit-cycle oscillations, either non-linearities or the impact of high amplitude oscillations on the operating parameters may change the frequency of linear instability. For instance, Moeck et al. [126] experimentally observed slight changes ($< 5\,\mathrm{Hz}$) between linear regime and limit-cycle in the same combustion test rig taken for this study. Larger frequency shifts of 40 Hz are also reported in the literature [165]. In most cases investigated in this study, however, the difference between the adjusted and the observed oscillation frequency was negligible. If this was not the case, deviations could be adjusted by an additional delay $\exp(-\mathrm{i}\omega_0\Delta\tau)$ implemented in the controller (Fig. 5.5). Using this delay, the phase of K and therefore the phase of R_{cl} could be changed, causing the system to get unstable at the desired frequency ω_0. Note that the implementation of an additional phase might not necessarily always be a possibility to adjust the control circuit appropriately. However, if only slight differences between ω_0 and the actual oscillation frequency exist, this method is likely to deliver the desired results.

If the system is tuned at discrete frequencies, no controller identification is necessary, as the controller only consists of a band-pass filter, a gain, and a delay. For almost all conditions observed with the multi-tuning approach, the test rig exhibited oscillations at the frequency which corresponded to the $\lambda/4$-mode according to the adjusted virtual length. If so, tuning the system to higher resonance frequencies with the conventional approach is limited, as this physically corresponds to a reduction of test rig length. Theoretically, the shortest length realizable then is the one at which the upstream travelling wave generated by the actuator and the downstream travelling f-wave, serving as the control input, meet. However, it is by all means possible that in different setups a different mode becomes unstable as, for example, the 3/4-λ-mode or the 5/4-λ-mode. If this is the case, the system might be forced

to oscillate at higher frequencies than the limit frequency stated above. Tuning at discrete frequencies completely avoids this problem, as Eq. (5.12a) can be solved for all frequencies. Another important advantage is that the delay between the actuator response and its input signal is not important, as the phase has only to be shifted by a constant value. Regarding a controller for a frequency band, this is not the case, as its phase usually cannot be described by a single time-delay.
Besides these important advantages, one has to account for some disadvantages, too. As the test rig has to be tuned for each frequency of interest, measurement campaigns will take longer. Furthermore, tuning R_{cl} to fully reflecting at discrete frequencies might lead to limit-cycle oscillations at two different modes ω_1 and ω_2. If R_{cl} is adjusted to fully reflecting in a frequency band covering ω_1 and ω_2, the mode with the larger growth rate (ω_1, say) might completely dominate the limit-cycle due to nonlinear effects, as was, for instance, reported in references [128, 232]. Thus, at ω_2, no limit-cycle oscillations will be observed. The burner's behaviour to this respect can, therefore, not be observed when tuning at discrete frequencies.

5.5 Schemes for Online Wave Decomposition

As stated previously, to obtain the f-wave serving as the control input signal, a suitable algorithm is required that separates the up- and downstream travelling waves from the pressure sensor signals. In the frequency domain, this can be accomplished by using the Multi-Microphone Method explained in Sec. 3.3.2. However, in contrast to the traditional MMM, the wave decomposition cannot be performed as a post-processing step in the frequency domain. The f-wave has to be identified instantaneously and therefore its calculation from the sound pressure sensors has to be accomplished online in the time domain. It will first be shown how this can be done for two microphones. According to Eqs. (2.38), the expressions for the Riemann invariants in a uniform duct read

$$f = f(t - \frac{x}{\bar{c} + \bar{u}}), \tag{5.14a}$$

$$g = g(t + \frac{x}{\bar{c} - \bar{u}}). \tag{5.14b}$$

With reference to Fig. 5.7, Eqs. (5.14) are evaluated at two axial locations, x_1 and x_2 (say),

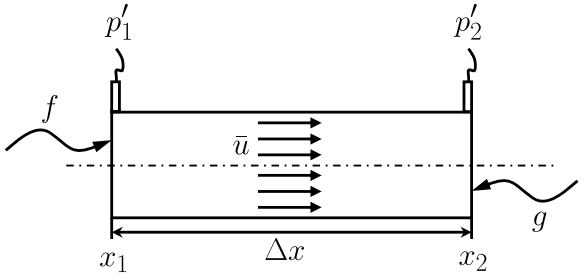

Figure 5.7: Duct with constant cross-section instrumented with 2 microphones. Setup for online wave identification with two microphones.

to give the relations

$$p_1'(t) = f(t) + g(t - \tau^-), \tag{5.15}$$
$$p_2'(t) = f(t - \tau^+) + g(t), \tag{5.16}$$

where $\tau^\pm$ represents the respective propagation times the acoustic waves need to travel from one microphone location to the other, i.e., $\tau^\pm = \Delta x/(\bar{c} \pm \bar{u})$ and $\Delta x = x_2 - x_1$. In these equations, g can be eliminated by evaluating Eq. (5.16) at $t - \tau^-$ and using the result in Eq. (5.15) yielding

$$p_1'(t) = f(t) + p_2(t - \tau^-) - f(t - \tau^- - \tau^+), \tag{5.17}$$

from which it is concluded that the f-wave can be identified in real-time by using the scheme shown in Fig. 5.8. One drawback of this approach is that the feedback loop in Fig. 5.8 is

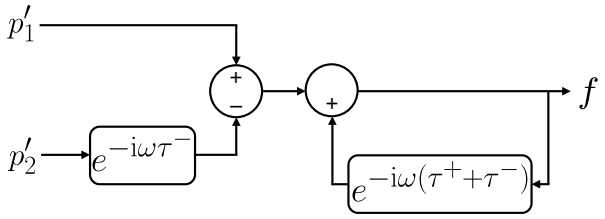

Figure 5.8: Block diagram mapping two measured pressures to the downstream travelling wave f.

only marginally stable. To see this, Eq. (5.17) is solved for $\hat{f}$ in frequency domain:

$$\hat{f} = \frac{\hat{p}_1 - \hat{p}_2 e^{-i\omega\tau^-}}{1 - e^{-i\omega(\tau^+ + \tau^-)}}. \tag{5.18}$$

The purely real eigenvalues are located at

$$\omega_n = \frac{2\pi n}{\tau^+ + \tau^-}, \quad n = 0, \pm 1, \pm 2... \tag{5.19}$$

This relation can be recast in the form

$$\frac{\omega_n}{\bar{c}} \Delta x = \pi n (1 - M^2), \tag{5.20}$$

which was given by Åbom and Bodén [1] in their analysis of the Two-Microphone Method (TMM) in frequency domain. Equation (5.19) is satisfied when the microphone spacing matches half the wave-length. It is important to note that, as the above authors pointed out, not only the frequencies given by Eq. (5.19) are excluded from data processing, but also the error in the TMM increases dramatically close to these frequencies. Also, decreasing the microphone spacing to move ω_1 to higher frequencies is not an option since, in this case, the accuracy of the TMM significantly deteriorates at low frequencies [1]. In practice, this means that the identification algorithm cannot be used close to frequencies for which Eq. (5.19) holds. Moreover, oscillations can be excited that would have to be suppressed with suitable notch filters.

In the frequency domain, this issue is resolved by using the MMM. Here, several microphones at multiple axial locations, corresponding to unequal propagation delays, are used. This resolves the issue of singularities at frequencies given by Eq. (5.19). The wave decomposition is then obtained from a least squares fit to the measured complex pressure amplitudes, as was described in Sec. 3.3.2. As stated there, an additional advantage of the MMM is that, by averaging over several microphones, flow noise is suppressed. This is even more important in a real-time application, where noise rejection techniques, such as cross-correlations with the excitation signal, cannot be used. For the impedance tuning control scheme, the decomposition has to be accomplished in real-time. Therefore, application of the traditional MMM is not feasible. Simply finding a time domain representation of $\mathbf{H}^{\dagger}$ in Eq. (3.2) by means of frequency system identification tools is not possible, since $\mathbf{H}^{\dagger}$ always has unstable poles. However, a time domain scheme, having similar advantages like the MMM in frequency domain (i.e., using more pressure signals to reject flow noise and removal of singular frequencies), can be constructed as follows. With respect to the

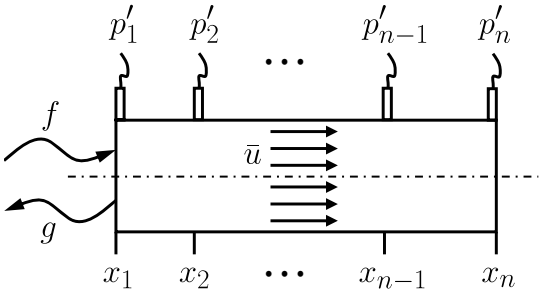

Figure 5.9: Duct with constant cross-section instrumented with n microphones. Setup for online wave identification with multiple microphones.

setup shown in Fig. 5.9, n equations for the pressure signals are obtained as

$$p'_1(t) = f(t) + g(t), \tag{5.21a}$$
$$p'_2(t) = f(t - \tau^{+}_{1,2}) + g(t + \tau^{-}_{1,2}), \tag{5.21b}$$
$$\vdots$$
$$p'_n(t) = f(t - \tau^{+}_{1,n}) + g(t + \tau^{-}_{1,n}), \tag{5.21c}$$

where $\tau^{\pm}_{n,m} = (x_m - x_n)/(\bar{c} \pm \bar{u})$. Note that, in contrast to the procedure with two microphones, f and g at time t, here, are defined at the same axial position. The aim is now to find a causal relation for $f(t)$ that accounts for all n pressure recordings. The pressure at location x_j is written at time $t - \tau^{-}_{1,j}$, viz.,

$$p'_1(t) = f(t) + g(t), \tag{5.22a}$$
$$p'_2(t - \tau^{-}_{1,2}) = f(t - \tau^{+}_{1,2} - \tau^{-}_{1,2}) + g(t), \tag{5.22b}$$
$$\vdots$$
$$p'_n(t - \tau^{-}_{1,n}) = f(t - \tau^{+}_{1,n} - \tau^{-}_{1,n}) + g(t). \tag{5.22c}$$

Equations (5.22) are considered as an overdetermined linear system for $f(t)$ and $g(t)$, whose least squares solution takes the form

$$\begin{bmatrix} f(t) \\ g(t) \end{bmatrix} = \begin{bmatrix} 1 & -1/(n-1) & \dots & -1/(n-1) \\ 0 & 1/(n-1) & \dots & 1/(n-1) \end{bmatrix} \begin{bmatrix} p_1'(t) \\ p_2'(t-\tau_{1,2}^-) - f(t-\tau_{1,2}^+ - \tau_{1,2}^-) \\ \vdots \\ p_n'(t-\tau_{1,n}^-) - f(t-\tau_{1,n}^+ - \tau_{1,n}^-) \end{bmatrix}. \quad (5.23)$$

Based on Eq. (5.23), it can be concluded that the Riemann invariants at time t are functions of the number of pressure sensors, the measured acoustic pressures, and the downstream travelling wave f lagged by certain delays. It is, however, more instructive to consider the frequency domain solution for $\hat{f}$, which is obtained from Eq. (5.23) as

$$\hat{f} = \frac{\hat{p}_1 - \frac{1}{n-1}\left(\hat{p}_2 e^{-\mathrm{i}\omega\tau_{1,2}^-} + \ldots + \hat{p}_n e^{-\mathrm{i}\omega\tau_{1,n}^-}\right)}{1 - \frac{1}{n-1}\left(e^{-\mathrm{i}\omega(\tau_{1,2}^+ + \tau_{1,2}^-)} + \ldots + e^{-\mathrm{i}\omega(\tau_{1,n}^+ + \tau_{1,n}^-)}\right)}. \quad (5.24)$$

The denominator in Eq. (5.24) has real zeros only where $\omega(\tau_{1,j}^+ + \tau_{1,j}^-) \bmod 2\pi = 0$ for all j. If the microphone spacings are incommensurate, this will happen only at large frequencies (besides at $\omega = 0$), orders of magnitude above the cut-on frequency and will, therefore, not influence the measurements. Additionally, to avoid aliasing, the pressure signals are anyway low-pass filtered at half the sampling frequency. Doing so, frequencies at which the MMM could theoretically become marginally stable are suppressed. The mathematical proof of the validity of this statement is given in Appendix A by means of mathematical induction.

A plot of the first few poles of Eqs. (5.18) and (5.24) for the case $n = 3$ is shown in Fig. 5.10. Here, it is assumed that the ratio of the two microphone spacings satisfies $\Delta x_{1,2}/\Delta x_{1,3} = \sqrt{2}$. Evidently, in practice, the ratio of two microphone spacings cannot be

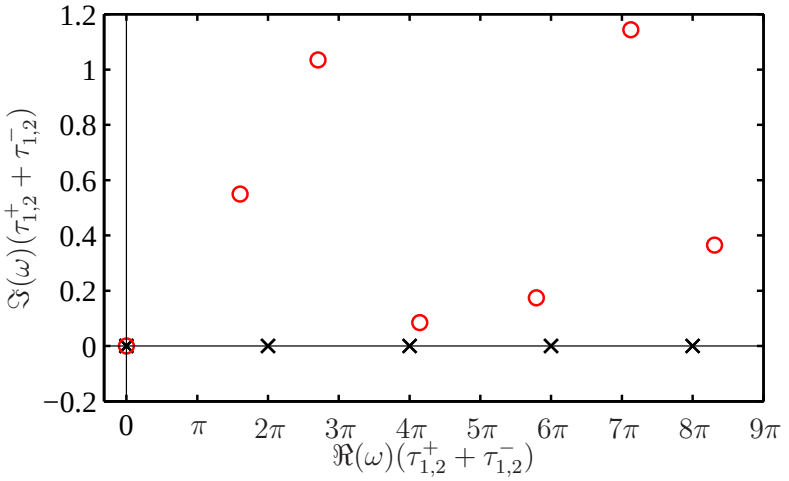

Figure 5.10: Poles of the two-microphone identification scheme (Eq. (5.18), black ×) and the Multi-Microphone Method (Eq. (5.24) for $n = 3$, red ○) with $(\tau_{1,2}^+ + \tau_{1,2}^-)/(\tau_{1,3}^+ + \tau_{1,3}^-) = \Delta x_{1,2}/\Delta x_{1,3} = \sqrt{2}$.

equal to an irrational number. Here, this is only chosen for a convenient visualization in

the graph. Apart from the pole at $\omega = 0$, all poles lie in the upper half of the ω-plane. When designing an acoustic measurement section, the microphone locations should not be arranged in distances that are multiples of each other.
According to the statements above, a state-space realization of Eq. (5.24) is asymptotically stable and can be used to serve as the wave decomposer D, mapping n pressures to the downstream propagating wave, as shown in Fig. 5.1. The feedback scheme, mapping n pressures to the downstream travelling wave, is shown in Fig. 5.11.

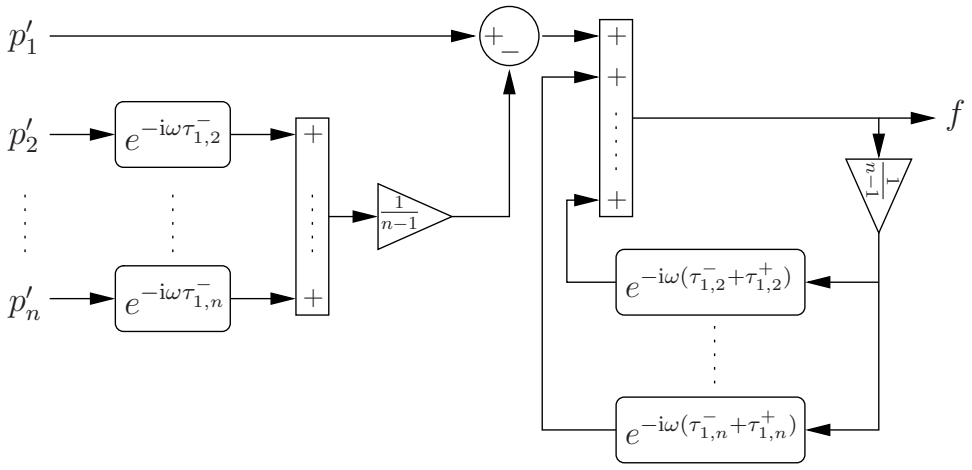

Figure 5.11: Block diagram mapping n measured pressures to the downstream travelling wave f.

Note, however, that for implementation of Eq. (5.18) or Eq. (5.24) on a digital control board, Padé approximations for the time-delays should be used. Otherwise, rounding the time-delays to sample time will introduce inaccuracies, which might have a significant effect on the quality of the wave decomposition – even if the control board is run at several kilohertz. The more microphones are used to determine the acoustic field, the more time-delays are involved and the larger is the state dimension of the controller. Using the online MMM instead of the TMM yields more accurate results on the one hand but requires more processor capacity on the other.
A result of this is that with the TMM approach the determination of the g-wave, analogous to the f-wave, does not pose a great deal in terms of processor capacity. Thus, the quality of the wave decomposition scheme can easily be monitored instantaneously by taking the sum of f and g and comparing it to the time trace of the measured pressure p_1 at the reference location. Additionally, having both waves, it is possible to quasi directly observe the actually adjusted reflection coefficient by averaging over short periods as, for example, 1 second, and calculating their Fourier transforms. If the quality of the wave decomposition should be monitored with the MMM approach, a system analogous to the one derived for the f-wave in Eq. (5.23) had to be set up for g. Yet, the MMM approach requires rather a lot processor capacity and this then would be doubled. Directly using Eq. (5.23) to determine g is not an option since the sum of f and g would always be identical to p_1, as can be seen in the first matrix on the right hand side.
Calculation of the Padé approximations can be accomplished with built-in MATLAB functions. However, when doing so, the numerator and denominator of the resulting transfer function are of same order. This means that the step response is non-zero at $t = 0\,\mathrm{s}$ and

that there is a direct feedthrough between inputs and outputs. In terms of state-space systems, this corresponds to a non-zero $\mathbf{D}$ matrix in Eq. (4.1). Thus, in the block diagram depicted in Fig. 5.11 the feedback loops of the terms $e^{\tau^+_{1,j}+\tau^-_{1,j}}$ would cause a singularity, rendering the decomposition scheme unstable. To avoid this problem, a modified Padé approximation is calculated for which the denominator degree is larger than that of the numerator. Thereby, the step response at $t = 0\,\mathrm{s}$ is zero, i.e., the transfer function provides no direct feedthrough and the scheme does not have singularities.
Figure 5.12 compares the extracted $\hat{f}$-waves which have been obtained by three different identification schemes. As the downstream propagating wave is the control input, its identification has a huge impact on the accuracy of the adjusted closed-loop reflection coefficient. For the spectra shown, the combustion test rig was operated at $\phi = 0.65$ and a thermal

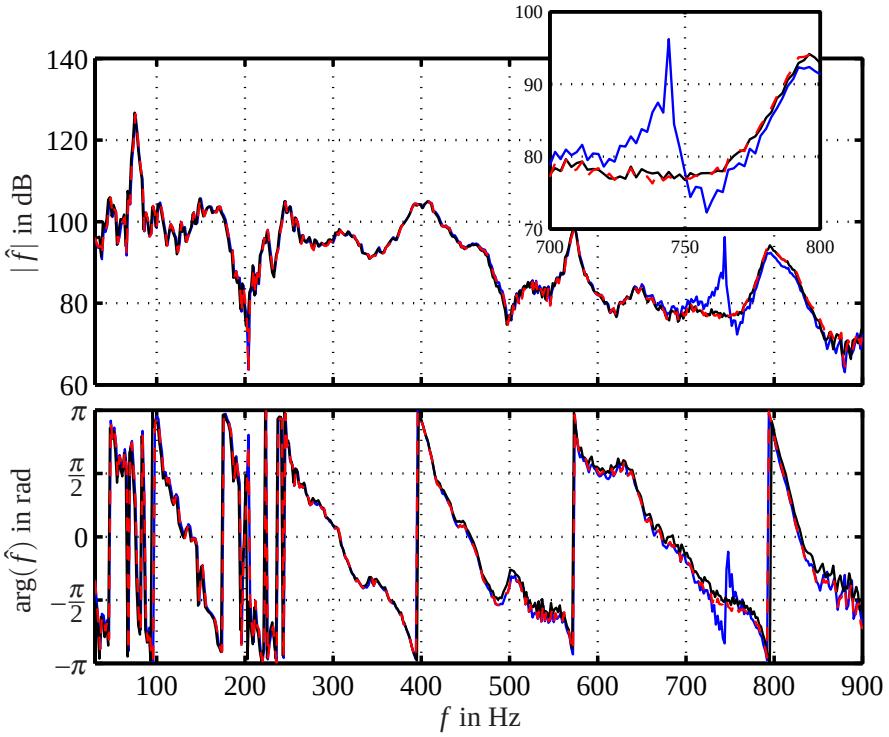

Figure 5.12: Comparison of $\hat{f}$-wave (control input) calculated with MMM in frequency domain (black), MMM in time domain (red dashed), TMM in time domain (blue). Top: magnitude, bottom: phase between $\hat{f}$-wave and excitation signal of loudspeaker.

power of approximately 100 kW. Additionally, it was excited by a woofer with a frequency sweep ranging from 20 Hz to 1000 Hz. The $\hat{f}$-waves were calculated by cross-correlation with the excitation signal.
In Figure 5.12 (top), the magnitudes are compared proving that the $\hat{f}$-wave identified with the MMM in time domain (red dashed) is nearly identical to the one obtained from the traditional MMM in frequency domain (black). Results for the TMM in time domain (blue) are equally well, except for frequencies between 700 Hz and 800 Hz. In this region, the restrictions of using the TMM close to frequencies given by Eq. (5.19) become obvious. At 744 Hz the microphone spacing is equal to half the wave-length. As can be seen in the enlarged frame, the error is not limited to this frequency but also affects neighbouring frequencies. Not only the magnitude but also the phase between the excitation signal and the

generated $\hat{f}$-wave has to be determined accurately. Results shown in the bottom frame of Fig. 5.12 prove that the phases are in very good agreement, too. Note that if the impedance is tuned for cold flow conditions, the speed of sound and therefore the frequencies, at which Eq. (5.19) is satisfied, decrease.

In industrial test rigs, the conditions for wave identification might not be as perfect as they are for lab-scale tests. For instance, the measurement section, which is instrumented with the microphones might not have a constant diameter, i.e., be a conical duct or a duct with area jumps. If the test rig walls are protected with a ceramic coating or are film-cooled, acoustic waves are damped. Moreover, in presence of an axial temperature gradient, the assumption of a constant speed of sound might not be justified. In these cases, the online wave decomposition scheme would have to be extended by deriving a more general form of the wave equation accounting for the changes. An analytical solution, however, will only be possible for special cases. Equations relating acoustic pressure and particle velocity to the Riemann invariants for wave propagation in conical ducts were, for example, given by Munjal [133][1]. The influence of damping can be considered by a complex instead of a purely real propagation constant. To do so, the damping characteristics of the walls would have to be known. The wave attenuation has then to be included in the wave propagation constant, see, for example, references [132, 220] for more information. An additional problem of the latter issue is the accurate determination of the damping effect. Finally, the impact of a temperature dependence in axial direction on the determination of the Riemann invariants was investigated by Sujith et al. [213] and Manoj Kumar & Sujith [117] and could also be implemented in the identification scheme. Subrahmanyam et al. [211, 212] presented solutions for a dedicated family of mean temperature and cross sectional area profiles in the absence of mean flow. It is assumed that these modifications would involve some laborious calculation steps but in principle should be possible.

[1] See pp. 65 therein

"Pulchritude: not just the concept but the whole physical word – beauty where you would least suspect it, hidden in a word that looked like it should signify a belch or skin infection."
Z. Smith, White Teeth.

Chapter 6

Results and Discussion

In this chapter, results obained with the impedance tuning concept are presented. Prior to experiments, application of the control scheme was simulated with a network model. The network model was set up for the cold acoustic test rig described in Sec. 3.1.1. Different acoustic boundary conditions were adjusted (Sec. 6.1). In Sec. 6.3, simulation results are then compared to the corresponding cold flow experiments. All test cases that were adjusted in the experiments are summarized in an overview documented in Sec. 6.2.
Subsequently, results for tuning the acoustic boundary condition of the combustion test rig with and without combustion are documented. For the reactive case, results obtained with three different actuator concepts – woofers, proportional valves, and an electro-pneumatic actuator – are presented. Section 6.4 closes with a comparison of the different actuators.
If the actuator lacks sufficient control authority, it is not possible to impose the full control signal prescribed by the control law. It has to be limited and is, thus, not processed correctly. However, it was observed that in most cases the control objective was achieved nonetheless. The behaviour of the control concept in case of a saturated controller output is presented in Sec. 6.5.
In most of the reactive cases, the impedance tuning concept was applied to operating conditions that featured strong self-excited instabilities. Prior to control, the combustion test rig was first passively stabilized by imposing a low-reflecting outlet termination. Starting from this stabilized case, the dynamics of the uncontrolled, unstable system were reproduced and also changed. In Sec. 6.6, the influence of the passive stabilization on the flame position and shape are studied. This was done in order to investigate the influence of a change in the aerodynamic downstream boundary condition on the flow field in the system and thus to examine the reproducibility of the self-excited instability by only adjusting the acoustic boundary condition.
Regarding the adjusted closed-loop reflection coefficients, a remark has to be made. As was stated in Sec. 2.3, the reflection coefficient can take values ranging from -1 (pressure node) via 0 (anechoic) to $+1$ (velocity node). It is reasonable to assume that if the control scheme is able to adjust the extremal values and $R = 0$, it will be able to adjust values in between,

too. Results shown in Secs. 6.3, 6.4, and 7.2 with the reflection coefficient tuned to a range of values lying between those for acoustically soft and hard terminations, suggest that this assumption is valid. Note, however, that this is a purely intuitive assumption, which might not be always correct.
One major objective of the impedance tuning approach is to actively tune the test rig to resonance frequencies different from those in the uncontrolled case. Thereby, it is, for instance, possible to simulate the acoustics of a system that is longer than the test rig used. Several different lengths and thus different resonance frequencies were simulated in the experiments. The choice of the actually adjusted virtually lengths was random.
In all pressure spectra shown in the following, the sound pressure amplitudes are depicted on a logarithmic scale in dB. Since we are interested in peak amplitudes at single frequencies, the relationship between acoustic pressure in Pa and dB meets the following equation:

$$\hat{p}_{\mathrm{dB}} := 20 \log \frac{\hat{p}_{\mathrm{Pa}}}{p_0}, \tag{6.1}$$

where $p_0 = 2 \cdot 10^{-5}\,\mathrm{Pa}$ is taken as the reference pressure. Note that this definition differs from the usual definition for the sound pressure level in dB, which is not calculated from the amplitude but the effective value of the sound pressure in Pa, as it represents an average value over all frequencies.

6.1 Simulation

To test the control scheme and to ensure a stable closed-loop system, simulations were carried out prior to experiments. According to the procedure explained in Chapter 4, a network model of the cold acoustic test rig was set up. The schematic of the modelled system is shown in Fig. 6.1. It consists of ducts, end-elements, the controller, and elements

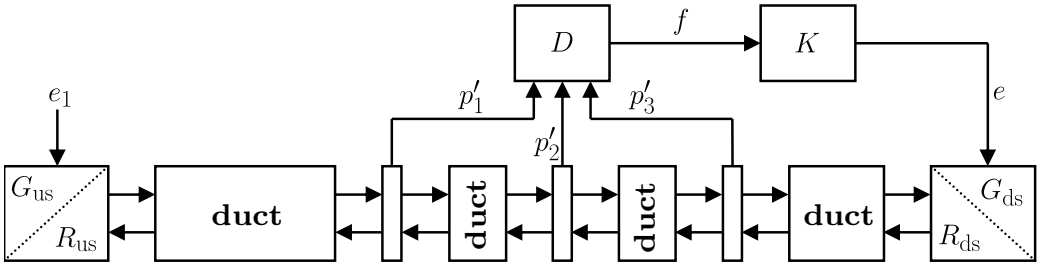

Figure 6.1: Setup of the 1-d network model for the cold acoustic test facility.

which write out the acoustic pressure at the location at which they are implemented. These elements are not part of the real system but only artificial components of the model. Since the subsystems are connected in terms of up- and downstream propagating waves, a simple routine is necessary to calculate the pressure. The output element is modelled in state-space

as a static gain without additional dynamics:

$$\begin{bmatrix} f_{\mathrm{ds}} \\ g_{\mathrm{us}} \\ \frac{p'}{\overline{\rho c}} \end{bmatrix} = \begin{bmatrix} 1 & 0 \\ 0 & 1 \\ 1 & 1 \end{bmatrix} \begin{bmatrix} f_{\mathrm{us}} \\ g_{\mathrm{ds}} \end{bmatrix}. \tag{6.2}$$

Apart from the **D** matrix, all other matrices of the state-space system (**A**, **B**, and **C**, cf. to Eq. (4.1)) are empty. The output element has a physical length of zero. Up- and downstream travelling waves are neither delayed nor changed in amplitude and consequently, the output element does not influence the acoustic behaviour of the total system.
The modelled transfer function from the upstream excitation command e_1 to microphone 2 in the uncontrolled case is shown in Fig. 6.2 (red dashed). For comparison, the measured transfer function is also displayed (black). Based on this result, the model is found to be accurate in the frequency range considered. To test the impedance tuning approach, the wave decomposition scheme D and the control law K are added to the model, as shown in Fig. 6.1.

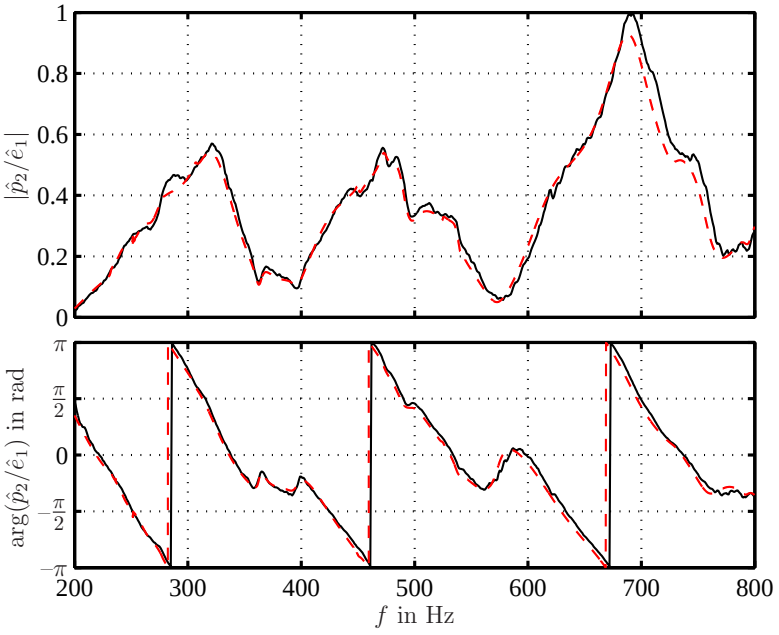

Figure 6.2: Transfer function from upstream speaker command to pressure in the duct; results from network model (red dashed) and experiment (black). Top: magnitude, bottom: phase.

Impedance tuning simulation

The acoustic system was simulated in time domain with reflection coefficients and actuator transfer functions identified from the frequency response measurements at the experimental facility. Different control laws were used in the simulations to impose various acoustic boundary conditions.
Figure 6.3 shows the measured reflection coefficient without control and the results of the simulation for different prescribed closed-loop reflection coefficients R_{cl}. For the impedance

tuning tests, the downstream end was tuned. Without actuation (black curve), the reflection coefficient approximately agrees with that of an open end, i.e., $R_{\mathrm{ol}} = -1$ for low frequencies. The phase of R corresponds to the length of the duct plus the end-correction of an open end, as analytically derived by Levine & Schwinger [105]. In the next section, a more detailed comparison between measurements and theoretical considerations is given.
With the control scheme, a non-reflecting end could be established. For $R_{\mathrm{cl}} = 0$, the reflection coefficient calculated is below 0.05 (green curve), according to a quasi non-reflecting end. The red curve represents results for the simulation of an acoustically closed end

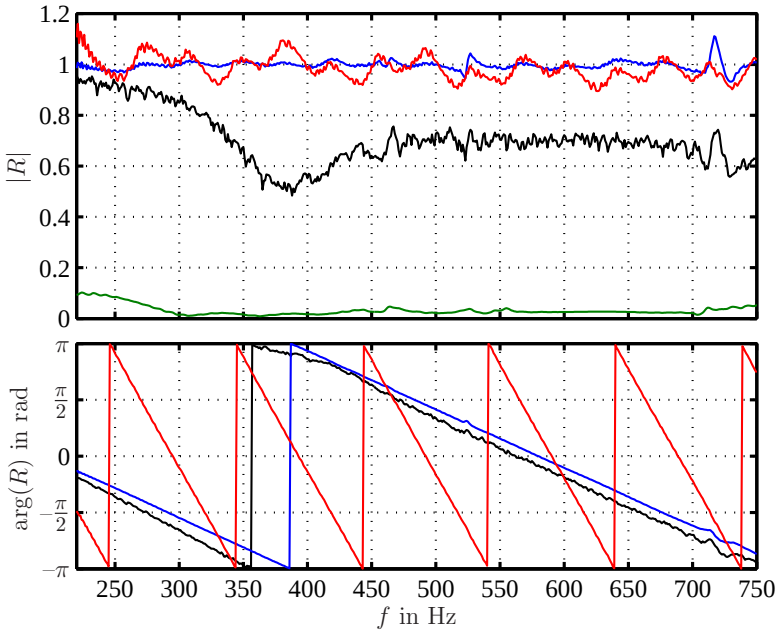

Figure 6.3: Reflection coefficients for the uncontrolled case (black), adjusted anechoic end (green), sound soft end (blue), and sound hard end with additional virtual length of $\Delta l = 1.3\,\mathrm{m}$ (red). Top: magnitude, bottom: phase.

($R_{\mathrm{cl}} = +1$, velocity node) with an additional phase lag of $2\omega\Delta\tau$ ($\Delta\tau = 3.7\,\mathrm{ms}$), where the additional length is directly related to the time lag by the speed of sound $\Delta l = \bar{c}\Delta\tau$. In this way, an additional virtual length of 1.3 m is added. All values of $|R|$ are between 0.9 and 1.1. Compared to the case without control, the slope is steeper, which is related to the additional length. Hence, the control scheme simulated the acoustic properties of a test rig now being longer than the original one and exhibiting different resonance frequencies, accordingly. If this length is taken into account, the phase has the same slope as in the uncontrolled case and differs by π, i.e., the prescribed difference in signs.
As a last example, the simulation was run with $R_{\mathrm{cl}} = -1$. Here, the results are even better (blue curve). Almost in the complete frequency range considered, $|R|$ takes values between 0.98 and 1.02. This is because the desired boundary condition is much closer to the uncontrolled case, as the uncontrolled open end has a reflection coefficient of $R = -1$ (pressure node) for low frequencies. Another evidence are the phase plots; both are almost identical. Consequently, the controller had to work less in this case when compared to the case of establishing a velocity node.

The simulations show the impedance tuning scheme to work accurately. Thus, in a next step, experiments were conducted.

6.2 Overview of Tests Cases

Tables 6.1 and 6.2 give an overview of all reflection coefficients that were adjusted in the cold flow and reactive experiments, respectively. Additionally to the prescribed values, the Tables provide the numbers of the figures in which the results are shown.

Table 6.1: Overview of adjusted reflection coefficients in cold flow experiments.

Actuator	cold acoustic rig	combustion test rig
Woofers	$R_{\mathrm{cl}} = 0$	$R_{\mathrm{cl}} = 0$
Secs. 6.3	Figs. 6.7 and 6.9	Figs. 6.14 and 6.15
	$R_{\mathrm{cl}} = -1$, $\Delta l = 0\,\mathrm{m}$	$R_{\mathrm{cl}} = -1$, $\Delta l = 0.5\,\mathrm{m}$
	Figs. 6.10 and 6.12	Figs. 6.14 and 6.15
	$R_{\mathrm{cl}} = +1$, $\Delta l = 1.3\,\mathrm{m}$	$R_{\mathrm{cl}} = +1$, $\Delta l = 0.5\,\mathrm{m}$
	Figs. 6.11 and 6.12	Figs. 6.14 and 6.15
	$\lvert R_{\mathrm{cl}} \rvert = 0 \ldots 1$	–
	Fig. 6.13	–
Proportional valves	–	–
Ling Driver	–	–

With the woofers, reactive tests were conducted at different operating conditions. For most of them, the equivalence ratio was set to $\phi = 0.65$ at a power of 110 kW and an orifice was mounted at the downstream end of the test rig. Entries marked with † represent results for $\phi = 0.7$, a preheat temperature of 423 K, and an open-end termination. These changes in operating conditions were adjusted in order to study the control concept for a case in which the combustion system initially was unstable. For those entries marked with *, the system was tuned to exhibit an instability at its 5/4-λ-mode in contrast to the other cases in which the $\lambda/4$-mode was adjusted.

6.3 Cold Flow

Prior to tests with combustion, the control scheme was validated at cold flow conditions. This was done to validate the scheme in a first step under "friendly" conditions and to study the influence of an increased noise level on the performance of the control scheme.

Table 6.2: Overview of adjusted reflection coefficients in experiments with combustion.

Actuator	multi-frequency tuning	discrete-frequency tuning
Woofers	$R_{\mathrm{cl}} = +1$, $\Delta l = 0\,\mathrm{m}$	–
Secs. 6.4.1	Figs. 6.17 – 6.20	–
	$R_{\mathrm{cl}} = +1$, $\Delta l = 0.5\,\mathrm{m}$, $2\,\mathrm{m}$	–
	Figs. 6.21 – 6.23	–
	$R_{\mathrm{cl}} = -1$, $\Delta l = 0.5\,\mathrm{m}$	–
	Figs. 6.24 and 6.25	–
	$R_{\mathrm{cl}} = -1$, $\Delta l = 0.5\,\mathrm{m}$, $0.75\,\mathrm{m}$ *	–
	Fig. 6.31	–
	$R_{\mathrm{cl}} = \pm 0.7$, $\Delta l = 0\,\mathrm{m}$, $0.5\,\mathrm{m}$	–
	Figs. 6.27 and 6.28	–
	$\lvert R_{\mathrm{cl}}\rvert = \lvert R_{\mathrm{ol}}\rvert$, $\Delta l = 0.5\,\mathrm{m}$ †	–
	Figs. 6.29 and 6.30	–
	$R_{\mathrm{cl}} = 0$	–
	Figs. 6.24 and 6.25	–
	$R_{\mathrm{cl}} = 0$ †	–
	Figs. 6.29 and 6.30	–
Proportional valves	$\lvert R_{\mathrm{cl}}\rvert = 1$ (72 Hz, 82 Hz)	$\lvert R_{\mathrm{cl}}\rvert = 1$
Sec. 6.4.2	Figs. 6.38 – 6.40	Figs. 6.42 – 6.44 (70 Hz, 85 Hz)
		Figs. 6.45 – 6.47 (175 Hz, 185 Hz)
	–	$\lvert R_{\mathrm{cl}}\rvert = 0 \ldots 1$ (175 Hz)
	–	Fig. 6.48
	–	$\lvert R_{\mathrm{cl}}\rvert = 0$ (165 Hz, 175 Hz, 185 Hz)
	–	Fig. 6.49
Ling Driver	–	$\lvert R_{\mathrm{cl}}\rvert = 1$, $\varphi_{\mathrm{cl}} = \varphi_{\mathrm{ol}}$ (78 Hz)
Sec. 6.4.3	–	Figs. 6.58 – 6.62
	–	$\lvert R_{\mathrm{cl}}\rvert = 1$, $\varphi_{\mathrm{cl}} = -\varphi_{\mathrm{us}}$ (72 Hz, 92 Hz)
	–	Figs. 6.63 – 6.65

6.3.1 Cold Acoustic Test Rig

The impedance tuning concept was first applied to the rather simple acoustic system without including area changes or a burner geometry (see Sec. 3.1.1). Control was possible in a broader frequency range as it was the case for the more complex system of the combustion test rig. In this section, the results are compared to the simulations. As the test rig could be equipped with an anechoic termination, the impedance tuning can also directly be compared to this passive solution.

Experiments were conducted without mean flow and with flow at a Mach number of 0.05 and a temperature of 310 K. Figure 6.4 shows the schematic setup. Seven 1/4" condenser microphones were installed at different axial positions. All microphones were used for frequency domain model identification but only three of them for time domain wave decomposition in the control scheme.

The uncontrolled reflection coefficients of the downstream end for both Mach numbers are

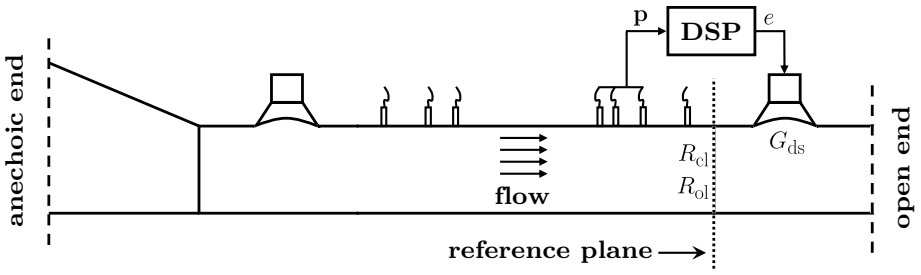

Figure 6.4: Schematical setup of impedance tuning concept at cold acoustic test rig.

shown in Fig. 6.5. They are scaled by a factor depending on the Mach number, according to the explanations given in Sec. 2.3. The time delays apparent in both phase responses

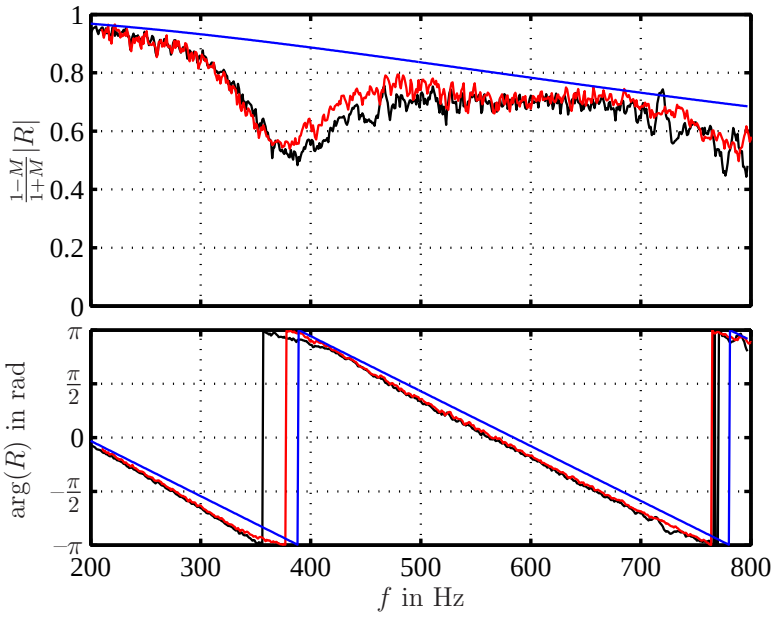

Figure 6.5: Reflection coefficient without mean flow (black) and with mean flow scaled by $(1+M)/(1-M)$ (red, $M = 0.05$). The theoretical result of Levine & Schwinger [105] (confer to Eq. (6.3)) is shown in blue. Top: magnitude, bottom: phase.

are due to the fact that the reference plane is located 0.4 m upstream of the actual duct outlet (Fig. 6.4). Although the duct was terminated by an unflanged open end, the magnitude of the reflection coefficient does not fully agree with the theoretical result from Levine & Schwinger [105] for the zero mean flow case (blue). They derived an expression for the theoretical magnitude of R:

$$|R_{\mathrm{LS}}| = \left(1 + \frac{1}{6}He^4\left(\log\frac{1}{He} + 1.00613\right)\right) e^{-He^2/2}. \tag{6.3}$$

Here, He is the Helmholtz number, which is defined as

$$He = \frac{kd}{2} = \frac{\pi f d}{\bar{c}}, \tag{6.4}$$

where d is the duct diameter. Up to $He = 1$, which for a given geometry and speed of sound poses a limit for the frequency, Eq. (6.3) deviates less than 3% from the exact value.
As the loudspeaker was located downstream of the reference plane, its influence is comprised in the reflection coefficients plotted in Fig. 6.5. The largest deviation occurs at approximately 380 Hz. This is because the loudspeaker was mounted to the main duct via a side channel with a $\lambda/4$-frequency of about 380 Hz. In Fig. 6.6, the loudspeaker transfer functions are depicted. Around the side channel's resonance frequency, the impact of the mean flow on the actuator transfer function is also largest. With mean flow (red), the amplification of the transfer function is weaker. Though somewhat more moderate, this behaviour can also be observed for the reflection coefficients in Fig. 6.5. Regarding the phases

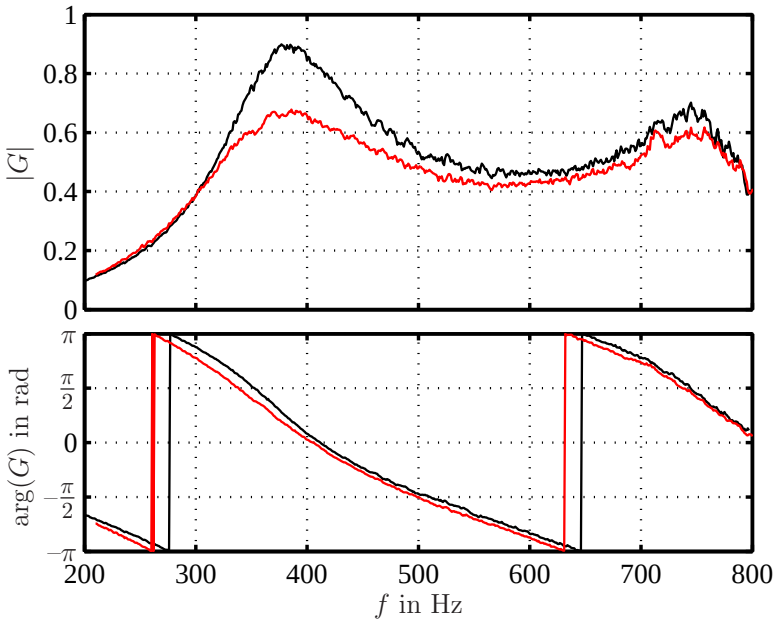

Figure 6.6: Loudspeaker transfer function without (black) and with (red, $M = 0.05$) mean flow. Top: magnitude, bottom: phase.

of the uncontrolled reflection coefficients, shown in Fig. 6.5 (bottom), the correspondence between measurement (red and black) and analytical results (blue) is very good. For an open end, a length correction has to be added to the physical length of the duct accounting for the air volume fluctuating outside of the duct. Levine & Schwinger [105] determined this correction to be

$$l_{\text{corr}} = 0.6133\frac{d}{2}. \tag{6.5}$$

If the end-correction is added to the distance between reference plane and open end, this perfectly agrees to the length represented by the slope of the measured phase response in Fig. 6.5.
As the loudspeakers used for these experiments were rather small, it was not possible to change the acoustic boundary conditions of the test rig at frequencies below 200 Hz. Below the resonance frequency of the system loudspeaker/side tube, the speaker transfer function sharply decreases, as can be seen in Fig. 6.6.
It may be desirable to model the open-loop reflection coefficient and/or the actuator transfer

function analytically to be able to design the controller completely a priori. For loudspeakers, such analytical models were, for instance, derived by Venugopal & Bernstein [226] or Pota & Kelkar [171]. However, to achieve a reasonable result, R_{ol} and K have to be known quite accurately, and it seems doubtful that a completely theoretical model will suffice, except for the simplest configurations. Especially when different actuators than loudspeakers are used and the test rig geometries are complex, this will not be possible.

Anechoic end

Results for the case of an imposed anechoic end, i.e., $R_{\mathrm{cl}} = 0$, are shown in Fig. 6.7 for both Mach numbers. The experimentally obtained magnitudes are slightly higher when com-

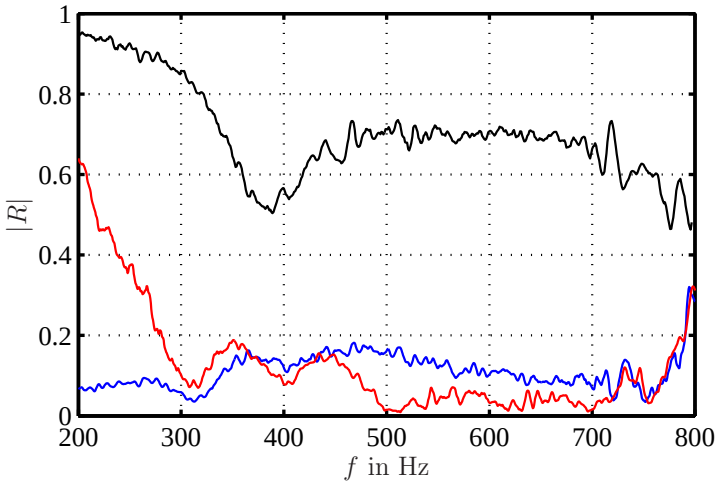

Figure 6.7: Control results for a desired anechoic end. Magnitudes of the uncontrolled (black) and the closed-loop reflection coefficients without (blue) and with (red, $M = 0.05$) mean flow.

pared to the simulation results. Without mean flow (blue), $|R|$ remains below 0.2 in the considered frequency range. The reflection coefficient obtained with mean flow (red curve) is lower than the one without flow, except for frequencies below 350 Hz. Here, the controller was actually only required to operate above 300 Hz. For frequencies above 500 Hz, the reflection coefficient is as low as the one obtained from the simulation both being around 0.03.

The increase for low frequencies stems from the fact that the loudspeaker's response deteriorates (see Fig. 6.6). Also, the controller transfer function has a high gain (Eq. (5.4)) and, therefore, the absolute error of the model grows quickly, as can be seen in Fig. 6.8. Two reasons are responsible for this: i) the uncontrolled reflection coefficient increases for lower frequencies and ii) the control authority of the speaker that was used deteriorates for smaller frequencies. Better results could certainly be obtained by using a woofer with a higher response at low frequencies. However, the intermediate conclusion is that the impedance control scheme successfully managed to tune an almost fully reflecting boundary with a pressure node to an anechoic end.

Technically realizable anechoic terminations manufactured by a diverging channel equipped with resonators and damping materials exhibit reflection coefficients around 0.2 for frequencies above 100 Hz, sharply increasing with decreasing frequency [45, 78]. A comparison with an anechoic termination mounted at the downstream end of the cold acoustic test rig is

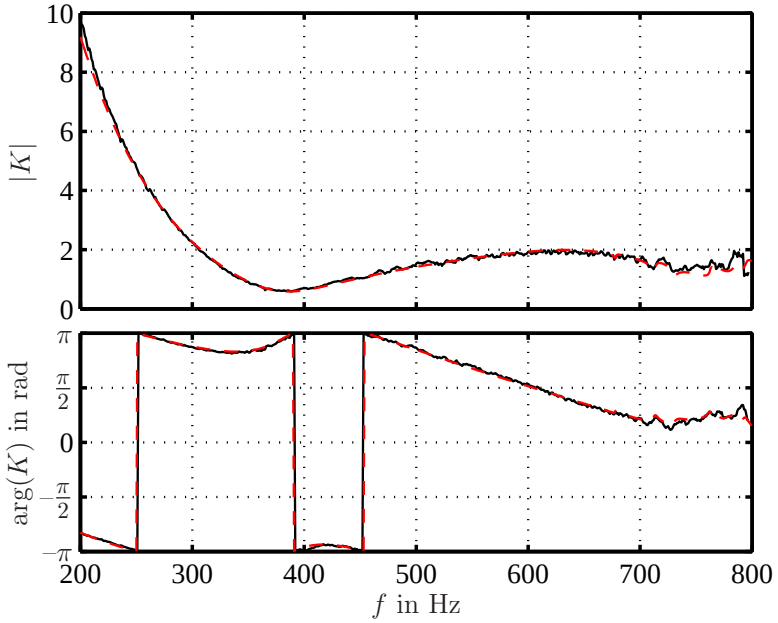

Figure 6.8: Controller transfer function to mimic an anechoic end computed from Eq. (5.4) with experimental open-loop reflection coefficient and actuator transfer function; discrete data (black) and identified model (red dashed) are plotted. Top: magnitude, bottom: phase.

shown in Fig. 6.9. Except for frequencies around 500 Hz, the magnitudes of the reflection

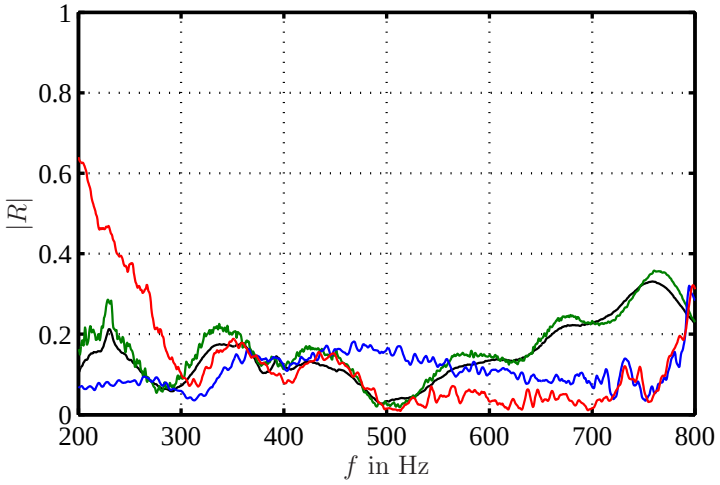

Figure 6.9: Comparison of magnitudes of actively adjusted reflection coefficients (without mean flow (blue) and with $M = 0.05$ (red)) and mounted anechoic end (without mean flow (black) and with $M = 0.05$ (green)).

coefficients for the anechoic case adjusted by the control scheme (blue and red) are smaller than the ones of typical anechoic hardware terminations (black and green). Passive anechoic terminations cannot damp low-frequency acoustic waves unless their dimensions are very large. As will be seen in the next paragraph, this does not pose a problem for the impedance tuning approach when appropriate woofers are used. Using the control concept,

anechoic terminations could be generated with a fraction of the space needed for the passive solution. Also, the active approach could be of great value in vent systems that suffer from high noise levels, as in these devices space is at a premium. By actively adjusting low reflecting ends, this issue could be overcome.

Fully reflecting boundary and virtual length

In a next step, the control scheme was used to generate fully reflecting terminations. Figures 6.10 and 6.11 present results for imposed pressure and velocity nodes, respectively. Here, the nodes were assumed to be located at the axial position of the open end – not at

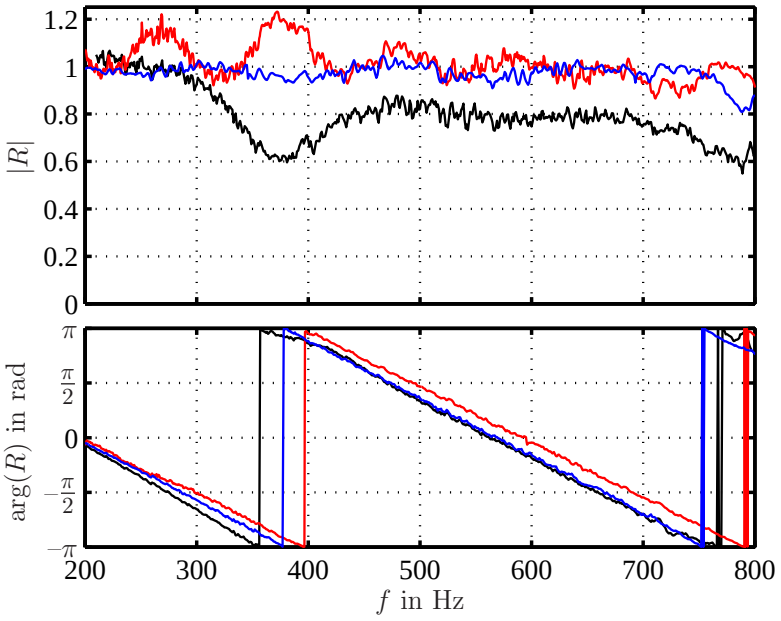

Figure 6.10: Boundary condition tuned to fully reflecting $R_{\mathrm{cl}} = -1$ without additional virtual length; uncontrolled (black), without (blue) and with (red, $M = 0.05$) mean flow. Top: magnitude, bottom: phase.

the reference plane (see Fig. 6.4). When $R_{\mathrm{cl}} = \mp 1$ is mentioned in the following, this refers to a pressure/velocity node at the duct end. The phase of R_{cl} was then required to have a phase lag corresponding to the propagation time from the reference plane to the duct end and back.

In Fig. 6.10, results for an imposed pressure node are presented. For the case without mean flow (blue curve), the control objective is almost exactly achieved. Over the whole frequency range considered, the reflection coefficient magnitude deviates less than 5% from the desired value, except close to 800 Hz. With mean flow (red), the results are almost as good as in the no flow case. Overall, the control scheme manages to establish a pressure node, however, around 260 and 380 Hz, $|R|$ reaches values of up to 1.2. Less successful results at 380 Hz are probably due to resonance effects in the speaker side channel. Presumably, a small deviation in the controller model or the wave decomposition of the microphone signals was present, which was amplified by resonance effects.

Results for an imposed sound hard end are shown in Fig. 6.11. In addition to a velocity node, the phase of R_{cl} was adjusted to mimic a duct elongated by 1.3 m, as was done before in the simulation (see Fig. 6.3). The magnitudes of the reflection coefficients achieved

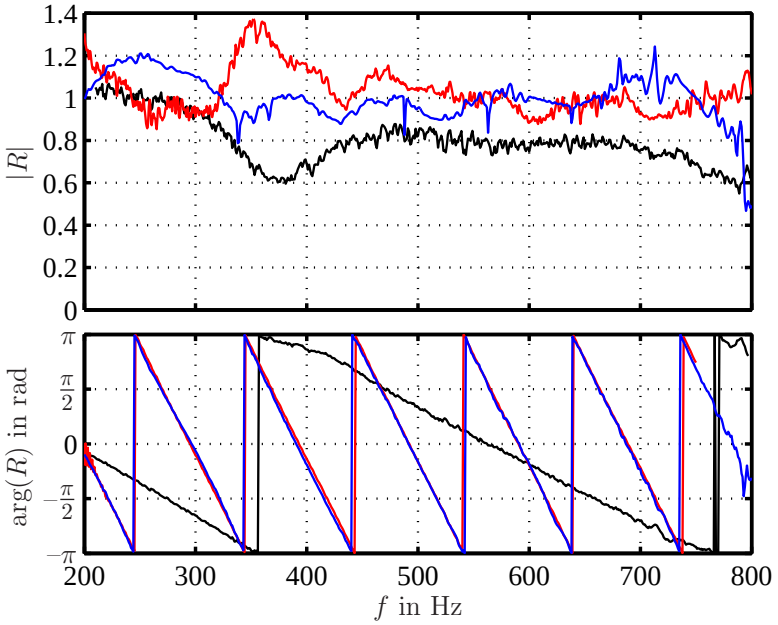

Figure 6.11: Boundary condition tuned to fully reflecting $R_{\mathrm{cl}} = +1$. The phase of the reflection coefficient was additionally tuned so as to mimic an additional length of 1.3 m; uncontrolled (black), without (blue), and with (red, $M = 0.05$) mean flow. Top: magnitude, bottom: phase.

does not compare as well to the simulated results as in the case of a pressure node. This is reasonable since the uncontrolled boundary condition more closely resembles a pressure node. Consequently, the control scheme and the actuator had to perform less when mimicking a sound soft termination. This again is in correspondence with the simulation results. However, good results are obtained at all frequencies except for the resonance frequency of the laterally mounted speaker ducts. Also, the phase with the additional delay simulating an acoustically longer tube is well established. This is a particularly important case that can be used to generate resonance frequencies different from those imposed by the actual geometry.

Pressure spectra for the uncontrolled case (black), a simulated pressure node (red), and a velocity node with an additional virtual length of 1.3 m (blue) are presented in Fig. 6.12. As expected, the results for the uncontrolled case and the closed-loop reflection coefficient of -1 are quite similar. It can be noted, however, that the nodes were more pronounced in case of the simulated fully reflecting boundary. This can be attributed to the fact that for the uncontrolled case the magnitude of the reflection coefficient is somewhat smaller than the one in presence of control (Fig. 6.10). For the imposed elongated duct end, the number of nodes and lobes increases due to an increased total length of the system. The lobes represent the duct's resonance frequencies. These does not take the form of sharp peaks, as the upstream end was still low reflecting.

Different levels of reflection

To show that different levels of reflection can be realized using the control scheme, a second low-reflecting end was mounted at the downstream boundary. When doing so, different levels of reflection can be established by introducing a factor α into the expression for the

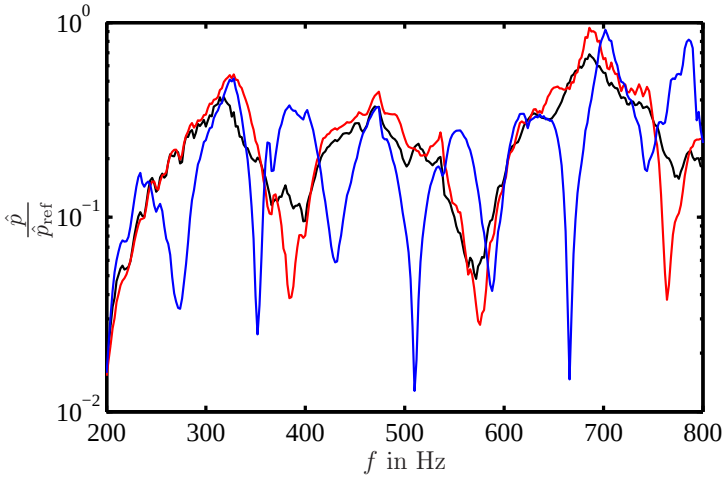

Figure 6.12: Pressure spectra in the duct for the uncontrolled case (black), an imposed pressure node (red), and an imposed velocity node with a virtual length of 1.3 m (blue) – without mean flow.

control law

$$K = \alpha \frac{R_{\mathrm{cl}} - R_{\mathrm{ol}}}{G}, \tag{6.6}$$

where R_{cl} corresponds to a pressure node at the duct exit, and α takes values between 0 and 1. Results for $\alpha = 0, 0.2, ..., 1$ are presented in the top frame of Fig. 6.13. The reflection coefficient's magnitude for the uncontrolled case corresponds to the lowest curve (purple). With increasing α, the reflection coefficient's magnitude gradually increases. If the open-loop reflection coefficient was equal to zero, the magnitude of R_{cl} would correspond to α. As this is not the case and $|R_{\mathrm{ol}}|$ starts to increase for frequencies above 500 Hz (see Fig. 6.9), $|R_{\mathrm{cl}}|$ slightly varies with frequency. However, the level of reflection can be set as desired. Pressure spectra corresponding to the different values of α are shown in the bottom frame of Fig. 6.13. For strong levels of reflection, distinct pressure nodes and frequencies with large response are visible. For smaller values of α, i.e., less reflection, nodes and lobes vanish, and the pressure spectrum becomes more flat, corresponding to the pure propagating wave. Note that even for $\alpha = 1$, no sharp resonance peaks are observable since the upstream end is low-reflecting.

Imposing different levels of reflection at the outlet of a combustion chamber is a useful method to study thermoacoustic instabilities in premixed combustors. Since stability and oscillation amplitude strongly depend on the degree of reflectivity, a controlled transition from stable to unstable conditions can be invoked with the method presented. This is described in detail in Chapter 7.

6.3.2 Combustion Test Rig

In the next step, the control scheme was applied to the combustion test rig in presence of an isothermal flow. The air mass flow was set to 60 g/s, corresponding to $M < 0.01$ in the measurement section. Figure 6.14 shows the uncontrolled downstream reflection coefficient

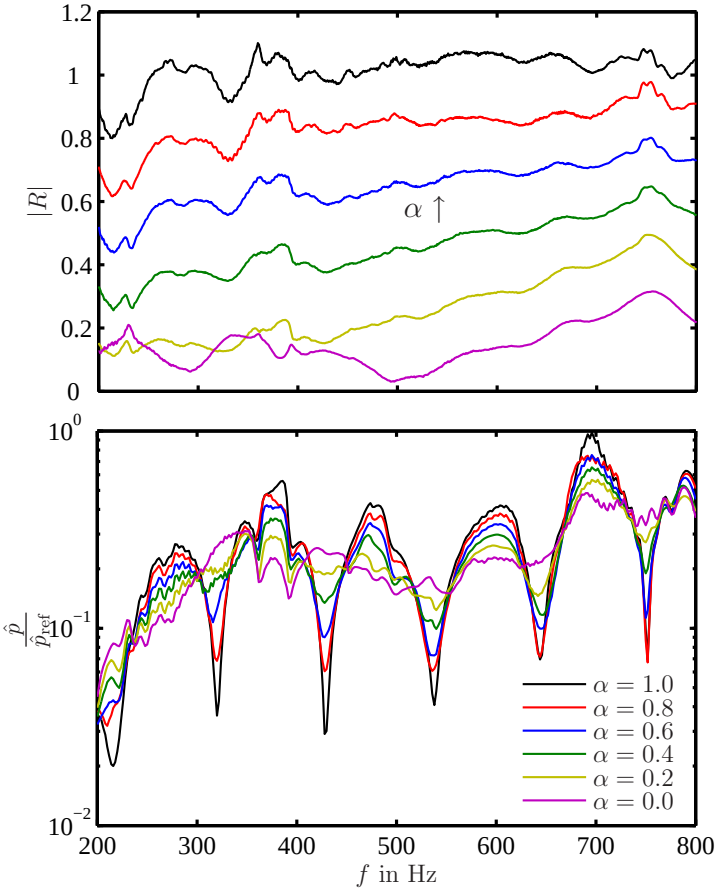

Figure 6.13: Increasing levels of reflection, realized with a low-reflecting end mounted. Top: reflection coefficient magnitude. Bottom: sound pressure spectrum in the duct.

(black) with an orifice plate mounted. It exhibits only slight reflection at frequencies below 300 Hz. Therefore, the pressure spectrum in Fig. 6.15 shows no distinct resonance peaks. The test rig was excited with the upstream mounted woofer driven by a frequency sweep, ranging from 30 Hz to 500 Hz. First, a non-reflecting boundary condition ($R_{\mathrm{cl}} = 0$) was simulated. The green curves in Figs. 6.14 and 6.15 show the results for this case. The magnitude of the reflection coefficient is reduced to values below 0.1 and in the range of 100 Hz to 350 Hz even below 0.02, which is considerably lower than the reflection coefficient of technically realizable anechoic terminations [45, 78] (see also previous paragraph).
The system was also adjusted to fully reflecting conditions as opposed to perfectly absorbing conditions in the case of $R_{\mathrm{cl}} = 0$. For convenience, the two cases are denoted as $R_{\mathrm{cl}} = -1$ and $R_{\mathrm{cl}} = +1$ in the following. The graphs shown in Fig. 6.14 prove that both cases were realized with high accuracy (red and blue curves, respectively). The magnitude of both reflection coefficients is between 0.9 and 1.1 over the whole controlled frequency interval. The constant difference of π between the adjusted acoustically soft and acoustically hard end is clearly visible in the phase plot for all frequencies.
To show that the rig can be tuned to desired resonance frequencies, an additional length of 0.5 m was simulated. The actual test rig has an effective length of 2 m (including the end correction). Table 6.3 shows the calculated resonance frequencies of a 2.5 m long duct with an acoustically hard boundary at its upstream end and an acoustically soft, respectively

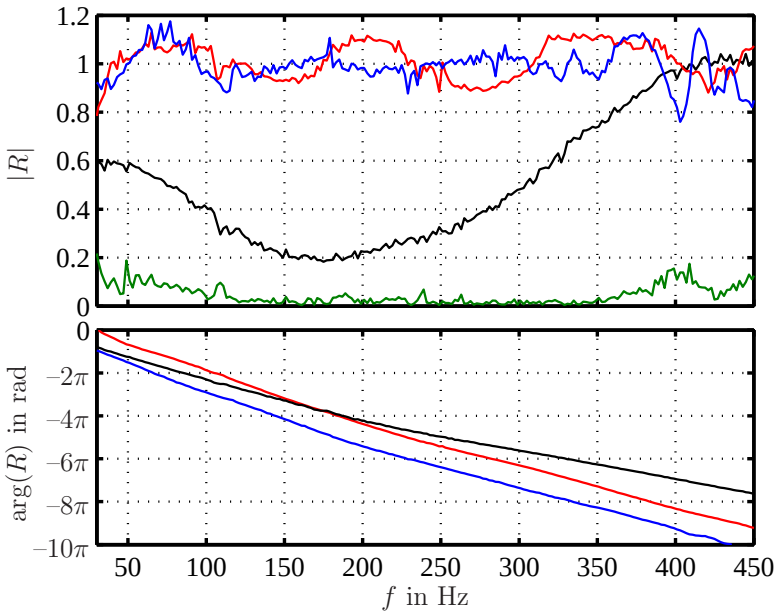

Figure 6.14: Downstream reflection coefficient for the baseline case without control (black), $R_{\mathrm{cl}} = 0$ (green), $R_{\mathrm{cl}} = +1$ with additional length $\Delta l = 0.5\,\mathrm{m}$ (red), and $R_{\mathrm{cl}} = -1$ with additional length $\Delta l = 0.5\,\mathrm{m}$ (blue); non-reacting flow. Top: magnitude, bottom: phase.

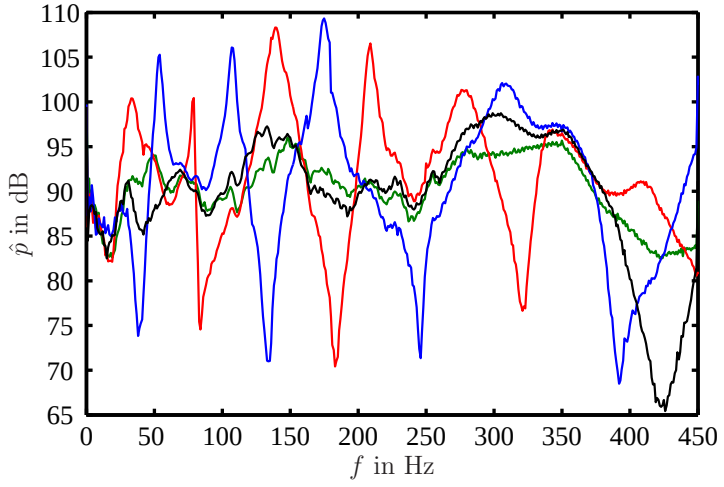

Figure 6.15: Spectra of acoustic pressure for the baseline case without control (black), $R_{\mathrm{cl}} = 0$ (green), $R_{\mathrm{cl}} = +1$ with additional length $\Delta l = 0.5\,\mathrm{m}$ (red), and $R_{\mathrm{cl}} = -1$ with additional length $\Delta l = 0.5\,\mathrm{m}$ (blue); non-reacting flow.

acoustically hard, boundary at its downstream end. These frequencies are compared to the

Table 6.3: Resonance frequencies in Hz of a 2.5 m long duct with acoustically hard end upstream and acoustically hard ($R_{\mathrm{cl}} = +1$), respectively acoustically soft ($R_{\mathrm{cl}} = -1$), boundary at its downstream end.

n	$\hat{u} = 0$, ($R_{\mathrm{cl}} = +1$)		$\hat{p} = 0$, ($R_{\mathrm{cl}} = -1$)	
	calculation	experiment	calculation	experiment
1	69.2	78.5	39.4	54
2	138.4	138.5	103.8	107.5
3	207.6	209	173	175
4	276.8	276	242.2	-
5	346	347	311.4	308.5
6	415.2	410	380.6	-
7	484.4	484.5	449.8	452.5

resonances found in the experiments (see Fig. 6.15). If both boundaries of the duct are acoustically hard ($\hat{u} = 0$), the resonance frequencies are given by

$$f = \frac{n\bar{c}}{2l}. \tag{6.7}$$

For an acoustically soft downstream end ($\hat{p} = 0$), the resonance frequencies are defined by

$$f = \frac{(2n-1)\bar{c}}{4l}. \tag{6.8}$$

Here, n is an integer ($n = 1, 2, ...$) and l is the duct length. The frequencies were calculated for a speed of sound of 346 m/s corresponding to the measured air temperature in the duct. Comparing the calculated resonance frequencies with the ones obtained from the experiments (Fig. 6.15 and Tab. 6.3) proves the feasibility of the proposed scheme. Except for $n = 1$, the maximum deviation between theory and experiments is less than 1%. For the acoustically soft downstream end, two resonance frequencies, at 242.2 Hz and 380.6 Hz, are not observed in the experiments. This is due to pressure nodes at the reference location.

6.4 Reactive Flow

This section is subdivided into three parts that show results for the different actuators and closes with a comparison of them. First, results obtained with woofers are presented. Thereafter, those of the proportional valves and the Ling Driver are shown. For the Ling Driver, the control scheme must be extended to account for its non-linear response characteristics. The modifications needed are explained in Sec. 6.4.3.
In Sec. 3.3.3 it was explained that the OH*-chemiluminescence is a qualitative indicator for heat release fluctuations. Whenever it is referred to heat release fluctuations in the text

or the graphs, this corresponds to fluctuations of the OH-radical. Since only the qualitative behaviour of heat release fluctuations is sought to be assessed, this is entirely sufficient.

6.4.1 Woofers

In Fig. 6.16, the woofer casings can be seen mounted at the downstream end of the test rig. For the experiments, the test rig was operated in lean-premixed mode using natural gas with an equivalence ratio of $\phi = 0.65$ at a thermal power of 110 kW. The flow entering

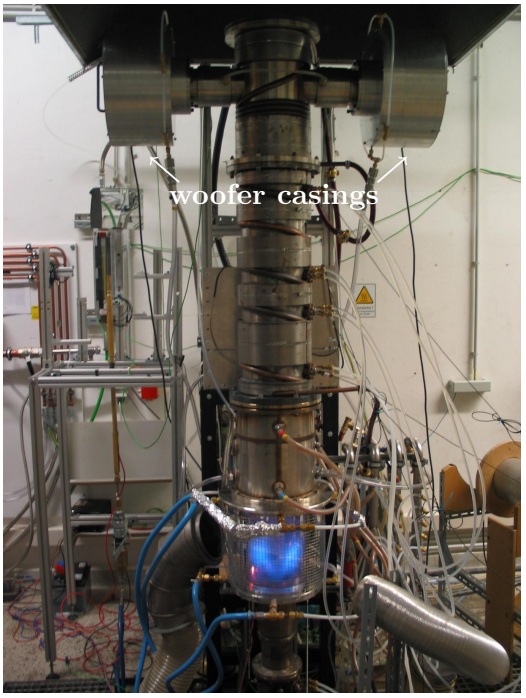

Figure 6.16: Combustion test rig equipped with woofers at its downstream end.

the combustion chamber was not preheated. Two different end configurations of the downstream termination were used. One was an open end, thus, generating a pressure node at the downstream exit. In the other case, the test rig was equipped with an orifice. With this configuration it is possible to produce a relatively small magnitude of the reflection coefficient as explained in Sec. 3.1.2. If the combustion system exhibits strong pressure oscillations, as it is the case for the open end, the modification of the reflection coefficient is more intricate. This is most probably due to the fact that the uncontrolled system is in a limit-cycling state and even slight inaccuracies in the controller identification or an unwanted saturation of the control signal may hinder successful control. In this case, the system is prone to stay in its limit-cycle. Additionally, the controller identification is also more difficult. Therefore, if not explicitly mentioned in the following, the controller was applied to the configuration with orifice and its transfer function, defined by Eq. (5.4), was identified for frequencies between 70 Hz and 300 Hz. At the end of this section and in Sec. 7.1, results for tuning an initially unstable system are reported showing control to be

possible for selected cases.
In Fig. 6.17, the acoustic pressure spectra for the two configurations without control are shown. For the open-end case (green), distinct peaks at 82 Hz and its multiples can be

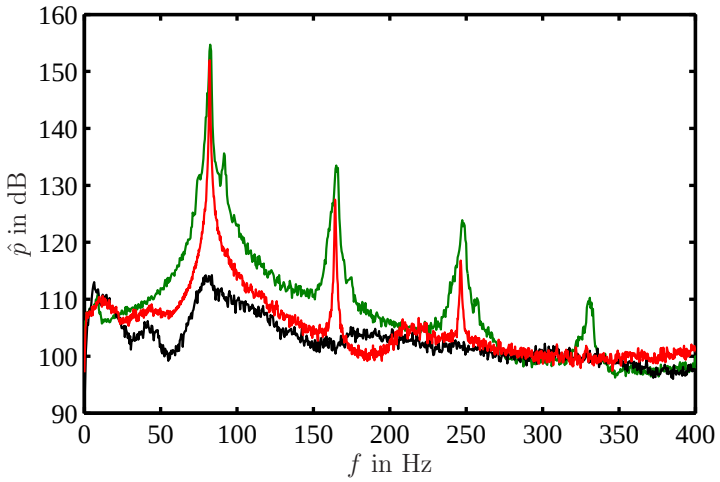

Figure 6.17: Spectra of acoustic pressure for the baseline case without control (with orifice, black – without orifice, green) and $R_{\mathrm{cl}} = +1$ with $\Delta l = 0\,\mathrm{m}$ (red); reacting flow.

observed, representing the $\lambda/4$-mode of the rig. The effect of the orifice can clearly be seen (black). No strong pressure oscillations are present in the spectra anymore as the combustion process was stabilized by increasing the loss of acoustic energy across the downstream boundary. Installation of the orifice results in a peak amplitude reduction from 153 dB to 111 dB, i.e., a reduction to less than 1% of the pressure amplitude for the open end. The standing wave pattern is not visible anymore, thus, indicating that mainly propagating acoustic waves are present, which is the case for a low-reflecting boundary.
Figure 6.18 depicts the reflection coefficients for these two configurations. For the open end (green curve) the reflection coefficient is similar to the one described by the formula of Levine & Schwinger [105] for long wave-lengths. With the orifice mounted, $|R|$ is decreased to values around 0.3.
Using the impedance tuning concept, the reflection coefficient was changed to fully reflecting conditions ($|R_{\mathrm{cl}}| = 1$):

$$R_{\mathrm{cl}} = +1 \cdot e^{\mathrm{i}(\arg(R_{\mathrm{ol}}) - \omega 2\Delta l/\bar{c})}. \tag{6.9}$$

Different virtual lengths were simulated by adding an additional length Δl to the phase of R_{cl}.
At first, the controller was used to generate an instability at 82 Hz corresponding to the frequency of the $\lambda/4$-mode of the open end. As shown in the phase plots of Fig. 6.18, the reflection coefficients' phases of both uncontrolled cases are almost identical at the instability frequency. Therefore, the controller transfer function was calculated to produce $|R_{\mathrm{cl}}| = 1$ without changing the phase of the uncontrolled R_{ol} (i.e., $\Delta l = 0\,\mathrm{m}$). The red curve shows the result for this case. Distinct peaks at 82 Hz and its multiples can be observed in Fig. 6.17, proving that the anechoic end was virtually tuned to one with a higher reflection coefficient. Note that the test rig was not additionally excited by the upstream loudspeaker for all spectra shown. The spectral peak amplitude is 150 dB, 3 dB less than

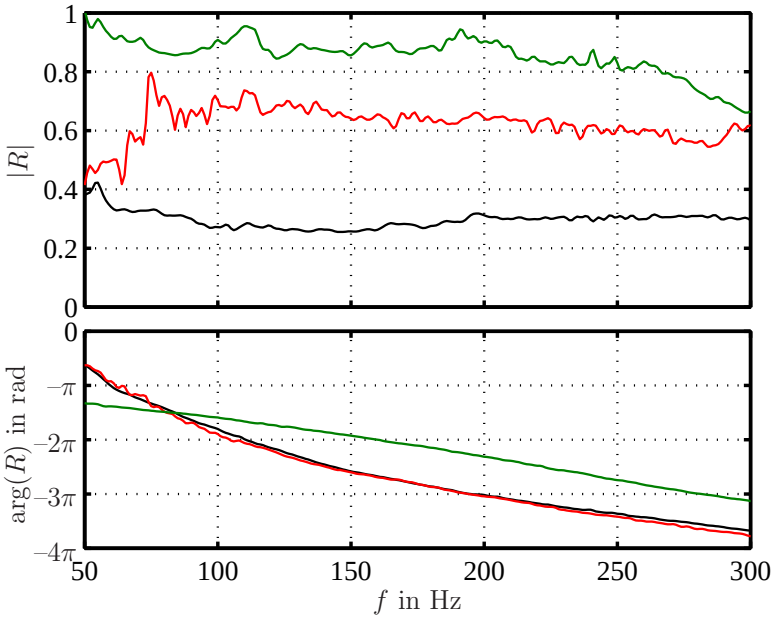

Figure 6.18: Downstream reflection coefficient for the baseline case without control (with orifice, black – without orifice, green) and $R_{\mathrm{cl}} = +1$ with $\Delta l = 0\,\mathrm{m}$ (red); reacting flow. Top: magnitude, bottom: phase.

in the uncontrolled case without orifice.
Figure 6.19 shows the impact of the generated acoustic field on the heat release fluctuation. Here, the scaled OH*-chemiluminescence signals for the two uncontrolled cases (black and

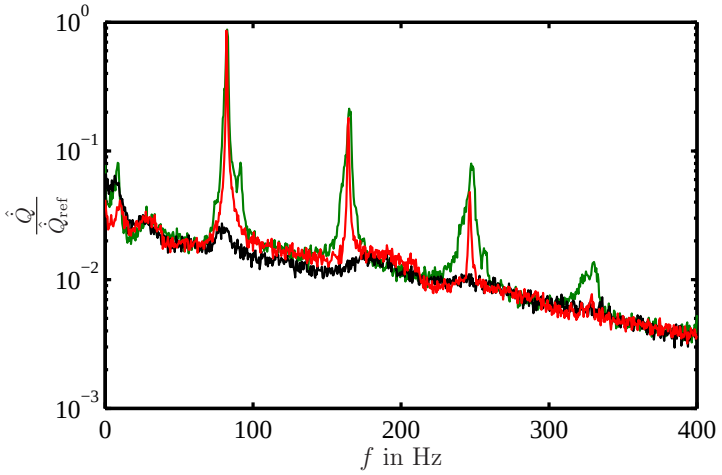

Figure 6.19: Spectra of OH*-chemiluminescence for the baseline case without control (with orifice, black – without orifice, green) and $R_{\mathrm{cl}} = +1$ with $\Delta l = 0\,\mathrm{m}$ (red).

green) and the one for $|R_{\mathrm{cl}}| = 1$ with $\Delta l = 0\,\mathrm{m}$ (red) are depicted. A behaviour similar to the one of the pressure fluctuations in Fig. 6.17 can be observed. Large heat release fluctuations occur at the instability frequency of 82 Hz (open end, green), whereas no peaks are visible for the anechoic termination without control (black). In case of control (red), the effect of the thermoacoustic behaviour is the same as for the open end without control. Figure 6.20 depicts the phase portrait of the pressure fluctuation. The time-delay phase

portrait is a convenient means to visualize the properties of dynamical systems. In the

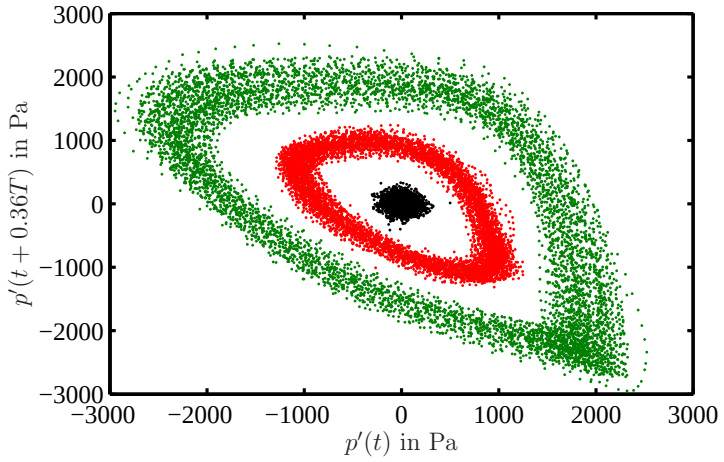

Figure 6.20: Phase portrait of acoustic pressure for the baseline case without control (with orifice, black – without orifice, green) and $R_{\mathrm{cl}} = +1$ with $\Delta l = 0\,\mathrm{m}$ (red); reacting flow.

phase portrait shown here, the unsteady acoustic pressures at time t and $t + \Delta t$ are plotted against each other. The time-delay Δt has been set to $0.36\,T$, T being the period of the main instability frequency. The choice of Δt is somewhat arbitrary and orientated to the one chosen in [113]. Choosing a different time-delay would yield similar results. A system which oscillates at one single frequency (limit-cycle) has an elliptic orbit. If harmonics occur, this elliptic shape will be distorted. The presence of noise causes the orbit to become fuzzy, i.e., the orbit changes slightly from cycle to cycle. If the system is stable and only forced by noise, it will be concentrated around one point. Lieuwen [113] and Rowley et al. [181] investigated this visualization method in detail.

For the uncontrolled case (open end), the phase portrait of the pressure shows the characteristic noisy limit-cycle (Fig. 6.20 green orbit). With orifice mounted, the system is only driven by noise (confer also to Fig. 1.3 and its description). In this case, the pressure fluctuations are scattered around the origin (black). For the controlled case, the system is pushed to an orbit (red), proving that it is in a limit-cycling state. However, this orbit is smaller than in the uncontrolled case without orifice. The difference between the orbit radii is larger than that of the peak amplitudes at 82 Hz (3 dB, i.e., a factor of $\sqrt{2}$, Fig. 6.17). This is due to the fact that in the uncontrolled case the system exhibits slight variations in the oscillation frequency. Generally, a highly unsteady combustion process causes cycle-to-cycle variations and thus the oscillation frequency to fluctuate around its main oscillation frequency. The peak in the spectrum is much broader, as can be seen in Fig. 6.17. Additionally, in case of no control, the orbit is more scattered as the overall noise level was higher.

Regarding the phases of the reflection coefficients (Fig. 6.18 bottom), it can be stated that they are equal for the case of control (red) and the uncontrolled case (black), as prescribed. The magnitude of the measured reflection coefficient, however, is between 0.6 and 0.7, thus, differing from the desired value of $|R_{\mathrm{cl}}| = 1$. This is due to the fact that the output calculated by the controller had to be restricted to 70% of the actual value, as otherwise the woofers' amplifiers went into saturation. Hence, the saturation is not system-inherent

compared to the uncontrolled case without orifice, in which the nonlinear saturation can be attributed to the flame response. Here, the actuator power is the limiting factor.
In a next step, the test rig length was virtually extended by manipulation of the reflection coefficient's phase. Consequently, the instability peak is shifted to lower frequencies. The blue and red curves in Fig. 6.21 show the pressure spectra for additional lengths of $\Delta l = 0.5\,\mathrm{m}$ and $\Delta l = 2\,\mathrm{m}$, shifting the pressure peaks to 79 Hz and 66 Hz, respectively. The

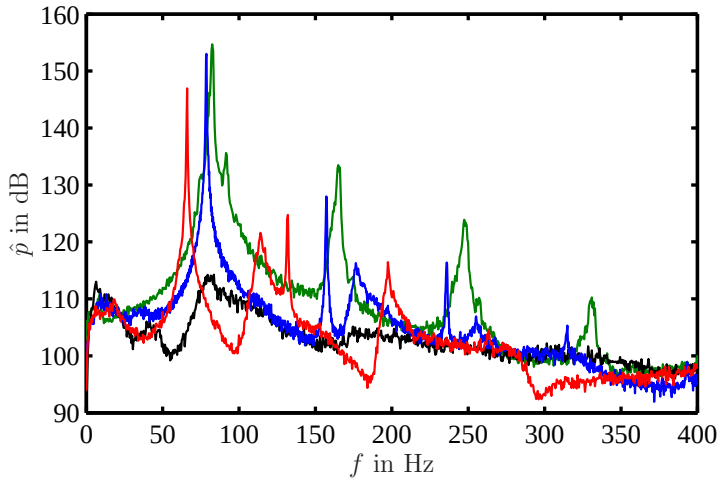

Figure 6.21: Spectra of acoustic pressure for the baseline case without control (with orifice, black – without orifice, green), $R_{\mathrm{cl}} = +1$ with $\Delta l = 0.5\,\mathrm{m}$ (blue), and $R_{\mathrm{cl}} = +1$ with $\Delta l = 2\,\mathrm{m}$ (red); reacting flow.

same holds for the heat release fluctuations depicted in Fig. 6.22. Virtually extending the

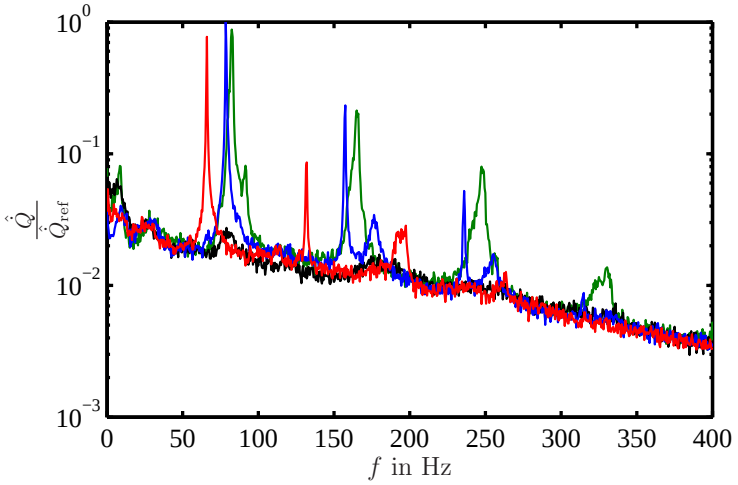

Figure 6.22: Spectra of OH*-chemiluminescence for the baseline case without control (with orifice, black – without orifice, green), $R_{\mathrm{cl}} = +1$ with $\Delta l = 0.5\,\mathrm{m}$ (blue), and $R_{\mathrm{cl}} = +1$ with $\Delta l = 2\,\mathrm{m}$ (red).

test rig length results in a larger slope of the reflection coefficient's phase as the propagation time of, and thus the time-delay between, the incident and the reflected wave becomes larger (blue and red curves in Fig. 6.23).
If the phase decrease $\partial\varphi/\partial f$ is merely associated with a time-delay, the adjusted additional length Δl can easily be calculated from the phase of the measured reflection coefficient.

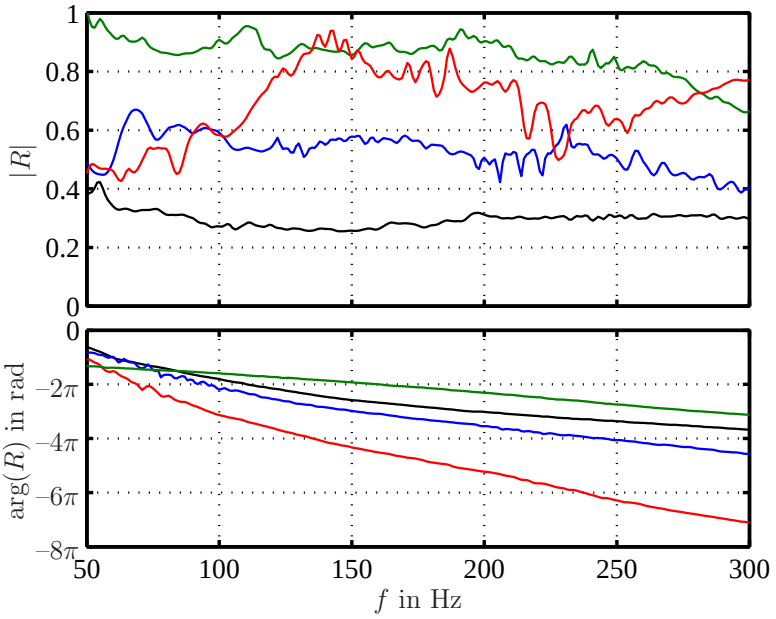

Figure 6.23: Downstream reflection coefficient for the baseline case without control (with orifice, black – without orifice, green), $R_{\mathrm{cl}} = +1$ with $\Delta l = 0.5\,\mathrm{m}$ (blue), and $R_{\mathrm{cl}} = +1$ with $\Delta l = 2\,\mathrm{m}$ (red); reacting flow. Top: magnitude, bottom: phase.

Using

$$\Delta l = -\frac{1}{4\pi\bar{c}}\frac{\Delta\left(\varphi_{\mathrm{cl}} - \varphi_{\mathrm{ol}}\right)}{\Delta f} \tag{6.10}$$

yields this length, because the difference of φ_{cl} and φ_{ol} is only related to the prescribed additional length. For both virtual extensions, the phase difference matches perfectly the prescribed difference in length.

Apparently, imposing a fully reflecting boundary results in an unstable system. By manipulating the phase of the downstream reflection coefficient, the frequency of oscillation can be adjusted. Regarding the magnitudes of the downstream reflection coefficient for the controlled cases (red and blue curves in Fig. 6.18 and Fig. 6.23), it must be noted that they all differ from the prescribed value of $|R_{\mathrm{cl}}| = 1$ due to limited actuator power. However, as evident in the spectra of all controlled cases (Fig. 6.17 and Fig. 6.21), the peaks are generated at the desired frequencies nonetheless. If actuators with sufficient acoustic power were available, the desired impedances could exactly be imposed, even for the case of an unstable system with high oscillation amplitudes. Validity of this statement is verified in the following sections.

In contrast to the previously imposed reflection coefficient of $R_{\mathrm{cl}} = \mathbf{+1} \cdot \exp(\mathrm{i}\arg(R_{\mathrm{ol}}) - \mathrm{i}\omega 2\Delta l/\bar{c})$, the controller was then used to generate $R_{\mathrm{cl}} = \mathbf{-1} \cdot \exp(\mathrm{i}\arg(R_{\mathrm{ol}}) - \mathrm{i}\omega 2\Delta l/\bar{c})$ with different lengths Δl. Note that unlike the results shown in the cold flow section, here the phase of the uncontrolled R_{ol} is considered in the prescribed reflection coefficients, too (confer to Eq. (6.9)). Since this phase cannot be related to an open- or closed end, $R_{\mathrm{cl}} = \pm 1$ cannot be referred to as acoustically hard and acoustically soft. In Figs. 6.24 and 6.25, the results for these cases are depicted. The reference configuration with orifice and without control is again plotted in black. For $R_{\mathrm{cl}} = -1$ (red) and $R_{\mathrm{cl}} = +1$ (blue), Δl is

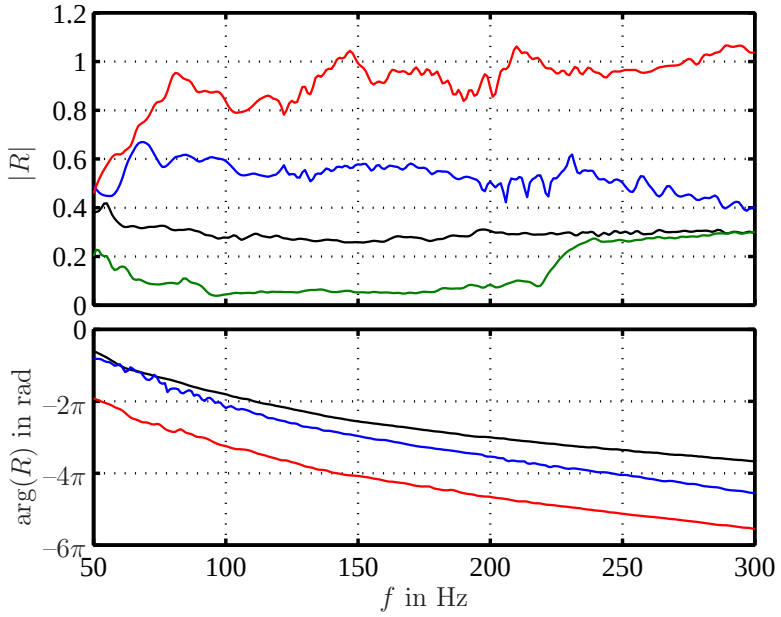

Figure 6.24: Downstream reflection coefficient for the baseline case without control (with orifice, black), $R_{\mathrm{cl}} = +1$ with $\Delta l = 0.5\,\mathrm{m}$ (blue), $R_{\mathrm{cl}} = -1$ with $\Delta l = 0.5\,\mathrm{m}$ (red), and $R_{\mathrm{cl}} = 0$ (green); reacting flow. Top: magnitude, bottom: phase.

0.5 m. Here and in the following, the phase of R_{ol} (see Eq. (6.9)) is not explicitly indicated but has to be considered nonetheless. Both phase plots (Fig. 6.24 bottom) display the characteristic larger slope of an extended duct. The constant difference of π between them corresponds to the difference in the signs of the imposed reflection coefficients. Note that in case of $R_{\mathrm{cl}} = -1$, it was possible to adjust a controller gain of 1 without getting into loudspeaker saturation. Therefore, the magnitude of the actually imposed reflection coefficient for $R_{\mathrm{cl}} = -1$ is close to 1, whereas the one for $R_{\mathrm{cl}} = +1$ is 0.6, as seen previously.
In addition, an anechoic boundary condition was imposed ($R_{\mathrm{cl}} = 0$, green). Here, the controller transfer function was only identified up to 220 Hz. In this frequency range, the magnitude of R is decreased to values around 0.05, which is as good as in the cold flow case.
Pressure spectra for the cases described above are shown in Fig. 6.25. With R_{cl} set to -1 and $\Delta l = 0.5\,\mathrm{m}$, two pressure peaks can be observed at 55 Hz and 110 Hz. For $R_{\mathrm{cl}} = 0$ (green), the spectra of the uncontrolled and controlled case are almost the same, due to the fact that the orifice already produced a low-reflecting end.
A question possibly arising when comparing the spectra of $R_{\mathrm{cl}} = +1$ and $R_{\mathrm{cl}} = -1$ in Fig. 6.25 with their corresponding downstream reflection coefficients in Fig. 6.24 is, why the pressure fluctuations for $R_{\mathrm{cl}} = +1$ (blue) are six times higher (15 dB), although the magnitude of the downstream reflection coefficient is 25% smaller, i.e., more acoustic energy is lost through the downstream end. To understand, consider the upstream reflection coefficient R_{us} shown in Fig. 6.26. It was measured by excitation with the downstream woofers. Nonlinear effects resulting from high amplitude pressure oscillations caused by the thermoacoustic feedback cycle were eliminated by mounting the orifice plate at the downstream end. Since the reference plane depicted in Fig. 3.3 lies downstream of the combustion zone, R_{us} comprises the flame response, the burner, and the fuel supply lines. In some frequency

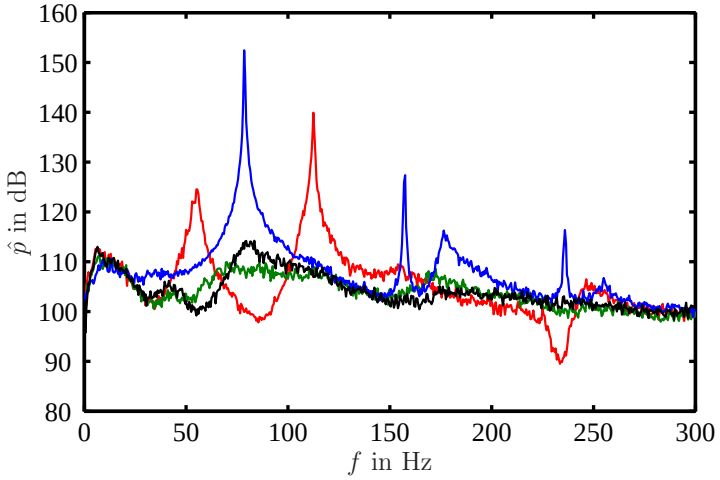

Figure 6.25: Spectra of acoustic pressure for the baseline case without control (with orifice, black), $R_{\mathrm{cl}} = +1$ with $\Delta l = 0.5\,\mathrm{m}$ (blue), $R_{\mathrm{cl}} = -1$ with $\Delta l = 0.5\,\mathrm{m}$ (red), and $R_{\mathrm{cl}} = 0$ (green); reacting flow.

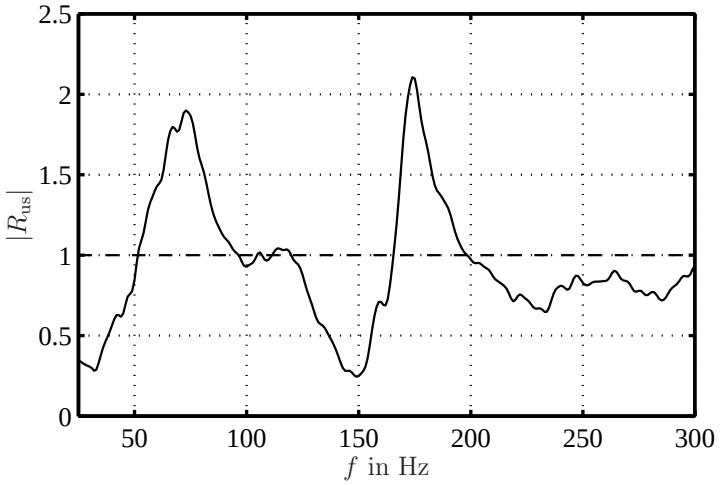

Figure 6.26: Magnitude of the upstream reflection coefficient R_{us} for the uncontrolled case with the orifice plate mounted.

regions, it is larger than unity, showing the influence of the flame as an acoustically active element. These are the regions in which the system could get unstable if the phase relationship between up- and downstream reflection coefficient provided constructive interference and the magnitude of the downstream reflection coefficient was high enough. The shape of R_{us} explains why the spectral peak for the case of $R_{\mathrm{cl}} = +1$ is higher than the response for the case of $R_{\mathrm{cl}} = -1$: At 82 Hz, the acoustic wave amplification caused by the flame is considerably higher than at 55 Hz and 110 Hz. Therefore, the flame produces more acoustic energy in this case. Note that the accuracy of the phase adjustment also has a governing influence on the amplitude of oscillation as for the thermoacoustic feedback cycle the phase relationship between R_{us} and R_{cl} is crucial. Thus, additionally to the difference in $|R_{\mathrm{us}}|$, it might also be possible that the phase for $R_{\mathrm{cl}} + 1$ was adjusted slightly more accurately than it was the case for $R_{\mathrm{cl}} = -1$.

Because in most previous settings the controller gain had to be limited to 70% of the

prescribed value to prevent the woofer control signals from saturation, R_{cl} was set to $\pm 0.7 \cdot \exp(\mathrm{i}\arg(R_{\mathrm{ol}}) - \mathrm{i}\omega 2\Delta l/\bar{c})$. Doing so, the full control gain could be used to prove that the magnitude of R can be adjusted properly if the loudspeaker signals are not saturated. As shown in Fig. 6.27, the magnitude of R is almost exactly 0.7 as prescribed: $R_{\mathrm{cl}} = +0.7$, $\Delta l = 0\,\mathrm{m}$ (blue) and $R_{\mathrm{cl}} = -0.7$, $\Delta l = 0.5\,\mathrm{m}$ (red). Again, the phases differ by

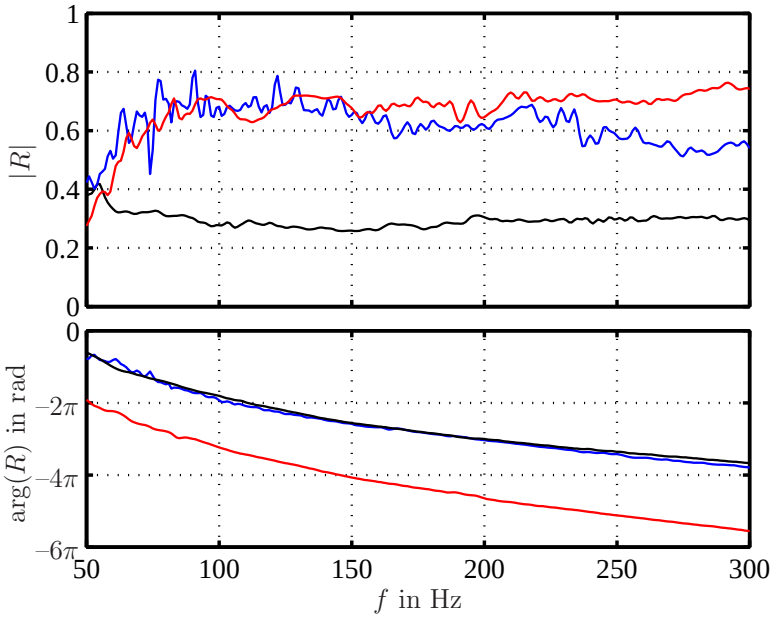

Figure 6.27: Downstream reflection coefficient for the baseline case without control with orifice (black), $R_{\mathrm{cl}} = +0.7$ with $\Delta l = 0\,\mathrm{m}$ (blue), and $R_{\mathrm{cl}} = -0.7$ with $\Delta l = 0.5\,\mathrm{m}$ (red); reacting flow. Top: magnitude, bottom: phase.

π and the different additional lengths.

For completeness, the pressure spectra are shown in Fig. 6.28. For $R_{\mathrm{cl}} = +0.7$ (blue),

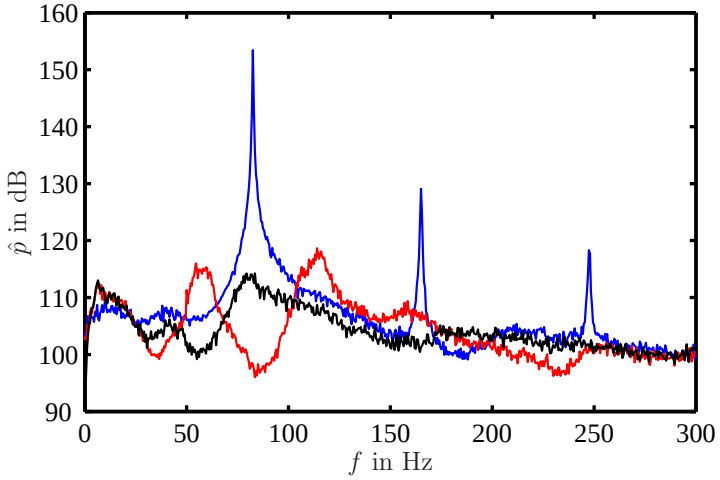

Figure 6.28: Spectra of acoustic pressure for the baseline case without control(with orifice – black), $R_{\mathrm{cl}} = +0.7$ with $\Delta l = 0\,\mathrm{m}$ (blue), and $R_{\mathrm{cl}} = -0.7$ with $\Delta l = 0.5\,\mathrm{m}$ (red); reacting flow.

strong oscillations are visible at 82 Hz, as was observed for $R_{\mathrm{cl}} = +1$ with the same additional length in Fig. 6.17. In contrast to $R_{\mathrm{cl}} = -1$, no distinct peaks are observable for a magnitude of $R_{\mathrm{cl}} = -0.7$ (red).
The control scheme was also applied to a configuration in which relatively strong pressure pulsations were initially present. As mentioned at the beginning of this section, this is much more intricate as tuning a stable system. By doing so, another advantage of the control scheme is revealed as it can also be used to suppress oscillations caused by thermoacoustic feedback. In Sec. 7.1, this is investigated in more detail and it is shown that even very high amplitude pressure pulsations can be mitigated. Figure 6.29 depicts the results for this case. Without control (black), a peak is observed at 94 Hz, some 15 dB higher than in the

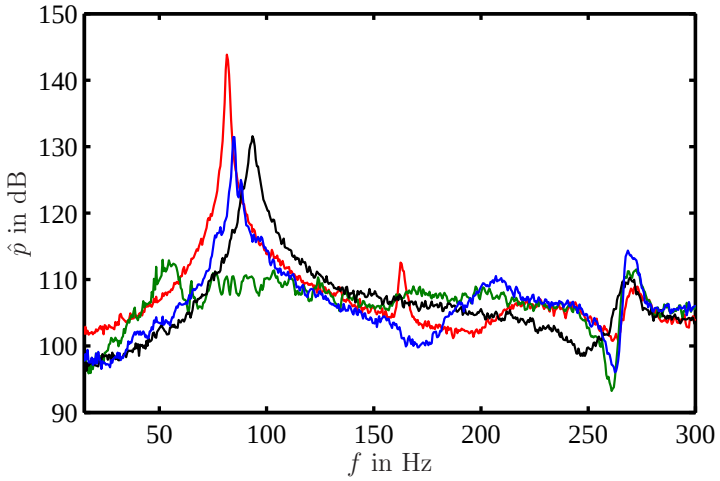

Figure 6.29: Spectra of acoustic pressure for the baseline case without control (black), $R_{\mathrm{cl}} = 0$ (green), $R_{\mathrm{cl}} = +1$ with $\Delta l = 0.5\,\mathrm{m}$ (red), and $R_{\mathrm{cl}} = R_{\mathrm{ol}}$ with $\Delta l = 0.5\,\mathrm{m}$ (blue); reacting flow.

operating conditions discussed above, because here, the air was preheated to 423 K and ϕ was set to 0.7. The green curve represents the results for $R_{\mathrm{cl}} = 0$. The controller is able to attenuate the peak by more than 20 dB.
Additionally, R_{cl} was adjusted to $R_{\mathrm{cl}} = +1 \cdot \exp(\mathrm{i}\arg(R_{\mathrm{ol}}) - \mathrm{i}\omega 2\Delta l/\bar{c})$ (red) and $R_{\mathrm{cl}} = |R_{\mathrm{ol}}| \cdot \exp(\mathrm{i}\arg(R_{\mathrm{ol}}) - \mathrm{i}\omega 2\Delta l/\bar{c})$ (blue), both with $\Delta l = 0.5\,\mathrm{m}$. Both prescribed conditions are successfully achieved as the pressure peaks are shifted to lower frequencies, according to the additional virtual lengths. For $R_{\mathrm{cl}} = +1$, the system oscillates at 82 Hz and for $R_{\mathrm{cl}} = R_{\mathrm{ol}}$ with a changed phase, the peak is shifted to 85 Hz. Since the amplitude of the pressure pulsation remains the same, it can be concluded that the flame response for 85 Hz is equal to that for 94 Hz. The results prove that, as well as in the case with anechoic termination, the impedance tuning concept is able to impose the desired boundary conditions in presence of pressure oscillations in the uncontrolled case. However, the frequency band in which a controller could be identified was smaller than in the cases shown previously. The downstream reflection coefficient was only adjusted between 60 Hz and 160 Hz (instead of 70 Hz to 300 Hz). The corresponding reflection coefficients are shown in Fig. 6.30.
Additional tests, conducted at an operating point near the lean blowout limit, prove that the concept is also able to tune modes different from the $\lambda/4$-mode. For these tests, ϕ was set to 0.6 at a thermal power of 48 kW and the test rig featured an open end. The control scheme was applied to frequencies between 150 Hz and 450 Hz. In this frequency range, the

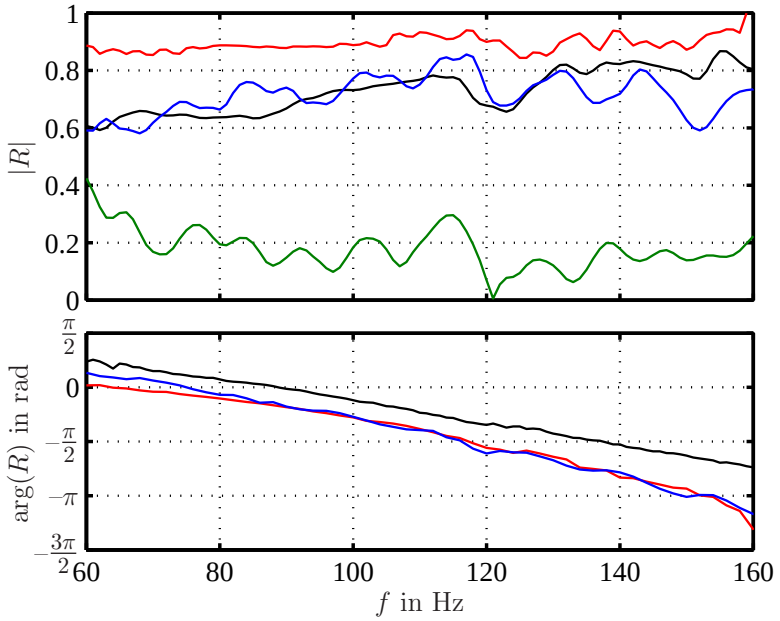

Figure 6.30: Downstream reflection coefficient for the baseline case without control (black), $R_{\mathrm{cl}} = 0$ (green), $R_{\mathrm{cl}} = +1$ with $\Delta l = 0.5\,\mathrm{m}$ (red), and $R_{\mathrm{cl}} = R_{\mathrm{ol}}$ with $\Delta l = 0.5\,\mathrm{m}$ (blue); reacting flow. Top: magnitude, bottom: phase.

reflection coefficient was set to $R_{\mathrm{cl}} = 0$ and sound soft ($R_{\mathrm{cl}} = 1 \cdot \exp(\mathrm{i}\arg(R_{\mathrm{ol}}))$. For the latter case, the phase of R was also tuned, simulating two different additional lengths. The test rig was artificially extended by 0.5 m and 0.75 m resulting in the characteristic change in resonance frequencies.

Figure 6.31 shows the spectra of the acoustic pressure for the different control objectives. For all cases, low frequency flame noise (below 100 Hz) caused by the lean limit can be

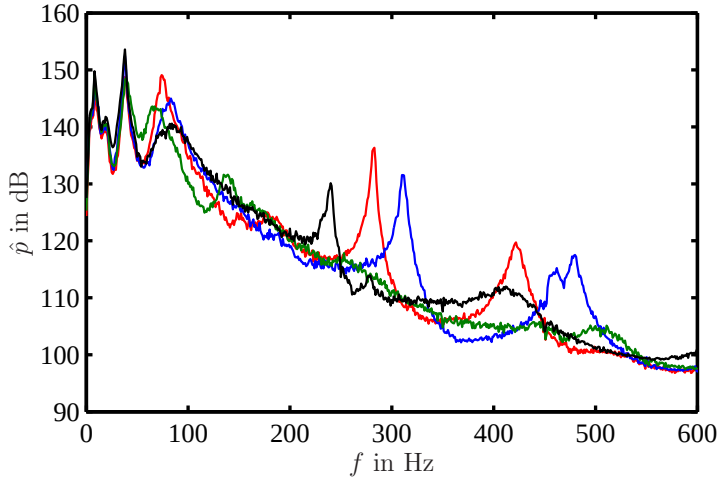

Figure 6.31: Spectra of acoustic pressure for the baseline case without control (black), $R_{\mathrm{cl}} = 0$ (green), sound soft downstream end with $\Delta l = 0.5\,\mathrm{m}$ (blue) and $\Delta l = 0.75\,\mathrm{m}$ (red); reacting flow.

observed. The black curve represents the baseline case without control. At the chosen operating condition, the $\lambda/4$-mode is not strongly developed. In contrast to the previous

results, a distinct peak at the 3/4-λ-mode can be seen at 240 Hz. Calculating this frequency from the test rig length (see Eq. (6.8)) and the speed of sound accurately predicts this resonance mode.
Results for a reflection coefficient of $R_{\mathrm{cl}} = 0$ are plotted in green. It can clearly be seen that in the controlled frequency band, the resonance peak at 240 Hz, representing the standing wave pattern, disappears, thus indicating that only propagating acoustic waves are present. The blue curve shows the pressure spectra for a fully reflecting sound soft end. For this case, an additional length of 0.5 m was simulated. In this way, the test rig could be tuned to a different resonance behaviour. The resonance peak at 310 Hz accurately matches the 5/4-λ-mode for a 0.5 m-longer test rig. Other than in the uncontrolled case, the 3/4-λ-mode is not developed, because it is out of the controlled frequency regime. For the fourth case (red curve), the test rig was artificially extended by 0.75 m. Consequently, the resonance frequency is shifted to a lower value of 282 Hz, again corresponding to the 5/4-λ-mode. Also in the latter case, the resonance frequency matches the one calculated from the altered test rig length and the speed of sound.

6.4.2 Proportional Valves

Figure 6.32 shows the setup with two proportional valves mounted at the downstream end of the test rig. An extension tube was used to connect the valves to the main duct. This was done to enhance the response at low frequencies. Additionally, the extension duct could be instrumented with microphones to investigate the influence of the T-junction on the acoustic waves generated by the valves.
For a better understanding of the valve's excitation characteristic, hot-wire measurements were conducted. Figure 6.33 gives an overview of the setup. The hot-wire probe was located directly downstream of the valve outlet. A mean mass flow of 30 g/s was adjusted. The control voltage was set to $\pm$ 9.8 V corresponding to a quasi fully opened and closed valve. At 0 V, the piston was in the 50% open position. Excitation was applied at discrete frequencies. The phase averaged mass flow cycles for four excitation frequencies are depicted in Fig. 6.34. Following observations can be made: The lower the frequency, the more distorted is the mass flow response. This distortion is due to relatively strong harmonics occurring at 50 Hz (blue) and 110 Hz (red). With increasing frequency, the cycles adopt a more sinusoidal shape. It seems that except for 250 Hz (black), a saturation kicks in for the fully open position limiting the maximum mass flow to values below 40 g/s. Furthermore, the minimum mass flow strongly deviates from the expected value. As the valve piston was controlled between its fully open and close position, theoretically, it should be close to 0 g/s. Especially for low frequencies, this is not the case.
In Fig. 6.35, the minimum (blue) and maximum (red) mass flows are shown for excitation frequencies between 50 Hz and 350 Hz. Additionally, the adjusted (black dashed) and the actual (green) mean mass flows are plotted. With increasing frequency, the actual mean mass flow deviates stronger from the adjusted one. In the worst case, it is 20% less than prescribed causing a decrease in excitation amplitude. However, this trend is compensated as the modulation amplitude, i.e., the fraction of mean air being modulated, increases up to 250 Hz. This explains the weaker excitation characteristic of the valve at low frequencies (see results presented below). As expected, the modulation amplitude is largest at 250 Hz,

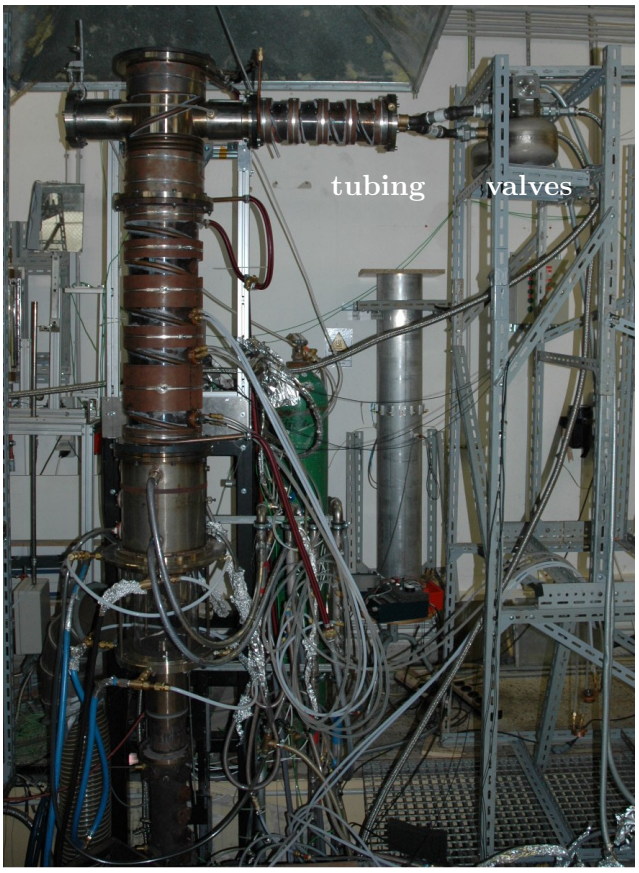

Figure 6.32: Combustion test rig equipped with proportional valves at its downstream termination.

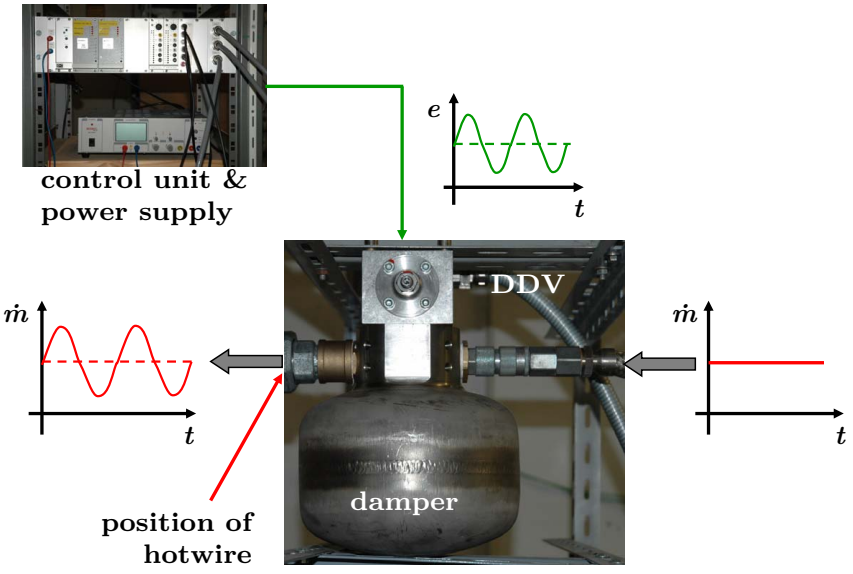

Figure 6.33: Setup for hot-wire measurements at valve exit.

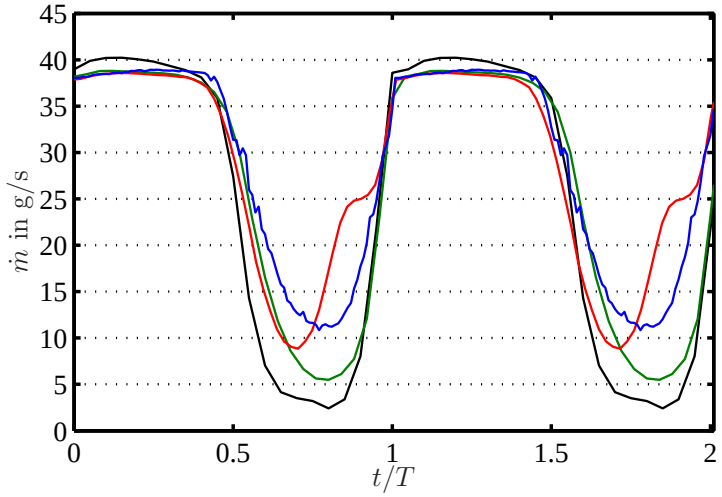

Figure 6.34: Phase averaged cycles of mass flow through the valve for four different excitation frequencies versus time scaled by period T. Blue: 50 Hz, red: 110 Hz, green: 200 Hz, and black: 250 Hz.

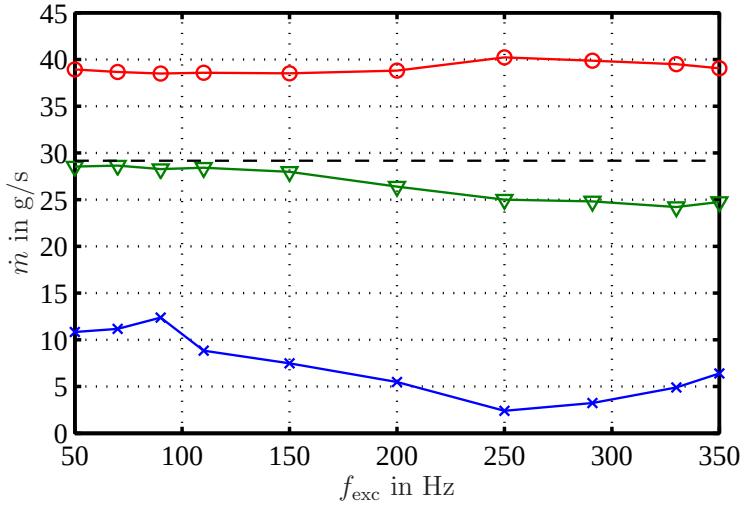

Figure 6.35: Averaged mass flows through valve versus excitation frequency. Blue ×: minimum, red ○: maximum, green ▽: mean, and black dashed: adjusted mean.

the resonance frequency of the spring-mass system represented by the valve.
A possible reason for these characteristics could be that the valve outlet is too small, thus, causing saturation. Because of the pressure loss, the air expands across the valve resulting in an increased volume flow. Furthermore, previous investigations [75] showed that the valve exhibits a static saturation for high mean mass flows. This means that for the piston being in its fully open position, the maximum mass flow will not increase, although the upstream pressure is increased, indicating that it is choked. This point could explain why the maximum mass flow seems to be saturated at approximately 40 g/s. Another reason could be that the damper body, acting as a reservoir, is too small. Also, since the flow is strongly deflected from damper inlet to valve outlet, it is most probably not fully developed at the measurement location.

Besides this, the saturation mechanism could also stem from dynamic processes. To fully understand the reason for this (initially unexpected) modulation behaviour, detailed studies of the flow channels in and the flow through the valve would have to be performed, which is not within the scope of this thesis.
The tubing's geometry between test rig and valves was optimized by 1-d network simulations and experiments to compensate these observations. Figure 6.36 exemplarily depicts three different ways of mounting the valves at the test rig. Differing in length and diame-

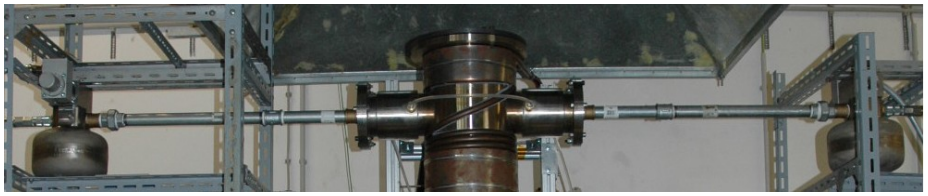

(a) DDVs on both sides long tubing (d = 1")

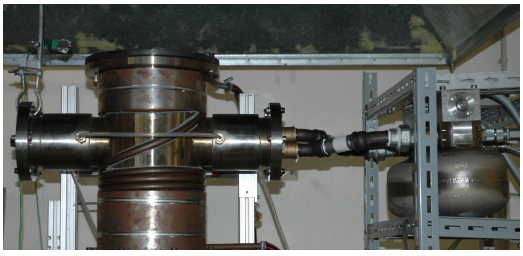

(b) DDVs on one side short tubing (d = 1")

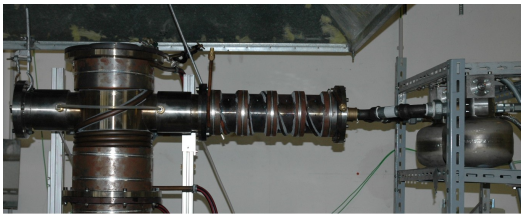

(c) DDVs on one side, long tubing (d = 105 mm)

Figure 6.36: Three different tubing alternatives to mount the valves at the test rig.

ter, the acoustic transfer characteristics of the system side channel/actuator to test rig are influenced.
Figure 6.37 shows the corresponding actuator transfer functions between actuator command and g-wave generated by the actuator at the reference location (see Eq. (4.6) and Fig. 5.3). Since the control objective is to tune the downstream reflection coefficient between 50 and 200 Hz, the actuator authority should be highest in this frequency range. Connecting the valves directly to the test rig, as it was done with the woofers, results in a relatively poor response characteristic (black curve in Fig. 6.37). Thus, by mounting additional extension tubes, the low-frequency response was sought to be enhanced. Exhibiting the highest response in the frequency range considered, the setup shown in Fig. 6.36(c) was chosen. The corresponding actuator transfer function G is represented by the blue curve in Fig. 6.37. However, as can be seen in the phase plots, this setup results in the steepest slope, i.e., the largest time-delay between actuator input signal and generated wave. Recalling the statements made in Sec. 5.4, this has an unfavourable influence on the controller identification. The larger the time-delay of G, the harder is the identification of the controller transfer function, calculated from Eq. (5.4).

Impedance tuning results obtained with proportional valves

The combustion test rig was operated at an equivalence ratio of 0.75 and a thermal power of 100 kW, slightly differing from the operating conditions adjusted for the woofer experiments. This was necessary because the large cold air insertion did not allow to run the test

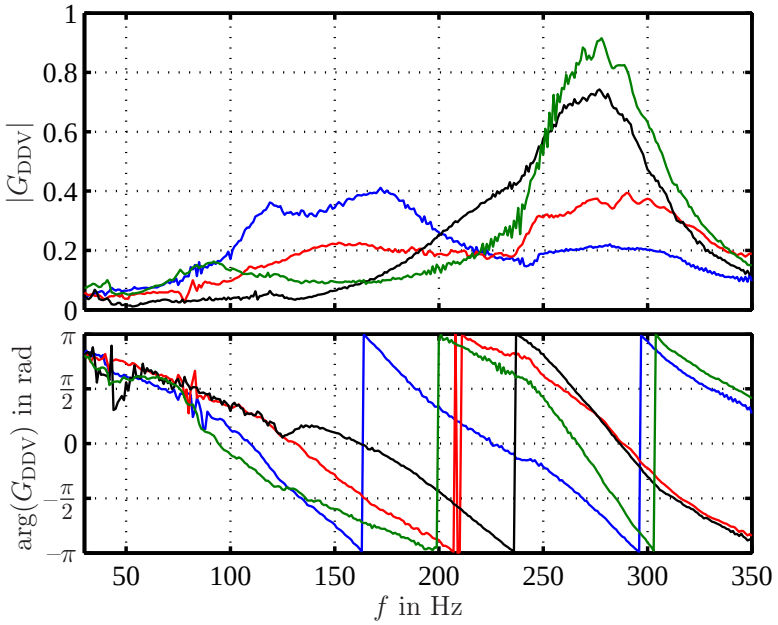

Figure 6.37: Actuator transfer functions resulting from the setups shown in Fig. 6.36; black: no additional tubing, blue: DDVs on one side, long tubing (d = 105 mm), red: DDVs on one side short tubing (d = 1”), and green: DDVs on both sides long tubing (d = 1”). Top: magnitude, bottom: phase.

rig at the same conditions. Without control, no pressure oscillations are present as can be seen in Fig. 6.38 (black). Again, the orifice was mounted at the downstream end of the

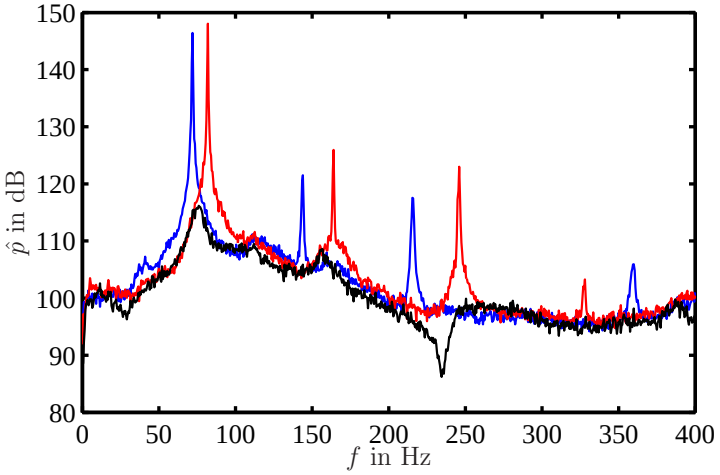

Figure 6.38: Spectra of acoustic pressure without control (black), $|R_{\mathrm{cl}}| = 1$ and with different additional lengths (red and blue). Downstream reflection coefficient is tuned for frequency range.

test rig.

Although, at low frequencies nonlinearities were observed in the modulated mass flows, as discussed above, the reflection coefficient was first attempted to be tuned over a frequency range. According to the woofer results shown previously, the magnitude of R_{cl} was

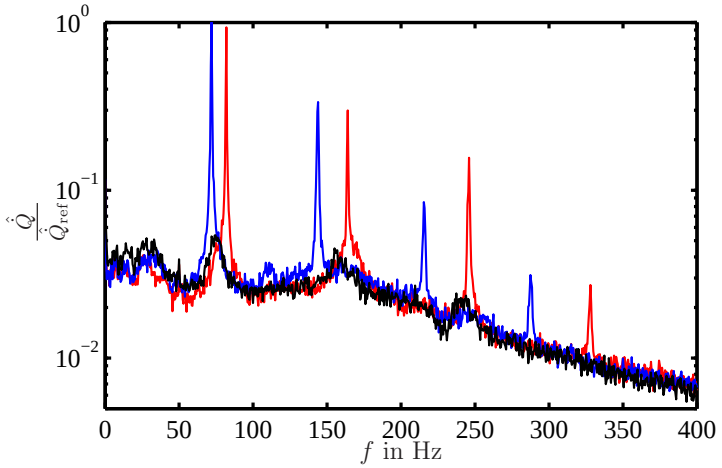

Figure 6.39: Spectra of OH*-chemiluminescence without control (black), $|R_{\mathrm{cl}}| = 1$ and with different additional lengths (red and blue). Downstream reflection coefficient is tuned for frequency range.

again set to unity. For comparison, the additional length (see Eq. (6.9)) was adjusted to produce instabilities at the same frequencies as it was the case for the woofers. Pressure and OH*-chemiluminescence spectra for the controlled cases, shown in Figs. 6.38 and 6.39 (red and blue), display peaks at 82 Hz and 72 Hz. The imposed pressure amplitudes are approximately of the same magnitude as in Figs. 6.17 and 6.21 proving the concept to work with the valves as well.
Figure 6.40 shows the corresponding downstream reflection coefficients R_{cl}. Comparison of

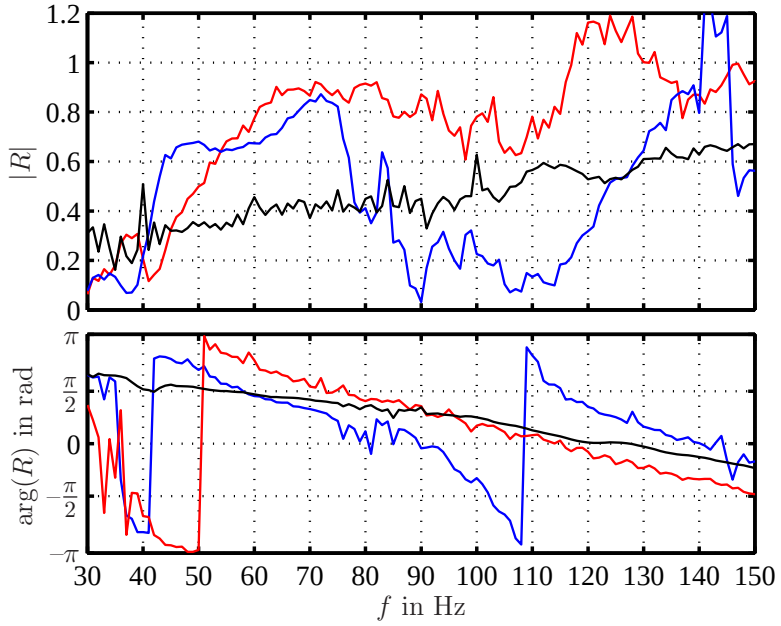

Figure 6.40: Downstream reflection coefficient without control (black), $|R_{\mathrm{cl}}| = 1$ and with different additional lengths (red and blue). Top: magnitude, bottom: phase.

R_{ol} for the baseline case with that of the woofer experiments (see Fig. 6.18) reveals some

deviations. With the valves mounted, the reflection coefficient is higher. These differences were to be expected and can be attributed to the fact that an orifice with a larger diameter was mounted. This was necessary due to the increased mass flows resulting from the valves. The mean air mass flow through the valves was set to 60 g/s (two valves à 30 g/s), equal to the main combustion air. In contrast to that, the speakers were only purged with 10 g/s. The difference of cold air insertion influenced the downstream reflectivity as the characteristic impedance of the medium, $\bar{\rho}\bar{c}$, was changed abruptly. Furthermore, the actuator setups were different and the operating parameters were slightly changed.
Regarding the controlled downstream reflection coefficients, a major difference between the actuator concepts becomes obvious. Using the valves, it is cumbersome to identify a controller for a broad frequency range. For the reported test cases, the frequency band is limited to 35 Hz – 75 Hz (blue) and 60 Hz – 150 Hz (red), respectively. With the woofers, it was possible to adjust a controller bandwidth of approximately 250 Hz. According to the descriptions made earlier, this is due to the transfer function G of the valves. As stated previously, the tubing between valve and test rig increases the propagation time of the generated acoustic wave travelling from the valve exit to the reference plane and has a significant effect, as the speed of sound is much lower in the side branch than in the main duct. The low-pass characteristic of the valve causes an additional time-delay. However, especially for low frequencies, this influence is much smaller than that of the increased duct length. Due to the different setup, the phase decrease of the valves' transfer function is higher than that of the woofers. Moreover, the non-linear behaviour in the modulation of the mass flow, especially at low frequencies, might have an influence on the generated acoustic wave. Still, if the magnitudes of R_{cl} at the frequencies of oscillation are considered, better results are obtained with the valves. In both cases, the magnitudes lie above 0.9. Therefore, it is assumed that the influence of the non-linear modulation behaviour at low frequencies does not play such a crucial role for the acoustics.
The controller identification can be avoided if the system is tuned at discrete frequencies. This is also of major advantage when tuning for high frequencies. Generally, thermoacoustic instabilities might arise if the the phase relation between heat release and pressure fluctuations provides constructive interference and the flame response is sufficiently high. The flame response can be thought of as a contribution to the upstream reflection coefficient R_{us} if it is determined at the reference plane in Fig. 3.3. In Fig. 6.41, R_{us} is shown, measured for the uncontrolled stable baseline case by sweep excitation with the valves. The influence of the flame as an acoustically active element causes R_{us} to be larger than unity in two frequency bands (30 Hz – 90 Hz and 170 Hz – 190 Hz). These are the frequencies for which the system can get unstable if the downstream reflection coefficient is adequately manipulated.
The downstream reflection coefficient was first tuned at 70 Hz and 85 Hz to

$$R_{\mathrm{cl}}(\omega_0) = 1 \cdot e^{-\mathrm{i}\varphi_{\mathrm{us}}(\omega_0)}. \tag{6.11}$$

With this prescribed reflection coefficient, $K(\omega_0)$ can be calculated from Eq. (5.4) to set up the band-pass controller. At both frequencies, R_{us} is larger than unity and with the phase of R_{cl} being set to $-\varphi_{\mathrm{us}}$, the phase relationship for constructive interference between heat release and pressure fluctuation is given (see Eq. (5.12a)).

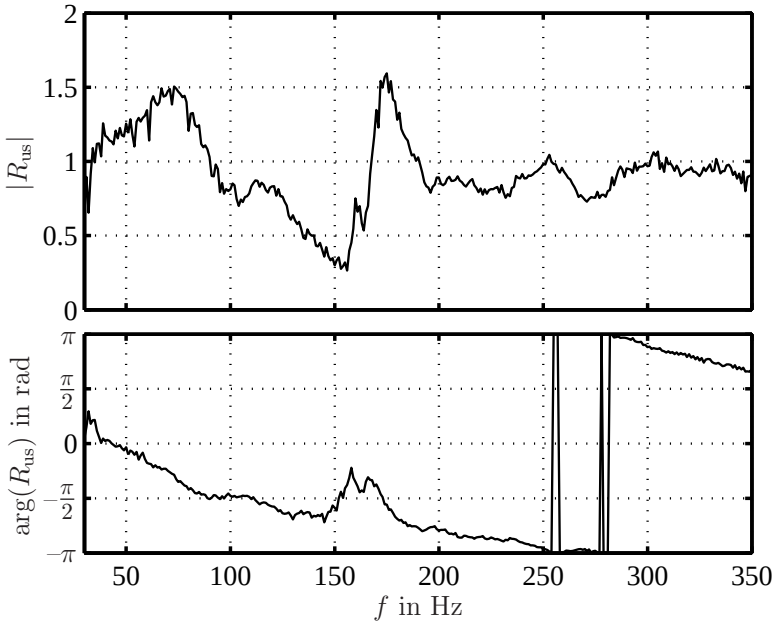

Figure 6.41: Upstream reflection coefficient R_{us} comprising the flame response. Top: magnitude, bottom: phase.

The spectra shown in Figs. 6.42 and 6.43 prove that for the low frequency region, similar results are obtained when compared to the multi-frequency tuning approach. Both

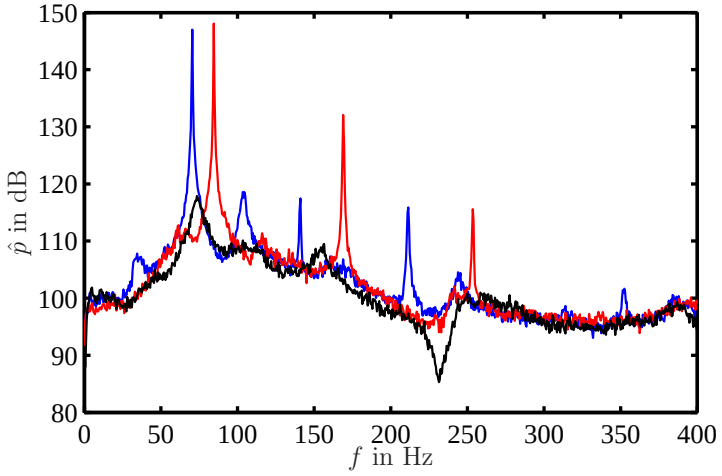

Figure 6.42: Spectra of acoustic pressure without control (black) and $|R_{\mathrm{cl}}| = 1$ for 85 Hz (red) and 70 Hz (blue). Downstream reflection coefficient is tuned at discrete frequencies.

pressure and OH*-chemiluminescence spectra exhibit distinct peaks at the prescribed frequencies. The resulting pressure peak amplitudes are found to be equally high (compared to Fig. 6.38). Note that in case of control at 70 Hz, the additional delay (see Fig. 5.5) was set to 0.24 ms, as otherwise the instability frequency was 71 Hz.
Figure 6.44 depicts the corresponding reflection coefficients. The magnitude of the tuned reflection coefficient is above 0.8 for 70 Hz and around 0.95 for 85 Hz. In the bottom frame,

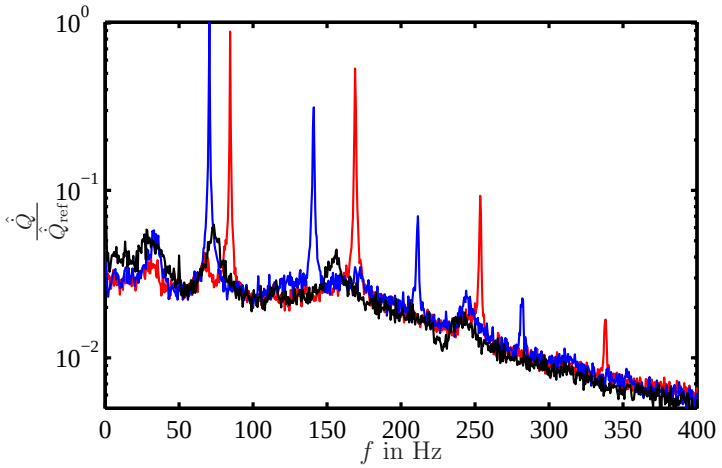

Figure 6.43: Spectra of OH*-chemiluminescence without control (black) and $|R_{\mathrm{cl}}| = 1$ for 85 Hz (red) and 70 Hz (blue). Downstream reflection coefficient is tuned at discrete frequencies.

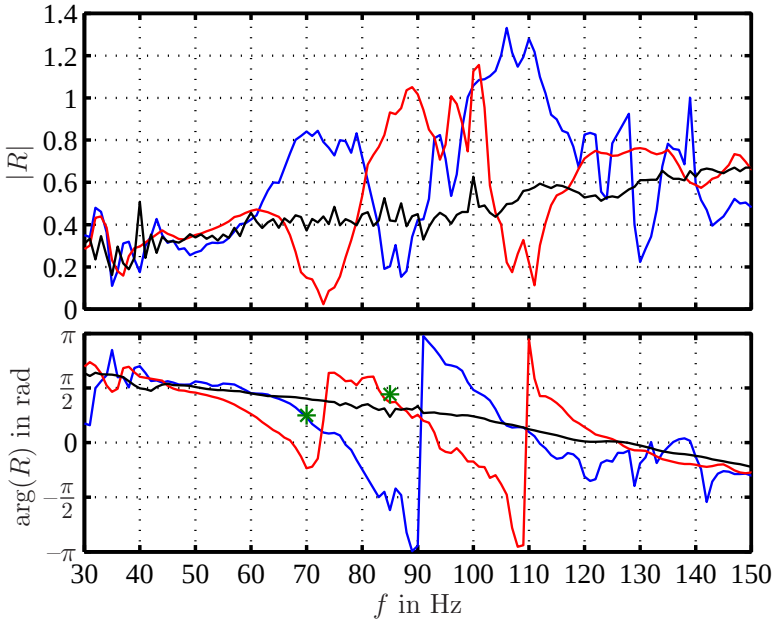

Figure 6.44: Downstream reflection coefficient without control (black) and $|R_{\mathrm{cl}}| = 1$ for 85 Hz (red) and 70 Hz (blue). The green asterisks mark the values to which the reflection coefficient's phase should have been tuned, i.e., $-\varphi_{\mathrm{us}}$. Top: magnitude, bottom: phase.

also the prescribed phases are plotted. According to Eq. (5.12a), they should be equal to $-\varphi_{\mathrm{us}}$, denoted by the green asterisks. They are indeed adjusted quite accurately. The same conclusion can be drawn from the spectral responses as the system oscillates at the correct frequencies.
Results for tuning in the second frequency band (170 Hz to 190 Hz), in which R_{us} is also larger than unity, are depicted in Figs. 6.45 and 6.46. The combustion system was forced

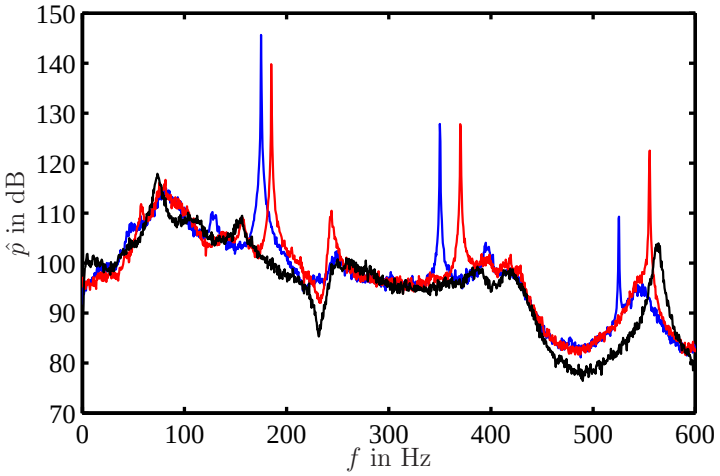

Figure 6.45: Spectra of acoustic pressure without control (black) and $|R_{\mathrm{cl}}| = 1$ for 185 Hz (red) and 175 Hz (blue). Downstream reflection coefficient is tuned at discrete frequencies.

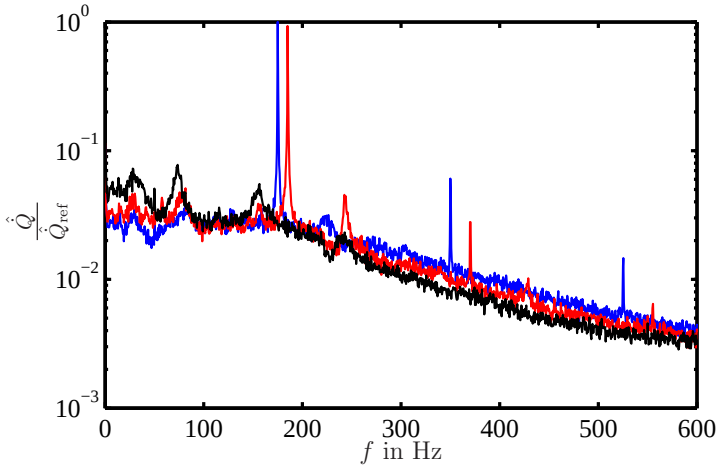

Figure 6.46: Spectra of OH*-chemiluminescence without control (black) and $|R_{\mathrm{cl}}| = 1$ for 185 Hz (red) and 175 Hz (blue). Downstream reflection coefficient is tuned at discrete frequencies.

to oscillate at 175 Hz and 185 Hz, respectively. Neither were the actuators in saturation, nor was it necessary to introduce the additional delay. The fact that the valves have a higher response at these frequencies (see Fig. 6.37) facilitates the test rig tuning. Additionally, it is supposed that the growth rates and therefore the imaginary parts of the instability frequencies are smaller than for the lower frequencies around 70 Hz.

Looking at magnitude and phase of the tuned reflection coefficient, the results in Fig. 6.47 prove that the prescribed values are nearly perfectly adjusted. At 175 Hz, the magnitude

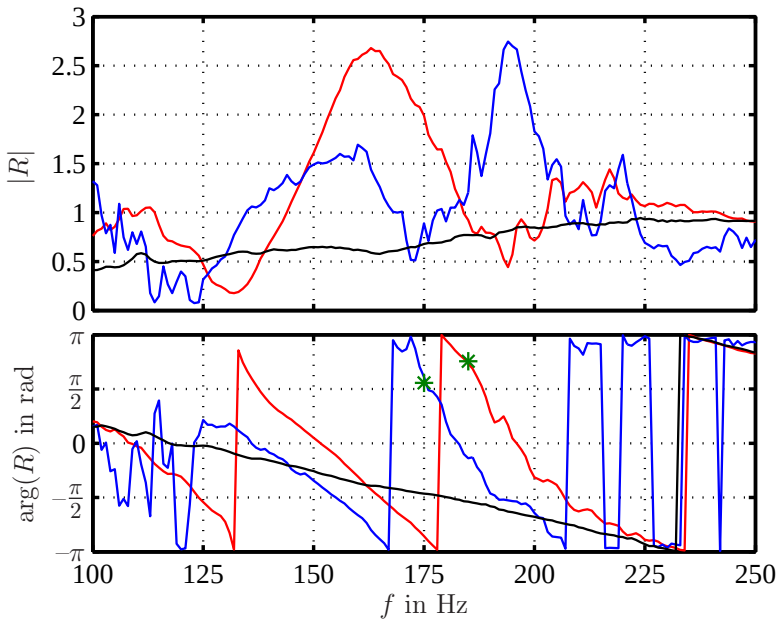

Figure 6.47: Downstream reflection coefficient without control (black) and $|R_{\mathrm{cl}}| = 1$ for 185 Hz (red) and 175 Hz (blue). The green asterisks mark the values to which the reflection coefficient's phase should have been tuned, i.e., $-\varphi_{\mathrm{us}}$. Top: magnitude, bottom: phase.

is above 0.9, whereas at 185 Hz it is even almost unity. It can be seen that the magnitude exceeds unity for both cases at neighbouring frequencies. The reason is that the band-pass filter has a finite bandwidth causing a modification of R_{cl} at frequencies adjacent to the one to be tuned. Although this effect in most cases did not influence the measurements here, it might play a role in different setups. Consider, for instance, the case for which the reflection coefficient for an adjacent frequency is tuned to result in an unwanted instability. This would render control impossible at the frequency of interest. A possibility to obviate this is to reduce the influence on adjacent frequencies by using a narrower filter bandwidth. However, attention has to be paid as this results in a higher order of the band-pass filter. The higher the filter order, the more processor capacity is needed. Additionally, it was observed that for high-order filters, i.e., with orders larger than 20, inaccuracies are introduced by MATLAB when calculating a discrete transfer function for the filter.

As shown in the bottom frame of Fig. 6.47, for the cases presented here, both phases (red and blue) perfectly coincide with the green asterisks representing the values $-\varphi_{\mathrm{us}}$.

For 175 Hz, the magnitude of R_{cl} was also varied between zero and unity. The phase was held constant for these cases. In Fig. 6.48, the actually adjusted magnitudes $|R_{\mathrm{cl}}|$ are plotted versus the prescribed ones $|R_{\mathrm{set}}|$. The graph proves the control scheme to be of high accuracy for tuning to these intermediate values, as well.

Finally, the valves were also used to tune the combustor end to be anechoic. Particularly at frequencies between 150 Hz and 200 Hz, it was possible to decrease R_{cl} to values between 0.03 and 0.05. This is shown for 165 Hz (blue), 175 Hz (green), and 185 Hz (red) in Fig. 6.49.

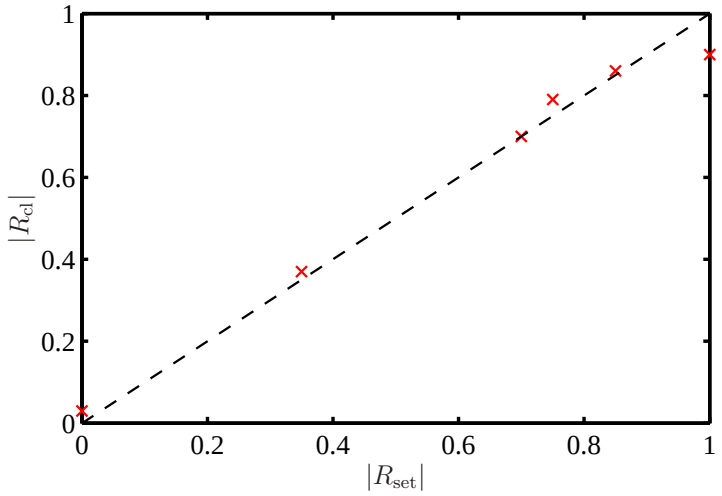

Figure 6.48: Experimentally adjusted reflection coefficient $|R_{\mathrm{cl}}|$ versus prescribed one $|R_{\mathrm{set}}|$ at 175 Hz.

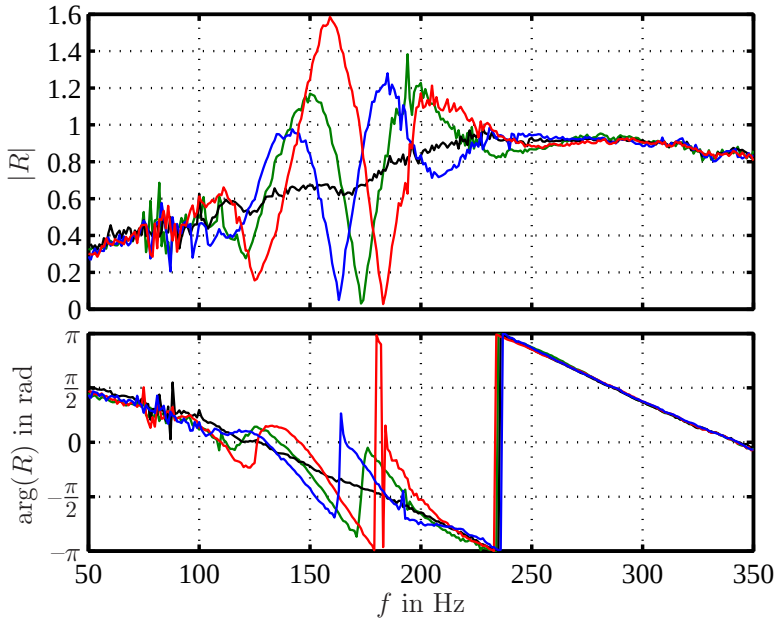

Figure 6.49: Downstream reflection coefficient tuned to $|R_{\mathrm{cl}}| = 0$. Without control: black; 165 Hz: blue, 175 Hz: red, and 185 Hz: green. Top: magnitude, bottom: phase.

6.4.3 Pneumatic Actuator: Ling Driver

In principle, the DDV has proven to be an excellent actuator for the industrial-scale realization of the impedance tuning concept. However, application to industrial test rigs is rather expensive since, depending on the desired fluctuation amplitudes, approximately 10 to 20 valves are needed. Therefore, the Ling Driver's capabilities of being used in the control scheme are assessed in the following as it exhibits more control authority than one single DDV. Open-loop tests at SIEMENS PG combustion rigs have already proven that it is able to deliver sufficient fluctuation amplitudes for medium static pressures.
Figure 6.50 shows the Ling Driver mounted at the downstream end of the combustion test rig. As in case of the valves, an extension tube was used. To avoid corrosion, the air has to be filtered (black cylinder on the right side).

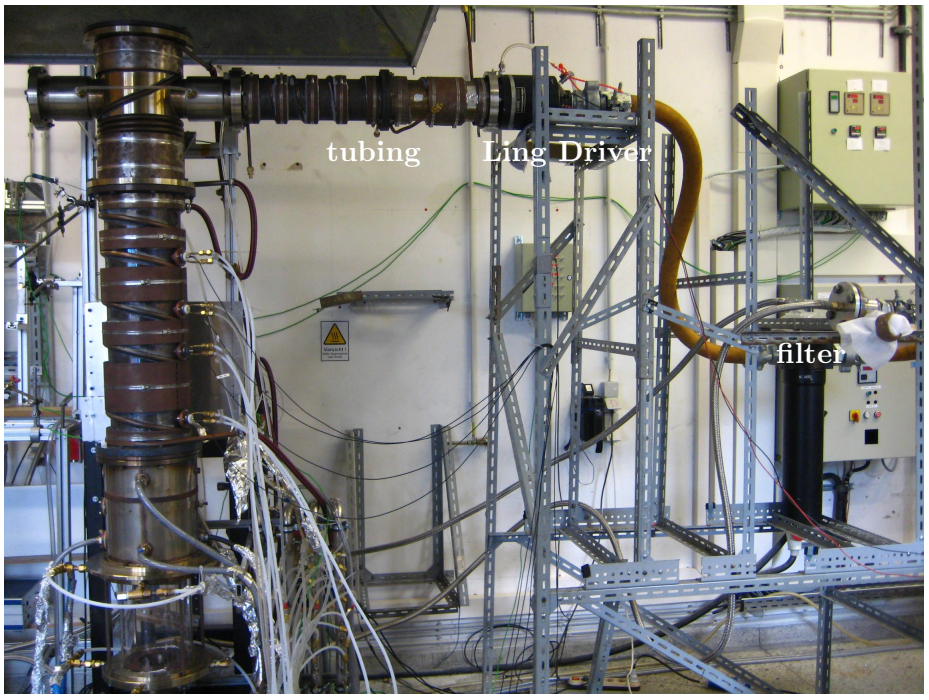

Figure 6.50: Ling Driver mounted at the downstream end of the combustion test rig.

Linearity of the Ling Driver

Prior to application of the Ling Driver as an actuating device for the impedance tuning concept, it was examined whether it can be used for broadband tuning or mono-frequency tuning only. Besides the problem of identifying a suitable controller model, the major requirement for broadband tuning is a linear response. Basically two different non-linearities might occur:

(i) An amplitude non-linearity; the generated amplitude of the acoustic excitation does not linearly increase with an increase of control voltage or imposed mass flow.

(ii) A frequency non-linearity; the generated response at a distinct frequency is not only dependent on the input signal at this frequency but also on (sub-)harmonics of it.

First, the dependence of the excitation amplitude was investigated. For this purpose, the Ling Driver's control unit was driven with different control voltages e_{exc} ranging from 0.05 to 0.55 V with an increment of 0.025 V. The control unit allows a maximum amplitude of 0.6 V only. To have a safety margin, 0.55 V was chosen as the maximum excitation amplitude. The transfer function from input signal to generated acoustic wave at the reference location, G_{LD}, was measured for discrete excitation frequencies f_{exc} between 22 and 402 Hz, in steps of 10 Hz. Figure 6.51 shows the resulting magnitude of the actuator transfer function in $f_{\mathrm{exc}} - \hat{e}_{\mathrm{exc}}$ parameter space. For the experiments, the cold air mass flow in the test

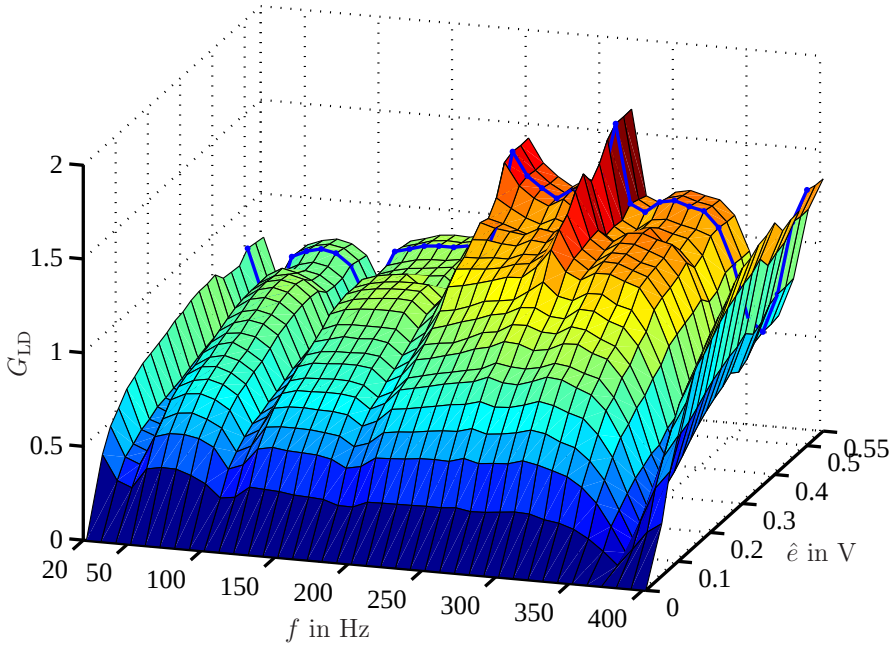

Figure 6.51: Magnitude of Ling Driver transfer function versus excitation frequency and amplitude of control signal. Cold flow conditions with main air and mean Ling Driver mass flow of 60 g/s, respectively. Each grid point corresponds to a measured value.

rig and the mean Ling Driver mass flow were both set to 60 g/s, respectively.
In the definition for the actuator transfer function given in Eq. (4.6), G is related to the applied control voltage. Thus, if the amplitude response was linear, G_{LD} should not change with excitation amplitude; a doubling of the control voltage would then result in a doubling of the acoustic excitation, which would be cancelled out in Eq. (4.6). Clearly, this is not the case for the Ling Driver as can be observed in Fig. 6.51. The graph suggests a coarse trend of increasing transfer function magnitude with increasing control signal amplitude. Note that $\hat{e}_{\mathrm{exc}}$ here denotes the peak amplitude of the sinusoidal control signal.
Also for the phase, a moderate non-linear effect is discernible. For clarity, the phase plotted in Fig. 6.52 is not the absolute phase of the transfer function, φ_{LD}, but is weighted with the phase at 0.5 V, i.e., the graph shows $\varphi_{\mathrm{LD}} - \varphi_{\mathrm{LD}}(0.5\ \mathrm{V})$. This implies that if the phase was not affected by non-linear effects, $\varphi_{\mathrm{LD}} - \varphi_{\mathrm{LD}}(0.5\ \mathrm{V})$ would be equal to zero for all control voltages. In terms of the amount of modulated mass flow, the Ling Driver's response is linear for both amplitude and phase.
The chosen resolution of excitation frequency and voltage results in more than 1000 measurement points. With a data acquisition time of 8 s for each frequency per voltage, the mere measurement time is nearly 2 h for one single look-up table. Thus, the experimental

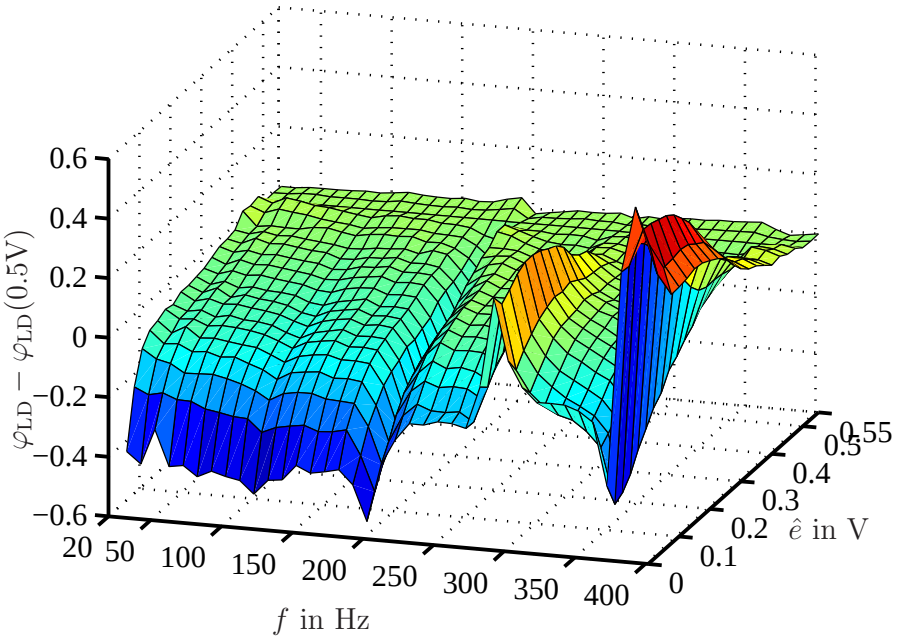

Figure 6.52: Phase of Ling Driver transfer function versus excitation frequency and amplitude of control signal. The phase value for 0.5 V is subtracted for scaling. Cold flow conditions with main air and mean Ling Driver mass flow of 60 g/s. Each grid point corresponds to a measured value.

determination of the look-up tables is a rather time-consuming task. For impedance tuning experiments in practice, it may be convenient to not measure it for all frequencies but only for the frequency at which the system shall be tuned and at adjacent frequencies.
Not only an amplitude but also a frequency non-linearity can be observed. This frequency non-linearity is much stronger than the one observed for the DDVs and restricted the Ling Driver's use to the discrete-frequency tuning scheme only. This non-linearity is mainly due to the Ling Driver's control unit, which processes and amplifies the input signal and drives the Ling Driver. The non-linear response is shown in Fig. 6.53, where the spectra of the input signal (red) and the resulting spectra of the signal fed to the Ling Driver (black) are plotted. Strong harmonics occur which in the worst case – that is not shown in Fig. 6.53 – can reach values up to 40% of the fundamental frequency.

Modification of controller setup to account for non-linear effects

Exhibiting the non-linear features described above, the Ling Driver cannot be utilized with the controller setup as it is described in Chapter 5. Broadband tuning is not possible at all because of the strong frequency non-linearity. For tuning at discrete frequencies, the controller has to be modified to account for the amplitude non-linearity.
Depending on the actuator transfer function G_{LD}, the control law K is calculated from Eq. (5.4). As G_{LD} is a function of its input signal amplitude, the control law has to be adjusted accordingly. Here, the strategy followed is that the control law K is only derived for one single signal amplitude, i.e., for 0.5 V, and for different amplitudes appropriate correction factors are implemented by means of look-up tables.
Figure 6.54 shows the ratio of $|G_{\mathrm{LD}}|$ and $|G_{\mathrm{LD}}(0.5\,\mathrm{V})|$ versus the amplitude of the input signal $\hat{e}_{\mathrm{set}}$. The amplitude dependence for two excitation frequencies is displayed. If the

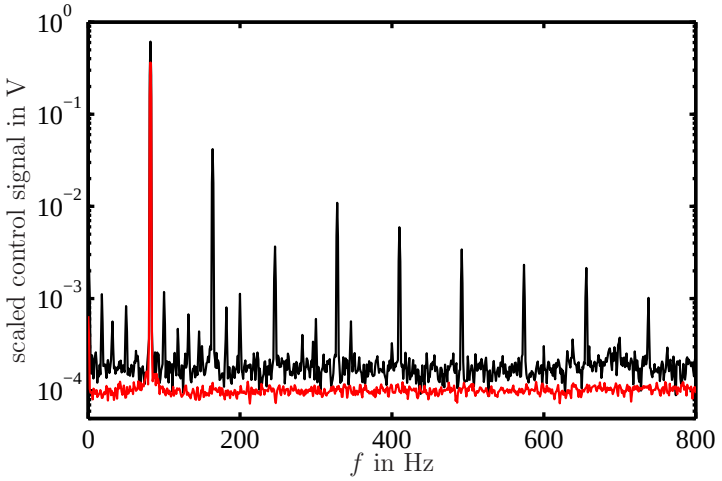

Figure 6.53: Spectra of input signal from function generator (red) and output signal of the Ling Driver's support unit (black).

actuator transfer function had been linear, this ratio would have always been unity. For

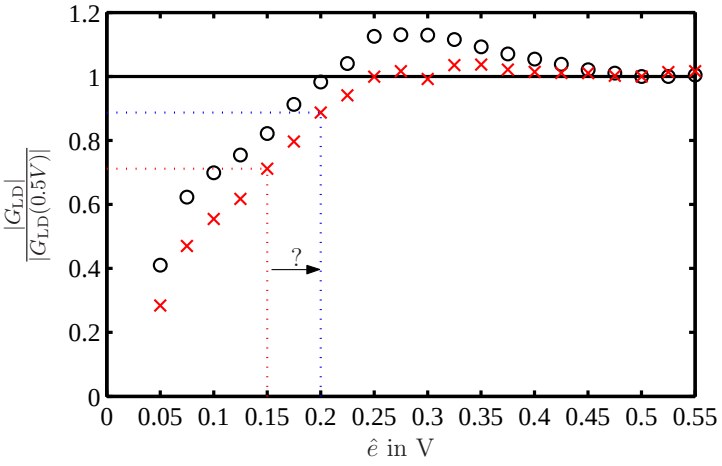

Figure 6.54: Non-linearity of actuator transfer function $|G_{\mathrm{LD}}|$ (scaled with $|G_{\mathrm{LD}}(0.5\,\mathrm{V})|$) versus amplitude of excitation signal. Measurements for two different excitation frequencies are shown: 102 Hz: red $\times$ and 112 Hz black $\circ$.

102 Hz (red), the behaviour between 0.25 V and 0.55 V is almost linear. Below 0.25 V, the scaled $|G_{\mathrm{LD}}|$ sharply decreases. In the case of 112 Hz, a similar trend can be seen. However, between 0.25 V and 0.45 V, $|G_{\mathrm{LD}}|$ is even up to 15% higher than at 0.5 V. As a matter of fact, for each amplitude *and* frequency a different correction coefficient has to be calculated. By means of the dotted red and blue lines, the consequence of this non-linear behaviour is explained. It is assumed that the control law calculates a control voltage amplitude of 0.15 V to realize a fictive control objective. If no correction factor is implemented, the input signal to the Ling Driver is 0.15 V. However, at 0.15 V, $|G_{\mathrm{LD}}|/|G_{\mathrm{LD}}(0.5\,\mathrm{V})|$ is approximately 0.71 (red dotted line) and therefore the wave generated by the Ling Driver is less than what is "expected" by the linear controller, which has been designed for 0.5 V. In other words, the amplitude of the acoustic wave generated in the system is only 71% of the one actually needed to achieve the control objective. The question now is, to which value the signal,

calculated by the controller, has to be increased so that the generated wave is equal to the one which would have been generated if the controller had had a linear response. This means to solve (a priori)

$$\hat{e}_{\mathrm{set}}(f)\tilde{G}_{\mathrm{LD}}(\hat{e}_{\mathrm{set}}, f) - \hat{e}_{\mathrm{calc}}(f) = 0, \tag{6.12}$$

where $\hat{e}_{\mathrm{calc}}$ corresponds to the control signal calculated by the controller, $\hat{e}_{\mathrm{set}}$ is the signal that has to be fed to the Ling Driver to satisfy the control objective, and

$$\tilde{G}_{\mathrm{LD}}(\hat{e}_{\mathrm{set}}, f) = \frac{|G_{\mathrm{LD}}(\hat{e}_{\mathrm{set}}, f)|}{|G_{\mathrm{LD}}(0.5\ \mathrm{V}, f)|}. \tag{6.13}$$

In the example given in Fig. 6.54, the control signal driving the Ling Driver has to be increased to 0.186 V to generate the same amplitude as an actuator with linear response would generate at 0.15 V. At a control signal of $\hat{e}_{\mathrm{set}} = 0.186\,\mathrm{V}$, $\tilde{G}_{\mathrm{LD}}(0.186\,\mathrm{V}, 102\,\mathrm{Hz})$ is equal to $\hat{e}_{\mathrm{set}}(102\,\mathrm{Hz})/\hat{e}_{\mathrm{calc}}(102\,\mathrm{Hz}) = 0.186\,\mathrm{V}/0.15\,\mathrm{V}$, as required by Eq. (6.12). As $|G_{\mathrm{LD}}|$ is a function of $\hat{e}_{\mathrm{set}}$, Eq. (6.12) has to be solved iteratively. A polynomial is fitted to the measured data of $\tilde{G}_{\mathrm{LD}}(\hat{e}_{\mathrm{exc}}, f_{\mathrm{exc}})$ to enable interpolation between the discrete excitation frequencies and voltages.

As a consequence, a look-up table for the magnitude has to be stored in the controller, which writes out the control signal that is, after being multiplied with the real Ling Driver transfer function, equal to the one calculated by the controller. Figure 6.55 shows the look-up table for the case discussed above. Note, a second look-up table accounting for phase

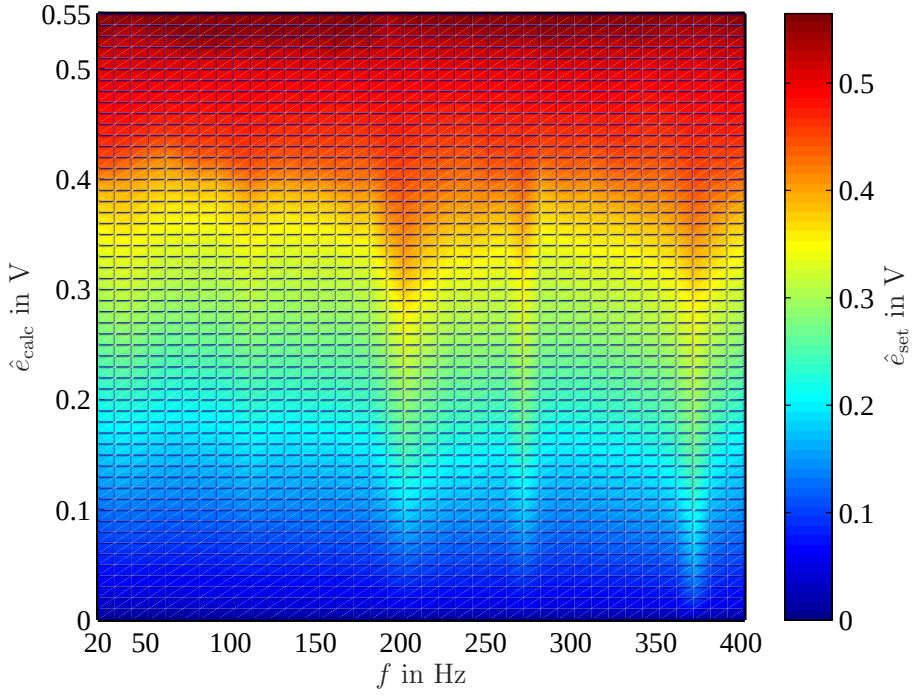

Figure 6.55: Look-up table for correction of Ling Driver control signal. Depending on tuning frequency and calculated control signal, a corrected signal $\hat{e}_{\mathrm{set}}$ is written out.

corrections is also needed.

A schematic of the modified controller setup including both look-up tables is shown in

Fig. 6.56. As in case of the control scheme for the linear actuator, the measured micro-

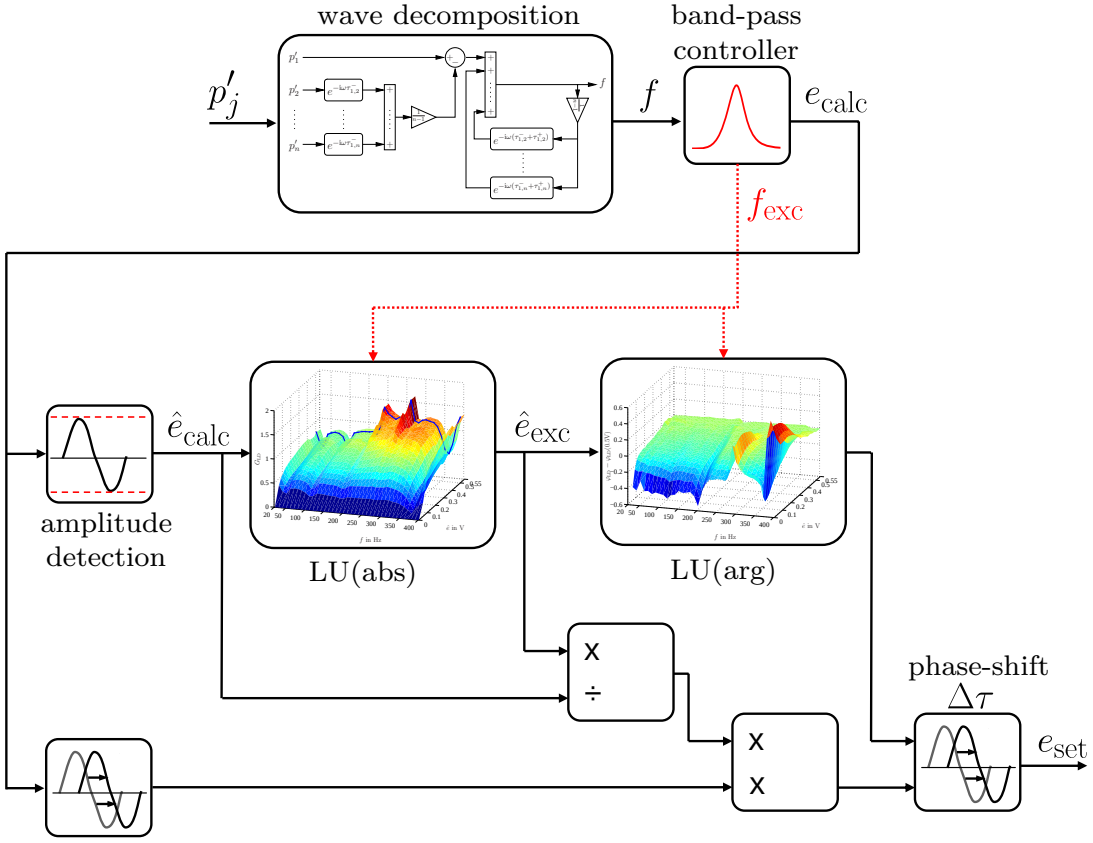

Figure 6.56: Modified controller setup accounting for the non-linear amplitude response characteristic of the Ling Driver.

phone signals are decomposed to extract the downstream travelling wave, which is then processed by the band-pass controller. The look-up tables are implemented after the controller. Besides the look-up tables, some additional adaptations have to be made to the basic setup.

Since the amplitude dependence of the Ling Driver is not a function of the actual oscillating signal value but its peak amplitude, an algorithm has to be implemented, which determines the actual peak amplitude *instantaneously* and feeds this constant value to the look-up table. To obtain the peak value at the frequency of interest, this algorithm has to be preceded by the band-pass controller. The corresponding element is labelled "amplitude detection" in Fig. 6.56. It basically consists of filters and adequate mathematical manipulations visualized in Fig. 6.57. The oscillating input signal is first high-pass filtered

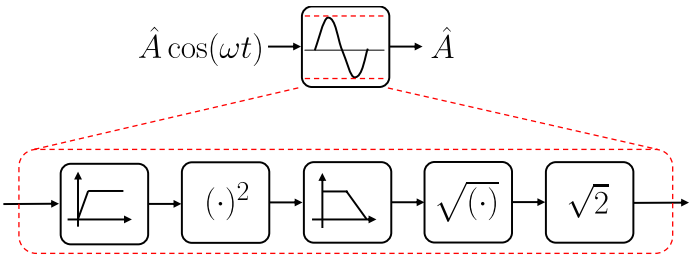

Figure 6.57: Scheme to instantaneously detect the amplitude of a sinusoidal signal.

at 5-8 Hz. This is only strictly necessary if the signal contains an offset. As this offset is already cancelled prior to the online wave decomposition scheme, the high-pass filter could in principle be omitted here. However, it turned out that the resulting amplitude is slightly more accurate with the high-pass filter. Taking the square of the signal results in a positive amplitude. The latter operation causes the signal to have an offset, which is equal to the squared effective amplitude. This offset is determined by using a low-pass filter at 5-8 Hz. Finally, taking the root and multiplying with $\sqrt{2}$ yields the instantaneous amplitude of the input signal. This detection scheme was already proposed by Wang & Krstić [227] before. The identified peak amplitude is fed to both look-up tables, whose second input is the frequency at which the system is to be tuned (see Fig. 6.56). According to Eq. (6.12), the amplitude is corrected and the effect of the phase-non-linearity is considered by a variable delay.

Impedance tuning results obtained with the Ling Driver

Experiments were conducted at an equivalence ratio of $\phi = 0.71$ and a thermal power of 115 kW. An air mass flow of approximately 80 g/s was modulated by the Ling Driver. The Ling Driver's input signal was saturated in order to stay below the maximum allowable current of 6 A. At this current, the piston moves between its fully open and close position. The pressure spectra of the uncontrolled system are displayed in Fig. 6.58. Again, results

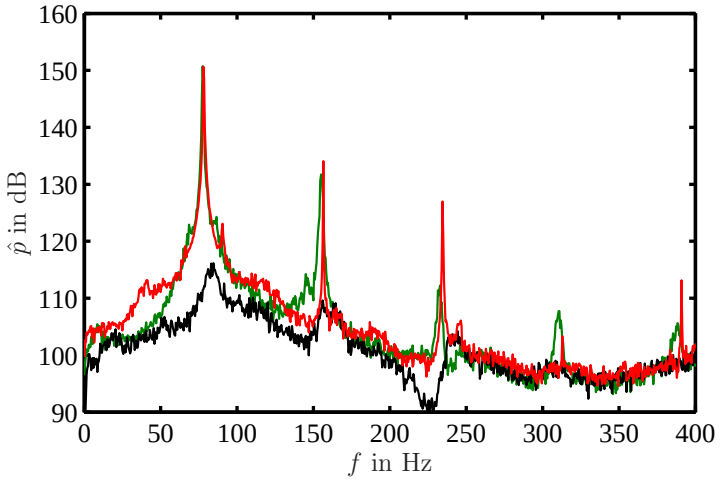

Figure 6.58: Spectra of acoustic pressure for the baseline case without control (with orifice, black – without orifice, green) and $|R_{\mathrm{cl}}(78\,\mathrm{Hz})| = 1$ with $\varphi_{\mathrm{cl}} = -\varphi_{\mathrm{ol}}$ (red).

for two uncontrolled tests are shown, one for the open-end case (green) and the other for conditions with orifice mounted (black). For the open-end case, the combustion system exhibits strong pressure fluctuations with a peak amplitude of 151 dB at 78 Hz, the $\lambda/4$-mode of the test rig. As in the results reported in the preceding sections, the orifice has a strong stabilizing effect. The thermoacoustic feedback cycle is interrupted resulting in a peak reduction of 35 dB. In this case, only combustion noise is responsible for the acoustic spectra. Regarding the OH*-chemiluminescence spectra shown in Fig. 6.59, the corresponding behaviour is seen.

The reflection coefficients plotted in Fig. 6.60 display the reducing effect the orifice has on the magnitude. The phase is only slightly influenced. At 270 Hz, a decrease in $|R|$ is

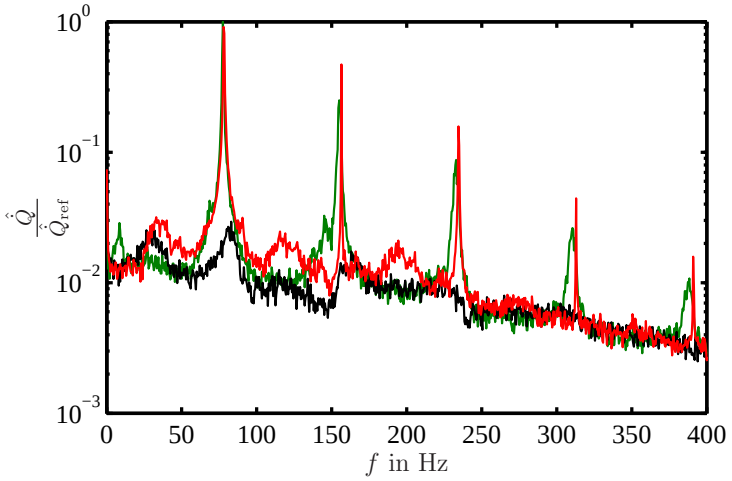

Figure 6.59: OH*-chemiluminescence for the baseline case without control (with orifice, black – without orifice, green) and $|R_{\mathrm{cl}}(78\,\mathrm{Hz})| = 1$ with $\varphi_{\mathrm{cl}} = -\varphi_{\mathrm{ol}}$ (red)

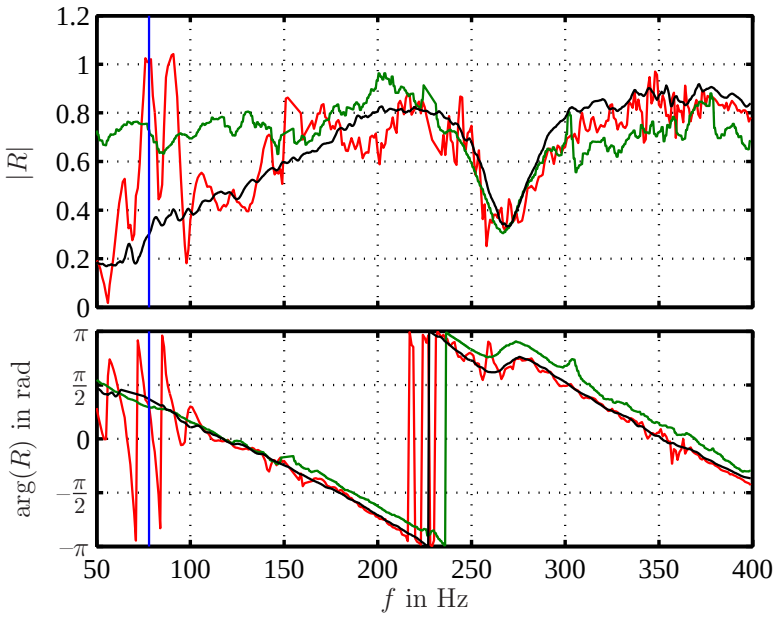

Figure 6.60: Reflection coefficient for the baseline case without control (with orifice, black – without orifice, green) and $|R_{\mathrm{cl}}(78\,\mathrm{Hz})| = 1$ with $\varphi_{\mathrm{cl}} = -\varphi_{\mathrm{us}}$ (red). Top: magnitude, bottom: phase.

visible, which most probably can be attributed to a resonance phenomenon of the actuator mounting; similar observations are made for the cold flow in Sec. 6.3.

As in the previous sections, the control concept was applied to the stabilized system. It was first examined if the Ling Driver is capable of reproducing the instability of the open end case. At 78 Hz, the closed-loop reflection coefficient R_{cl} was set to a magnitude of unity and a phase equal to $-\varphi_{\mathrm{us}}$, the negative phase of the upstream reflection coefficient. Results shown in Fig. 6.60 (red) prove that the Ling Driver in conjunction with the modified controller setup is able to achieve the control objective. At 78 Hz, magnitude and phase correspond accurately to the prescribed values. Note that for the uncontrolled unstable case (green), the phase of R is also equal to $-\varphi_{\mathrm{us}}$ verifying the simplification of calculating

the control law at a real frequency (confer to Sec. 5.4).
Also, pressure and OH*-chemiluminescence spectra show the expected results. Although the magnitude of R_{cl} is even tuned to a higher value than in the uncontrolled case of the open end, the pressure peaks at the fundamental frequency are of the same height. In case of control, the harmonics have a higher amplitude. The reason for this could be the different damping characteristics of open end and orifice.
In addition to the merely global observations obtained with the photomultiplier, the ICCD camera was used to visualize the locally distributed heat release fluctuations of the flame. Figure 6.61 shows the line-of-sight integral of the RMS fluctuation of the OH-radical for the three cases, averaged over 280 pictures. To allow for a quantitative comparison with

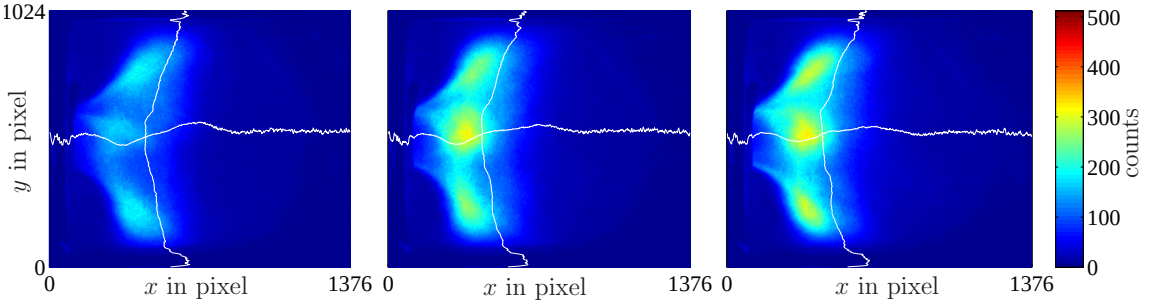

Figure 6.61: RMS value of OH*-chemiluminescence of the flame (colour code in counts). Left: uncontrolled with orifice; middle: uncontrolled without orifice; right: controlled with orifice – controller is adjusted to reproduce natural instability of the uncontrolled case without orifice.

the mean heat release (shown in Sec. 6.6) the range of the colour code is not fully utilized. The resolution in axial and radial direction is 1376 × 1024 pixels. In the left frame, the uncontrolled stable baseline case, i.e., with orifice mounted, is shown. In correspondence to the spectra displayed in Fig. 6.59, only small overall fluctuations are present, caused by combustion noise. Without orifice, the system exhibits strong self-excited instabilities (center graph). Fluctuation maxima are located in the shear layers between inner and outer recirculation zone. Since the pictures are line-of-sight integrated, it is not clear whether the central peak is located in the inner recirculation zone or also in the outer shear layer. Using the impedance tuning to generate a thermoacoustic instability results in a quite similar distribution of the fluctuating OH-radical, as can be seen in the right frame. Both the location and the intensity of the RMS fluctuation are quasi equal to the uncontrolled, unstable case; the latter being also evident from the global observations shown above.
Additional to the OH*-distribution also the center of gravity lines are depicted in Fig. 6.61. In Fig. 6.62, these lines are plotted into one graph allowing a more detailed comparison of the flame position. For both unstable cases (red and blue), the lines nearly coincide. The stable flame (black) seems to have the maximum perturbation a bit further downstream.
Shifting the resonance frequency is also possible. Figures 6.63 and 6.64 show results for tuning the downstream reflection coefficient to $R_{\mathrm{cl}} = 1\,\exp(-\mathrm{i}\varphi_{\mathrm{us}})$ at 72 Hz (yellow) and 92 Hz (blue). Both in the spectra of pressure and the unsteady heat release, distinct peaks at the prescribed frequencies and their harmonics can be seen. The corresponding reflection coefficients are plotted in Fig. 6.65. For 92 Hz, the magnitude (top) perfectly agrees to unity, whereas for 72 Hz, only a value of 0.83 is obtained. The latter is most probably due to a lack of actuator control authority.

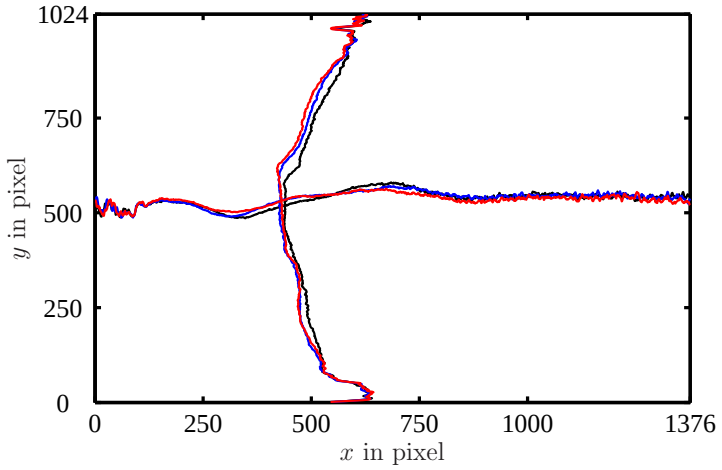

Figure 6.62: Center of gravity lines of RMS value of OH*-chemiluminescence of the flame. Black: uncontrolled with orifice; blue: uncontrolled without orifice; red: controlled with orifice – controller is adjusted to reproduce natural instability of the uncontrolled case without orifice.

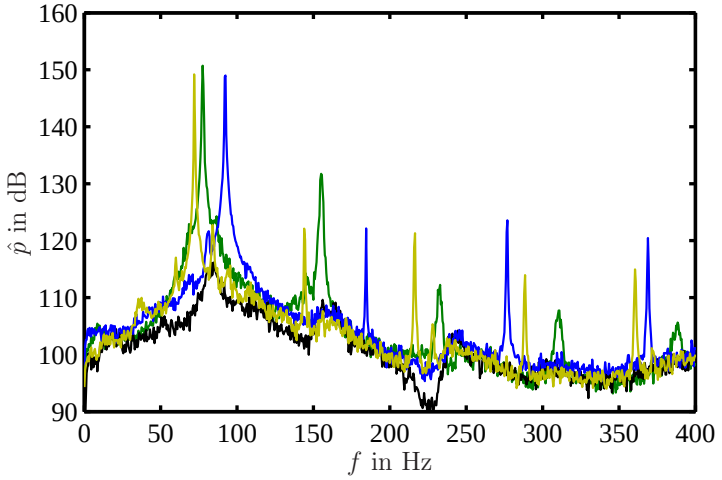

Figure 6.63: Spectra of acoustic pressure for the baseline case without control (with orifice, black – without orifice, green) and $R_{\mathrm{cl}} = 1\ \exp(-\mathrm{i}\varphi_{\mathrm{us}})$ for 72 Hz (yellow) and 92 Hz (blue).

The finite bandwidth of the controller is responsible for the magnitude's characteristic shape. For all cases for which the reflection coefficient has been tuned at a discrete frequency, two maxima adjacent to the tuned frequency are observable. In Fig. 6.65, also the generation of harmonics due to the support unit, i.e., the frequency non-linearity, is visible. Except for the frequencies covered by the band-pass controller, the control signal is zero. Since the Ling Driver support unit generates harmonics of its input signal (confer to Fig. 6.53), the reflection coefficient is influenced at these frequencies as well. The characteristic two maxima can be seen up to the fifth harmonic (360 Hz) for tuning at 72 Hz (and the fourth (368 Hz) for 92 Hz). This behaviour is not observed when using the DDVs, proving once again that the non-linearity can be neglected there. Regarding the phases, results for both cases prove that they are accurately set to $-\varphi_{\mathrm{us}}$ (red asterisks), as prescribed. Tuning to higher frequencies, different levels of reflection, as well as quasi arbitrary phases is not

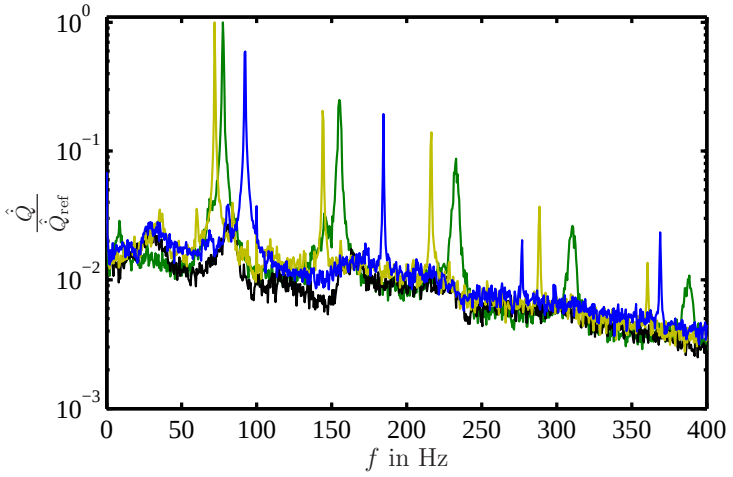

Figure 6.64: Spectra of OH*-chemiluminescence for the baseline case without control (with orifice, black – without orifice, green) and $R_{\mathrm{cl}} = 1\ \exp(-\mathrm{i}\varphi_{\mathrm{us}})$ for 72 Hz (yellow) and 92 Hz (blue).

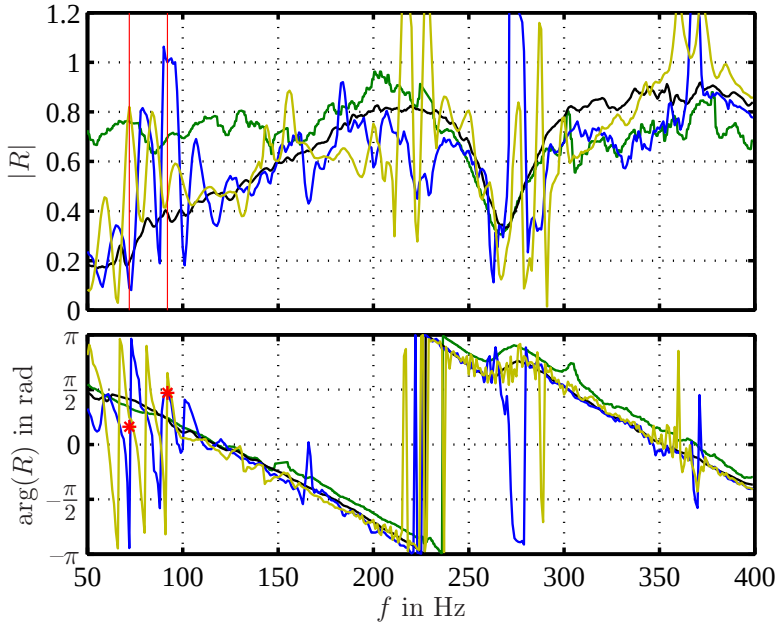

Figure 6.65: Reflection coefficient for the baseline case without control (with orifice, black – without orifice, green) and $R_{\mathrm{cl}} = 1\ \exp(-\mathrm{i}\varphi_{\mathrm{us}})$ for 72 Hz (yellow) and 92 Hz (blue). Red asterisks mark the values to which the reflection coefficient's phase should be tuned, i.e., $-\varphi_{\mathrm{us}}$. Top: magnitude, bottom: phase.

explicitly shown here but is also possible.

6.4.4 Conclusions

This section briefly summarizes the observations made for the different actuator concepts. In Fig. 6.66, a comparison between all three actuators can be seen. For each actuator, the

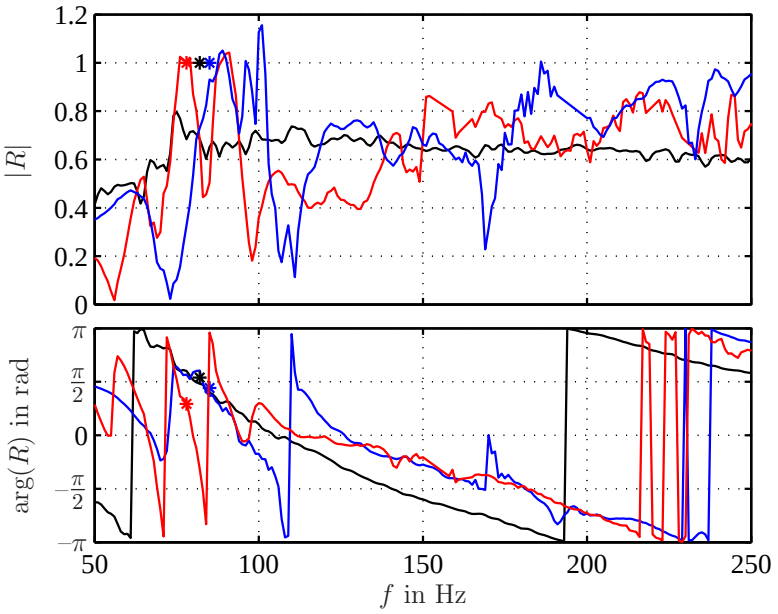

Figure 6.66: Comparison of adjusted reflection coefficients for the different actuator concepts. Black: Woofer, blue: DDVs, red: Ling Driver. Asterisks denote the prescribed values. Top: magnitude, bottom: phase.

test case is chosen for which the instability of the uncontrolled unstable system should be reproduced in the experiments. Because of the differences in actuator setups and operating conditions described above, the prescribed values are slightly different (asterisks in Fig. 6.66). The black curves represent the results for the woofers. The magnitude (top) at the instability frequency of 82 Hz is smaller than prescribed, but in return the reflection coefficient is tuned for the whole frequency range between 70 Hz and 300 Hz. The results for the DDVs are shown in blue. Here, the magnitude at 85 Hz is close to unity. For the Ling Driver, it is even equal to unity (78 Hz, red). However, in both latter cases, the reflection coefficients are only adjusted at discrete frequencies. For the phases, displayed in the bottom graph of Fig. 6.66, the values correspond exactly to the ones prescribed by the control law for all cases. In conclusion, all actuator concepts yield excellent results. The woofers are capable of tuning over a broad frequency range with the drawback that they do not exhibit sufficient control authority. Valves and Ling Driver are able to accurately adjust both magnitude and phase, suffer, however, from the fact that control is only possible at discrete frequencies. Note that for the valves tuning in a limited frequency range is also possible as reported in Sec. 6.4.2.
In Table 6.4, a summary of the investigated actuator concepts is given. Their advantages and disadvantages as well as some comments are given on when to use which actuator.

Table 6.4: Comparison of actuators used for impedance tuning.

Actuator	Pros	Cons	Comment
Woofers	• Best actuator in terms of frequency response over broad range • Easy to handle and cheap • Small time delays of actuator transfer function and thus model identification for controller easiest	• Insufficient actuator control authority especially for high pressure applications • Lack of robustness for harsh environmental conditions in industrial rigs	• Actuator of choice for validation, optimization and modification of control concept • Application under atmospheric laboratory-scale and probably small industrial-scale experiments
Proportional Valves (Moog DDV)	• High control authority • Fulfills requirements for application in industrial test rigs in terms of robustness • Tuning over small frequency band possible	• Application to industrial test rigs expensive • Tedious controller identification if used for tuning at multiple frequencies	• If several devices are used, DDV promises to be an excellent actuator for industrial high pressure applications • Excitation amplitude might be further enhanced by optimization of flow paths
Electro-Pneumatic Actuator (Ling Driver)	• High control authority (proved to generate sufficiently high excitation amplitude at SIEMENS PG medium pressure rigs) • High robustness	• Amplitude and frequency non-linearities restrict to tuning at discrete frequencies • Due to non-linearities tedious and complex controller setup • Old-fashioned control & support unit	• Ling Driver can be used for atmospheric and first medium pressure tests at industrial test rigs

6.5 Saturation of Control Signal

If the actuator power is not sufficient to meet the control objective, the calculated control output has to be decreased. Otherwise, the actuator could be damaged or the signal is clipped and therefore not processed correctly. For the experiments, an additional gain $K_\mathbf{g}$ was implemented in the control scheme to avoid this. In the results shown previously, this gain limited the control signal to approximately 70% to 90% of its actual value. This was almost always the case when woofers were used for the reactive tests and also sometimes for the proportional valves. Nonetheless, the system was forced to oscillate at the prescribed frequency (although the amplitude of oscillation would have been higher in case of $K_\mathrm{g} = 1$). This raises the question, why the adjustment of the phase of the downstream reflection coefficient, which determines the oscillation frequency, is less sensitive to K_g than it is the case for the magnitude. Note that the accuracy of the phase adjustment also has a governing influence on the amplitude of oscillation as for the thermoacoustic feedback cycle, the phase relationship between R_us and R_cl is crucial.
If K_g is introduced, the controller transfer function (see Eq. (5.4)) is written as

$$K = K_\mathrm{g} \frac{R_\mathrm{set} - R_\mathrm{ol}}{G}. \tag{6.14}$$

Equation (5.3) can then be rearranged to yield

$$R_\mathrm{cl} = R_\mathrm{ol}(1 - K_\mathrm{g}) + R_\mathrm{set} K_\mathrm{g}, \tag{6.15}$$

where R_set is the prescribed reflection coefficient to be adjusted and R_cl the one which is actually adjusted. R_set is used to calculate K in Eq. (5.4). If $K_\mathrm{g} = 1$, i.e., if the control signal has not to be limited, they are identical. However, if the actuator does not exhibit sufficient control authority, the actual reflection coefficient differs from the prescribed one. The influence of K_g on $|R_\mathrm{cl}|$ and φ_cl can be seen, if Eq. (6.15) is split into magnitude and phase:

$$|R_\mathrm{cl}| = \sqrt{\left[\Re\left\{R_\mathrm{ol}\right\}(1 - K_\mathrm{g}) + \Re\left\{R_\mathrm{set}\right\} K_\mathrm{g}\right]^2 + \left[\Im\left\{R_\mathrm{ol}\right\}(1 - K_\mathrm{g}) + \Im\left\{R_\mathrm{set}\right\} K_\mathrm{g}\right]^2}, \tag{6.16a}$$

$$\varphi_\mathrm{cl} = \arctan \frac{\Im\left\{R_\mathrm{ol}\right\}(1 - K_\mathrm{g}) + \Im\left\{R_\mathrm{set}\right\} K_\mathrm{g}}{\Re\left\{R_\mathrm{ol}\right\}(1 - K_\mathrm{g}) + \Re\left\{R_\mathrm{set}\right\} K_\mathrm{g}}. \tag{6.16b}$$

Calculating the derivatives of Eqs. (6.16) with respect to K_g produces

$$\frac{\partial |R_\mathrm{cl}|}{\partial K_\mathrm{g}} = \frac{\Re\left\{R_\mathrm{cl}\right\}\left[-\Re\left\{R_\mathrm{ol}\right\} + \Re\left\{R_\mathrm{set}\right\}\right] + \Im\left\{R_\mathrm{cl}\right\}\left[-\Im\left\{R_\mathrm{ol}\right\} + \Im\left\{R_\mathrm{set}\right\}\right]}{|R_\mathrm{cl}|}, \tag{6.17a}$$

$$\frac{\partial \varphi_\mathrm{cl}}{\partial K_\mathrm{g}} = -\frac{\Im\left\{R_\mathrm{ol}\right\}\Re\left\{R_\mathrm{set}\right\} - \Im\left\{R_\mathrm{set}\right\}\Re\left\{R_\mathrm{ol}\right\}}{|R_\mathrm{cl}|^2}. \tag{6.17b}$$

The interested reader may find the complete calculation steps in Appendix B.
Figure 6.67 shows how $|R_\mathrm{cl}|$ and φ_cl (top) and their derivatives (bottom) develop with increasing control gain K_g. The curves represent the case for which the downstream reflection coefficient was tuned to form an instability at 85 Hz (compare to results shown in Figs. 6.42

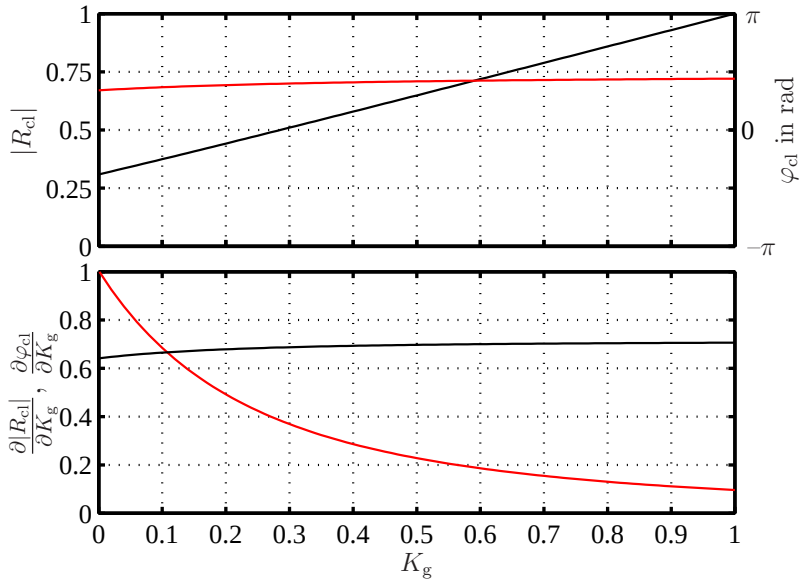

Figure 6.67: Influence of limitation of control signal on closed-loop reflection coefficient ($|R_{cl}|$ black, φ_{cl} red). System is tuned with proportional valves to generate an instability at 85 Hz.

– 6.44). Due to a limited control authority, in these experiments, the control gain had to be limited to 0.8. For $K_g = 0$, $|R_{cl}|$ and φ_{cl} correspond to those of the uncontrolled case. If the actuator had had sufficient control authority, it would have been possible to impose the full control gain $K_g = 1$. The adjusted downstream reflection coefficient $|R_{cl}|$ would then have matched the prescribed one ($|R_{set}|$ see Eq. (6.15)). In the example shown, $|R_{cl}|$ (black) increases almost linearly with K_g, whereas φ_{cl} (red) has a larger slope for small K_g, which decreases with K_g. Consequently, if the control gain is high enough, which is the case for $K_g = 0.8$, the deviation of the actual phase to the prescribed one is relatively small compared to the deviation in magnitude. In this example, the difference between the uncontrolled phase and the one to be adjusted is, thus, quite small.

Figure 6.68 displays results for generating an instability at 175 Hz (compare to Figs. 6.45 – 6.47). Although the initial phase difference is much larger in this case, similar observations can be made. Increasing K_g at first results in a decrease of $|R_{cl}|$. The phase is only slightly affected. Between $K_g = 0.3$ and 0.5, φ_{cl} is rapidly changed and almost tuned to its end value at $K_g = 0.6$. For this control gain, however, the magnitude of R_{cl} is still relatively low. Given an actuator with limited control authority, this means that the phase relationship and therefore the frequency of oscillation would not change when K_g is further increased from 0.6 to 1 – unless non-linear effects would have a non-negligible influence. In contrast to that, the amplitude of oscillation might be strongly influenced. Note that the actuator in this case had sufficient power and K_g could be adjusted to unity.

A simple network analysis is conducted for the latter case. As described previously, the network consists of an up- and downstream reflection coefficient and the control circuit. Figure 6.69 displays the resulting pressure spectra for different control gains, starting with $K_g = 0$ in the upper left frame and going up to $K_g = 0.84$ in the bottom right one.

The graphs show results for a simulation for which the system is excited by a frequency

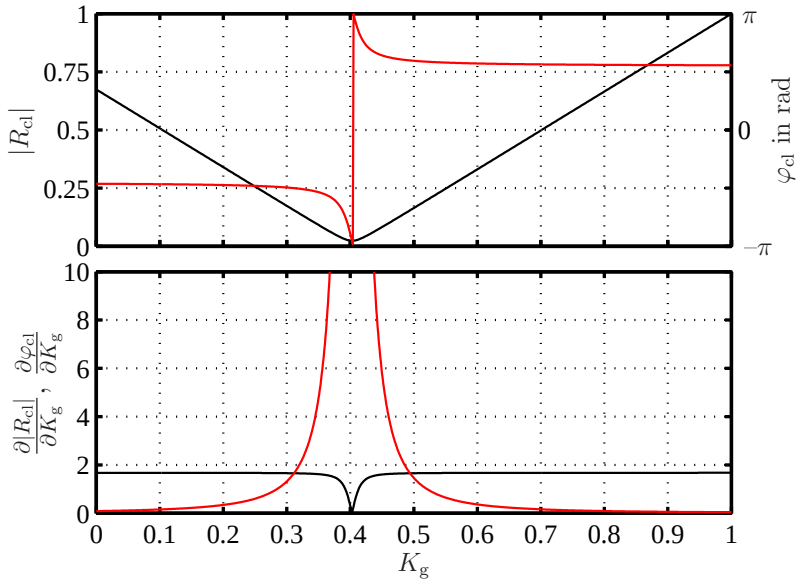

Figure 6.68: Influence of limitation of control signal on closed-loop reflection coefficient ($|R_{cl}|$ black, φ_{cl} red). System is tuned with proportional valves to generate an instability at 175 Hz.

sweep ranging from 30 Hz to 350 Hz. Acoustic excitation is generated with the upstream woofer. Evidently, the resulting spectra can only be compared to the experiment in terms of stating whether the system is unstable or not and at which frequency it oscillates. To allow for a quantitative and qualitative comparison of the spectra, the source term of the flame would have to be implemented into the simulation. Moeck et al. [127] considered the flame source term for the same combustion test rig in their simulations. They simulated the excitation with coloured white noise weighted by the measured source term. Paschereit et al. [146] also incorporated an experimentally determined flame source term into the network model of their combustion test facility. However, for the purpose of this study, this is not necessary.

Figure 6.70 depicts the corresponding control gains marked by the vertical blue line as well as magnitude (black ∘) and phase (red ∘) of the adjusted reflection coefficient. For the first four control gains (Figs. 6.69(a) – 6.69(d)), the pressure spectra are not affected, as the system is stable so that no constructive interference occurs. The phase quasi stays the same and the amount reflected at 175 Hz does not play an important role. At control gains $K_g = 0.48$ and $K_g = 0.6$ (Figs. 6.69(e) and 6.69(f)), a slight increase in the spectra at 175 Hz can be observed caused by the fact that the phase has nearly reached its end value as can be seen in Figs. 6.70(e) and 6.70(f). Further increasing the gain results in a strong increase of the pressure peak at 175 Hz as now the reflection coefficient's magnitude is increased at the correct phase for constructive interference. Beyond a gain of $K_g = 0.84$, the system gets linearly unstable. As no saturation is considered, analysis is not possible for higher control gains. The simulation results clearly show that the system is markedly only tuned at 175 Hz. This is due to dependence of the phase of the reflection coefficient on the control gain.

In both examples, the sensitivity of φ_{cl} decreases with increasing K_g. If K_g is high enough,

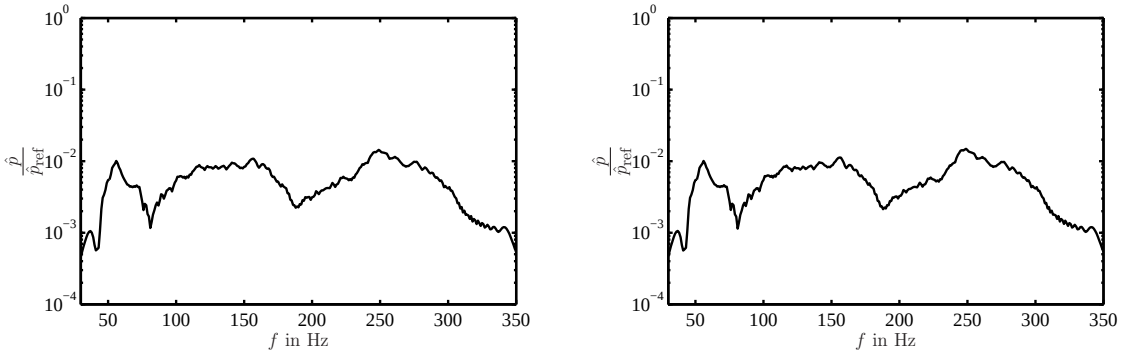

(a) $K_{\mathrm{g}} = 0.0$

(b) $K_{\mathrm{g}} = 0.12$

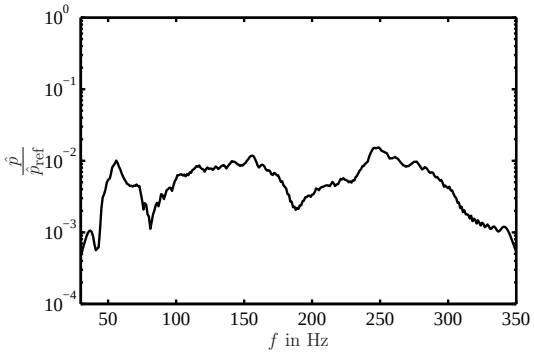

(c) $K_{\mathrm{g}} = 0.24$

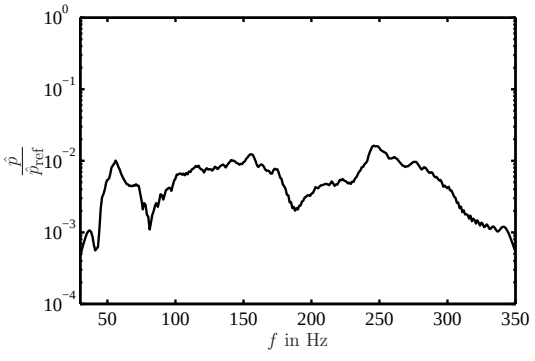

(d) $K_{\mathrm{g}} = 0.36$

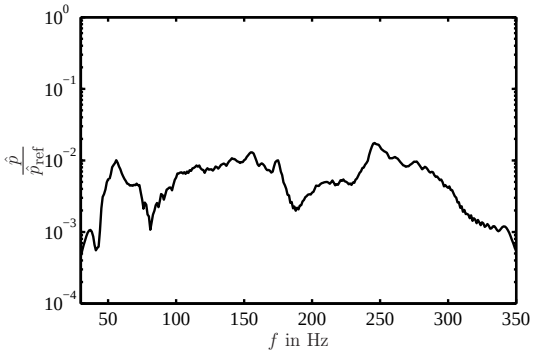

(e) $K_{\mathrm{g}} = 0.48$

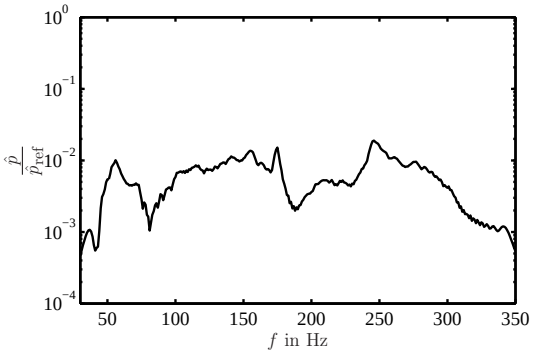

(f) $K_{\mathrm{g}} = 0.60$

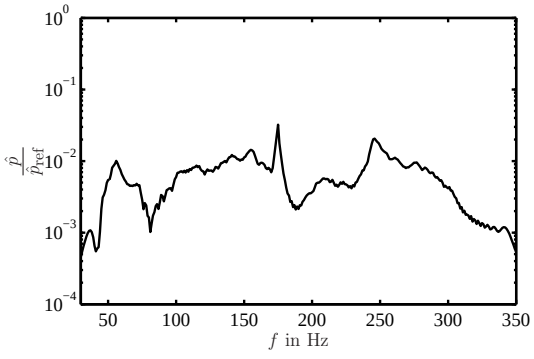

(g) $K_{\mathrm{g}} = 0.72$

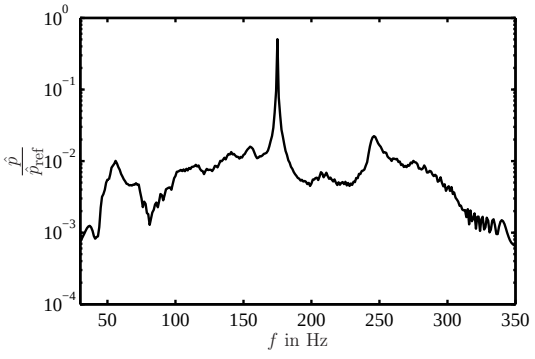

(h) $K_{\mathrm{g}} = 0.84$

Figure 6.69: Scaled pressure spectra for increasing control gain from network simulation. Controller is adjusted to generate an instability at 175 Hz. Control gain starts with $K_{\mathrm{g}} = 0$ in the upper left frame and increases up to $K_{\mathrm{g}} = 0.84$ in the bottom left frame.

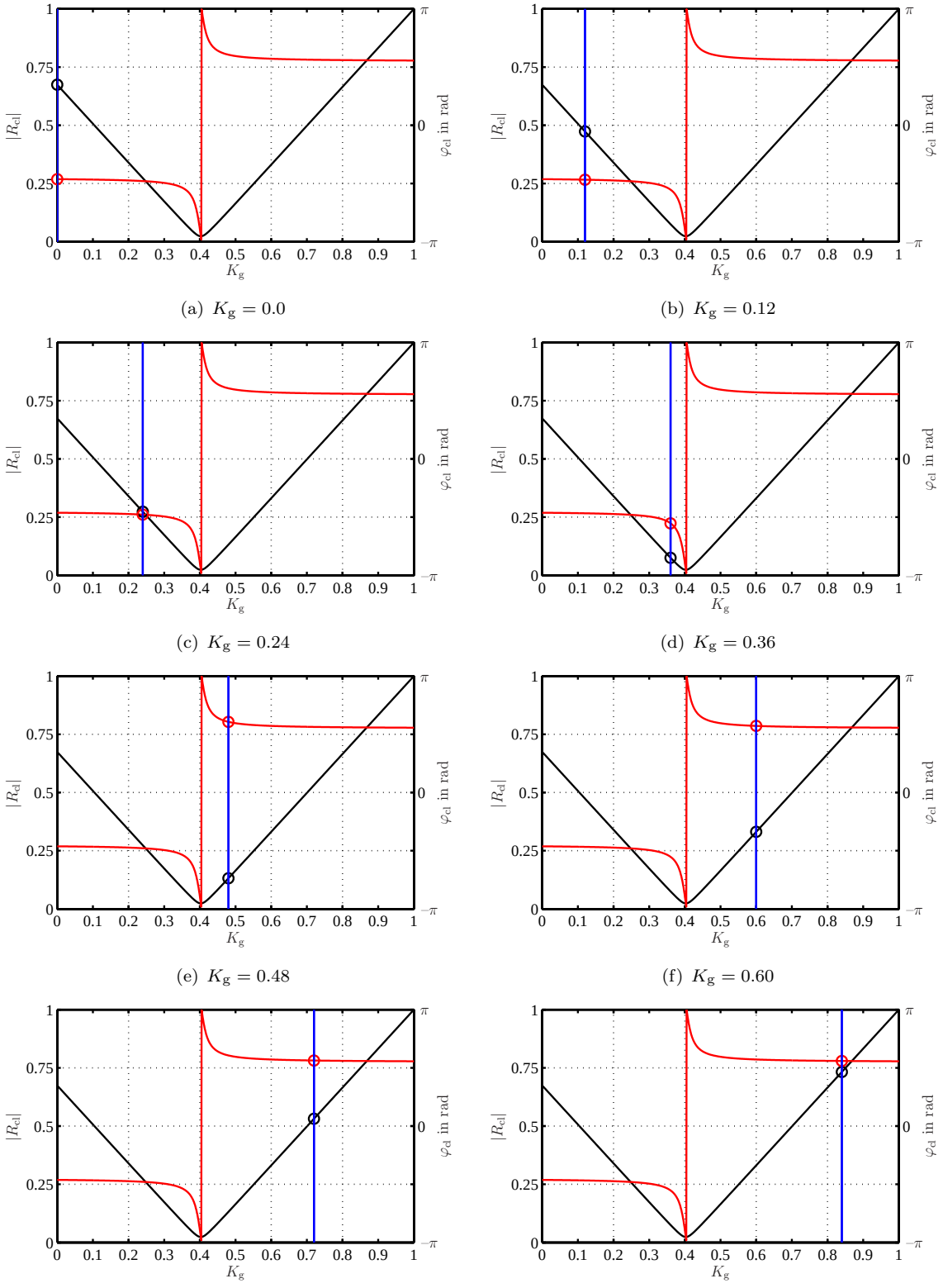

(a) $K_g = 0.0$ (b) $K_g = 0.12$

(c) $K_g = 0.24$ (d) $K_g = 0.36$

(e) $K_g = 0.48$ (f) $K_g = 0.60$

(g) $K_g = 0.72$ (h) $K_g = 0.84$

Figure 6.70: Control gain (vertical blue line) and corresponding magnitude (black ○) and phase (red ○) of the reflection coefficient adjusted for 175 Hz. The control gain starts with $K_g = 0$ in the upper left and increases up to $K_g = 0.84$ in the bottom left frame.

the influence on φ_{cl}, and therefore on the frequency of oscillation, can be neglected. This explains why the system oscillates at the prescribed frequency, although the control gain is limited. For all experiments described in this work, in which the control gain had to be limited, a similar behaviour was found. However, it should be noted that the dependences of $|R_{cl}|$ and φ_{cl} may differ for other cases.

6.6 Influence of Boundary Condition on Flame Shape and Position

In almost all experiments reported, the same tuning strategy was followed. Starting from the passively stabilized system, the self-excited instability of the unstable system was re-established and/or its frequency was changed. The natural thermoacoustic instability was suppressed by using an orifice mounted at the downstream termination (see also explanations in Sec. 6.4.1). Doing so, the pressure drop of the whole combustion system and thus the absolute pressure in the system is changed. The same procedure is suggested for application of the impedance tuning concept in industrial test rigs. Here, the downstream boundary condition is usually realized by a vane simulation section representing the first stage of turbine inlet guide vanes. In this way, a choked outlet flow condition can be achieved for high pressure rigs similar to that in the gas turbine. Usually, industrial test rigs, therefore, exhibit self-excited thermoacoustic instabilities at frequencies different from those in the engine. If this vane simulation section is replaced by a low-reflecting end, e.g., an orifice, to apply the impedance tuning scheme, it should be verified that the influence of the modified hardware on the flame shape and position and thus the dynamics is negligible. If this is not the case, the onset of thermoacoustic instabilities as well as their frequency and amplitude that are observed in the test rig, might not be the same as in the engine, although the acoustic boundary conditions are the same. Escudier & Keller [54, 55] studied the effect of different contraction levels of the downstream outlet on the flow pattern of the recirculation zone at the exit of a swirl burner. Depending on the swirl number of the burner, a strong impact of the downstream boundary condition on upstream flow regions was found.

Here, for the cold flow, the influence of the orifice on the pressure drop of the burner and thus its pressure loss coefficient ζ was measured. Having a physical length that is small compared to the considered wavelengths, the transfer function of the burner might be characterized by a so-called $L-\zeta$ model, as was shown by Paschereit, Schuermans, and Polifke [154, 195]. Therefore, a change in ζ causes a change in the acoustic transfer function of the burner. Furthermore and probably more important, a change of pressure drop across the burner causes a change of the flow field downstream of the burner, so that the momentum equation (see Eq. (2.4)) is satisfied.

To determine ζ, the static pressure was measured up- and downstream of the burner. Figure 6.71 depicts the pressure drop $\Delta\bar{p}$ versus the dynamic pressure $\rho\bar{u}^2/2$ for three different configurations. The mean flow velocity $\bar{u}$ was calculated at the burner outlet ($d = 0.082\,\mathrm{m}$). The black curve shows the result for the open end, the red for the orifice used for the woofer experiments ($d = 0.062\,\mathrm{m}$), and the blue for that of the DDV and Ling Driver ($d = 0.105\,\mathrm{m}$). Measured data points are marked with symbols. Since the pressure loss coefficient is defined

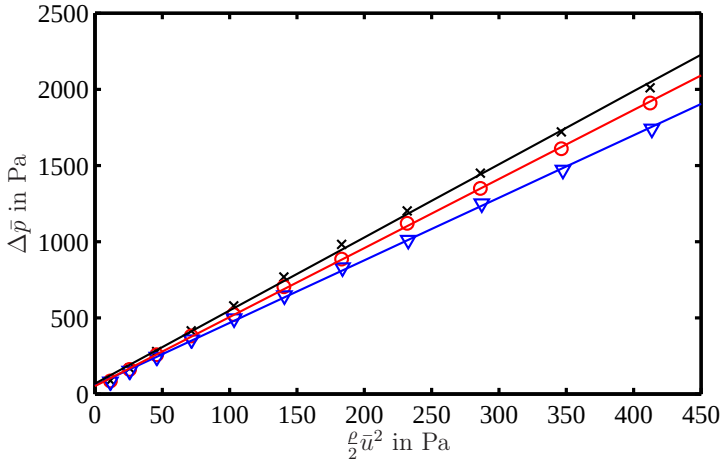

Figure 6.71: Pressure drop of burner versus dynamic pressure at burner outlet. Measured values: black ×: open end, without orifice; ○: orifice with $d = 0.105\,\mathrm{m}$; ▽: orifice with $d = 0.062\,\mathrm{m}$. Linear interpolations shown as solid lines.

as

$$\zeta = \frac{\Delta\bar{p}}{\frac{\rho}{2}\bar{u}^2}, \tag{6.18}$$

it is equal to the slope of the linear interpolations of the measurement points in Fig. 6.71. The influence of the orifices on the loss coefficient can clearly be seen. Using the passive damping devices results in a decrease of 6% and 15%, respectively, i.e., a decreasing pressure loss coefficient with increasing contraction at the downstream end.

To determine the influence of the changed pressure drop, the flame shape and position were recorded with the ICCD camera equipped with an OH-filter (see Sec. 3.3.3). This was done for the impedance tuning experiments reported in Figs. 6.58 – 6.62 in Sec. 6.4.3. These experiments were conducted with the Ling Driver. In case of control, the orifice with a diameter of 0.105 m was mounted.

Figure 6.72 depicts the mean, line-of-sight integrated flame shape, represented by the intensity of the local OH*-chemiluminescence, averaged over 280 pictures. In axial and radial direction, the resolution is 1376 and 1024 pixels, respectively. Three cases are compared.

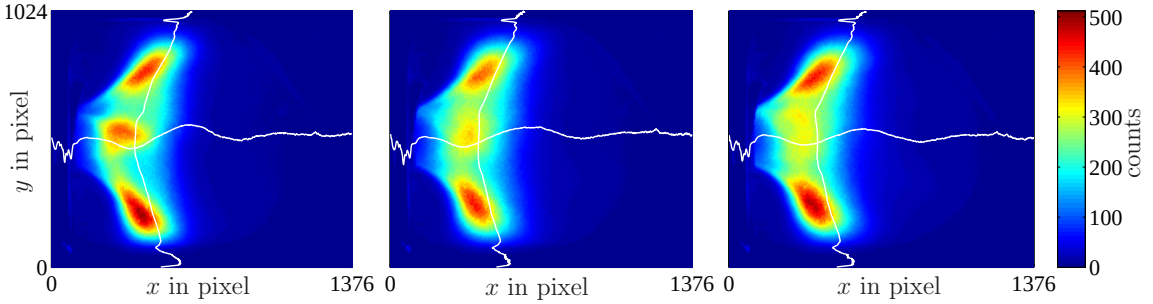

Figure 6.72: Mean OH*-chemiluminescence distribution of the flame (colour code in counts). Left: uncontrolled with orifice; middle: uncontrolled without orifice; right: controlled with orifice – controller is adjusted to reproduce natural instability of the uncontrolled case without orifice.

The left frame of Fig. 6.72, shows the local OH*-chemiluminescence for the uncontrolled

case with orifice mounted, i.e., the configuration to which the impedance tuning scheme has been applied. In the mid frame, the open-end case exhibiting strong thermoacoustic instabilities is depicted. Finally, on the right side, the controlled case is shown. The controller was set to reproduce the self-excited instability, which has been achieved very accurately (confer to Fig. 6.58). For all cases, the strongest heat release is located in the shear layer between inner and outer recirculation zone. Noticeably, for the case without strong pressure and heat release fluctuations (Fig. 6.72 left), also in the center, a maximum in heat release rate is observed. According to the explanations made in Sec. 6.4.3, it cannot be concluded whether this zone is located in the inner recirculation bubble or in the outer shear layer. Comparing both unstable cases, only slight deviations are visible. The artificially induced instability causes the flame to be slightly shifted into the burner. However, this cannot be attributed to the orifice as is seen in the left frame. Also the flame flanks are a bit more inclined. Regarding the mean flame shapes and positions, the pictures suggest that the orifice has quasi no influence. This is even better visible if the white lines, representing the gravity center in axial and radial direction of the flame, are plotted into one graph (Fig. 6.73). Both unstable cases (blue and red) nearly coincide, whereas the uncontrolled

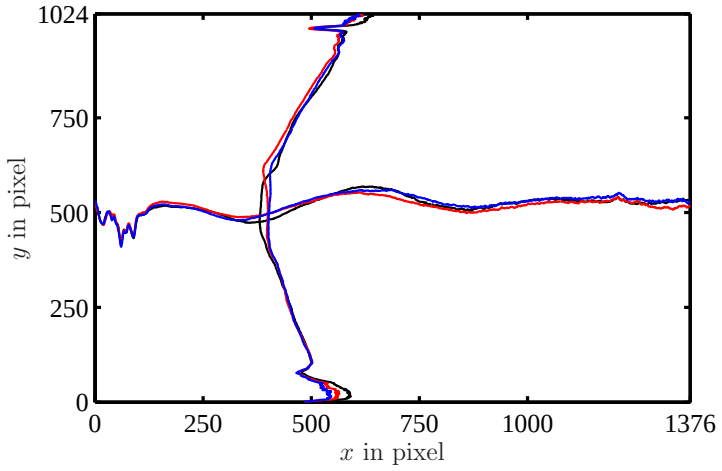

Figure 6.73: Center of gravity lines of mean OH*-chemiluminescence of the flame. Black: uncontrolled with orifice; blue: uncontrolled without orifice; red: controlled with orifice – controller is adjusted to reproduce natural instability of the uncontrolled case without orifice.

case with orifice shows a small deviation due to the higher heat release in the center.
Also, the integrated OH*-chemiluminescence in both axial and radial direction, shown in Figs. 6.74 and 6.75, exhibit only small deviations. In both graphs, the controlled system featured a slightly higher overall heat release.
In conclusion, it can be stated that the orifice's influence on the flame can be neglected for the experiments of this study. However, the change in pressure drop across the burner is only 6%. For smaller orifices or other changes in the downstream boundary that introduce higher deviations, this might not be the case. Therefore, it is recommended to check the influence in the respective setup. An alternative to a passive stabilization is the use of a second control loop with a separate actuator to actively suppress the natural self-excited instability. As it is often difficult to mount one actuator, it might, though, be even more challenging to install another one.

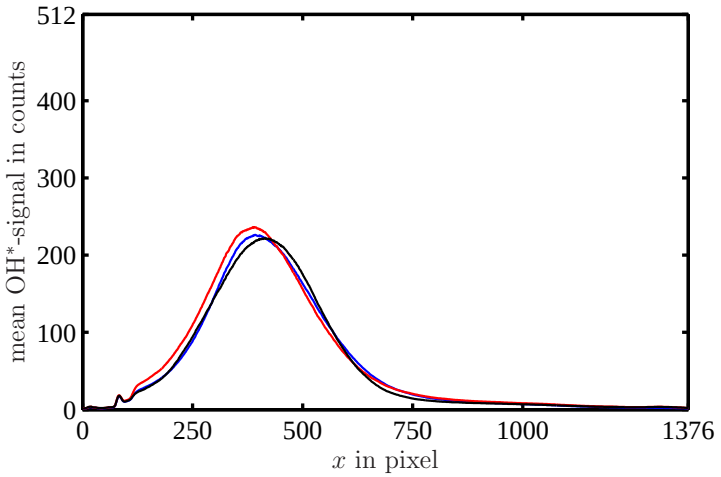

Figure 6.74: Integrated mean OH*-chemiluminescence of the flame (counts vs. pixels in axial direction). Black: uncontrolled with orifice; blue: uncontrolled without orifice; red: controlled with orifice – controller is adjusted to reproduce natural instability of the uncontrolled case without orifice.

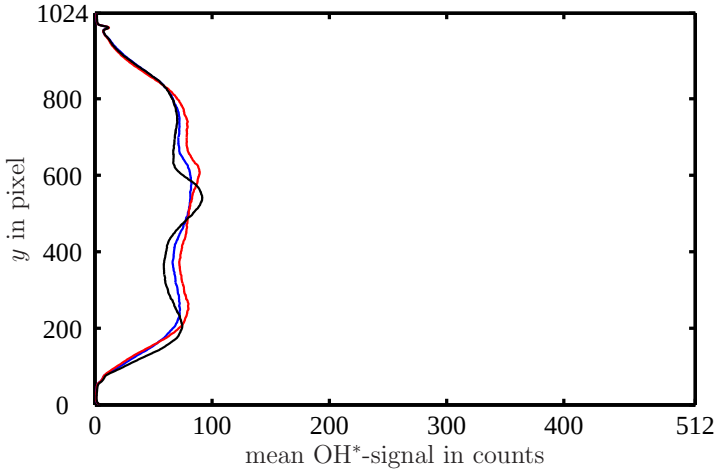

Figure 6.75: Integrated mean OH*-chemiluminescence of the flame (counts vs. pixels in radial direction). Black: uncontrolled with orifice; blue: uncontrolled without orifice; red: controlled with orifice – controller is adjusted to reproduce natural instability of the uncontrolled case without orifice.

"Our doubts are traitors,
And make us lose the good we oft might win,
By fearing to attempt."
W. Shakespeare, Measure for Measure.

Chapter 7

Alternative Applications of Impedance Tuning

Besides its potential of improving the development process of new burner generations, the impedance tuning principle has also significant applications in additional fields. By adequately tuning the acoustic boundary conditions, the thermoacoustic feedback cycle can be interrupted to stabilize self-excited thermoacoustic systems. In Sec. 7.1, it is shown that a manipulation of the downstream reflection coefficient of the combustion test rig is a powerful tool to suppress thermoacoustic instabilities. Furthermore, the control concept can be used to assess the quality of linear stability analysis of network models (Sec. 7.2). For this purpose, the impedance tuning scheme is used to impose a controlled transition from stability to instability, allowing an experimental determination of the linear growth rates and the stability borders. These as well as the frequency of the least stable mode are then compared to predictions from the model.

7.1 Active Instability Control

The impedance tuning scheme can be used to suppress thermoacoustic instabilities. The idea is to interrupt the thermoacoustic feedback cycle by decreasing the magnitude of the downstream reflection coefficient. Reducing the downstream reflection coefficient corresponds to an increase of the acoustic energy loss across the system boundaries. If the energy loss exceeds the net energy gain through the feedback mechanism, this results in a stable system as was mathematically shown in Sec. 2.6. Equivalently, its phase could be changed in such a way that unsteady heat release and acoustic pressure destructively interfere with each other.
The concept of changing the acoustic boundary condition to render a system stable was

also followed by other authors. Bloxsidge et al. [26] used this fact to suppress thermoacoustic instabilities in an afterburner in a semi-active semi-passive manner. They altered the upstream boundary condition of their test facility by feedback control of a movable centerbody. Axial movement of the centerbody changed the blockage of the flow and thus caused a change of the upstream reflection coefficient due to an oscillating mass flow into the combustion chamber. The acoustic pressure peak could be reduced by approximately 20 dB.

Tran, Ducruix, and Schuller [222, 223] have chosen a passive tuning approach to reduce the upstream reflection coefficient at single frequencies. They modified the inlet boundary condition of a laboratory-scale swirler test rig by using perforated plates backed by a cavity. The reflectivity could by decreased by adequately adjusting cavity depth, bias flow, and plate perforation. At the oscillation frequency, the reflection coefficient's magnitude could be reduced to 0.15 – 0.2 causing a pressure peak reduction of 10 dB in the combustion chamber.

Both mitigation strategies concentrated on the cold section of the combustion test facilities, where application of active or passive means is easier to accomplish than in the hot gas path. Probably, modification of the reflectivity in the latter exhibits more control authority, as the effectiveness of tuning at the upstream side is somehow limited, because of the burner geometry situated downstream of the tuned boundary condition. The system composed of burner and flame on the one side and downstream boundary condition on the other is less affected. This issue can be overcome by tuning on the downstream side, which is possible with the impedance tuning approach.

Not only experimentalists changed the boundary conditions to render an unstable system stable. Martin et al. [119] conducted LES simulations in which they controlled a self-excited instability by modifying the downstream reflection coefficient to increase the damping.

Paschereit et al. [144, 149, 150] also modified the downstream reflection coefficient of an atmospheric swirl-stabilized combustion test rig. However, their intention was to generate an instability at various axisymmetric and helical unstable modes. They could passively adjust the downstream end from almost non-reflecting to open end. By doing so, they investigated the individual unstable modes, compared them to water channel flow investigations, and assessed the control authority of different active feedback control approaches to render the system stable.

For the results reported subsequently, experiments were conducted with an open-end boundary condition at the downstream termination of the combustion test rig. The downstream reflection coefficient was reduced in a controlled frequency band ranging from approximately 75 Hz to 95 Hz. This is the frequency interval in which the combustion system got unstable at an equivalence ratio of $\phi = 0.75$ and a thermal power of 130 kW. The multi-frequency tuning approach was used. For the controller identification weighting factors, as described in Sec. 5.3, were used to obtain an accurate model around the instability frequency. For frequencies outside the above mentioned interval, it was only made sure that the controller was stable and proper and did not cause an instability. Woofers were used as actuators.

Figure 7.1 shows the uncontrolled reflection coefficient for the open end (black). The red curve represents the controlled case for imposing a low-reflecting end, proving that the magnitude (top) can be considerably decreased. The phase is also modified as can be seen in the bottom frame. Although the change is relatively small, this definitely also might

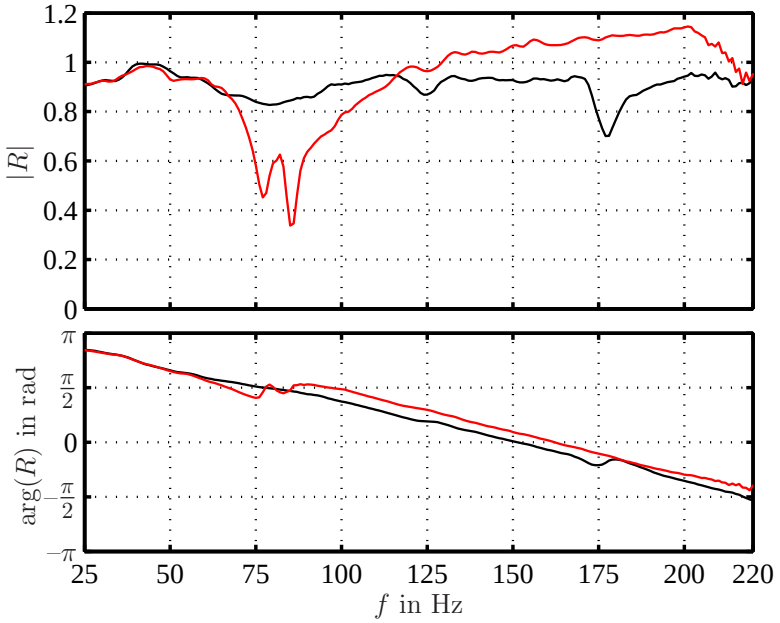

Figure 7.1: Magnitude (top) and phase (bottom) of downstream reflection coefficient. Black: baseline case without control; red: controlled case for a control gain of $K_g = 0.4$.

have a stabilizing effect. Two remarks should be made here. First, by imposing above mentioned weighting factors for the controller identification, the controller model was forced to accurately match the calculated control law at the frequency of instability, accepting slight deviations at adjacent frequencies. This explains the waved form within the controlled frequency band. Second, as has already been elucidated in Sec. 6.4.1, control in presence of high amplitude pressure oscillations is intricate. To obtain the best results, a control gain was introduced in the control circuit (see also Sec. 6.5), which was continuously increased from 0 (no control) towards 1 (full control). The gain was adjusted to yield the best results, which was in this case 0.4. At larger control gains, the system reacted too strong at higher frequencies, thus, complicating control.

The corresponding pressure spectra are shown in Fig. 7.2. For the uncontrolled baseline case, distinct peaks at 88 Hz and its multiples are observable. The $\lambda/4$-mode at 88 Hz has an amplitude of 158.5 dB. Using the impedance tuning scheme, this self-excited instability can be successfully suppressed. A peak reduction of 35 dB is achieved. The harmonics – indicators of a highly unstable system oscillating in its limit-cycle – are not present anymore. Also, reducing $|R|$ provokes two additional peaks adjacent to the natural instability frequency in the spectrum of the combustor pressure. As the system was controlled in a quite narrow frequency band, this feature might be similar to the so-called peak-splitting phenomenon, typically encountered when using phase-shift controllers for stabilization [11, 12, 13, 41, 125]. Under the influence of the phase-shift controller, the frequency of the dominant mode slightly changes. At an optimal phase-shift, the neighbouring peaks are of the same height; one slightly shifted to lower and one to higher frequencies. Referring to Fig. 7.2, two peaks can clearly be seen, however, the one at 100 Hz is higher than the one at 70 Hz. Furthermore, at the instability frequency of 88 Hz, still a very small peak is present. In analogy to the phase-shift controller, this would correspond to the fact that not the optimal phase-shift is adjusted.

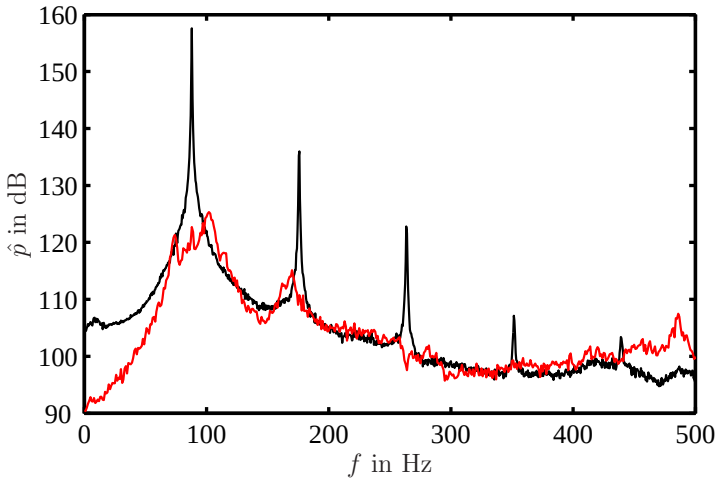

Figure 7.2: Spectra of acoustic pressure. Black: baseline case without control; red: controlled case for a control gain of $K_g = 0.4$.

Noticeably, application of a two-parameter extremum seeking controller for phase-shift control at the same combustion test rig showed that the stabilizing influence of this active control scheme could also be attributed to a reduction of the downstream reflectivity. The results reported in reference [126] also show the occurrence of peak-splitting.

7.2 Validation of Linear Stability Analysis

Application of low-order network models for linear stability analysis is widely spread in industry and academia to predict the thermoacoustic characteristics of combustion systems. A comprehensive overview on the network approach has already been given in Chapter 4. Even though a vast amount of publications on this topic exists (see Tab. 4.1), much less is reported on the predictive capabilities of such stability analyses with respect to real system behaviour. This is due to the fact that often only single operating conditions were considered or the models were not verified with experimental data. In this sense, little effort has been made on investigating whether predicted critical parameter values, for which the combustion system switches from stability to instability, agree with experimental observations. In the following, a brief overview of existing approaches reported in the literature is given.

Matveev & Culick [121, 122] studied this transition by varying the heat input to a Rijke tube and compared it to the predictions of their model. The model was based on the one-dimensional wave equation accounting for heat addition, a non-uniform temperature field, and boundary layer losses but neglecting mean flow. Since the transition is dependent on the mode shapes, which in turn are sensitive to the temperature field, they set up a comprehensive heat transfer model to simulate the unsteady heat addition by the heating grid. Regarding the stability border, a quite good agreement was found, however, linear in nature, the model could not predict hysteresis effects, which were observed in the experiments.

Kopitz et al. [87] set up a low-order network model and compared simulations to experimental investigations conducted in an annular type combustion test rig. The flame transfer function was measured at stable conditions. By using scaling laws for both equivalence ratio and power, they calculated the flame transfer function for different operating conditions. Through this, they were able to qualitatively predict the transition from instability to stability for the axial mode, which they found in experiments.
The predictive capabilities of a network model were also compared to experiments by Bohn & Deuker [28, 44]. Experiments were conducted in an atmospheric combustion test rig equipped with a matrix burner. They investigated several setups and found satisfactory agreement in terms of determination of the stability border as a function of power and equivalence ratio.
Bloxsidge et al. [27] predicted the frequency of oscillation in afterburners with reasonable accuracy. Also, the trends in frequency variation caused by equivalence ratio, inlet Mach number, and duct geometry were captured. However, their model was not able to calculate the transition between two different unstable operating regimes.
Bellucci et al. [19] accurately predicted engine pressure spectra for unstable operation conditions by fitting analytical models to measured burner and flame transfer functions. Limit-cycle amplitudes were obtained by fitting a non-linear fuel saturation term. They were also able to predict the damping effect of Helmholtz resonators.
Recently, prediction of non-linear phenomena as, for example, hysteresis, triggering, or frequency shifts, were compared to experiments, conducted at the swirl-stabilized burner also investigated in this study, by Moeck et al. [127] and to measurements at a perforated plate burner by Noiray et al. [141]. Both groups incorporated non-linear flame responses in their network models. Good agreement between simulations and experiments was found.
Here, the importance of experimental validation is addressed by using the impedance tuning scheme. It is employed to continuously vary the downstream reflection coefficient of the combustion chamber from fully reflecting to anechoic. By doing so, the transient behaviour of the system can be studied. The transition from stability to instability is accomplished by introducing an additional control gain into the control circuit. In addition to that, an extension of the common linear procedure, where the stability of an operating point is classified solely based on the presence of high amplitude pressure pulsations and their frequency, is given. Generally, the predicted growth rates are only compared to measurements with respect to their sign, which obviously lacks a quantitative component. In this thesis, validation of linear stability analysis is conducted by comparing calculated and experimentally determined linear growth rates of unstable modes.
The acoustic field in the combustion system is described by the most basic form of a network model, similar to the one that is used to calculate the control law for discrete-frequency tuning (see Sec. 5.4). Again, the total system is divided into experimentally determined upstream and downstream reflection coefficients. The former comprises the flame response. This approach has been chosen to minimize modeling uncertainties.

Prediction of the stability border

The system was operated at the same conditions described in the previous section. The controller transfer function K was adjusted to generate an anechoic downstream end, i.e., $R_{\mathrm{cl}} = 0$ in Eq. (5.4) for frequencies between 75 Hz and 95 Hz. In order to find the stability border, the downstream reflection coefficient, however, had to be changed continuously

from the uncontrolled case towards $R_{\mathrm{cl}} = 0$. Therefore, an additional gain K_{g} (confer to Sec. 6.5) was inserted into the controller, ranging from 0 to 1. If set to 0, no signal was given to the actuator, i.e., $R_{\mathrm{cl}} = R_{\mathrm{ol}}$ (no control), and $K_{\mathrm{g}} = 1$ resulted in $R_{\mathrm{cl}} = 0$. Continuously changing this gain was expected to result in a continuous change of R_{cl}.
Figure 7.3 shows the magnitude (top) and phase (bottom) of R_{cl} for four different control gains. The uncontrolled case is again represented by the black curve. The blue, green,

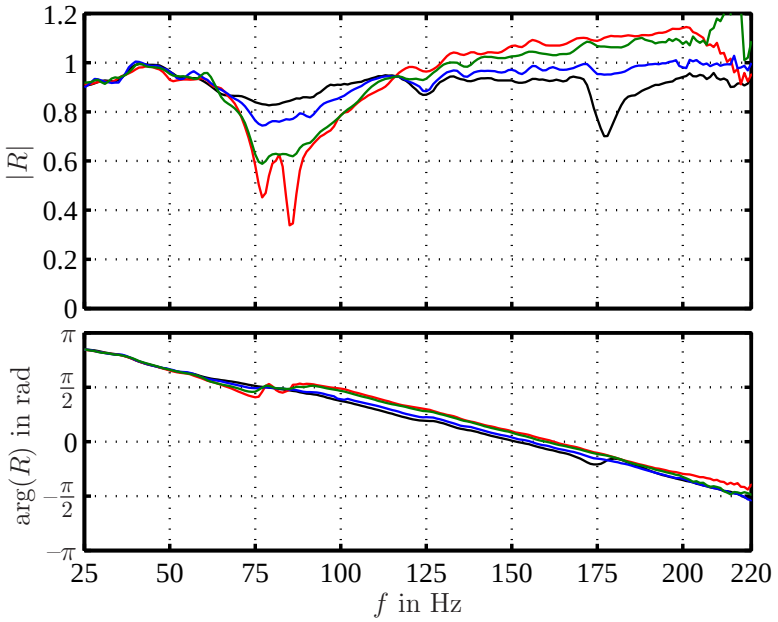

Figure 7.3: Magnitude (top) and phase (bottom) of reflection coefficient for different control gains. Black: $K_{\mathrm{g}} = 0$ (w/o control), blue: $K_{\mathrm{g}} = 0.15$, green: $K_{\mathrm{g}} = 0.325$. red: $K_{\mathrm{g}} = 0.4$.

and red curves show results for control gains of 0.15, 0.325, and 0.4, respectively. Within the controlled frequency band, R_{cl} is decreased from 0.85 over 0.75 and 0.63 down to 0.5. Above 120 Hz, R_{cl} is increased to values larger than unity. This is due to the fact that the controller transfer function has only been identified to satisfy the control objective between 75 Hz to 95 Hz. For frequencies outside this interval, the identification algorithm sets K to values which cause an increase of R_{cl}.
In Fig. 7.4, the pressure spectra for these four cases are shown. Without control (black), a distinct peak at 88 Hz occurs indicating a strong thermoacoustic instability with a peak amplitude of approximately 158.5 dB. Decreasing $|R_{\mathrm{cl}}|$ to 0.8 ($K_{\mathrm{g}} = 0.15$) results in an attenuation of the peak amplitude of 16 dB. No harmonics are observed anymore. For a downstream reflectivity of $|R_{\mathrm{cl}}| = 0.63$ ($K_{\mathrm{g}} = 0.325$), the pressure peak is further decreased by 16 dB. At a control gain of 0.4 ($R_{\mathrm{cl}} = 0.5$), the peak amplitude is completely suppressed (peak reduction of 35 dB, see previous section). According to the results shown, the combustion system switches from unstable to stable somewhere around $R_{\mathrm{cl}} = 0.8$.
A phenomenon possibly occurring when changing the operating conditions from unstable to stable is hysteresis of this transition. In this case, the dynamics of the system depend on the fact whether the system parameter, which governs stability, is increased or decreased. Hysteresis related to thermoacoustic instabilities was, for instance, observed by Lieuwen [113], Matveev & Culick [121, 122], Knoop et al. [86], and Lepers et al. [104]. In the works cited,

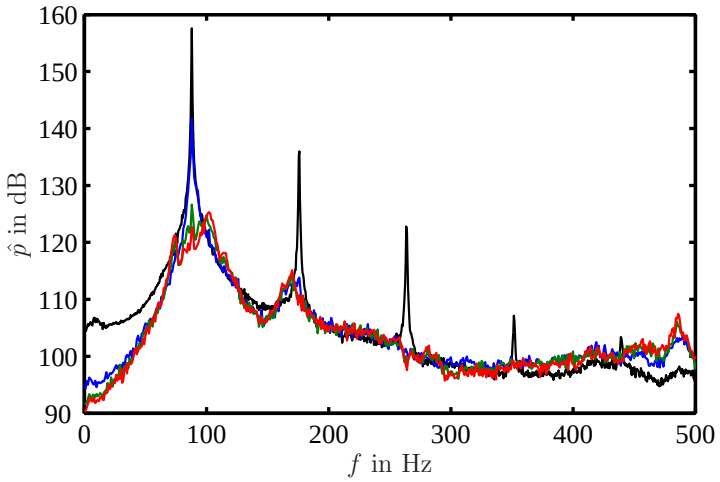

Figure 7.4: Spectra of acoustic pressure for different control gains. Black: $K_g = 0$ (w/o control), blue: $K_g = 0.15$, green: $K_g = 0.325$. red: $K_g = 0.4$.

fundamentally different experimental configurations were investigated. Lieuwen [113] used a premixed swirl-stabilized combustor, which is closest to the configuration considered in the present work. He observed a hysteretic dependence of the oscillation amplitude on the combustor inlet velocity. As mentioned above, Matveev & Culick [121, 122] studied thermoacoustic oscillations in a Rijke tube with an electrically heated grid. They found hysteresis over a considerable range of heater power. Subcritical instabilities in a premixed dump combustor were investigated by Knoop et al. [86] and Isella et al. [82]. Hysteresis was observed with respect to the equivalence ratio. Lepers et al. [104] found a hysteretic dependence of the oscillation amplitude of an azimuthal mode on the fuel/air mixture ratio in a full scale annular combustion chamber. Recently, the hysteretic behaviour of the combustor used in this investigation was investigated [127] showing that subcritical behaviour might occur for the variation of air and gas mass flow as well as preheat temperature. As the linear stability analysis is merely valid in the linear regime, it is obvious that if hysteresis occurs, the model can only capture the transition from stable to unstable conditions.

Figures 7.5 and 7.6 prove that hysteresis can be excluded for the variation of the downstream reflection coefficient for the operating conditions considered here. They depict spectral peak amplitudes of the acoustic pressure $\hat{p}_{\max}$ and scaled fluctuation of the OH-radical $\hat{\hat{Q}}_{\max}/\hat{\hat{Q}}_{\mathrm{ref}}$ for increasing (black $\times$) and decreasing (red $\circ$) control gain, respectively. Only slight deviations are visible. Between a control gain of 0 and 0.15, $\hat{p}_{\max}$ rapidly decreases, whereas it remaines almost constant for $K_g > 0.2$. This indicates a transition from stable to unstable behaviour.

Figure 7.7 shows that an increase of the control gain K_g corresponds to a monotonic decrease of the controlled downstream reflection coefficient's magnitude R_{cl}. Here, the magnitude of R_{cl} at the frequency at which the acoustic pressure is maximal is plotted versus the control gain.

In the upper frame of Fig. 7.8, the calculated growth rates $-\Im\{\omega_{\mathrm{eig}}\}$ for the least stable mode versus the magnitude of the adjusted downstream reflection coefficient $|R_{\mathrm{cl}}|$ are shown. The red line represents the stability border with a growth rate of 0. As can be seen, the model predicts a transition from stable to unstable for $|R_{\mathrm{cl}}| = 0.81...0.83$ corresponding

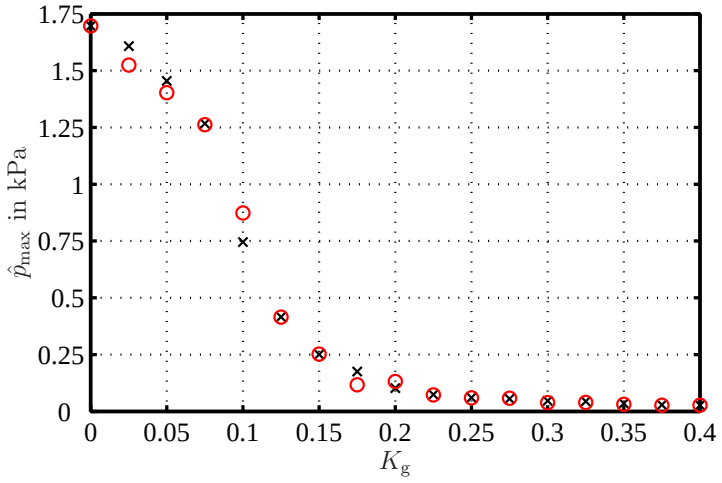

Figure 7.5: Spectral peak amplitude of acoustic pressure for increasing (black ×) and decreasing (red ○) the control gain K_g.

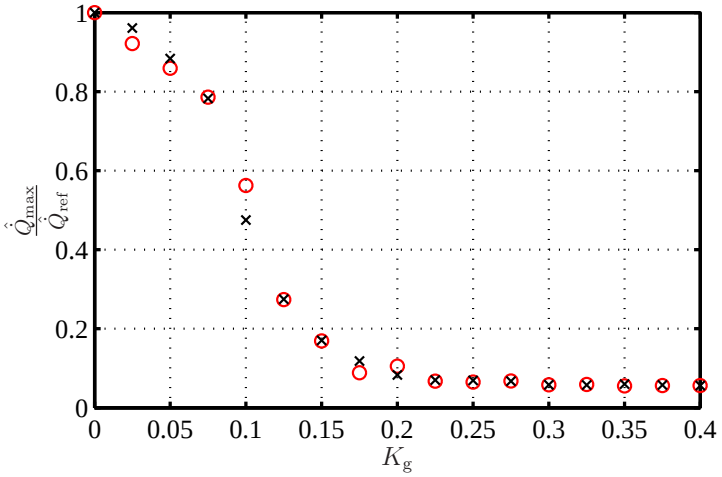

Figure 7.6: Spectral peak amplitude of OH*-fluctuation for increasing (black ×) and decreasing (red ○) the control gain K_g.

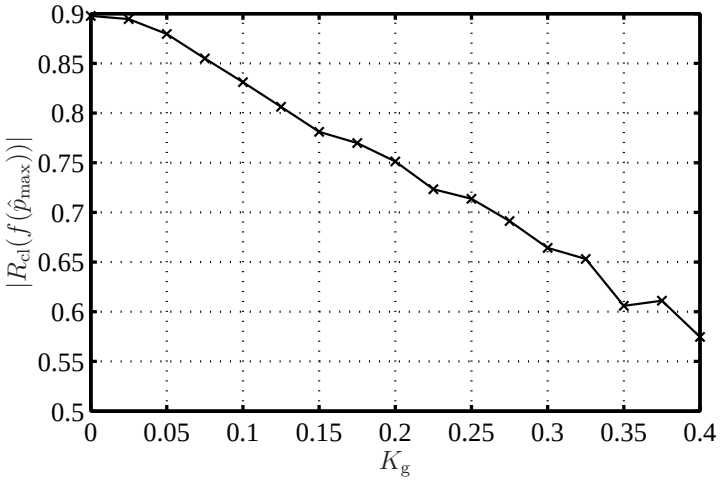

Figure 7.7: $|R_{\text{cl}}|$ at the frequency $f(\hat{p}_{\max})$ at which the acoustic pressure is maximal versus the control gain K_g.

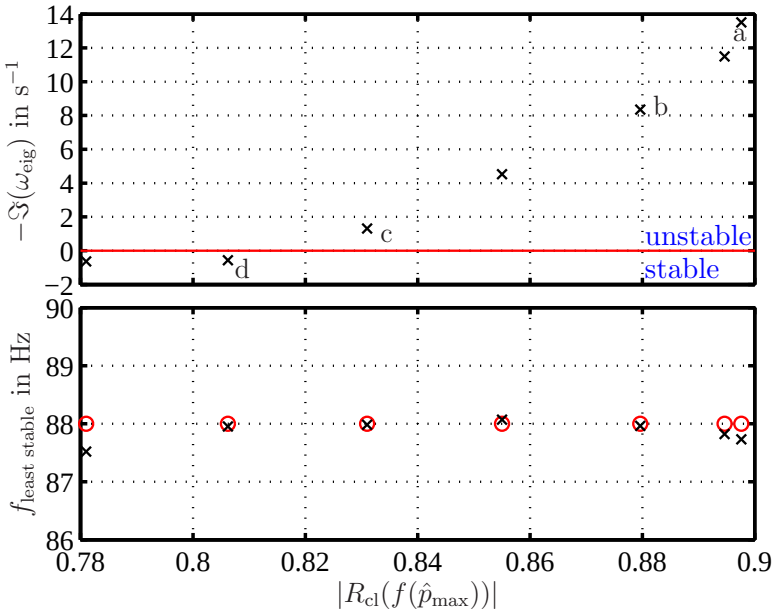

Figure 7.8: Growth rate $-\Im\{\omega_{\mathrm{eig}}\}$ (top) and frequency (bottom) of the least stable mode as a function of $|R_{\mathrm{cl}}|$.

to a control gain between 0.125 and 0.1. Decreasing K_{g}, i.e., increasing $|R_{\mathrm{cl}}|$, is computed to have a clearly destabilizing effect as the growth rate increases. For $|R_{\mathrm{cl}}| < 0.81$, a negative growth rate is calculated, thus, predicting all modes to be damped.

The model results agree with the intuitive interpretation of the experimental observations. However, these observations are purely visual and obviously do not allow to unambiguously decide at which point the combustion system switches from unstable to stable. To assess how accurate the model determines the stability border, the probability density functions (PDF) of the pressure fluctuations are calculated. The PDF of a harmonic signal (limit-cycle at the instability frequency) superposed with noise typically shows a clearly bimodal structure. The reason is that the system spends more time near the extremal values of the limit-cycle. For a rigorous treatment of this visualization method, the reader is referred to references [113, 181].

Figure 7.9 shows the PDFs of the points denoted a–d in Fig. 7.8. Starting from the upper left frame (a), the graphs show decreasing magnitudes of the reflection coefficient in clockwise direction. Both upper frames (a, b) display cases for a positive growth rate. Peaks at approximately 1.7 kPa and 1.4 kPa indicate strong limit-cycle pressure oscillations. Close to the predicted stability border (c) only small humps at 0.5 kPa are observable, which vanish when $|R_{\mathrm{cl}}|$ is further decreased to the stable regime (d). The unsteady pressure distribution in Fig. 7.9 d typically occurs during stable operation [113]. The model also predicts a stable system for this setting. As stated by Rowley et al. [181], a system is in a limit-cycling state if two distinct peaks are present in the PDF. However, if only a single peak (Fig. 7.9 d) is observed, it cannot be concluded for sure that the system is not in a limit-cycle, as it may be hidden in the noise. Nevertheless, it can be stated that noise is the dominant mechanism and that the model is clearly mature in predicting the operating conditions, which are governed by the limit-cycle. To gain further insight, the growth rates are experimentally determined and compared to those obtained from the model. Results

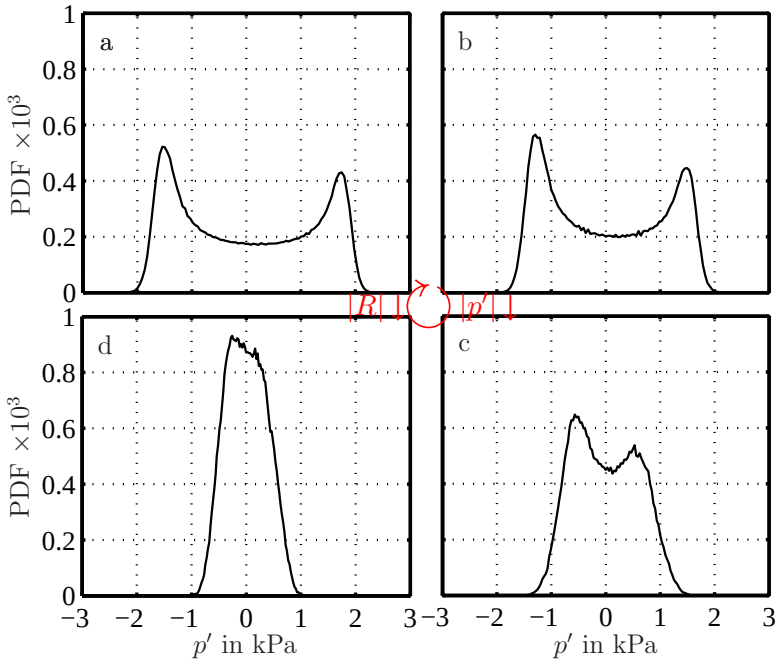

Figure 7.9: Probability density functions of acoustic pressure for different $|R_{\mathrm{cl}}|$ specified in Fig. 7.8.

are shown in the next paragraph.
Concerning the frequency of the least stable mode, the simulations almost exactly match the experimental observations. This is shown in Fig. 7.8 (bottom), where the measured frequencies (○) and the computed ones (×) are plotted versus $|R_{\mathrm{cl}}|$. The deviation is smaller than 0.5 Hz. It should be mentioned that the determination of the stability border is sensitive to the accuracy of the system identification. Slight inaccuracies in the model can cause large variations in the computed growth rates. This is in contrast to the determination of the least stable mode's frequency, which is found to be less sensitive to inaccuracies.

Comparison of predicted and experimentally determined growth rates

The idea of investigating the transition from stability to instability by actively controlling the system is not new. Poinsot et al. [162, 164, 165] initially suggested to use active instability control to study the initiation process of thermoacoustic instabilities. They used a simple phase-shift controller driving a loudspeaker upstream of the flame to switch between stability and instability. From their observations, they suggested that the growth process can be divided into different stages, i.e., linear growth, transition, limit-cycle.
For a comparison of experiment and prediction, the linear growth rate $-\Im\{\omega_{\mathrm{eig}}\}$ of the unstable $\lambda/4$-mode has somehow to be determined from experiments. Here, this was done by ensemble averaging the transition process from stable to unstable, induced by the impedance tuning. Unsteady pressure data of a large number of these transition processes were captured by automatically switching the controller between two different control gains K_{g} at a frequency of 1 to 2 Hz. The variation of the combustor pressure with time during this process is displayed in Fig. 7.10. The trigger signal used to turn the controller on and off, is plotted in the same graph (red).
As has been shown above, the combustion system was unstable over a range of $|R_{\mathrm{cl}}|$. Thus,

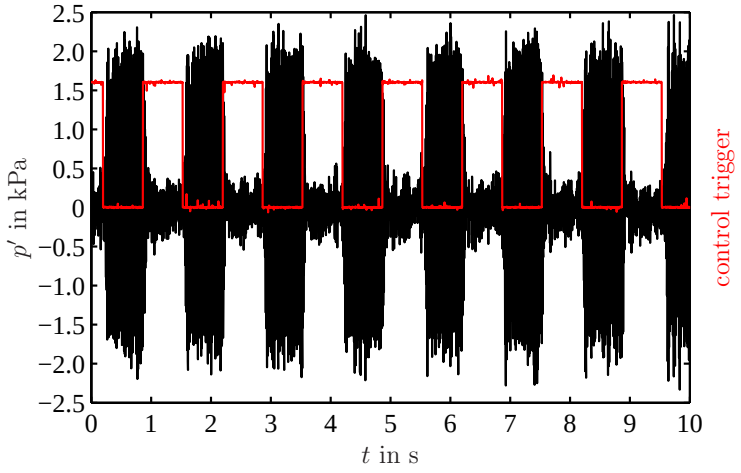

Figure 7.10: Time traces of acoustic pressure (black) and trigger signal (red) during transition from controlled to uncontrolled state.

$-\Im\{\omega_{\mathrm{eig}}\}$ was determined always starting from the same stabilized state, which was then switched to different values of K_{g} corresponding to different values of $|R_{\mathrm{cl}}|$. It was ensured that both, stabilization and growth to limit-cycle amplitude, were fully captured.
To obtain the linear growth rate of the unstable mode, an exponentially growing harmonic wave given by

$$x(t) = \hat{A} e^{\omega_{\mathrm{GR}} t} \cos(\omega t + \varphi) \tag{7.1}$$

was identified to each realization of the linear stage of the transition process. Here, $\hat{A}$, ω, φ, and ω_{GR} denote initial amplitude, frequency, phase, and linear growth rate of the wave. All parameters were subject to the identification process.
As the model is only valid in the linear regime, it has to be ensured that only the linear part of the growth rate is determined from the experimental data, i.e., before the process starts to be saturated. The four parameters describing the exponentially growing harmonic wave were found by using a non-linear optimization routine to minimize the error between the analytic expression Eq. (7.1) and the measured sensor signal in a least squares sense:

$$\min_{\hat{A},\omega,\varphi,\omega_{\mathrm{GR}}} \sum_n \left[x(t_n) - x_{\mathrm{exp}}(t_n)\right]^2 . \tag{7.2}$$

Here, $x_{\mathrm{exp}}(t_n)$ is one of the measured microphone signals at the sampling time t_n. The parameters governing the growing wave were determined individually for each sensor. In the linear stage of the transition process, all sensor signals grow at the same rate [126]. One realization of the transition process capturing the linear growth of the combustor pressure is displayed in Fig. 7.11. The graph shows a good agreement between measured acoustic pressure (black dots) and identified harmonic wave (red).
However, due to a high noise level and slight variations in the mean operating conditions, the measured growth rate might deviate from the statistical mean. For this reason, ensemble averages based on a large number of realizations were determined. A histogram of the growth rates of these realizations, comprising the signals of three microphones and a photomultiplier, is shown in Fig. 7.12. The high variance in the distribution of the exper-

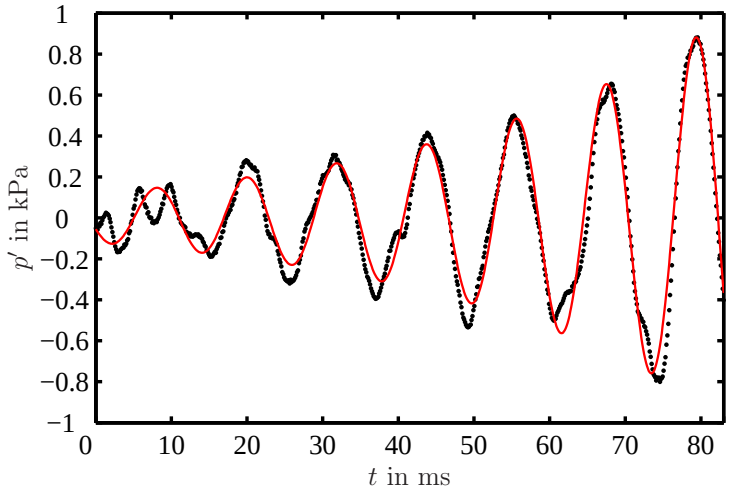

Figure 7.11: Time traces of acoustic pressure (black dotted) during transition from controlled to uncontrolled state and identified exponential wave (red).

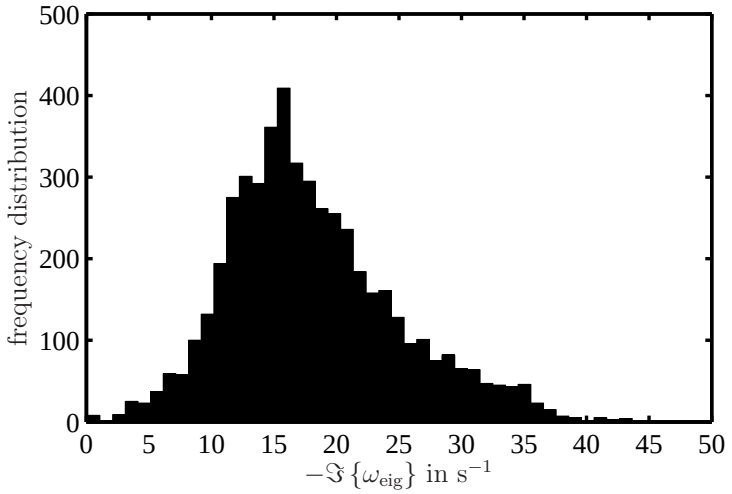

Figure 7.12: Histogram of linear growth rates $-\Im\{\omega_{\text{eig}}\}$ from controlled to uncontrolled state calculated with Eq. (7.1).

imentally determined growth rates underlines the importance of taking ensemble averages of a large number of realizations.

In Fig. 7.13, the averaged growth rates $-\Im\{\omega_{\text{eig}}\}$ obtained from the four sensors (red ∘) and the predictions from the model (black ×) are displayed. For each adjusted downstream reflection coefficient, a model was identified. The experimentally determined and predicted growth rates are plotted over different values of $|R_{\text{cl}}|$. This is because the instability frequencies predicted by the model exhibit some variations when compared to the measured ones and so do the corresponding values of $|R_{\text{cl}}|$. For Fig. 7.13, always the value of $|R_{\text{cl}}|$ is taken that corresponds to the calculated instability frequency.

The operating conditions were changed to $\phi = 0.7$ at 120 kW. This shifts the natural instability frequency to 86 Hz. In contrast to the experiments conducted to find the stability border, a decrease of $|R_{\text{cl}}|$ is accompanied by a variation of the oscillation frequency between 86.5 Hz and 83 Hz. As a consequence, the values for $|R_{\text{cl}}|$ on the x-axis differ from

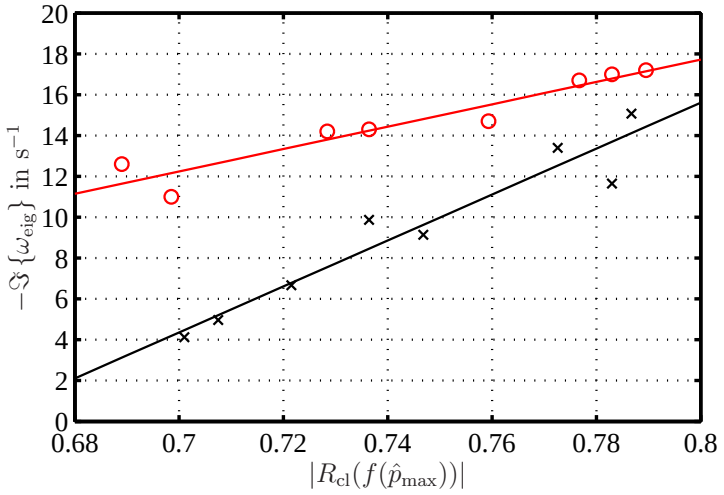

Figure 7.13: Growth rates $-\Im\{\omega_{\mathrm{eig}}\}$ in s^{-1} determined from experiments (red ∘) and predicted by the model (black ×) as a function of the downstream reflection coefficient $|R_{\mathrm{cl}}|$ at the instability frequency.

those shown in Fig. 7.11. Also, the different operating points cause a change in growth rates. Note that the same control law has been used as for the determination of the stability border, proving that the controller is sufficiently robust to cope with changes in the operating conditions, which, although small, yet have a markedly influence on the system behaviour.

In both cases, the growth rates in Fig. 7.13 show the same ascending trend. The models were determined based on the downstream reflection coefficients measured for the unstable cases. In presence of high amplitude pressure fluctuations, the reflection coefficient might be affected by non-linear dissipation at the downstream end. This was also observed by Heckl [73], who showed that the reflection is reduced by approximately 1% at a pressure amplitude of 145 dB. As shown in Fig. 7.4, the pressure amplitude is 158.5 dB in this investigation, evidently causing further reduction of R_{cl}. For a pressure amplitude of 158 dB, experiments showed that the non-linear dissipation causes a decrease of 4.4% at the instability frequency when compared to the stable case. This deviation continuously decreases with decreasing amplitude. Therefore, the reflection coefficients were corrected to take this effect into account.

However, as shown in Fig. 7.13, the computed growth rates still have an offset from the experimentally determined ones, which gets smaller for larger growth rates. The reason might be twofold: First, the computed growth rates are very sensitive to the identified model. Small inaccuracies in the measurements, the calculation of the growth rates from the experiments, and the model identification might have a relatively large impact. Furthermore, the growth rates determined from the experiments might be somewhat overestimated. To understand this phenomenon, consider the case where the combustion system is switched between two reflection coefficients for which it is stable. For the higher $|R_{\mathrm{cl}}|$, a higher pressure amplitude would arise and thus the corresponding experimentally determined growth rate would be positive. However, as the system is stable for both cases, the model would predict a negative growth rate. The question is, whether this difference has a non-negligible influence on the "unstable" growth rates. This assumption is supported by the fact that

the difference gets smaller for larger growth rates.
Given the uncertainties explained above, the agreement obtained between experiments and model prediction is quite remarkable.

"Heavy crates and the rhyme books near me
Minds gone weary but the lines come clearly
Einstein's theory, answer to your query
We = MC squared can you hear me!"
Wax Tailor, Hope & Sorrow.

Chapter 8

Conclusions and Outlook

Experimental investigations of new burners in combustion test rigs are indispensable for the whole development process of gas turbine burners. Reliable predictions of thermoacoustic instabilities and emission characteristics in an early design stage strongly rely on the acoustic boundary conditions of these test rigs. Since the acoustic boundary conditions usually differ from those in the full-scale engine, burners whose performance is assessed in combustion test rigs might show a completely different behaviour when installed in the engine. This discrepancy between test rig and engine performance is not revealed until the very end of the design process when first full-scale engine tests are conducted. At this stage, changes in components are extremely expensive and might cause severe delays in the schedule. Alternatives to these changes are only active and passive control strategies or restrictions in engine envelope, both certainly not wanted by manufacturers and customers. As a consequence of this lack of reliable predictions, a method is proposed, which is able to actively change the acoustic boundary conditions of combustion test rigs. This active impedance tuning control scheme allows to impose quasi arbitrary reflection coefficients both in isothermal and reactive flow. As was also mentioned and confirmed by several researchers from different industrial companies as well as academia, the matching of engine and test rig conditions is of utmost importance [32, 38, 84, 90, 115, 119, 129, 231]. Impedance tuning, therefore, could be a crucial step in the development process of new burner generations, as new burners could be tested under realistic engine conditions regarding their thermoacoustic behaviour. Thereby, limit-cycle amplitudes and thus engine operating regimes could be predicted. Since the occurrence of high amplitude thermoacoustic instabilities in the full-scale engine has to be avoided, the impedance tuning concept could save a considerable amount of time and result in financial benefits in the design process.

8.1 Conclusions

The developed feedback control scheme has proven to able to act on the acoustic boundary conditions, i.e., the downstream reflection coefficient, of a combustion test rig. Multiple pressure measurements were used to decompose the acoustic field in the system *online* to create the control input. To allow for this instantaneous wave decomposition, a modified, time-domain-stable version of the Multi-Microphone Method was derived. The signal containing the information of the actual pressure field in the system was processed by a suitable model-based controller and fed back via an acoustic actuator mounted to the downstream boundary. The actuator manipulated the acoustic field in the system according to the prescribed boundary condition. Through an adequate adjustment of the control law, the system behaviour, subject to quasi arbitrary acoustic boundary conditions, could be studied.

Several actuators were used in the control scheme. First validation experiments, both in isothermal and reactive flow, were conducted with woofers. The reflection coefficient was adjusted to fully reflecting (acoustically hard and acoustically soft). Note that the turbine inlet of a gas turbine typically represents a choked boundary condition corresponding to an acoustically hard termination. Therefore, the control scheme allows imposing the acoustics of a choked flow to an atmospheric test rig, where the flow is not choked. Furthermore, a non-reflecting termination was realized resulting in a reflection coefficient of 0.05 in a frequency band of several hundred Hertz. In addition to that, different virtual additional lengths were imposed to simulate different acoustic resonance frequencies at the same test rig. The concept proved to be of high accuracy in tuning the test rig to the desired resonance frequencies. Woofers were identified to be the actuator of choice for atmospheric conditions as well as the optimization and modification of the control concept. However, application to industrial test rigs is limited, as they do not exhibit enough acoustic power and will not withstand the harsh environmental conditions, especially at high thermal powers and elevated pressures.

These shortcomings could be overcome by a another type of actuators, whose principle relies on a modulation of an air mass flow to generate an acoustic wave. Two different actuators were tested, one being a proportional high-bandwidth valve, the other an electro-pneumatic transducer.

Results obtained with the direct-drive valves proved the concept to work equally well. The capability to tune over a broad frequency range at once, however, was limited to a maximum bandwidth of 90 Hz due to the actuator transfer function, particularly, the time-delay. In many cases, this also impeded an accurate controller identification. Therefore, the control concept was modified to work at discrete frequencies. In this way, also tuning at high frequencies became more feasible. Applying the impedance tuning concept to industrial test rigs would require 10 to 20 of these proportional valves. As they are not off-the-shelf technology but a special design allowing for the modulation of high mass flows up to relatively high frequencies, tests should in a first step be conducted with a reduced number at medium pressure.

The second air-modulating actuator, the Ling Driver, already has proven to generate sufficiently high pressure amplitudes in industrial test rigs operating at medium pressures. Since its amplitude response was found to be strongly non-linear, application of the Ling

Driver required a further extension of the control scheme. Therefore, the control loop was modified by means of look-up tables and a routine able to extract the instantaneous control signal amplitude. Because of its frequency non-linearity, control was only possible at discrete frequencies. Results attained with the Ling Driver showed that it can be used in the control scheme and is able to accurately produce desired reflection coefficients. The extension of the control scheme is not limited to the Ling Driver and might be adapted for other actuators exhibiting non-linear responses.
Being able to control the acoustic boundary conditions of the combustion test rig enabled also for alternative applications of the control scheme. By reducing the downstream reflection coefficient, i.e., increasing the acoustic energy losses across the system boundary, an initially unstable system could be stabilized. The transition from instability to stability was also used to assess the predictive capabilities of a low-order network model of the combustion test rig. Predicted linear growth rates, the frequency of the least stable mode, as well as transition from instability to stability were compared to experimental observations and showed excellent correspondence. Here, the same control law was applied to different operating conditions and proved to be quite robust. The changes in operating conditions were rather small, yet had, however, a distinct influence on the system stability.

8.2 Outlook

In this section, issues of ongoing work and suggestions for further research as well as possible amendments of the control scheme are discussed.

8.2.1 Industrial Realization

Certainly, the most obvious and most important next step is the validation of the impedance tuning scheme at industrial test rigs. In a first iteration, this should be done under atmospheric conditions with woofers and valves. If the concept is proven to work, the system pressure might be increased towards engine conditions. The control concept requires certain conditions to be successfully applied. A measurement section in which at least two, but preferably three or more, microphones can be mounted is needed to determine the plane wave pressure field. Furthermore, the test rig must be equipped with appropriate actuators. Even if the upstream end might be considered to represent engine conditions, a possibility for excitation must be given there as well in order to be able to determine the uncontrolled and adjusted downstream reflection coefficients. Note, if the upstream end significantly differs from that in the engine, it has to be tuned, too. Currently, SIEMENS PG combustion test rigs are modified to allow for application of the active impedance tuning scheme.
Since space for mounting pressure probes in combustion test rigs often is at a premium, it might not be possible to mount multiple microphones with sufficient spacing in a straight duct, as reported here. Therefore, the time-domain Multi-Microphone Method has to be extended to be able to account for variations in the cross section. Munjal [133] derived equations relating primitive acoustic variables to Riemann invariants in case of conical

ducts. It might also be possible to find analytical solutions for the convective wave equation for more complex geometries. In case of a non-negligible temperature change in axial direction, the MMM has to be modified as well as otherwise reflections, which are caused by a gradual change in the characteristic impedance, could introduce severe errors. Sujith et al. [213] and Manoj Kumar & Sujith [117] gave analytical solutions for wave propagation in the presence of linear, exponential, and polynomial axial temperature profiles. Evidently, the actual temperature distribution also has to be determined somehow. Subrahmanyam et al. [211, 212] presented solutions for a dedicated family of mean temperature and cross sectional area profiles in the absence of mean flow. Finally, as industrial combustion chambers often are equipped with ceramic coatings, dissipative effects might reach a level at which they have to be considered. This wave attenuation has then to be included in the wave propagation constant, see, for example, references [132, 220] for more information. An additional problem of the latter issue is the accurate determination of the damping effect. In general, these modifications might involve some laborious calculation steps but in principle, it should be possible to include them into an extended version of the MMM.
To be used as a standard tool in industrial burner development processes, the handling of the control scheme has to be improved. The scheme as it is requires a fundamental knowledge of system identification, experimental determination of transfer functions, controller implementation, data evaluation and interpretation, handling of hardware, etc. For this purpose, a graphical user interface should be set up to facilitate certain steps.

8.2.2 Further Development and Application Fields of Impedance Tuning

- Up to know, the control concept only works for plane waves. As a consequence, only the flame response to longitudinal pressure perturbations can be studied. Here, the acoustic particle velocity only acts on the flame in axial direction. In industrial full-scale engines, the combustion chamber often is of annular type so that neighbouring burners and flames might influence each other. Even for can combustors, individual flames are not perfectly decoupled, as they are connected by the turbine inlet, ignition tubes, and the plenum. Therefore, also azimuthal modes might be responsible for thermoacoustic instabilities to occur. In this case, the flame is not only exposed to perturbations in axial but also azimuthal direction. To account for this interaction, the control scheme has to be extended to be able to generate a transversal acoustic field, i.e., to simulate the influence of neighbouring burners. In addition, single burner combustion test rigs must be extended to allow for a two-dimensional manipulation of the acoustic field. The one-dimensional approach also limits its application to single burner combustion test rigs. By extending the scheme, it is possible to apply it to sector test rigs and thus to simulate the effect of azimuthal modes on system stability.

- Except for the woofers, tuning in a broad frequency range was at least cumbersome if not impossible. Due to this, the control scheme was modified to allow for discrete frequency tuning. As was stated before, this forbids the investigation of the interaction of two unstable modes. Tuning the test rig to fully reflecting for each frequency of interest separately, might lead to limit-cycle oscillations at more than one frequency. If the system is tuned in a broad frequency range covering all frequencies at which

the system gets unstable, the modes most probably will interact with each other, and the one with the largest growth rate might completely dominate the limit-cycle due to non-linear effects, as was, for instance, observed by Moeck et al. [128] and Zhao & Morgans [232]. To account for mode interaction with the discrete-frequency tuning approach, the control scheme could be divided into several control loops each of which controls the system at a different frequency. This, however, is anything but trivial as on the one hand multiple actuators have to be installed and if the tuned frequencies are too close to each other, the controllers might influence themselves.

- If the combustion system exhibits strong pressure oscillations, a modification of the reflection coefficient is much more intricate as it is the case for a stable system. This is most probably due to the fact that the uncontrolled system is in a limit-cycling state and even slight inaccuracies in the controller identification or an unwanted saturation of the control signal may hinder successful control. Therefore, in most of the cases, the impedance tuning concept was applied after having passively stabilized the system. This was done by means of an orifice, which replaced the open-end termination and produced a low reflecting end. Through this, the pressure drop in the system and across the burner was changed and thus also the flow profile. In the experiments reported here, the influence was negligible. As was point out by Escudier & Keller [54, 55], this might, however, not always be the case. It is possible that the outlet flow condition influences the heat release so that it is different from that in the engine. Evidently, in the latter case, the burner's performance in test rig and engine might be different, although the acoustic boundary conditions are the same. To circumvent this problem, it might be possible to actively stabilize the system by using a second control loop. For example, a simple phase shift controller could be used.

- For full-scale systems in which entropy waves have a dominant effect on the instability, it is important to simulate these effects also in test rigs. Entropy waves can be regarded as portions of hot and cold gas pockets that are convected downstream with the mean flow. If they are accelerated in a nozzle, i.e., the turbine inlet, they might become a source of sound. The acoustic waves, which are generated in that way, travel back to the flame and close the feedback loop. The difficulty in simulating entropy waves in test rigs, where they might not be present, are, for example, the correct consideration of the convective delays by the controller, the non-uniform temperature distribution, which complicates the wave decomposition, as well as the sound generation mechanisms, which have to be simulated by the actuator. For the latter, probably the one-dimensional approach of Marble & Candel [118] can be used. However, this has to be verified since the simplified approach might lead to considerable errors, as was recently experimentally observed by Bake et al. [8]. Impedance tuning could also improve fundamental investigations of entropy noise. If this phenomenon is not the dominant mechanism, because it is superposed by pure acoustic reflections, actively imposing a non-reflecting end could allow for an isolation of the waves generated by temperature non-uniformities.

- Since the acoustic characteristics of a test rig are determined by both the downstream *and* the upstream boundary condition, evidently, both have to match those of the

full-scale engine. In some cases, the approximation of similar upstream boundary conditions might be valid, as the burner to be tested itself is part of it, and the influence of plenum as well as supply lines might either be negligible or designed to exhibit similar acoustic characteristics as those in the engine. However, if they are as such that they impose noticeable differences in the acoustic fields, they have to be tuned, too. The impedance tuning scheme could be extended to account for differences in up- and downstream boundary conditions by manipulating both. This gets even more important if the plenum in the engine allows for a "communication" between adjacent burners.

- A possible shortcoming of the impedance tuning scheme is that if reflection coefficients are adjusted which invoke high amplitude pressure fluctuations, their magnitudes might be influenced by non-linear effects (cf. to explanations given in Sec. 7.2). This means that if the *linear* controller is set up to produce a magnitude of unity, the actual magnitude might be smaller than that. The non-linear effects which are responsible for the reduction of the magnitude might differ from that in the engine, and thus the reflection coefficients might differ as well. Even if the difference is only 1 or 2%, this might have considerable effects on the growth rates (see Sec. 7.2) and probably the limit-cycle amplitude. This issue should be investigated in more detail. It could, for instance, be possible to first adjust the desired reflection coefficient that causes high pressure oscillations and in a second step stabilize the system to get an estimate of the influence of the non-linearity.

- In terms of actuators, design rules might be proposed on how the actuator should be mounted to deliver the best performance, i.e., distance from wave decomposition location, inclination of connection tubes, or use of extension tubes. Results presented in Sec. 6.4.2 suggest that the valve's response characteristic might be enhanced by an optimization of the flow path geometry and a larger damper body. Furthermore, a higher excitation amplitude might be obtained by modulating around a neutral position different than the 50%-open position, which was adjusted in the experiments conducted here.

- For cases for which uncertainties or slight modifications in the operating conditions cause a deterioration of the controller performance, an additional control loop might be incorporated, which processes the control deviation. This compensator could, for example, be fed by the difference of the actual, measured reflected g-wave and the one which results from the measured f-wave multiplied by the prescribed reflection coefficient, i.e., the prescribed g-wave. Probably, the filtered-X least mean squares algorithm could be useful, which was also applied by Orduña-Bustamente & Nelson [143] in the adaptive control scheme they used for impedance control. This item should be accompanied by a detailed study of the control scheme's robustness.

- A further application of the control concept lies in the assessment and validation of the implementation of time-domain boundary conditions in CFD codes, which is far from trivial. Results from impedance tuning experiments can serve as test data for numerical simulations. For this, a cooperation with the numerics group of the Institute of Combustion Technology of the DLR Stuttgart was initiated. Currently,

they run unsteady Reynolds Averaged Navier-Stokes simulations of the complete atmospheric combustion test rig used for the impedance tuning experiments reported in Chapter 6. Experimental data of dedicated isothermal and reactive test cases, for which different acoustic boundary conditions were adjusted in the experiments, will be simulated.

- Impedance tuning could also alternatively be used to experimentally validate algorithms for the determination of sound sources in premixed flames. These algorithms are currently developed at our Institute [159]. The routines assume the considered combustion system to be of infinite length, i.e., exhibiting non-reflecting boundary conditions. As was shown, the control concept is able to impose reflection coefficients with $|R| < 0.03$ that are even smaller than that of technically realizable anechoic ends. Therefore, the active cancellation of reflections might result in conditions that allow for a better comparability of the predicted results.

Appendix A

Proof of Stability for the Modified Multi-Microphone Method

In this Appendix, the method of mathematical induction is used to verify the assumption made in Sec. 5.5, whereby the modified formulation of the Multi-Microphone Method given in Eq. (5.24) will never be unstable and will become marginally stable only for large frequencies (and at $\omega = 0$).
The frequency domain expression of the modified MMM is given by

$$\hat{f} = \frac{\hat{p}_1 - \frac{1}{n-1}\left(\hat{p}_2 e^{-\mathrm{i}\omega\tau^-_{1,2}} + \ldots + \hat{p}_n e^{-\mathrm{i}\omega\tau^-_{1,n}}\right)}{1 - \frac{1}{n-1}\left(e^{-\mathrm{i}\omega(\tau^+_{1,2}+\tau^-_{1,2})} + \ldots + e^{-\mathrm{i}\omega(\tau^+_{1,n}+\tau^-_{1,n})}\right)}. \tag{A.1}$$

To prove the assumption, it has to be investigated in which cases Eq. (A.1) has poles that are unstable or only marginally stable, i.e., finding solutions for ω that satisfy

$$e^{-\mathrm{i}\omega(\tau^+_{1,2}+\tau^-_{1,2})} + \ldots + e^{-\mathrm{i}\omega(\tau^+_{1,n}+\tau^-_{1,n})} = n - 1, \tag{A.2}$$

where $n \geq 3$ is the number of microphones used. Because we assumed a harmonic time dependence of the fluctuating variables, $p'(x,t) = \hat{p}(x)e^{\mathrm{i}\omega t}$ (see Sec. 2.3), this corresponds to the question whether there are poles

$$\omega = \omega_\mathrm{r} + \mathrm{i}\omega_\mathrm{i} \tag{A.3}$$

that solve Eq. (A.2) and have a negative (unstable) or vanishing (marginally stable) imaginary part.
In the *first step* of the mathematical induction, it has to be shown for which ω the assumption is valid for a certain n. We chose the easiest case of 3 microphones. Equation (A.2) then gives

$$e^{-\mathrm{i}\omega(\tau^+_{1,2}+\tau^-_{1,2})} + e^{-\mathrm{i}\omega(\tau^+_{1,3}+\tau^-_{1,3})} = 2. \tag{A.4}$$

For convenience, we introduce

$$\eta = \tau_{1,2}^{+} + \tau_{1,2}^{-} \tag{A.5}$$

and

$$\xi_j = \tau_{1,j}^{+} + \tau_{1,j}^{-} - \eta \qquad j = 3, \ldots, n. \tag{A.6}$$

Furthermore, we split Eq. (A.4) in its imaginary and real part to yield

$$e^{\omega_\mathrm{i}\eta}\left(\cos\omega_\mathrm{r}\eta + e^{\omega_\mathrm{i}\xi_3}\cos\omega_\mathrm{r}(\eta+\xi_3)\right) = 2, \tag{A.7a}$$

$$-e^{\omega_\mathrm{i}\eta}\left(\sin\omega_\mathrm{r}\eta + e^{\omega_\mathrm{i}\xi_3}\sin\omega_\mathrm{r}(\eta+\xi_3)\right) = 0. \tag{A.7b}$$

Here, use has been made of the trigonometric relations

$$\sin a \sin b = \frac{1}{2}\left(\cos(a-b) - \cos(a+b)\right), \tag{A.8a}$$

$$\cos a \cos b = \frac{1}{2}\left(\cos(a-b) + \cos(a+b)\right) \tag{A.8b}$$

and

$$e^{-\mathrm{i}a} = \cos a - \mathrm{i}\sin a. \tag{A.9}$$

The exponential terms in Eq. (A.7a) are smaller than 1 if $\omega_\mathrm{i} < 0$ and equal to 1 if $\omega_\mathrm{i} = 0$. If $\omega_\mathrm{i} < 0$, the expression in the brackets is smaller than 2 as $e^{\omega_i\xi_3}$ is smaller than 1. Thus, because $e^{\omega_\mathrm{i}\eta}$ is also smaller than 1, the equation has no solution. This means that no unstable poles exist. If $\omega_\mathrm{i} = 0$, Eq. (A.7a) can only be satisfied if both cosine terms are equal to 1. Therefore, the system might get marginally stable, i.e., has poles that lie on the imaginary axis, if

$$\begin{aligned} & \cos(\omega_\mathrm{r}\eta) = 1 \quad \wedge \quad \cos(\omega_\mathrm{r}(\eta+\xi_3)) = 1 \\ \Leftrightarrow \quad & \omega_\mathrm{r}\eta = 2k_1\pi \quad \wedge \quad \omega_\mathrm{r}(\eta+\xi_3) = 2k_2\pi \qquad k_1, k_2 \in \mathbb{N}. \end{aligned} \tag{A.10}$$

If these conditions are fulfilled, Eq. (A.7b) is satisfied as well. In words, this means that for a marginally stable system the propagation delays $\tau_{1,j-1}$ have to be integer multiples of each other. For most of the microphone setups in practical applications this will only happen for large frequencies.

The induction hypothesis – the *second step* of the proof – is that the assumption holds for some arbitrary number of microphones m. According to Eqs. (A.7), Eq. (A.2) is split into its real and imaginary part to give

$$e^{\omega_\mathrm{i}\eta}\left(\cos(\omega_\mathrm{r}\eta) + \sum_{j=3}^{m} e^{\omega_\mathrm{i}\xi_j}\cos(\omega_\mathrm{r}(\eta+\xi_j))\right) = m-1, \tag{A.11a}$$

$$-e^{\omega_\mathrm{i}\eta}\left(\sin(\omega_\mathrm{r}\eta) + \sum_{j=3}^{m} e^{\omega_\mathrm{i}\xi_j}\sin(\omega_\mathrm{r}(\eta+\xi_j))\right) = 0. \tag{A.11b}$$

Finally, in the *last step*, we show that the statement holds for $n = m + 1$:

$$e^{\omega_\mathrm{i}\eta}\left(\cos(\omega_\mathrm{r}\eta) + \sum_{j=3}^{n} e^{\omega_\mathrm{i}\xi_j}\cos(\omega_\mathrm{r}(\eta+\xi_j))\right) = n-1, \tag{A.12a}$$

$$-e^{\omega_\mathrm{i}\eta}\left(\sin(\omega_\mathrm{r}\eta) + \sum_{j=3}^{n} e^{\omega_\mathrm{i}\xi_j}\sin(\omega_\mathrm{r}(\eta+\xi_j))\right) = 0. \tag{A.12b}$$

Inserting $n = m + 1$, these equations can be rewritten as

$$e^{\omega_\mathrm{i}\eta}\left(\cos(\omega_\mathrm{r}\eta) + \sum_{j=3}^{m} e^{\omega_\mathrm{i}\xi_j}\cos(\omega_\mathrm{r}(\eta+\xi_j)) + e^{\omega_\mathrm{i}\xi_n}\cos(\omega_\mathrm{r}(\eta+\xi_n))\right) = m+1-1, \tag{A.13a}$$

$$-e^{\omega_\mathrm{i}\eta}\left(\sin(\omega_\mathrm{r}\eta) + \sum_{j=3}^{m} e^{\omega_\mathrm{i}\xi_j}\sin(\omega_\mathrm{r}(\eta+\xi_j)) + e^{\omega_\mathrm{i}\xi_n}\sin(\omega_\mathrm{r}(\eta+\xi_n))\right) = 0. \tag{A.13b}$$

If now the induction hypothesis from Eqs. (A.11) is considered, we get

$$e^{\omega_\mathrm{i}\eta}e^{\omega_\mathrm{i}\xi_n}\cos(\omega_\mathrm{r}(\eta+\xi_n)) = 1, \tag{A.14a}$$

$$-e^{\omega_\mathrm{i}\eta}e^{\omega_\mathrm{i}\xi_n}\sin(\omega_\mathrm{r}(\eta+\xi_n)) = 0. \tag{A.14b}$$

The solution for Eq. (A.14b) is given by

$$\omega_\mathrm{r}(\eta+\xi_n) = 2k_3\pi \qquad k_3 \in \mathbb{N}. \tag{A.15}$$

With this, Eq. (A.14a) becomes

$$e^{\omega_\mathrm{i}\eta}e^{\omega_\mathrm{i}\xi_n} = 1, \tag{A.16}$$

which has no solution for $\omega_\mathrm{i} < 0$ but only for $\omega_\mathrm{i} = 0$. This corresponds to the condition we found in the first step for $n = 3$.
In summary, this shows that the modified MMM cannot get unstable and that it might get marginally stable if the propagation delays for all n microphones are multiples of each other. The more microphones are used, the higher the frequency will be for which this will be the case.

Appendix B

Dependence of Reflection Coefficient on Imposed Control Gain

In Section 6.5, the dependence of the adjusted reflection coefficient's magnitude and phase on the imposed control gain K_g was given. It will be shown here how Eqs. (6.16) and (6.17) can be derived from Eq. (6.15).
Being a complex quantity, the reflection coefficients in Eq. (6.15) can be written as

$$R_j = \Re\{R_j\} + \mathrm{i}\Im\{R_j\}\,. \tag{B.1}$$

Introducing this into Eq. (6.15) yields

$$R_\mathrm{cl} = \Re\{R_\mathrm{ol}\}(1-K_\mathrm{g}) + \Re\{R_\mathrm{set}\}K_\mathrm{g} + \mathrm{i}\left[\Im\{R_\mathrm{ol}\}(1-K_\mathrm{g}) + \Im\{R_\mathrm{set}\}K_\mathrm{g}\right], \tag{B.2}$$

from which magnitude and phase can be calculated to yield

$$|R_\mathrm{cl}| = \sqrt{\left[\Re\{R_\mathrm{ol}\}(1-K_\mathrm{g}) + \Re\{R_\mathrm{set}\}K_\mathrm{g}\right]^2 + \left[\Im\{R_\mathrm{ol}\}(1-K_\mathrm{g}) + \Im\{R_\mathrm{set}\}K_\mathrm{g}\right]^2}, \tag{B.3a}$$

$$\varphi_\mathrm{cl} = \arctan\frac{\Im\{R_\mathrm{ol}\}(1-K_\mathrm{g}) + \Im\{R_\mathrm{set}\}K_\mathrm{g}}{\Re\{R_\mathrm{ol}\}(1-K_\mathrm{g}) + \Re\{R_\mathrm{set}\}K_\mathrm{g}}. \tag{B.3b}$$

The calculation for the derivative of the magnitude is straightforward. Taking the derivative of Eq. (B.3a) with respect to K_g gives

$$\frac{\partial|R_\mathrm{cl}|}{\partial K_\mathrm{g}} = \frac{1}{2}\frac{1}{|R_\mathrm{cl}|}\left\{2\Re\{R_\mathrm{cl}\}\frac{\partial\Re\{R_\mathrm{cl}\}}{\partial K_\mathrm{g}} + 2\Im\{R_\mathrm{cl}\}\frac{\partial\Im\{R_\mathrm{cl}\}}{\partial K_\mathrm{g}}\right\}. \tag{B.4}$$

Calculating the partial derivatives in the brackets by using the expressions for real and imaginary part from Eq. (B.2) then yields Eq. (6.17a):

$$\frac{\partial |R_{\mathrm{cl}}|}{\partial K_{\mathrm{g}}} = \frac{\Re\{R_{\mathrm{cl}}\}\left[-\Re\{R_{\mathrm{ol}}\}+\Re\{R_{\mathrm{set}}\}\right]+\Im\{R_{\mathrm{cl}}\}\left[-\Im\{R_{\mathrm{ol}}\}+\Im\{R_{\mathrm{set}}\}\right]}{|R_{\mathrm{cl}}|}. \tag{B.5}$$

For the derivation of the expression for the phase (Eq. (6.17b)), some laborious calculation steps are required. The derivative of the arctan-function is given by

$$\frac{\partial}{\partial x}(\arctan y) = \frac{1}{1+y^2}\frac{\partial y}{\partial x}. \tag{B.6}$$

Using this to calculate the derivative of φ_{cl}, one gets

$$\frac{\partial \varphi_{\mathrm{cl}}}{\partial K_{\mathrm{g}}} = \frac{1}{1+\left(\frac{\mathcal{N}}{\mathcal{D}}\right)^2}\frac{\left[-\Im\{R_{\mathrm{ol}}\}+\Im\{R_{\mathrm{set}}\}\right]\mathcal{D}-\mathcal{N}\left[-\Re\{R_{\mathrm{ol}}\}+\Re\{R_{\mathrm{set}}\}\right]}{\mathcal{D}^2}, \tag{B.7}$$

where $\mathcal{N}$ and $\mathcal{D}$ are numerator and denominator of the arctan-argument in Eq. (B.3b), i.e. imaginary and real part of R_{cl}, respectively. Expansion of Equation (B.7) yields

$$\begin{aligned}\frac{\partial \varphi_{\mathrm{cl}}}{\partial K_{\mathrm{g}}} = \frac{1}{\mathcal{N}^2+\mathcal{D}^2}[&-\Im\{R_{\mathrm{ol}}\}\Re\{R_{\mathrm{ol}}\}(1-K_{\mathrm{g}})+\Im\{R_{\mathrm{set}}\}\Re\{R_{\mathrm{ol}}\}(1-K_{\mathrm{g}})\\ &-\Im\{R_{\mathrm{ol}}\}\Re\{R_{\mathrm{set}}\}K_{\mathrm{g}}+\Im\{R_{\mathrm{set}}\}\Re\{R_{\mathrm{set}}\}K_{\mathrm{g}}\\ &+\Im\{R_{\mathrm{ol}}\}\Re\{R_{\mathrm{ol}}\}(1-K_{\mathrm{g}})+\Im\{R_{\mathrm{set}}\}\Re\{R_{\mathrm{ol}}\}K_{\mathrm{g}}\\ &+\Im\{R_{\mathrm{ol}}\}\Re\{R_{\mathrm{set}}\}(-1+K_{\mathrm{g}})-\Im\{R_{\mathrm{set}}\}\Re\{R_{\mathrm{set}}\}K_{\mathrm{g}}],\end{aligned} \tag{B.8}$$

where same-coloured expressions cancel each other to result in Eq. (6.17b)

$$\frac{\partial \varphi_{\mathrm{cl}}}{\partial K_{\mathrm{g}}} = -\frac{\Im\{R_{\mathrm{ol}}\}\Re\{R_{\mathrm{set}}\}-\Im\{R_{\mathrm{set}}\}\Re\{R_{\mathrm{ol}}\}}{|R_{\mathrm{cl}}|^2}. \tag{B.9}$$

Here, additionally, use has been made of

$$\mathcal{N}^2+\mathcal{D}^2 = |R_{\mathrm{cl}}|^2. \tag{B.10}$$

"Wir sind den kolossalen Bücherschatz abgeschritten, und ich kann sagen, es hat mich weiter nicht erschüttert, [...] Nur habe ich nach einer Weile anfangen müssen, im Kopf zu rechnen, und das hatte ein unerwartetes Ergebnis. Siehst du, ich hatte mir vorher gedacht, wenn ich jeden Tag da ein Buch lese, so müßte das zwar sehr anstrengend sein, aber irgendwann müßte ich damit zu Ende kommen und dürfte dann eine gewisse Position im Geistesleben beanspruchen, selbst wenn ich ein oder das andere auslasse. Aber was glaubst du, anwortet mir der Bibliothekar, wie unser Spaziergang kein Ende nimmt und ich ihn frage, wieviel Bände denn eigentlich diese verrückte Bibliothek enthält? Dreieinhalb Millionen Bände, antwortet er!! Wir sind da, wie er das sagte, ungefähr beim siebenhunderttausenden Buch gewesen, aber ich habe von dem Augenblick an ununterbrochen gerechnet; [...] Zehntausend Jahre würde ich auf diese Weise gebraucht haben, um mich mit meinem Vorsatz durchzusetzen."

R. Musil, Der Mann ohne Eigenschaften.

References

[1] Åbom, M., and Bodén, H., 1988. "Error analysis of two-microphone measurements in ducts with flow". *Journal of the Acoustical Society of America,* **83**(6), pp. 2429–2438.

[2] Advisory Council for Aeronautic Research in Europe, 2001. *European Aeronautics: A vision for 2020.* European Commission. http://www.acare4europe.com/docs/Vision%202020.pdf.

[3] Aigner, M., and Müller, G., 1993. "Second-Generation Low-Emission Combustors for ABB Gas Turbines: Field Measurements with GT11N-EV". *Journal of Engineering for Gas Turbines and Power,* **115**, pp. 533–536.

[4] Alemela, P. R., Fanca, D., Ettner, F., Hirsch, C., Sattelmayer, T., and Schuermans, B., 2008. "Flame Transfer Matrices of a Premixed Flame and a Global Check with Modelling and Experiments". ASME Paper GT2008-50111.

[5] Antoulas, A., and Sorensen, D., 2001. "Approximation of Large-Scale Dynamical Systems: An Overview". *International Journal of Applied Mathematics and Computational Science,* **11**(5), pp. 1093–1121.

[6] Backhaus, S., and Swift, G. W., 2000. "A thermoacoustic-Stirling heat engine: Detailed study". *Journal of the Acoustical Society of America,* **107**(6), pp. 3148–3166.

[7] Baehr, H. D., and Kabelac, S., 2006. *Thermodynamik*, 13th ed. Springer-Verlag Berlin Heidelberg.

[8] Bake, F., Kings, N., and Roehle, I., 2008. "Fundamental Mechanism of Entropy Noise in Aero-Engines: Experimental Investigation". *Journal of Engineering for Gas Turbines and Power,* **130**(1), pp. 011202–1–011202–6.

[9] Bake, F., Michel, U., and Roehle, I., 2007. "Investigation of Entropy Noise in Aero-Engine Combustors". *Journal of Engineering for Gas Turbines and Power,* **129**(2), pp. 370–376.

[10] Balachandran, R., Ayoola, B. O., Kaminski, C. F., Dowling, A. P., and Mastorakos, E., 2005. "Experimental investigation of the nonlinear response of turbulent premixed flames to imposed inlet velocity oscillations". *Combustion and Flame,* **143**(1–2), pp. 37–55.

[11] Banaszuk, A., Jacobson, C. A., Khibnik, A. I., and Mehta, P. G., 1999. "Linear and Nonlinear Analysis of Controlled Combustion Processes. Part I: Linear Analysis".

In Proceedings of the 1999 IEEE International Conference on Control Applications, pp. 199–205.

[12] Banaszuk, A., Jacobson, C. A., Khibnik, A. I., and Mehta, P. G., 1999. "Linear and Nonlinear Analysis of Controlled Combustion Processes. Part II: Nonlinear Analysis". In Proceedings of the 1999 IEEE International Conference on Control Applications, pp. 206–212.

[13] Banaszuk, A., Mehta, P., Jacobson, C., and Khibnik, A., 2006. "Limits of Achievable Performance of Controlled Combustion Processes". *IEEE Transactions on Control Systems Technology,* **14**(5), pp. 881–895.

[14] Batchelor, G. K., 1987. *An Introduction to Fluid Dynamics.* Cambridge University Press.

[15] Bechert, D. W., 1980. "Sound absorption caused by vorticity shedding, demonstrated with a jet flow". *Journal of Sound and Vibration,* **70**(3), pp. 389–405.

[16] Bellows, B. B., Bobba, M. K., Forte, A., Seitzmann, J. M., and Lieuwen, T., 2007. "Flame transfer function saturation mechanisms in a swirl-stabilized combustor". *Proceedings of the Combustion Institute,* **31**, pp. 3181–3188.

[17] Bellucci, V., 2008. Modeling & Control in Combustion Systems: Thermoacoustics. Lecture Notes Thermoacoustics Course, ISTA HFI, TU Berlin.

[18] Bellucci, V., Flohr, P., Paschereit, C. O., and Magni, F., 2004. "On the Use of Helmholtz Resonators for Damping Acoustic Pulsations in Industrial Gas Turbines". *Journal of Engineering for Gas Turbines and Power,* **126**(2), pp. 271–275.

[19] Bellucci, V., Schuermans, B., Nowak, D., Flohr, P., and Paschereit, C. O., 2005. "Thermoacoustic Modeling of a Gas Turbine Combustor Equipped With Acoustic Dampers". *Journal of Turbomachinery,* **127**(2), pp. 372–379.

[20] Berenbrink, P., and Hoffmann, S., 2000. "Suppression of Dynamic Combustion Instabilities by Passive and Active Means". ASME Paper 2000-GT-0079.

[21] Bernier, D., Ducruix, S., Lacas, F., Candel, S., Robart, N., and Poinsot, T., 2003. "Transfer function measurements in a model combustor: application to adaptive instability control". *Combustion Science and Technology,* **175**(5), pp. 993–1013.

[22] Bethke, S., Wever, U., and Krebs, W., 2005. "Stability Analysis of Gas-turbine Combustion Chamber". AIAA Paper 2005-2831.

[23] Beyene, S., and Burdisso, R. A., 1997. "A new hybrid passive/active noise absorption system". *Journal of the Acoustical Society of America,* **101**(3), pp. 1512–1515.

[24] Biagioli, F., 2006. "Stabilization mechanisms of turbulent premixed flames in strongly swirled flows". *Combustion Theory and Modelling,* **10**(3), pp. 389–412.

[25] Blomshield, F. S., 2001. "Historical Perspective of Combustion Instability in Motors: Case Studies". AIAA Paper 2001-3875.

[26] Bloxsidge, G. J., Dowling, A. P., Hooper, N., and Langhorne, P. J., 1988. "Active Control of Reheat Buzz". *AIAA Journal,* **26**(7), pp. 783–790.

[27] Bloxsidge, G. J., Dowling, A. P., and Langhorne, P. J., 1988. "Reheat buzz: an acoustically coupled combustion instability. Part 2. Theory". *Journal of Fluid Mechanics,* **193**, pp. 445–473.

[28] Bohn, D., and Deuker, E., 1993. "An Acoustical Model to Predict Combustion Driven Oscillations". In 20th International Congress on Combustion Engines, London, UK.

[29] Bonzani, F., and Piana, C., 2008. "From Test Rig to Field Operation: A Lesson Learned". ASME Paper GT2008-50833.

[30] Bothien, M. R., Moeck, J. P., Lacarelle, A., and Paschereit, C. O., 2007. "Time Domain Modelling and Stability Analysis of Complex Thermoacoustic Systems". *Proceedings of the Institution of Mechanical Engineers, Part A: Journal of Power and Energy,* **221**(5), pp. 657–668.

[31] Boudier, G., Lamarque, N., Staffelbach, G., Gicquel, L. Y. M., and Poinsot, T., 2009. "Thermo-acoustic stability of a helicopter gas turbine combustor using Large Eddy Simulations". *International Journal of Aeroacoustics,* **8**(1), pp. 69–94.

[32] Brogan, T. (Pratt & Whitney, East Hartford, CT, USA). Personal communication.

[33] Brown, J. G., 1911. "New Records of Sound Waves from a Vibrating Flame". *Physical Review (Series I),* **33**(5), pp. 442–446.

[34] Campos-Delgado, D., Schuermans, B., Zhou, K., Paschereit, C., Gallestey, E., and Poncet, A., 2003. "Thermoacoustic instabilities: modeling and control". *IEEE Transactions on Control Systems Technology,* **11**(4), pp. 429–447.

[35] Candel, S., 2002. "Combustion Dynamics and Control: Progress and Challenges". *Proceedings of the Combustion Insitute,* **29**, pp. 1–28.

[36] Candel, S. M., 1992. "Combustion Instabilities Coupled by Pressure Waves and their Active Control". *24th Symposium (International) on Combustion / The Combustion Institute,* **24**, pp. 1277–1296.

[37] Cargill, A. M., 1982. "Low Frequency Acoustic Radiation from a Jet Pipe – A Second Order Theory". *Journal of Sound and Vibration,* **83**(3), pp. 339–354.

[38] Cazalens, M., Roux, S., Sensiau, C., and Poinsot, T., 2008. "Combustion Instability Problems Analysis for High-Pressure Jet Engine Cores". *Journal of Propulsion and Power,* **24**(4), pp. 770–778.

[39] Chu, B.-T., 1965. "On the Energy Transfer to Small Disturbances in Fluid Flow (Part I)". *Acta Mechanica,* **1**(3), pp. 215–234.

[40] Chu, B.-T., and Kovásznay, L. S. G., 1958. "Non-linear interactions in a viscous heat-conducting compressible gas". *Journal of Fluid Mechanics,* **3**, pp. 494–514.

[41] Cohen, J. M., and Banaszuk, A., 2003. "Factors Affecting the Control of Unstable Combustors". *Journal of Propulsion and Power,* **19**(5), pp. 811–821.

[42] Correa, S. M., 1992. "A Review of NO_x Formation Under Gas-Turbine Combustion Conditions". *Combustion Science and Technology,* **87**, pp. 329–362.

[43] Culick, F. E. C., 2006. *Unsteady Motions in Combustion Chambers for Propulsion Systems*. NATO/RTO. RTO AGARDograph AG-AVT-039.

[44] Deuker, E., 1995. "Ein Beitrag zur Vorausberechnung des akustischen Stabilitätsverhaltens von Gasturbinen-Brennkammern mittels theoretischer und experimenteller Analyse von Brennkammerschwingungen". PhD thesis, RWTH Aachen. published as VDI Fortschritt-Bericht, Reihe 6: Energietechnik, Nr. 317, VDI-Verlag, Düsseldorf.

[45] DIN EN ISO 5136, 2003. *Acoustics – Determination of sound power radiated into a duct by fans and other air-moving devices*.

[46] Döbbeling, K., Hellat, J., and Koch, H., 2007. "25 Years of BBC/ABB/ALSTOM Lean Premix Combustion Technologies". *Journal of Engineering for Gas Turbines and Power,* **129**(1), pp. 2–12.

[47] Dowling, A. P., 1997. "Nonlinear self-excited oscillations of a ducted flame". *Journal of Fluid Mechanics,* **346**, pp. 271–290.

[48] Dowling, A. P., and Hubbard, S., 2000. "Instability in lean premixed combustors". *Proceedings of the Institution of Mechanical Engineers, Part A: Journal of Power and Energy,* **214**(4), pp. 317–332.

[49] Dowling, A. P., and Morgans, A. S., 2005. "Feedback Control of Combustion Oscillations". *Annual Review of Fluid Mechanics,* **37**, pp. 151–182.

[50] Dowling, A. P., and Stow, S. R., 2003. "Acoustic Analysis of Gas Turbine Combustors". *Journal of Propulsion and Power,* **19**(5), pp. 751–764.

[51] Ducruix, S., Schuller, T., Durox, D., and Candel, S., 2005. "Combustion Instability Mechanisms in Premixed Combustors". In *Combustion Instabilities in Gas Turbine Engines*, T. C. Lieuwen and V. Yang, eds., Progess in Astronautics and Aeronautics. AIAA, Inc., Reston, ch. 9, pp. 179–212.

[52] Eldredge, J. D., and Dowling, A. P., 2003. "The absorption of axial acoustic waves by a perforated liner with bias flow". *Journal of Fluid Mechanics,* **485**, pp. 307–335.

[53] Energy Information Administration, U.S. Department of Energy, 2008. *International Energy Outlook 2008*. www.eia.doe.gov/oiaf/ieo/index.html.

[54] Escudier, M. P., 1987. "Confined Vortices in Flow Machinery". *Annual Review of Fluid Mechanics,* **19**, pp. 27–52.

[55] Escudier, M. P., and Keller, J. J., 1985. "Recirculation in Swirling Flow: A Manifestation of Vortex Breakdown". *AIAA Journal,* **23**(1), pp. 111–116.

[56] Evesque, S., and Polifke, W., 2002. "Low-Order Acoustic Modelling for Annular Combustors: Validation and Inclusion of Modal Coupling". ASME Paper GT-2002-30064.

[57] Fischer, A., 2004. "Hybride, thermoakustische Charakterisierung von Drallbrennern". PhD thesis, Lehrstuhl für Thermodynamik, TU München.

[58] Furstoss, M., Thenail, D., and Galland, M. A., 1997. "Surface Impedance Control for Sound Absorption: Direct and Hybrid Passive/Active Strategies". *Journal of Sound and Vibration,* **203**(2), pp. 219–236.

[59] Gärtner, E., 2008. "Das Wind-Erdgas-Kartell". *Neue Züricher Zeitung,* **182**, p. 23.

[60] German Federal Ministry of Economics and Technology, 2008. *COORETEC Lighthouse Concept – The path to fossil-fired power plants for the future.* Research Report, No. 566,
http://www.bmwi.de/English/Navigation/Service/publications,did=259508.html.

[61] Giauque, A., Nicoud, F., and Brear, M., 2007. "Numerical assessment of stability criteria from disturbance energies in gaseous combustion". AIAA Paper 2007-3425.

[62] Graf Finck von Finckenstein, K., 1991. *Grundkurs Mathematik für Ingenieure*, 3rd ed. B. G. Teubner Stuttgart.

[63] Grassl, H., Kokott, J., Kulessa, M., Luther, J., Nuscheler, F., Sauerborn, R., Schellnhuber, H.-J., Schubert, R., and Schulze, E.-D., 2004. *World in Transition: Towards Sustainable Energy Systems.* Earthscan London and Sterling, VA. http://www.wbgu.de/wbgu_jg2003_engl.html.

[64] Gruschka, U., Janus, B., Meisl, J., Huth, M., and Wasif, S., 2008. "ULN System for the New SGT5-8000H Gas Turbine: Design and High Pressure Rig Test Results". ASME Paper GT2008-51208.

[65] Guicking, D., and Karcher, K., 1984. "Active Impedance Control for One-Dimensional Sound". *Journal of Vibration, Acoustics, Stress, and Reliability in Design,* **106**, pp. 393–396.

[66] Guicking, D., and Lorenz, E., 1984. "An Active Sound Absorber With Porous Plate". *Journal of Vibration, Acoustics, Stress, and Reliability in Design,* **106**, pp. 389–392.

[67] Gustavsen, B., 2005. *User's Manual for VECTFIT version 2.0 for Matlab.* http://www.energy.sintef.no/Produkt/VECTFIT/index.asp.

[68] Gustavsen, B., and Semlyen, A., 1999. "Rational Approximation of Frequency Domain Responses by Vector Fitting". *IEEE Transactions on Power Delivery,* **14**(3), pp. 1052–1061.

[69] Güthe, F., Lachner, R., Schuermans, B., Biagioli, F., Geng, W., Inauen, A., Schenker, S., Bombach, R., and Hubschmidt, W., 2006. "Flame imaging on the ALSTOM EV-burner: thermo acoustic pulsations and CFD-validation". AIAA Paper 2006-437.

[70] Güthe, F., and Schuermans, B., 2007. "Phase-locking in post-processing for pulsating flames". *Measurement Science and Technology,* **18**(9), pp. 3036–3042.

[71] Haber, L. C., Vandsburger, U., Saunders, W. R., and Khanna, V. K., 2000. "An Examination of the Relationship between Chemiluminescent Light Emission and Heat Release Rate under Non-adiabatic Conditions". ASME Paper 2000-GT-0121.

[72] Hardalupas, Y., and Orain, M., 2004. "Local measurements of the time-dependent heat release rate and equivalence ratio using chemiluminescent emission from a flame". *Combustion and Flame,* **139**, pp. 188–207.

[73] Heckl, M. A., 1990. "Non-linear Acoustic Effects in the Rijke Tube". *Acustica,* **72**, pp. 63–71.

[74] Hermann, J., and Orthmann, A., 2002. "Combustion Dynamics: Application of Active Instability Control to Heavy Duty Gas Turbines". In *Active Control of Engine Dynamics*. RTO/NATO, pp. 6.1–6.16. RTO Educational Notes 20 (RTO-EN-020).

[75] Hermann, J. (IfTA GmbH, Gröbenzell, Germany). Personal communication.

[76] Hoffmann, S., Weber, G., Judith, H., Hermann, J., and Orthmann, A., 1999. "Application of Active Combustion Control to Siemens Heavy Duty Gas Turbines". In *Gas Turbine Engine Combustion, Emissions and Alternative Fuels*. RTO/NATO, pp. 40.1–40.13. RTO Meeting Proceedings 14 (RTO-MP-14).

[77] Hofler, T. J., 1986. "Thermoacoustic Refrigerator Design and Performance". PhD thesis, Physics Department, University of California, San Diego.

[78] Holste, F., and Neise, W., 1992. "Experimental Comparison of Standardized Sound Power Measurement Procedures for Fans". *Journal of Sound and Vibration,* **152**(1), pp. 1–26.

[79] Hubbard, S., and Dowling, A. P., 2001. "Acoustic Resonances of an Industrial Gas Turbine Combustion System". *Journal of Engineering for Gas Turbines and Power,* **123**(4), pp. 766–773.

[80] Huber, A., Romann, P., and Polifke, W., 2008. "Filter-Based Time-Domain Impedance Boundary Conditions for CFD Applications". ASME Paper GT2008-51195.

[81] International Energy Agency, 2006. *World Energy Outlook 2006.* http://www.worldenergyoutlook.org/2006.asp.

[82] Isella, G., Seywert, C., Culick, F. E. C., and Zukoski, E. E., 1997. "A Further Note on Active Control of Combustion Instabilities Based on Hysteresis". *Combustion Science and Technology,* **126**, pp. 381–388.

[83] Jones, C. M., Lee, J. G., and Santavicca, D. A., 1999. "Closed-Loop Active Control of Combustion Instabilities Using Subharmonic Secondary Fuel Injection". *Journal of Propulsion and Power,* **15**(4), pp. 584–590.

[84] Kaufmann, P., Krebs, W., Valdes, R., and Wever, U., 2008. "3d Thermoacoustic Properties of Single Can and Multi Can Combustor Configurations". ASME Paper GT2008-50755.

[85] Keller, J. J., 1995. "Thermoacoustic Oscillations in Combustion Chambers of Gas Turbines". *AIAA Journal,* **33**(12), pp. 2280–2287.

[86] Knoop, P., Culick, F. E. C., and Zukoski, E. E., 1996. "Extension of the Stability of Motions in a Combustion Chamber by Non-Linear Active Control Based on Hysteresis". In 26th International Symposium on Combustion, Naples, Italy.

[87] Kopitz, J., Huber, A., Sattelmayer, T., and Polifke, W., 2005. "Thermoacoustic Stability Analysis of an Annular Combustion Chamber with Acoustic Low Order Modeling and Validation Against Experiment". ASME Paper 2005-GT-68797.

[88] Kopitz, J., and Polifke, W., 2008. "CFD-based application of the Nyquist criterion to thermo-acoustic instabilities". *Journal of Computational Physics,* **227**, pp. 6754–6778.

[89] Kostrzewa, K., Noll, B., Aigner, M., Lepers, J., Krebs, W., Prade, B., and Huth, M., 2007. "Validation of advanced computational methods for determining flame transfer functions in gas turbine combustion systems". ASME Paper GT2007-27267.

[90] Krebs, W., Bethke, S., Lepers, J., Flohr, P., Johnson, C., and Sattinger, S., 2005. "Thermoacoustic Design Tools and Passive Control: Siemens Power Generation Approaches". In *Combustion Instabilities in Gas Turbine Engines*, T. C. Lieuwen and V. Yang, eds., Progess in Astronautics and Aeronautics. AIAA Inc., Reston, VA, ch. 5, pp. 89–112.

[91] Krebs, W., Flohr, P., Prade, B., and Hoffmann, S., 2002. "Thermoacoustic Stability Chart for High-Intensity Gas Turbine Combustion Systems". *Combustion Science and Technology,* **174**(7), pp. 99–128.

[92] Krüger, U., Hüren, J., Hoffmann, S., Krebs, W., and Bohn, D., 1999. "Prediction of Thermoacoustic Instabilities with Focus on the Dynamic Flame Behavior for the 3A-Series Gas Turbine of Siemens KWU". ASME Paper 99-GT-111.

[93] Krüger, U., Hüren, J., Hoffmann, S., Krebs, W., Flohr, P., and Bohn, D., 2001. "Prediction and Measurement of Thermoacoustic Improvements in Gas Turbines with Annular Combustion Chambers". *Journal of Engineering for Gas Turbines and Power,* **123**(3), pp. 575–566.

[94] Lacarelle, A., Luchtenburg, D. M., Bothien, M. R., Noack, B. R., and Paschereit, C. O., 2008. "A Combination of Image Post-Processing Tools to Identify Coherent Structures of Premixed Flames". In Proceedings of the 2nd International Conference on Jets, Wakes and Separated Flows, Berlin, Germany.

[95] Lacy, B., Ziminsky, W., Lipinski, J., Varatharajan, B., Yilmaz, E., and Brumberg, J., 2008. "Low Emissions Combustion System Development for the GE Energy High Hydrogen Turbine Program". ASME Paper GT2008-50823.

[96] Lavrentjev, J., Åbom, M., and Bodén, H., 1995. "A Measurement Method for Determining the Source Data of Acoustic Two-Port Sources". *Journal of Sound and Vibration,* **183**(3), pp. 517–531.

[97] Lawson, C. L., and Hanson, R. J., 1974. *Solving Least Squares Problems.* Series in Automatic Computation. Prentice-Hall, Inc., Englewood Cliffs, NJ.

[98] Lazik, W., Doerr, T., Bake, S., von der Bank, R., and Rackwitz, L., 2008. "Development of Lean-Burn Low-NO_x Combustion Technology at Rolls-Royce Deutschland". ASME Paper GT2008-51115.

[99] Lechner, C., and Seume, J., eds., 2003. *Stationäre Gasturbinen.* Spinger-Verlag Berlin.

[100] LeConte, J., 1858. "On the Influence of Musical Sounds on the Flame of a Jet in Coal Gas". *American Journal of Science in Arts,* **23**, pp. 62–67.

[101] Lefebvre, A. H., 1999. *Gas Turbine Combustion*, 2. ed. Taylor & Francis, New York.

[102] Leibovich, S., 1978. "The Structure of Vortex Breakdown". *Annual Review of Fluid Mechanics,* **10**, pp. 221–246.

[103] Leonard, G., and Stegmaier, J., 1994. "Development of an Aeroderivative Gas Turbine Dry Low Emissions Combustion System". *Journal of Engineering for Gas Turbines and Power,* **116**(3), pp. 542–547.

[104] Lepers, J., Krebs, W., Prade, B., Flohr, P., Pollarolo, G., and Ferrante, A., 2005. "Investigation of Thermoacoustic Stability Limits of an Annular Gas Turbine Combustor Test-Rig with and without Helmholtz Resonators". ASME Paper GT2005-68246.

[105] Levine, H., and Schwinger, J., 1948. "On the Radiation of Sound from an Unflanged Circular Pipe". *Physical Review,* **73**(4), pp. 383–406.

[106] Li, Y., 2004. "Active and Adaptive-Passive Control of Acoustic Impedance with Thermoacoustic Cooling Applications". PhD thesis, Purdue University.

[107] Li, Y., Chiu, G.-C., and Mongeau, L., 2004. "Dual-Driver Standing Wave Tube: Acoustic Impedance Matching with Robust Repetitive Control". *IEEE Transactions on Control Systems Technology,* **12**(6), pp. 869–880.

[108] Lieuwen, T., 2001. "Theoretical investigation of unsteady flow interactions with a premixed planar flame". *Journal of Fluid Mechanics,* **435**, pp. 289–303.

[109] Lieuwen, T., and Neumeier, Y., 2002. "Nonlinear Pressure-Heat Release Transfer Function Measurements in a Premixed Combustor". *Proceedings of the Combustion Institute,* **29**, pp. 99–105.

[110] Lieuwen, T., Torres, H., Johnson, C., and Zinn, B. T., 2001. "A Mechanism of Combustion Instability in Lean Premixed Gas Turbine Combustors". *Journal of Engineering for Gas Turbines and Power,* **123**(1), pp. 182–189.

[111] Lieuwen, T., and Zinn, B. T., 1998. "Theoretical Investigation of Combustion Instability Mechanisms in Lean Premixed Gas Turbines". AIAA Paper 98-0641.

[112] Lieuwen, T., and Zinn, B. T., 2000. "Application of Multipole Expansions to Sound Generation from Ducted Unsteady Combustion Processes". *Journal of Sound and Vibration,* **235**(3), pp. 405–414.

[113] Lieuwen, T. C., 2002. "Experimental Investigation of Limit-Cycle Oscillations in an Unstable Gas Turbine Combustor". *Journal of Propulsion and Power,* **18**(1), pp. 61–67.

[114] Lieuwen, T. C., and Yang, V., eds., 2005. *Combustion Instabilities in Gas Turbine Engines.* Progess in Astronautics and Aeronautics. AIAA, Inc., Reston, VA.

[115] Lieuwen, T. C. (Georgia Institute of Technology, Atlanta, USA). Personal communication.

[116] Lucca-Negro, O., and O'Doherty, T., 2001. "Vortex breakdown: a review". *Progress in Energy and Combustion Science,* **27**, pp. 431–481.

[117] Manoj Kumar, B., and Sujith, R. I., 1998. "Exact Solution for One-Dimensional Acoustic Fields in Ducts With Polynomial Mean Temperature Profiles". *Journal of Vibration and Acoustics,* **120**, pp. 965–969.

[118] Marble, F. E., and Candel, S. M., 1977. "Acoustic Disturbance from Gas Non-Uniformities Convected through a Nozzle". *Journal of Sound and Vibration,* **55**(2), pp. 225–243.

[119] Martin, C. E., Benoit, L., Sommerer, Y., Nicoud, F., and Poinsot, T., 2006. "Large-Eddy Simulation and Acoustic Analysis of a Swirled Staged Turbulent Combustor". *AIAA Journal,* **44**(4), pp. 741–750.

[120] Marx, C., 1841. "Über das Tönen erhitzter gläserner Röhren". *Journal für Praktische Chemie,* **22**(1), pp. 129–135.

[121] Matveev, K., and Culick, F., 2002. "Experimental and Mathematical Modeling of Thermoacustic Instabilities in a Rijke Tube". AIAA Paper 2002-1013.

[122] Matveev, K. I., and Culick, F. E. C., 2003. "A study of transition to instability in a Rijke tube with axial temperature gradient". *Journal of Sound and Vibration,* **264**(3), pp. 689–706.

[123] McManus, K. R., Han, F., Dunstan, W., Barbu, C., and Shah, M., 2004. "Modelling and Control of Combustion Dynamics in Insdustrial Gas Turbines". ASME Paper GT2004-53872.

[124] McManus, K. R., Poinsot, T., and Candel, S. M., 1993. "A review of active control of combustion instabilities". *Progress in Energy and Combustion Science,* **19**, pp. 1–29.

[125] Moeck, J. P., Bothien, M. R., Guyot, D., and Paschereit, C. O., 2007. "Phase-Shift Control of Combustion Instability Using (Combined) Secondary Fuel Injection and Acoustic Forcing". In *Active Flow Control, Notes on Numerical Fluid Mechanics and Multidisciplinary Design Vol. 95*, R. King, ed. Springer-Verlag Berlin, pp. 408–421.

[126] Moeck, J. P., Bothien, M. R., Paschereit, C. O., Gelbert, G., and King, R., 2007. "Two-Parameter Extremum Seeking for Control of Thermoacoustic Instabilities and Characterization of Linear Growth". AIAA Paper 2007-1416.

[127] Moeck, J. P., Bothien, M. R., Schimek, S., Lacarelle, A., and Paschereit, C. O., 2008. "Subcritical thermoacoustic instabilites in a premixed combustor". AIAA Paper 2008-2946.

[128] Moeck, J. P., Oevermann, M., Klein, R., Paschereit, C. O., and Schmidt, H., 2009. "A two-way coupling for modeling thermoacoustic instabilities in a flat flame Rijke tube". *Proceedings of the Combustion Insitute,* **32**, pp. xx–yy. in press, doi:10.1016/j.proci.2008.05.062.

[129] Mongia, H., Held, T., Hsiao, G., and Pandalai, R., 2003. "Challenges and Progress in Controlling Dynamics in Gas Turbine Combustors". *Journal of Propulsion and Power,* **19**(5), pp. 822–829.

[130] MOOG Industrial Controls Division, 2007 (downloaded). *Electrohydraulic Valves. A Technical Look*. http://www.moog.com/Industrial/Servo/.

[131] Morfey, C. L., 1971. "Acoustic Energy in Non-Uniform Flows". *Journal of Sound and Vibration,* **14**(2), pp. 159–170.

[132] Morse, P. M., and Ingard, K. U., 1968. *Theoretical Acoustics*. Mc-Graw-Hill, Inc., New York.

[133] Munjal, M. L., 1987. *Acoustics of Ducts and Mufflers*. Wiley & Sons, Inc., New York.

[134] Munt, R. M., 1990. "Acoustic Transmission Properties of a Jet Pipe with Subsonic Jet Flow: I. The Cold Jet Reflection Coefficient". *Journal of Sound and Vibration,* **142**(3), pp. 413–436.

[135] Myers, M. K., 1986. "An Exact Energy Corollary for Homentropic Flow". *Journal of Sound and Vibration,* **109**(2), pp. 277–284.

[136] Myers, M. K., 1991. "Transport of energy by disturbances in arbitrary steady flows". *Journal of Fluid Mechanics,* **226**, pp. 383–400.

[137] Nagib, H. M., Kiedaisch, J. W., Wygnanski, I. J., Stalker, A. D., Wood, T., and McVeigh, M. A., 2005. "First-In-Flight Full Scale Application of Active Flow Control: The XV-15 Tiltrotor Download Reduction". RTO/NATO, pp. 29.1–29.34. RTO-MP-AVT-111.

[138] Nicoud, F., Benoit, L., Sensiau, C., and Poinsot, T., 2007. "Acoustic Modes in Combustors with Complex Impedances and Multidimensional Active Flames". *AIAA Journal,* **45**(2), pp. 426–441.

[139] Nicoud, F., and Poinsot, T., 2005. "Thermoacoustic instabilities: Should the Rayleigh criterion be extended to include entropy changes?". *Combustion and Flame,* **142**, pp. 153–159.

[140] Noiray, N., 2007. "Analyse linaire et non-linéaire des instabilités de combustion, application aux systèmes à injection multipoints et stratégies de contrôle". PhD thesis, EM2C, École Central Paris.

[141] Noiray, N., Durox, D., Schuller, T., and Candel, S., 2007. "A method for estimating the noise level of unstable combustion based on the flame describing function". In 11th CEAS-ASC Workshop on Combustion Noise, Lisbon, Portugal.

[142] Olson, H. F., and May, E. G., 1953. "Electronic Sound Absorber". *Journal of the Acoustical Society of America,* **25**(6), pp. 1130–1136.

[143] Orduña-Bustamente, F., and Nelson, P. A., 1992. "An adaptive controller for the active absorption of sound". *Journal of the Acoustical Society of America,* **91**(5), pp. 2740–2747.

[144] Paschereit, C. O., , and Gutmark, E. J., 2002. "Proportional Control of Combustion Instabilities in a Simulated Gas-Turbine Combustor". *Journal of Propulsion and Power,* **18**(6), pp. 1298–1304.

[145] Paschereit, C. O., Flohr, P., and Gutmark, E. J., 2006. "Combustion Control by Vortex Breakdown Stabilization". *Journal of Turbomachinery,* **128**(4), pp. 679–688.

[146] Paschereit, C. O., Flohr, P., and Schuermans, B., 2001. "Prediction of combustion oscillations in gas turbine combustors". AIAA Paper 2001-0484.

[147] Paschereit, C. O., and Gutmark, E., 2004. "The Effectiveness of Passive Combustion Control Methods". ASME Paper GT2004-53587.

[148] Paschereit, C. O., and Gutmark, E., 2006. "Control of High frequency Thermoacoustic Pulsations by Distributed Vortex Generators". *AIAA Journal,* **44**(3), pp. 550–557.

[149] Paschereit, C. O., Gutmark, E., and Weisenstein, W., 1998. "Structure and control of thermoacoustic instabilities in a gas-turbine combustor". *Combustion Science and Technology,* **138**, pp. 213–232.

[150] Paschereit, C. O., Gutmark, E., and Weisenstein, W., 2000. "Excitation of Thermoacoustic Instabilities by Interaction of Acoustics and Unstable Swirling Flow". *AIAA Journal,* **38**(6), pp. 1025–1034.

[151] Paschereit, C. O., and Gutmark, E. J., 2004. "A Combustion Chamber Burner Including a Corrugated Burner Outlet". UK Patent No. GB2397643.

[152] Paschereit, C. O., Gutmark, E. J., and Weisenstein, W., 1999. "Coherent structures in swirling flows and their role in acoustic combustion control". *Physics of Fluids,* **11**(9), pp. 2667–2678.

[153] Paschereit, C. O., Moeck, J. P., and Bothien, M. R., 2006. "State-Space Modeling of Thermoacoustic Systems for Stability Analysis and Time Domain Simulation". In Proceedings of the 13th International Congress on Sound and Vibration, Vienna, Austria.

[154] Paschereit, C. O., and Polifke, W., 1998. "Investigation of the Thermoacoustic Characteristics of a Lean Premix Gas Turbine Burner". ASME Paper 98-GT-582.

[155] Paschereit, C. O., Schuermans, B., and Campos-Delgado, D., 2001. "Active Combustion Control using an Evolution Algorithm". AIAA Paper 2001-0783.

[156] Paschereit, C. O., Schuermans, B., Polifke, W., and Mattson, O., 2002. "Measurement of Transfer Matrices and Source Terms of Premixed Flames". *Journal of Engineering for Gas Turbines and Power,* **124**(2), pp. 239–247.

[157] Peat, K. S., 1982. "Evaluation of Four-Pole Parameters for Ducts with Flow by the Finite Element Method". *Journal of Sound and Vibration,* **84**(3), pp. 389–395.

[158] Peters, M. C. A. M., Hirschberg, A., Reijnen, A. J., and J., W. A. P., 1993. "Damping and reflection coefficient measurements for an open pipe at low Mach and low Helmholtz numbers". *Journal of Fluid Mechanics,* **256**, pp. 499–534.

[159] Pfeifer, C., Moeck, J. P., Enghardt, L., and Paschereit, C. O., 2008. "Localization of Combustion Noise Sources in Enclosed Flames". In Proceedings of the 2nd International Conference on Jets, Wakes and Separated Flows, Berlin, Germany.

[160] Pierce, A. D., 1991. *Acoustics: An Introduction to Its Physical Principles and Applications*. Acoustical Society of America, New York.

[161] Pinaud, A., 1837. "Ueber eine neue Art der Ton-Erzeugung". *Annalen der Physik und Chemie,* **118**(13), pp. 610–618.

[162] Poinsot, T., Bourienne, F., Candel, S., Esposito, E., and Lang, W., 1989. "Suppression of Combustion Instabilities by Active Control". *Journal of Propulsion and Power,* **5**(1), pp. 14–20.

[163] Poinsot, T., Chatelier, C. L., Candel, S. M., and Esposito, E., 1986. "Experimental Determination of the Reflection Coefficient of a Premixed Flame in a Duct". *Journal of Sound and Vibration,* **107**(2), pp. 265–278.

[164] Poinsot, T., Veynante, D., Bourienne, F., Candel, S., Esposito, E., and Surget, J., 1988. "Initiation and Suppression of Combustion Instabilities by Active Control". *22nd Symposium on Combustion / The Combustion Institute*, pp. 1363–1370.

[165] Poinsot, T., Yip, B., Veynante, D., Trouvé, A., Samaniego, J. M., and Candel, S., 1992. "Active control: An investigation method for combustion instability". *Journal de Physique III,* **2**(7), pp. 1331–1357.

[166] Poinsot, T. J., Trouvé, A. C., Veynante, D. P., Candel, S. M., and Esposito, E. J., 1987. "Vortex-driven acoustically coupled combustion instabilities". *Journal of Fluid Mechanics,* **177**, pp. 265–292.

[167] Polifke, W., 2004. "Combustion Instabilities". VKI Lecture Series Advances in Acoustics and Applications, Brussels, Belgium.

[168] Polifke, W., Paschereit, C. O., and Döbbeling, K., 2001. "Constructive and Destructive Interference of Acoustic and Entropy Waves in a Premixed Combustor with a Choked Exit". *International Journal of Acoustics and Vibration,* **6**(3), pp. 135–146.

[169] Polifke, W., Paschereit, C. O., and Sattelmayer, T., 1997. "A Universally Applicable Stability Criterion for Complex Thermo-Acoustic Systems". In 18. Deutsch-Niederl¨ndischer Flammentag, Delft, NL, pp. 455–460. VDI Bericht 1313.

[170] Polifke, W., Poncet, A., Paschereit, C. O., and Döbbeling, K., 2001. "Reconstruction of Acoustic Transfer Matrices by Instationary Computational Fluid Dynamics". *Journal of Sound and Vibration,* **245**(3), pp. 483–510.

[171] Pota, H. R., and Kelkar, A. G., 2001. "Modeling and Control of Acoustic Ducts". *Journal of Vibration and Acoustics,* **123**, pp. 2–10.

[172] Putnam, A. A., 1971. *Combustion Driven Oscillations in Industry.* American Elsevier, New York.

[173] Putnam, A. A., Belles, F. E., and Kentfield, J. A. C., 1986. "Pulse Combustion". *Progress in Energy and Combustion Science,* **12**, pp. 43–79.

[174] Putnam, A. A., and Dennis, W. R., 1953. "A Study of Burner Oscillations of the Organ-Pipe Type". *Transactions of ASME,* **75**(1), pp. 15–28.

[175] Raun, R. L., Beckstead, M. W., Finlinson, J. C., and Brooks, K. P., 1993. "A Review of Rijke Tubes, Rijke Burners and Related Devices". *Progress in Energy and Combustion Science,* **19**, pp. 313–364.

[176] Rea, S., James, S., Goy, C., and Colechin, M. J. F., 2003. "On-line combustion monitoring on dry low NOx industrial gas turbines". *Measurement Science and Technology,* **14**(7), pp. 1123–1130.

[177] Richards, G. A., Straub, D. L., and Robey, E. H., 2003. "Passive Control of Combustion Dynamics in Stationary Gas Turbines". *Journal of Propulsion and Power,* **19**(5), pp. 795–810.

[178] Richards, G. A., Thornton, J. D., Robey, E. H., and Arellano, L., 2007. "Open-Loop Active Control of Combustion Dynamics on a Gas Turbine Engine". *Journal of Engineering for Gas Turbines and Power,* **129**(1), pp. 38–48.

[179] Rienstra, S. W., and Hirschberg, A., 2006. *An Introduction to Acoustics.* Eindhoven University of Technology. http://www.win.tue.nl/∼sjoerdr/papers/boek.pdf.

[180] Roux, S., Lartigue, G., Poinsot, T., Meier, U., and Bérat, C., 2005. "Studies of mean and unsteady flow in a swirled combustor using experiments, acoustic analyis, and large eddy simulations". *Combustion and Flame,* **141**, pp. 40–54.

[181] Rowley, C. W., Williams, D. R., Colonius, T., Murray, R. M., and Macmynoski, D. G., 2006. "Linear models for control of cavity flow oscillations". *Journal of Fluid Mechanics,* **547**, pp. 317–330.

[182] Sattelmayer, T., 2003. "Influence of the Combustor Aerodynamics on Combustion Instabilities From Equivalence Ratio Fluctuations". *Journal of Engineering for Gas Turbines and Power,* **125**(1), pp. 11–19.

[183] Sattelmayer, T., Felchlin, M. P., Haumann, J., Hellat, J., and Styner, D., 1992. "Second-Generation Low-Emission Combustors for ABB Gas Turbines: Burner Development and Tests at Atmospheric Pressure". *Journal of Engineering for Gas Turbines and Power,* **114**(1), pp. 118–125.

[184] Sattelmayer, T., and Polifke, W., 2003. "Assessment of Methods for the Computation of the Linear Stability of Combustors". *Combustion Science and Technology,* **175**, pp. 453–476.

[185] Sattelmayer, T., and Polifke, W., 2003. "A Novel Method for the Computation of the Linear Stability of Combustors". *Combustion Science and Technology,* **175**, pp. 477–497.

[186] Schadow, K. C., and Gutmark, E., 1992. "Combustion Instability Related to Vortex Shedding in Dump Combustors and their Passive Control". *Progress in Energy and Combustion Science,* **18**, pp. 117–132.

[187] Schlichting, H., and Gersten, K., 2006. *Grenzschicht-Theorie*, 10th ed. Springer-Verlag Berlin Heidelberg.

[188] Schmitt, P., Poinsot, T., Schuermans, B., and Geigle, K. P., 2007. "Large-eddy simulation and experimental study of heat transfer, nitric oxide emissions and combustion instability in a swirled turbulent high-pressure burner". *Journal of Fluid Mechanics,* **570**, pp. 17–46.

[189] Schuermans, B., 2003. "Modeling and Control of Thermoacoustic Instabilities". PhD thesis, École Polytechnique Fédéral de Lausanne.

[190] Schuermans, B., Bellucci, V., Guethe, F., Meili, F., Flohr, P., and Paschereit, C. O., 2004. "A Detailed Analysis of Thermoacoustic Interaction Mechanisms in a Turbulent Premixed Flame". ASME Paper GT2004-53831.

[191] Schuermans, B., Bellucci, V., and Paschereit, C. O., 2003. "Thermoacoustic Modeling and Control of Multi Burner Combustion Systems". ASME Paper 2003-GT-38688.

[192] Schuermans, B., Guethe, F., and Mohr, W., 2008. "Optical Transfer Function Measurements for Technically Premixed Flames". ASME Paper GT2008-51500.

[193] Schuermans, B., Luebcke, H., Bajusz, D., and Flohr, P., 2005. "Thermoacoustic Analysis of Gas Turbine Combustion Systems Using Unsteady CFD". ASME Paper GT2005-68393.

[194] Schuermans, B., Paschereit, C. O., and Monkewitz, P., 2006. "Non-linear Combustion Instabilities in Annular Gas-Turbine Combustors". AIAA Paper 2006-0549.

[195] Schuermans, B., Polifke, W., and Paschereit, C. O., 1999. "Modeling of Transfer Matrices of Premixed Flames and Comparison to Experimental Results". ASME Paper 1999-GT-0132.

[196] Schuermans, B. B. H., Polifke, W., Paschereit, C. O., and van der Linden, J. H., 2000. "Prediction of Acoustic Pressure Spectra in Combustion Systems Using Swirl Stabilized Gas Turbine Burners". ASME Paper 2000-GT-0105.

[197] Selle, L., Benoit, L., Poinsot, T., Nicoud, F., and Krebs, W., 2006. "Joint use of compressible large-eddy simulation and Helmholtz solvers for the analyis of rotating modes in an industrial swirled burner". *Combustion and Flame,* **145**, pp. 194–205.

[198] Sengissen, A. X., Giauque, A. V., Staffelbach, G. S., Porta, M., Krebs, W., Kaufmann, P., and Poinsot, T. J., 2007. "Large eddy simulation of piloting effects on turbulent swirling flames". *Proceedings of the Combustion Institute,* **31**, pp. 1729–1736.

[199] Sensiau, C., Nicoud, F., and Poinsot, T., 2008. "Computation of azimuthal combustion instabilities in an helicopter combustion chamber". AIAA Paper 2008-2947.

[200] Seume, J. R., Vortmeyer, N., Krause, W., Hermann, J., Hantschk, C.-C., Zangl, P., Gleis, S., Vortmeyer, D., and Orthmann, A., 1998. "Application of Active Combustion Instability Control to a Heavy Duty Gas Turbine". *Journal of Engineering for Gas Turbines and Power,* **120**(4), pp. 721–726.

[201] Sewell, J., Sobieski, P., and Beers, C., 2004. "Application of Continuous Combustion Dynamics Monitoring on Large Industrial Gas Turbines". ASME Paper GT2004-54310.

[202] Smith, J. P., Johnson, B. D., and Burdisso, R. A., 1999. "A broadband passive active sound absorption system". *Journal of the Acoustical Society of America,* **106**(5), pp. 2646–2652.

[203] Sondhauss, G., 1850. "Ueber die Schallschwingungen der Luft in erhitzten Glasröhren und in gedeckten Pfeifen von ungleicher Weite". *Annalen der Physik und Chemie,* **155**(1), pp. 1–34.

[204] Staffelbach, G., Gicquel, L., Boudier, G., and Poinsot, T., 2008. "Large eddy simulation of self excited azimuthal modes in annular combustors". *Proceedings of the Combustion Insitute,* **32**, pp. xx – yy.

[205] Stow, S. R., and Dowling, A. P., 2001. "Thermoacoustic Oscillations in an Annular Combustor". ASME Paper 2001-GT-0037.

[206] Stow, S. R., and Dowling, A. P., 2008. "A Time-Domain Network Model For Nonlinear Thermoacoustic Oscillations". ASME Paper GT2008-50770.

[207] Strahle, W. C., 1971. "On combustion generated noise". *Journal of Fluid Mechanics,* **49**(2), pp. 399–414.

[208] Strahle, W. C., 1972. "Some Results in Combustion Generated Noise". *Journal of Sound and Vibration,* **23**(1), pp. 113–125.

[209] Streb, H., Prade, B., Hahner, T., and Hoffmann, S., 2001. "Advanced Burner Development for the VX4.3A Gas Turbines". ASME Paper 2001-GT-0077.

[210] Strutt, J. W. (3rd Baron Rayleigh), 1878. "The Explanation of Certain Acoustical Phenomena". *Nature,* **18**, pp. 319–321.

[211] Subrahmanyam, P. B., Sujith, R. I., and Lieuwen, T. C., 2001. "A Family of Exact Transient Solutions for Acoustic Wave Propagation in Inhomogeneous Non-Uniform Area Ducts". *Journal of Sound and Vibration,* **240**(4), pp. 705–715.

[212] Subrahmanyam, P. B., Sujith, R. I., and Lieuwen, T. C., 2003. "Propagation of Sound in Inhomogeneous Media: Exact, Transient Solutions in Curvilinear Geometries". *Journal of Vibration and Acoustics,* **125**, pp. 133–136.

[213] Sujith, R. I., Waldherr, G. A., and Zinn, B. T., 1995. "An Exact Solution for One-Dimensional Acoustic Fields in Ducts with an Axial Temperature Gradient". *Journal of Sound and Vibration,* **184**(3), pp. 389–402.

[214] Swift, G. W., 1988. "Thermoacoustic engines". *Journal of the Acoustical Society of America,* **84**(4), pp. 1145–1180.

[215] Swift, G. W., 2007. "Thermoacoustics". In *Springer Handbook of Acoustics*, T. D. Rossing, ed. Springer New York, ch. Thermoacoustics, pp. 239–255.

[216] Swift, G. W., and Spoor, P. S., 1999. "Thermal diffusion and mixture separation in the acoustic boundary layer". *Journal of the Acoustical Society of America,* **106**(4), pp. 1794–1800.

[217] Thenail, D., Galland, M. A., and Sunyach, M., 1994. "Active enhancement of the absorbent properties of a porous material". *Smart Materials and Structures,* **3**(1), pp. 18–25.

[218] Thumuluru, S. K., Bobba, M. K., and Lieuwen, T., 2007. "Mechanisms of the Nonlinear Response of a Swirl Flame to Harmonic Excitation". ASME Paper GT2007-27932.

[219] Thumuluru, S. K., Ma, H.-H., and Lieuwen, T., 2007. "Measurements of the Flame Response to Harmonic Excitation in a Swirl Combustor". AIAA Paper 2007-845.

[220] Tijdeman, H., 1975. "On the Propagation of Sound Waves in Cylindrical Tubes". *Journal of Sound and Vibration,* **39**(1), pp. 1–33.

[221] Torres, H., Lieuwen, T. C., Johnson, C., Daniel, B. R., and Zinn, B. T., 1999. "Experimental Investigation of Combustion Instabilities in a Gas Turbine Combustor Simulator". AIAA Paper 99-0712.

[222] Tran, N., Ducruix, S., and Schuller, T., 2007. "Analysis and control of combustion instabilities by adaptive reflection coefficients". AIAA Paper 2007-3716.

[223] Tran, N., Ducruix, S., and Schuller, T., 2008. "Passive Control of the Inlet Acoustic Boundary of a Swirled Turbulent Burner". ASME Paper GT2008-50425.

[224] Tsien, H. S., 1952. "Servo-Stabilization of Combustion in Rocket Motors". *Journal of the American Rocket Society,* **22**, pp. 256–263 (+268).

[225] van Kampen, J. F., Kok, J. B. W., and van der Meer, T. H., 2007. "Efficient retrieval of the thermo-acoustic flame transfer function from a linearized CFD simulation of a turbulent flame". *International Journal for Numerical Methods in Fluids,* **54**, pp. 1131–1149.

[226] Venugopal, R., and Bernstein, D. S., 1999. "State Space Modeling of an Acoustic Duct with an End-Mounted Speaker". In Proceedings of the 1999 International Conference on Control Applications*, MI, USA*.

[227] Wang, H.-H., and Krstić, M., 2000. "Extremum Seeking for Limit Cycle Minimization". *IEEE Transactions on Automatic Control,* **45**(12), pp. 2432–2437.

[228] Wangher, A., Searby, G., and Quinard, J., 2008. "Experimental investigation of the unsteady response of premixed flame fronts to acoustic pressure waves". *Combustion and Flame,* **154**(1-2), pp. 310–318.

[229] Warnatz, J., Maas, U., and Dibble, R. W., 2006. *Combustion*, 4th ed. Spinger-Verlag Berlin Heidelberg.

[230] Widenhorn, A., Noll, B., and Aigner, M., 2008. "Impedance Boundary Conditions for the Numerical Simulation of Gas Turbine Combustion Systems". ASME Paper GT2008-50445.

[231] Zajadatz, M., Lachner, R., Bernero, S., Motz, C., and Flohr, P., 2007. "Development and Design of ALSTOM's Staged Fuel Gas Injection EV Burner for NO_x Reduction". ASME Paper GT2007-27730.

[232] Zhao, D., and Morgans, A. S., 2007. "Tuned Passive Control of Combustion Instabilities Using Multiple Helmholtz Resonators". AIAA Paper 2007-3423.

[233] Zhou, K., and Doyle, J., 1997. *Essentials of Robust Control.* Prentice Hall, Upper Saddle River, NJ.

[234] Zinn, B., and Lieuwen, T., 2005. "Combustion Instabilities: Basic Concepts". In *Combustion Instabilities in Gas Turbine Engines*, T. C. Lieuwen and V. Yang, eds., Progess in Astronautics and Aeronautics. AIAA, Inc., Reston, VA, ch. 1, pp. 3–26.

[235] Zinn, B., Neumeier, Y., and Lieuwen, T., 2002. Active Control of Combustion Instabilities in Low NOx Gas Turbines. Tech. rep., School of Aerospace Engineering, Georgia Tech.

Publications Associated with the Thesis

In the course of the work, parts of the thesis have already been published previously by the author. The following list gives an overview of these publications.

[1] Bothien, M. R., Moeck, J. P., and Paschereit, C. O., 2009. "Assessment of Different Actuator Concepts for Acoustic Boundary Control of a Premixed Combustor". *Journal of Engineering for Gas Turbines and Power*, in press, doi: 10.1115/1.2969088.

[2] Bothien, M. R., Moeck, J. P., and Paschereit, C. O., 2008. "Active control of the acoustic boundary conditions of combustion test rigs". *Journal of Sound and Vibration*, **318**(4-5), pp. 678–701, http://dx.doi.org/10.1016/j.jsv.2008.04.046.

[3] Moeck, J. P., Bothien, M. R., Schimek, S., and Paschereit, C. O., 2008. "Subcritical Thermoacoustic Instabilites in a Premixed Combustor". AIAA Paper 2008-2946.

[4] Bothien, M. R., Moeck, J. P., and Paschereit, C. O., 2008. "Assessment of Different Actuator Concepts for Acoustic Boundary Control of a Premixed Combustor". ASME Paper GT2008-50171.

[5] Bothien, M. R., Moeck, J. P., and Paschereit, C. O., 2007. "Experimental Validation of Linear Stability Analysis in Premixed Combustors Supported by Active Control". In Proceedings of the 14th International Congress on Sound and Vibration, Cairns, Australia.

[6] Bothien, M. R., Moeck, J. P., Lacarelle, A., and Paschereit, C. O., 2007. "Time Domain Modelling and Stability Analysis of Complex Thermoacoustic Systems". *Proceedings of the Institution of Mechanical Engineers, Part A: Journal of Power and Energy*, **221**(5), pp. 657–668, http://dx.doi.org/10.1243/09576509JPE384.

[7] Moeck, J. P., Bothien, M. R., and Paschereit, C. O., 2007. An Active Control Scheme for Tuning Acoustic Impedances". AIAA Paper 2007-3540.

[8] Bothien, M. R., Moeck, J. P., and Paschereit, C. O., 2007. "Impedance Tuning of a Premixed Combustor Using Active Control". ASME Paper GT2007-27796.

[9] Moeck, J. P., Bothien, M. R., and Paschereit, C. O., Gelbert, G., and R. King, 2007. "Two-Parameter Extremum Seeking for Control of Thermoacoustic Instabilities and Characterization of Linear Growth". AIAA Paper 2007-1416.

[10] Bothien, M. R., Moeck, J. P., and Paschereit, C. O., 2006. "A Modular Approach for Time Domain Modelling of Complex (Thermo-) Acoustic Systems". In Proceedings of the Conference on Modelling Fluid Flow, Budapest, Hungary.

References for Introductory Quotes

[1] Martel, Yann. *Life of Pi*, p. 65, Canongate, Edinburgh, 2003. (p. 60)

[2] Mitchell, David. *Cloud Atlas*, p. 451, Sceptre, London, 2004. (p. 1)

[3] Musil, Robert. *Der Mann ohne Eigenschaften I, Erstes und Zweites Buch*, p. 460, 21st ed. Rowohlt Taschenbuch Verlag, Reinbek Hamburg, 2006. (p. 171)

[4] Shakespeare, William. *Measure for Measure, Lucio, Act I, Scene iv*, p. 19, Reclam, Stuttgart, 2001. (p. 145)

[5] Smith, Zadie. *White Teeth*, p. 317, Penguin, London, 2001. (p. 84)

[6] von Goethe, Johann Wolfgang. *Faust I, Faust, Verses 1699+1700*, 3rd book special edition, C. H. Beck'sche Verlagsbuchhandlung, München, 1998. (p. ii)

[7] von Goethe, Johann Wolfgang. *Faust I, Faust, Verses 447+448*, 3rd book special edition, C. H. Beck'sche Verlagsbuchhandlung, München, 1998. (p. 25)

[8] von Goethe, Johann Wolfgang. *Wilhelm Meisters Wanderjahre, Drittes Buch, Aus Makariens Archiv, 73*, 8th book special edition, C. H. Beck'sche Verlagsbuchhandlung, München, 1998. (p. 47)

[9] von Schiller, Johann Christoph Friedrich. *Gedichte, Das Lied von der Glocke*, p. 188 ff. Kiepenheuer & Witsch, Köln Berlin, 1959. (p. 68)

[10] Wax Tailor. *Hope & Sorrow, Track 7: Positively Inclined*, Lab'Oratoi (Groove Attack), 2007. (p. 159)